Imperial College London
Department of Mechanical Engineering

Large Eddy Simulation of Supersonic Combustion using a Probability Density Function method

Yuri Paixão de Almeida

This PhD thesis is submitted for the degree of
Doctor of Philosophy in Mechanical Engineering
at Imperial College London, March 2019

Copyright declaration

Statement of originality

I certify that the work presented is, to the best of my knowledge, original and the result of my own research, except as acknowledged, and has not been submitted, either in part or whole, for a degree at any other university than Imperial College London.

Abstract

The scramjet propulsion system is regarded to be a key technology to deliver the next generation of hypersonic planes. It consists of a ramjet engine in which the combustion occurs at supersonic speed. Experiments have been used to investigate the scramjet engine, however, the high costs of gathering data is a limiting factor in its development. In this context, the numerical simulation is an affordable alternative to shed a light into supersonic combustion. The simulation of high-speed compressible and reactive flows, however, is not straightforward, including shock/boundary layer interactions and combustion. Nonetheless, most combustion models have been designed for subsonic flames and their portability to high-speed flows is non-trivial.

This work investigates the use of the Probability Density Function (PDF) method for supersonic combustion within the Large Eddy Simulation (LES) framework. Two methods are considered: one is an extension of a joint scalar PDF model (SPDF) for high speed flows and the other is a new joint velocity-scalar PDF formulation (VSPDF). The LES-PDF equations are solved using the Eulerian stochastic fields method, which is implemented into the in-house compressible code CompReal. Their performance are evaluated through a reactive shock-tube, mixing layers and a homogeneous isotropic turbulence cube simulation. Two supersonic burner configurations are simulated to validate the code against experimental data. The results show that sub-grid contributions are important at coarse meshes and the stochastic fields approach can reproduce experimental results. The University of Virginia scramjet configuration A is also simulated using the joint scalar PDF model. Results of topwall pressure, temperature and molar fractions are compared with experimental data.

Overall, the results suggest that the joint scalar PDF is the most robust and reliable formulation and the sub-grid closures for the joint velocity-scalar PDF require further investigation.

Acknowledgements

I would like to firstly acknowledge my Mom and sister for their unconditional love and for supporting my decision of pursuing my PhD at Imperial College. Moving from Rio de Janeiro to London would be a daunting task without their comprehension and encouragement.

I would like to express my gratitude to Jenna for all her love, kindness and inspiration, which make me feel the luckiest person ever for having found her. Her support, happiness and affection were of paramount importance to the conclusion of this work.

I am greatly indebted to all my friends, from Rio de Janeiro to London and beyond, which I do not cite names to avoid any unfairness. Their joy was vital in the moments of struggle and made my PhD experience extraordinary.

I would like to thank my supervisor Dr Salvador Navarro-Martinez, from whom I could always learn something new. Without his wisdom, work ethic and resourcefulness, this work would not be possible. I am grateful for all discussions and insights.

I would also like to acknowledge Prof. Andrew D. Cutler for providing copyright permission to reproduce CARS measurements pictures, which greatly improved the completeness of this work.

At last, I would like to acknowledge the financial support provided by the Brazilian National Council for Scientific and technological Development (CNPq) through the Science without Borders programme, grant no. 233815/2014-7. It would not be possible to perform my PhD studies without their financial support.

Thank you!

Contents

List of Tables

List of Figures

Nomenclature

A_i	drift coefficient
b_i	body force
B_{ij}	diffusion tensor
c_s	isothermal speed of sound
C_α	micromixing constant for variable α
C_μ	Smagorinsky model constant
$E(k)$	kinetic energy in Fourier space
err	normalised error
err_N	standard error
$\mathscr{E}_t$	total energy stochastic field
e_t	total energy
$\mathscr{F}$	mass density function
f	probability density function
f'	fine-grained probability density
G	LES filter function
G_{ij}	Langevin model tensor

g_i	gravity
$\mathscr{H}$	enthalpy stochastic field
h	enthalpy
H_i^{sgs}	total energy convective and pressure-velocity subgrid part
$\mathscr{H}_t$	total resolved enthalpy stochastic field
h_t	total enthalpy, $h + 1/2 u_i u_i$
i	imaginary number
$\boldsymbol{J}$	Jacobian matrix
J	mass diffusion flux
$\boldsymbol{k}$	wavelength
K	resolved kinetic energy
k	kinetic energy
M	molecular weight
Ma	Mach number
M_c	convective Mach number
N	number of samples
N_f	number of stochastic fields
N_s	number of chemical species
$\mathscr{P}$	pressure stochastic field
p	thermodynamic pressure
Pr	Prandtl number

Q	a function
q_i	heat flux
$\dot{Q}$	external heat source
$\mathscr{R}$	subgrid scale turbulence Reynolds number
R_u	universal gas constant
$\mathscr{S}$	sensor coefficient
S	source term
Sc	Schmidt number
S_{ij}	deformation tensor
T	temperature
t	time
$\mathscr{U}$	velocity stochastic field
u_i	velocity
U_c	convective velocity of large structures
V_i	diffusion velocity
v_i	sample velocity
W_i	Wiener process
X	molar fraction
x_i	physical coordinate
$\mathscr{Y}$	mass fraction stochastic field
Y	mass fraction

Greek Symbols

α	thermal diffusivity or perturbation amplitude
Δ	cut-off scale/filter width in space
δ	Dirac delta function
δ_{ij}	Kronecker delta function
δ_w	vorticity thickness
ϵ	rate of dissipation of the (subgrid) turbulent kinetic energy
ε	random number
γ	specific heat ratio
γ_a	dissipation coefficient
Γ	mass diffusion coefficient
$\Gamma_{\alpha\beta}$	binary mass diffusion coefficient
λ	thermal conductivity
λ_t	Taylor microscale
μ	dynamic viscosity
μ_b	bulk viscosity
ν	kinematic viscosity, μ/ρ
ω	turbulence frequency
ϕ	real scalar field
ϕ	scalar
Π_d	pressure dilatation

ψ	sample scalar
Ψ_τ	averaged characteristic function
ψ_τ	characteristic function
ρ	density
σ	standard deviation
σ^2	variance
σ_{ij}^{sgs}	viscous dissipation subgrid contribution
τ_{ij}	viscous stress tensor
τ^n, ξ_α^n	n^{th}-stochastic field
τ_{sgs}	subgrid timescale
ϱ	density stochastic field
ζ	Gaussian white noise

Subscripts

α, β	index for chemical species
p	perturbation
rms	root mean square
sgs	subgrid scale
t	turbulent, applied in RANS context

Superscripts

d	deterministic drift component
g	Gaussian random component

$+$	Lagrangian framework
$\prime$	temporal or filtered fluctuation
sgs	subgrid scale

Abbreviations

DNS	Direct Numerical Simulation
DRP	Dispersion-Relation-Preserving
FDF	Filtered Density Function
FMDF	Filtered Mass Density Function
HLLC	Harten-Lax-van Leer-Contact
LES	Large Eddy Simulation
MDF	Mass Density Function
PDF	Probability Density Function
RANS	Reynolds Averaged Navier-Stokes
TVD	Total Variation Diminishing

Chapter 1

Introduction

Hypersonic planes could play an important role in the future of civil aviation. For instance, they would enable flights from London to New York to be completed in an hour or less. Various propulsion systems for such aircraft have been investigated and the scramjet (supersonic combustion ramjet) engine is one of the most promising technology. The scramjet is an airbreathing engine and it uses ram compression to decelerate and pressurize the hypersonic incoming air, making the combustion occur at supersonic speeds. It therefore has a simple design, without the moving parts necessary in gas-turbine engines. On the other hand, scramjets involve more complex physical phenomena due to the supersonic combustion than conventional engines, where the combustion occurs at subsonic speed.

Figure 1.1 provides an overview of a typical scramjet along with its main physical features. As air enters the engine, oblique shock waves begin to be reflected at the walls and a shock train is formed. There are severe shock/boundary-layer interactions at this stage. The velocity is also reduced from hypersonic to supersonic as pressure increases. At last, gas fuel is injected from wall orifices allowing combustion to occur at supersonic speed and generating thrust.

Experimental investigation has been conducted to better understand the physics associated with supersonic combustion, such as shock waves and flame interaction. The HIFiRE (Hypersonic International Flight Research Experimentation) project is a leading

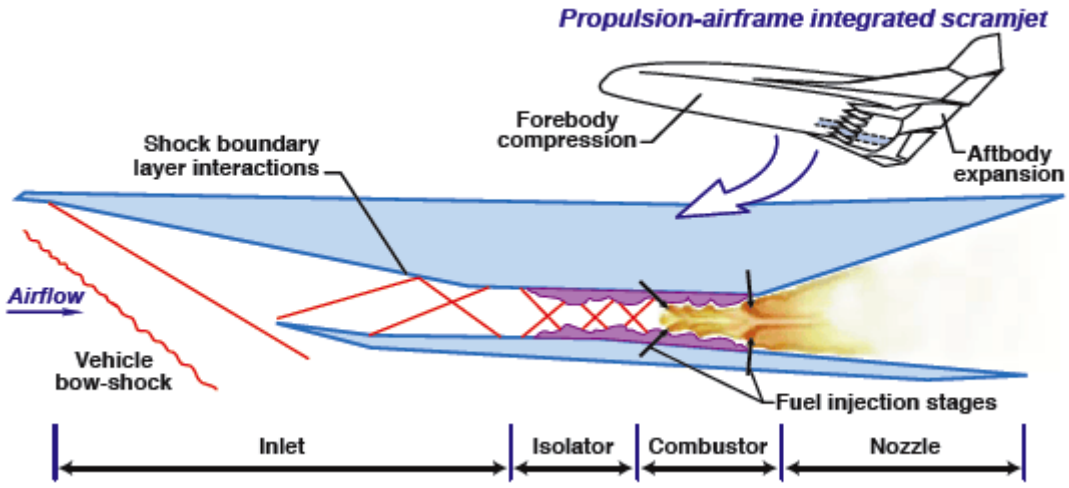

Figure 1.1: Typical scramjet model - figure extracted from NASA website[1].

initiative in scramjet development [1]. It has a jointly development including, but not limited to, the Air Force Research Laboratory (AFRL) and NASA in the USA, and the Defense Science Technology Organisation (DSTO) in Australia. The HyShot project from the University of Queensland, within the HIFire programme, have performed a successful launch of a re-entry vehicle, in which the supersonic combustion occurred for approximately 3 seconds, as reported by Hass *et al.* [2]. This experiment provided useful data as the wall pressure, being used for numerical modelling and validation [3, 4].

Ground-based experiments have also been conducted [5, 6, 7, 8], providing valuable insights into the physics of a scramjet. However, despite being the best method for obtaining reliable data, intensive experiments in such harsh conditions are very expensive. Researchers therefore have heavily relied on numerical simulation to investigate different parameters on scramjets, such as fuel injection position and velocity, geometrical factors and structural analysis [9, 3, 10, 11, 12]. The complex physical features present in supersonic combustion, however, imposes a severe numerical modelling challenge and state-of-the-art techniques are required to reproduce the scramjet behaviour in a computational simulation.

[1]Use of the figure is for educational and informational purposes only, following NASA Media Usage Guidelines for non-commercial use.

1.1 Motivation and Objectives

With increasing computing capacity, advanced turbulence modelling techniques have become largely popular for simulating reacting systems. The Large Eddy Simulation (LES) method has therefore been used for combustion research. This technique consists in applying a spatial filter to the transport and constitutive equations, thereby solving the filtered part and modelling the part within the spatial cutoff of the filter, called subgrid scale. However, the modelling of the filtered chemical source term in the conservation equation for the mass fractions due to the combustion reactions still poses a challenge. Because of its high non-linearity, the subgrid contribution of the source term is very difficult to predict.

In this context, the Probability Density Function (PDF) combustion model [13] has been investigated for supersonic combustion applications [9, 10, 14, 15, 16]. This is because of its ability to exactly solve the reacting term [17] even after filtering the transport equations. Therefore, the subgrid contribution of the reactive source term does not require explicit modelling in a LES simulation. This approach is potentially less computational demanding than the quasi-laminar approach, which uses the filtered values to model the reactive term and neglects the subgrid part. In this way, the mesh size has to be finer than conventional LES and the simulation can cost up to 200 millions nodes [18] to achieve a subgrid Damköhler number smaller than 0.1 in the domain and preserve accuracy.

The most common PDF models are able to close the reactive term and are called joint scalar PDFs, usually including one thermodynamic variable and the mass fractions into their sample space. The joint velocity-scalar PDF models have a very important property of closing not only the reactive term, but the convective terms as well within any turbulence modelling framework. These PDFs include the velocity components in addition to the scalar variables in their sample space. This work proposes a new formulation for the solution of a joint velocity-scalar PDF. All the variables of the flow are evaluated in the same one-point, one-time, fine-grained PDF, allowing exact solution for the convective and reactive terms, which represent the most dominant physics in supersonic

combustion. The novelty of this approach is the solution method proposed for solving the LES-PDF transport equation. A new compressible formulation for a joint-scalar PDF is also proposed, which models a quasi-closure for the reactive term and uses traditional LES modelling for the convective term.

The Eulerian stochastic fields technique by Valiño [19] is used to solve the filtered transport equations for the proposed PDFs, thereby resulting in a full Eulerian solver. In contrast to Lagrangian methods, widely used by Pope and co-workers [20, 21], the implementation of Eulerian stochastic fields in traditional CFD codes is straightforward. The present work develops Eulerian stochastic differential equations aiming for high-Mach number applications in a LES framework. The equations are implemented in the compressible finite difference in-house code CompReal. Several numerical tests are performed in order to verify and validate the models developed in this work. These numerical tests range from one to three-dimensional test cases, including the verification of statistical independence, mesh resolution and the simulation of real supersonic burners and a scramjet configuration. The proposed approach is able to simulate the complex features in a supersonic combustion system and hopes to push forward the development of scramjets engines.

1.2 Structure of the text

The following chapter presents the transport conservation equations along with the large eddy simulation method. Filtered equations are exposed and the unclosed subgrid terms are highlighted. Classical modelling for the unclosed terms are reviewed. A historical review of the probability density function method is performed, with focus on combustion applications and stochastic modelling.

Afterwards, Chapter 3 introduces the new developed PDF methods. A more classical compressible scalar PDF formulation is firstly presented. This method couples the thermodynamic pressure with the Eulerian stochastic fields information, potentially increasing its accuracy in comparison to the conventional scalar PDFs models. A joint

scalar-velocity-total energy PDF is also proposed. In this PDF, the convective and reactive terms are solved exactly, and the Eulerian stochastic fields are also employed as a solution method. The in-house compressible code CompReal, in which all the new equations are implemented, is introduced in the end of this chapter.

In Chapter 4, the numerical tests performed are presented. These tests aim the numerical verification and validation of the models developed in this work. The code discretisation accuracy, statistical convergence and experimental agreement are investigated to assess the new models and identify possible limitations and future improvement.

At last, Chapter 5 depicts a scramjet simulation performed with the code implemented. The simulated scramjet is the University of Virginia (UVa) configuration A, a ground-based test. This simulation exposes the advantages and limitations of the Eulerian stochastic fields formulation to perform complex simulations. The conclusions are then summarised in Chapter 6.

1.3 Scientific production

The present work has been presented in the following conferences:

- 16th Conference on Numerical Combustion (Orlando, USA), 3-5 April, 2017. Oral presentation: "Large eddy simulation and probability density function modelling of high-speed reacting flows".

- 8th European Combustion Meeting (Dubrovnik, Croatia), 18-21 April, 2017. Poster presentation: "Eulerian probability density function modelling of compressible reacting flows using Large Eddy Simulation".

- Special Interest Group Meeting (Newcastle, UK), 26th March, 2018. Oral and Poster presentation: "Large Eddy Simulation of Supersonic Combustion using Eulerian Stochastic Fields".

- Combustion Institute British Section Spring Meeting on Advanced Combustion Methods (Manchester, UK), 5th April, 2018. Oral presentation: "Large Eddy

Simulation of supersonic combustion using the Eulerian stochastic fields method".

- 9th Symposium on Turbulence, Heat and Mass Transfer (Rio de Janeiro, Brazil), 10-13 July, 2018. Oral presentation: "Large eddy simulation of supersonic combustion using the Eulerian stochastic fields method".

- 37th International Symposium on Combustion (Dublin, Ireland), 29 July - 3 August, 2018. Oral presentation: "Large Eddy Simulation of a supersonic lifted flame using the Eulerian stochastic fields method".

and has been published:

- Y. P. Almeida and S. Navarro-Martinez. Eulerian probability density function modelling of compressible reacting flows using Large Eddy Simulation. *8th European Combustion Meeting*, 18-21 April 2017, Dubrovnik, Croatia.

- Y. P. Almeida and S. Navarro-Martinez. Large eddy simulation of a supersonic lifted flame using the eulerian stochastic fields method. *Proceedings of the Combustion Institute*, 37(3):3693 – 3701, 2019.

- Y. P. Almeida and S. Navarro-Martinez. Large eddy simulation of supersonic combustion using the Eulerian stochastic fields method. *Flow, Turbulence and Combustion*, 2019. (Submitted).

Chapter 2

Numerical methods

2.1 Introduction

The numerical simulation of supersonic combustion and scramjets have been carried out by several research groups with different methods. A recent review by Urzay [22] describes the current challenges of scramjet experimental and numerical investigation. These challenges mainly derive from the high speed required of the air-intake into the combustion chamber, which results in a difficult environment to sustain the flame. The engine must also generate higher thrust than drag, which is complex because of the expected hypersonic speed of the aircraft. The Direct Numerical Simulation of the governing equations can in principle provide a better understanding of combustion phenomena along with a description of the flow properties within the scramjet, facilitating the optimisation of current models applicable to realistic combustion systems [23]. However, the DNS demands large computational effort and few authors have investigated it for supersonic combustion purposes.

Jin *et al.* [24, 25] performed a DNS investigation of a supersonic lifted hydrogen jet using 975 millions cells, for instance. Ferrer [26] simulated supersonic compressible reactive spatially developing mixing layers in which hydrogen and vitiated air mix and burn using almost a hundred million cells. Koo *et al.* [4] studied thermal nonequilibrium effects using DNS, simulating a hydrogen burner with Reynolds number of 6900 and

the same inlet conditions as the HyShot-2 experiment, employing 27.5 millions cells. However, a DNS investigation of a realistic configuration is still impractical for most applications and limited to small Reynolds numbers. In DNS, all scales of turbulence, including the Kolmogorov scale, and the flame thickness must be correctly captured, requiring extremely fine mesh and therefore great computational processing capacity.

Nonetheless, the main challenges for simulating supersonic combustion using less computational resources are the modelling of the convective and reactive terms, along with accurate discretisation methods demanded by compressible flow. Large Eddy Simulation (LES) modelling, exposed in the next section, has been intensively used to investigate supersonic combustion. LES filters the small scales of the flow and simulate only the large ones, saving computational resources.

Berglund and Fureby [27] employed a two-equation flamelet model to obtain the filtered reactive mass fractions, along with the Smagorinsky model [28] to close the subgrid convective part. They simulated the DLR scramjet and obtained reasonable agreement with experimental data. Gong *et al.* [29] also studied the DLR scramjet configuration employing LES, using an one-equation model to close the subgrid fluxes and the PDF model, coupled with the Eulerian stochastic fields method, to solve the reactive term. They compared the LES-PDF model with the quasi-laminar/well-stirred reactor model, which is the use of the filtered values in the reactive term, and obtained better experimental agreement with the former model. Genin and Menon [30] investigated the DLR configuration using a non-reactive LES simulation, employing a one-equation model for closure and a localised dynamic model to determine the model coefficients.

In Fureby *et al.* [3], a mixed subgrid scale flow model [31] is used to close the convective terms and the Partially Stirred Reactor (PaSR) model is employed to obtain the source term. The HyShot 2 [2] has been investigated and also good experimental agreement has been obtained.

The work of Moule *et al.* [32] investigated the hydrogen-air supersonic burner of Cheng *et al.* [7] through the use of an unsteady partially stirred reactor (UPaSR) using large eddy simulation and the Smagorinsky model. The simulation used a number of 31 millions cells,

though, being classified as a highly-resolved LES simulation. Bouheraoua *et al.* [18] also employed a highly-resolved LES mesh to simulate the Cheng *et al.* [7] burner, employing 268 millions cells. The authors used the Smagorinsky model to close the convective terms. However, they have not used an explicit combustion model, employing the quasi-laminar (QL) method. They justified this approximation because of the high resolution employed, which results in a subgrid Damköhler number smaller than unity for the whole domain.

Chan and Ihme [33] performed LES studies of the University of Virginia's Scramjet, using the Vreman eddy-viscosity subgrid-scale model [34] to close subgrid momentum terms. The quasi-laminar (QL) combustion assumption using finite-rate chemistry and the flamelet/progess variable model of Pecnik *et al.* [35] have been employed, the latter achieving better results. Another approach is the quadrature-based moment method, developed by Koo *et al.* [36] and Donde *et al.* [37]. This method has been investigated for the simulation of canonical test cases including a supersonic cavity stabilised combustor.

In summary, supersonic combustion researchers usually employ models such as flamelet, PaSR, PDF methods and quasi-laminar chemistry to model the source term subgrid contribution. However, with the exception of Gong *et al.* [29] that used a PDF method coupled with the Eulerian stochastic fields model, the combustion models have been employed along with a fast chemistry mechanism. This reduces the subgrid numerical error, however, the chemical mechanism may not be the most accurate. In contrast, the PDF methods are able to preserve accuracy when used with complex chemical mechanisms as well.

In this work, the probability density function (PDF) method along with the large eddy simulation is the chosen numerical approach to simulate supersonic combustion. The LES method provides a good compromise between accuracy and cost, and coupled with the PDF method to solve the filtered combustion part results in a very powerful approach for supersonic combustion. In the following sections, the governing equations, along with their filtered counterpart and respective modelling are shown. The PDF method is also introduced and its inherent advantages are exposed, clarifying its choice to investigate the supersonic combustion phenomena.

2.2 Governing equations

The following equations describe the conservation of mass, momentum, total energy (internal, kinetic and chemical energy) and chemical species in a multicomponent system using Einstein summation convention [38, 39]:

$$\frac{\partial \rho}{\partial t} + \frac{\partial \rho u_i}{\partial x_i} = 0 \tag{2.1}$$

$$\frac{\partial \rho u_i}{\partial t} + \frac{\partial \rho u_j u_i}{\partial x_j} = -\frac{\partial p}{\partial x_i} + \frac{\partial \tau_{ij}}{\partial x_j} + \rho \sum_{\alpha=1}^{N_s} Y_\alpha b_{\alpha,i} \tag{2.2}$$

$$\frac{\partial \rho e_t}{\partial t} + \frac{\partial \rho u_i e_t}{\partial x_i} = -\frac{\partial q_i}{\partial x_i} - \frac{\partial p u_i}{\partial x_i} + \frac{\partial \tau_{ij} u_j}{\partial x_i} + \rho \sum_{\alpha=1}^{N_s} Y_\alpha b_{\alpha,i} \left(u_i + V_{\alpha,i}\right) + \dot{Q} \tag{2.3}$$

$$\frac{\partial \rho Y_\alpha}{\partial t} + \frac{\partial}{\partial x_i} \left(\rho \left(u_i + V_{\alpha,i}\right) Y_\alpha\right) = \rho S_\alpha \tag{2.4}$$

where ρ is the density, u_i is the velocity, p is thermodynamic pressure, τ_{ij} is the viscous stress tensor, e_t is the total energy, q_i is the heat flux vector and $\dot{Q}$ is an external heat source. The diffusion velocity, mass fraction and reaction rate of the chemical specie α are represented by $V_{\alpha,i}$, Y_α and S_α, respectively. The body forces acting at the system are described by $b_{\alpha,i}$.

The viscous stress tensor can be described using the Newtonian approach:

$$\tau_{ij} = \left[\left(\mu_b - \frac{2}{3}\mu\right) \frac{\partial u_k}{\partial x_k} \delta_{ij} + \mu \left(\frac{\partial u_i}{\partial x_j} + \frac{\partial u_j}{\partial x_i}\right)\right] \tag{2.5}$$

where μ_b is the bulk viscosity, μ is the dynamic viscosity and δ_{ij} is the Kronecker delta function. The bulk viscosity is usually neglected following the Stokes' hypothesis [40], so the tensor τ_{ij} becomes deviatoric and its analysis simplified. This hypothesis is also used here and therefore $\mu_b \approx 0$.

The total heat flux vector, q_i, including the effects of heat diffusion is expressed by

Fourier's Law and interdiffusion heat flux:

$$q_i = -\lambda \frac{\partial T}{\partial x_i} + \rho \sum_{\alpha=1}^{N_s} h_\alpha Y_\alpha V_{\alpha,i} \tag{2.6}$$

where λ is the thermal conductivity. Hereafter the gravity g_i is the only body force considered, interdiffusion heat flux is neglected and external heat sources are not considered. Mass diffusion is approximated using the Fick's Law:

$$-\rho V_{\alpha,i} Y_\alpha = -J_{\alpha,i} = \rho \Gamma_\alpha \frac{\partial Y_\alpha}{\partial x_i} \tag{2.7}$$

and the equations of momentum, total energy and chemical species are therefore described as:

$$\frac{\partial \rho u_i}{\partial t} + \frac{\partial \rho u_j u_i}{\partial x_j} = -\frac{\partial p}{\partial x_i} + \frac{\partial \tau_{ij}}{\partial x_j} + \rho g_i \tag{2.8}$$

$$\frac{\partial \rho e_t}{\partial t} + \frac{\partial \rho u_i e_t}{\partial x_i} = -\frac{\partial q_i}{\partial x_i} - \frac{\partial p u_i}{\partial x_i} + \frac{\partial \tau_{ij} u_j}{\partial x_i} + \rho g_i u_i \tag{2.9}$$

$$\frac{\partial \rho Y_\alpha}{\partial t} + \frac{\partial \rho u_i Y_\alpha}{\partial x_i} = \frac{\partial}{\partial x_i}\left(\rho \Gamma_\alpha \frac{\partial Y_\alpha}{\partial x_i}\right) + \rho S_\alpha \tag{2.10}$$

Equations (2.1), (2.8), (2.9) and (2.10), coupled with a equation of state, are sufficient to describe a multicomponent reactive system, taking into account the simplifications aforementioned. However, they do not have analytical solution unless in very simple configurations, requiring numerical methods to be solved. As mentioned, the direct numerical simulation of these equations still requires a large amount of computational power.

In order to diminish the number of scales to be solved two main techniques exist, the Reynolds averaged Navier-Stokes (RANS) and the large eddy simulation (LES). In RANS, a temporal average is performed in the transport equations, requiring modelling to all scales of turbulence. In LES, a spatial filter is applied to the equations. The large scales remain in the flow and are directly simulated whereas the small ones are filtered and require modelling. As a consequence, LES demands less modelling effort and it is potentially more accurate. Its advantages and drawbacks are outlined in the next section.

2.3 Large Eddy Simulation

Large eddy simulation consists of applying a spatial filter to the flow variables, directly solving the large scales and modelling the small scales. The filtering operation is the convolution integral of a function and a filter in the space. It is defined as:

$$\overline{Q}\left(\boldsymbol{x},t\right)=\int_{-\infty}^{+\infty}Q\left(\boldsymbol{x'},t\right)G(\boldsymbol{x}-\boldsymbol{x'},\Delta)\,\mathrm{d}\boldsymbol{x'} \tag{2.11}$$

where the function $G(\boldsymbol{x}-\boldsymbol{x'},\Delta)$ is the filter and it respects the normalisation condition [41]:

$$\int_{-\infty}^{+\infty}G(\boldsymbol{x}-\boldsymbol{x'},\Delta)\,\mathrm{d}\boldsymbol{x'}=1 \tag{2.12}$$

The operator $\overline{(\cdot)}$ represents the filtering operation. Different sorts of filters can be applied such as the box, Gaussian, sharp spectral and Cauchy filters [42, 41]. In this work, the box or top-hat filter is used:

$$G(\boldsymbol{x}-\boldsymbol{x'},\Delta)=\begin{cases}\dfrac{1}{\Delta^3}, & \text{if } |\boldsymbol{x}-\boldsymbol{x'}|\leq\dfrac{\Delta}{2}\\ 0, & \text{otherwise}\end{cases} \tag{2.13}$$

where Δ is the cut-off scale or filter width in space, usually taken by the cubic root of the volume of the cell in the mesh, $\Delta=(\Delta x_1\Delta x_2\Delta x_3)^{1/3}$. This is called implicit filtering in this text to avoid confusion with numerical damping techniques, which are called explicit filtering. This filter satisfies the normalization condition and it is also considered that the filtering operation commutes with spatial differentiation:

$$\int_{-\infty}^{+\infty}\frac{\partial Q\left(\boldsymbol{x'},t\right)}{\partial\boldsymbol{x}}G(\boldsymbol{x}-\boldsymbol{x'},\Delta)\,\mathrm{d}\boldsymbol{x'}\approx\frac{\partial}{\partial\boldsymbol{x}}\int_{-\infty}^{+\infty}Q\left(\boldsymbol{x'},t\right)G(\boldsymbol{x}-\boldsymbol{x'},\Delta)\,\mathrm{d}\boldsymbol{x'} \tag{2.14}$$

Equation (2.14) becomes an equality if the filter is constant in the domain, like in an uniform mesh mesh using the box filter. It is useful to introduce the Favre filtering

operation in variable density flows, defined below:

$$\widetilde{Q}_i(\boldsymbol{x},t) = \frac{\displaystyle\int_{-\infty}^{+\infty} \rho\left(\boldsymbol{x'},t\right) Q_i\left(\boldsymbol{x'},t\right) G(\boldsymbol{x}-\boldsymbol{x'},\Delta)\,\mathrm{d}\boldsymbol{x'}}{\displaystyle\int_{-\infty}^{+\infty} \rho\left(\boldsymbol{x'},t\right) G(\boldsymbol{x}-\boldsymbol{x'},\Delta)\,\mathrm{d}\boldsymbol{x'}} = \frac{\overline{\rho Q_i}}{\overline{\rho}}; \qquad \overline{\rho Q_i} = \overline{\rho}\widetilde{Q}_i \tag{2.15}$$

where the operator $\widetilde{(\cdot)}$ denotes the Favre filtering. Applying the filtering operation to Equations (2.1), (2.8), (2.9) and (2.10) it is possible to obtain the following system of partial differential equations:

$$\frac{\partial\overline{\rho}}{\partial t} + \frac{\partial\overline{\rho}\widetilde{u}_i}{\partial x_i} = 0 \tag{2.16}$$

$$\frac{\partial\overline{\rho}\widetilde{u}_i}{\partial t} + \frac{\partial\overline{\rho}\widetilde{u}_j\widetilde{u}_i}{\partial x_j} = -\frac{\partial\overline{p}}{\partial x_i} + \frac{\partial}{\partial x_j}\left(\overline{\tau}_{ij} - \tau_{ij}^{sgs}\right) + \overline{\rho}g_i \tag{2.17}$$

$$\begin{aligned}\frac{\partial\overline{\rho}\widetilde{e}_t}{\partial t} + \frac{\partial\overline{\rho}\widetilde{u}_i\widetilde{e}_t}{\partial x_i} = &- \frac{\partial\overline{q}_i}{\partial x_i} - \frac{\partial\overline{p}\widetilde{u}_i}{\partial x_i} + \frac{\partial\overline{\tau}_{ij}\widetilde{u}_j}{\partial x_i} + \overline{\rho}g_i\widetilde{u}_i \\ &+ \frac{\partial}{\partial x_i}\left(-H_i^{sgs} + \sigma_{ij}^{sgs}\right)\end{aligned} \tag{2.18}$$

$$\frac{\partial\overline{\rho}\widetilde{Y}_\alpha}{\partial t} + \frac{\partial\overline{\rho}\widetilde{u}_i\widetilde{Y}_\alpha}{\partial x_i} = \frac{\partial}{\partial x_i}\left(\overline{\rho}\Gamma_\alpha\frac{\partial\widetilde{Y}_\alpha}{\partial x_i}\right) + \overline{\rho\,S_\alpha\left(p,Y_\alpha,T\right)} - \frac{\partial J_i^{sgs}}{\partial x_i} \tag{2.19}$$

where the new subgrid terms are defined using the same notation as Gong *et al.* [29]:

$$\tau_{ij}^{sgs} = \overline{\rho}\widetilde{u_j u_i} - \overline{\rho}\widetilde{u}_j\widetilde{u}_i \tag{2.20}$$

$$H_i^{sgs} = \overline{\rho}\widetilde{u_i e_t} - \overline{\rho}\widetilde{u}_i\widetilde{e}_t + \overline{p}\widetilde{u}_i - \overline{pu_i} \tag{2.21}$$

$$\sigma_{ij}^{sgs} = \overline{\tau_{ij}u_j} - \widetilde{\tau}_{ij}\widetilde{u}_j \tag{2.22}$$

$$J_i^{sgs} = \overline{\rho}\widetilde{u_i Y_\alpha} - \overline{\rho}\widetilde{u}_i\widetilde{Y}_\alpha \tag{2.23}$$

The filtered continuity Equation(2.16) is perfectly closed, however, comparing Equations (2.17), (2.19) and (2.18) with Equations (2.8), (2.9) and (2.10) it is possible to verify that extra terms arise due to the filtering operation. The last two terms on Equations (2.17) and (2.19) and the last six terms on Equation (2.18) must be modelled. On the derivation of Eqs.(2.17), (2.19) and (2.18) it is assumed that diffusion coefficients vary slowly in space and therefore do not have subgrid scales themselves.

2.3.1 Momentum equation

The filtered momentum Equation (2.17) requires modelling for the filtered viscous stress tensor and the convective terms. Convective terms can be modelled using classical LES closure models, such as the Smagorinsky model [28] or the Germano dynamic model [43, 44]. The Smagorinsky model assumes isotropy on the small scales of turbulence and it models the convective term using a turbulent subgrid viscosity concept, where the subgrid viscous stress tensor is modelled as:

$$-\tau_{ij}^{sgs} = 2\overline{\rho}\nu_{sgs}\left[\frac{1}{2}\left(\frac{\partial\widetilde{u}_i}{\partial x_j}+\frac{\partial\widetilde{u}_j}{\partial x_i}\right)-\frac{1}{3}\frac{\partial\widetilde{u}_k}{\partial x_k}\delta_{ij}\right]+\frac{2}{3}\overline{\rho}k_{sgs}\delta_{ij} \tag{2.24}$$

where ν_{sgs} is the kinematic subgrid viscosity and k_{sgs} is the subgrid kinetic energy. The filtered viscous tensor in Eq. (2.17) is approximated as:

$$\overline{\tau}_{ij} \approx 2\overline{\rho}\nu\left[\frac{1}{2}\left(\frac{\partial\widetilde{u}_i}{\partial x_j}+\frac{\partial\widetilde{u}_j}{\partial x_i}\right)-\frac{1}{3}\frac{\partial\widetilde{u}_k}{\partial x_k}\delta_{ij}\right] \tag{2.25}$$

The filtered momentum equation is therefore modelled as:

$$\begin{aligned}\frac{\partial\overline{\rho}\widetilde{u}_i}{\partial t}+\frac{\partial\overline{\rho}\widetilde{u}_j\widetilde{u}_i}{\partial x_j} =& -\frac{\partial\overline{p}}{\partial x_i}+\frac{\partial}{\partial x_j}\left[\overline{\rho}\left(\nu+\nu_{sgs}\right)\left(\frac{\partial\widetilde{u}_i}{\partial x_j}+\frac{\partial\widetilde{u}_j}{\partial x_i}-\frac{2}{3}\frac{\partial\widetilde{u}_k}{\partial x_k}\delta_{ij}\right)\right]\\ &+\frac{\partial}{\partial x_j}\left(\frac{2}{3}\overline{\rho}k_{sgs}\delta_{ij}\right)+\overline{\rho}g_i\end{aligned} \tag{2.26}$$

whereas the subgrid kinematic viscosity, ν_{sgs}, and the subgrid kinetic energy, k_{sgs}, requires closure. Using the Smagorinsky model the subgrid kinematic viscosity is modelled as:

$$\nu_{sgs} = (C_\mu \Delta)^2 \, ||\widetilde{S}_{ij}||; \quad \widetilde{S}_{ij} = \frac{1}{2}\left(\frac{\partial \widetilde{u}_i}{\partial x_j} + \frac{\partial \widetilde{u}_j}{\partial x_i}\right) \tag{2.27}$$

where the operator $||\cdot||$ represents the module of a tensor and the $\widetilde{S}_{ij}$ is the filtered deformation tensor. The subgrid kinetic energy is defined as:

$$k_{sgs} = \frac{1}{2}\left(\widetilde{u_i u_i} - \widetilde{u}_i^2\right) \tag{2.28}$$

and it can be modelled using the Yoshizawa model [45]:

$$k_{sgs} = C_Y \left(||\widetilde{S}_{ij}||\Delta\right)^2 \tag{2.29}$$

where the constant C_Y is taken to be equal to 0.0066 [42], unless stated otherwise. It is also possible to use a one-equation model to obtain the subgrid kinetic energy, where a transport equation is used to solve for k_{sgs} as investigated by Gong *et al.* [29] and Genin and Menon [30]. The Yoshizawa model is used here to avoid the inclusion of an extra transport equation and preserve computational effort to the combustion part. The present closure models have been used in compressible LES flows within the context of not too large turbulent Mach number [46, 30, 29].

Along with the models shown in Eqs.(2.27) and (2.29) the filtered momentum equation is closed, apart from thermodynamic variables such as pressure and dynamic viscosity. The models for these and other thermodynamical properties calculated in a large eddy simulation framework are reviewed in section 2.3.4.

2.3.2 Total energy equation

It is useful to first redefine the total energy including the subgrid kinetic energy:

$$\overline{\rho}\widetilde{e}_t = \overline{\rho}\widetilde{U} + \frac{1}{2}\overline{\rho}\widetilde{u}_i\widetilde{u}_i + \overline{\rho}k_{sgs} \tag{2.30}$$

where $\widetilde{U}$ is the Favre filtered internal energy. The subgrid convective, pressure-velocity correlation and viscous dissipation terms on Equation (2.18) can be jointly modelled as a function of gradient of total enthalpy, in a similar fashion as Gong *et al.* [29]:

$$-H_i^{sgs} + \sigma_{ij}^{sgs} = \overline{\rho}\frac{\nu_{sgs}}{\mathrm{Pr}_{sgs}}\left(\frac{\partial \widetilde{h}}{\partial x_i} + \widetilde{u}_j\frac{\partial \widetilde{u}_j}{\partial x_i} + \frac{\partial k_{sgs}}{\partial x_i}\right) \tag{2.31}$$

where Pr_{sgs} is the subgrid Prandtl number, usually taken as unity, and $\widetilde{h}$ is the resolved enthalpy $\widetilde{U} + \overline{p}/\overline{\rho}$ of the mixture. The filtered heat flux can also be rewritten in terms of enthalpy using the molecular Prandtl number:

$$\overline{q}_i = -\overline{\rho}\frac{\nu}{\mathrm{Pr}}\frac{\partial \widetilde{h}}{\partial x_i} \tag{2.32}$$

The filtered total energy equation can therefore be finally obtained with all terms already closed:

$$\begin{aligned}\frac{\partial \overline{\rho}\widetilde{e}_t}{\partial t} + \frac{\partial \overline{\rho}\widetilde{u}_i\widetilde{e}_t}{\partial x_i} =& \frac{\partial}{\partial x_i}\left[\overline{\rho}\left(\frac{\nu}{\mathrm{Pr}} + \frac{\nu_{sgs}}{\mathrm{Pr}_{sgs}}\right)\frac{\partial \widetilde{h}}{\partial x_i}\right] - \frac{\partial \overline{p}\widetilde{u}_i}{\partial x_i} + \frac{\partial \widetilde{\tau}_{ij}\widetilde{u}_j}{\partial x_i} + \overline{\rho}g_i\widetilde{u}_i \\ &+ \frac{\partial}{\partial x_i}\left[\overline{\rho}\frac{\nu_{sgs}}{\mathrm{Pr}_{sgs}}\left(\widetilde{u}_j\frac{\partial \widetilde{u}_j}{\partial x_i} + \frac{\partial k_{sgs}}{\partial x_i}\right)\right]\end{aligned} \tag{2.33}$$

Equation (2.33) presents closures for all subgrid terms and few assumptions have been performed. The closure in Eq. (2.31) considers an eddy-viscosity model typically used in non-reacting flows, which implicitly assumes that scales in turbulence are well separated from those important to combustion [46]. In other words, the subgrid combustion terms would only affect the turbulence field at the resolved scale, which would only be accurate when using a fine mesh. Terms with medium to large influence in the solution of the equation are still modelled, like the subgrid convective terms [42]. Although the potential modelling error in LES environment is considered small in comparison to RANS approach, it can still be somewhat large in regions where small scales are very difficult to simulate, like in flame fronts, shock-waves and near wall flow.

2.3.3 Mass fraction equation

The Favre filtered mass fraction transport equation requires closure for the convective and reactive term. The convective term can be modelled in same fashion as before, using the subgrid viscosity concept:

$$-J_i^{sgs} = \overline{\rho}\frac{\nu_{sgs}}{\mathrm{Sc}_{sgs}}\frac{\partial \widetilde{Y}_\alpha}{\partial x_i} \tag{2.34}$$

where Sc_{sgs} is the subgrid Schmidt number, usually taken as unity. By considering unity Lewis number and that all species share the same diffusion coefficient, the filtered equation is therefore written as:

$$\frac{\partial \overline{\rho}\widetilde{Y}_\alpha}{\partial t} + \frac{\partial \overline{\rho}\widetilde{u}_i\widetilde{Y}_\alpha}{\partial x_i} = \frac{\partial}{\partial x_i}\left[\overline{\rho}\left(\frac{\nu}{\mathrm{Sc}} + \frac{\nu_{sgs}}{\mathrm{Sc}_{sgs}}\right)\frac{\partial \widetilde{Y}_\alpha}{\partial x_i}\right] + \overline{\rho}\,\overline{S_\alpha\left(p, Y_\alpha, T\right)} \tag{2.35}$$

It should be pointed out that the source term, S_α, is a function of the empirical Arrhenius law, resulting in exponential expressions [38, 39]. It is therefore highly non-linear and the filtering operation yields subgrid terms that requires strong modelling effort because:

$$\overline{S_\alpha\left(p, Y_\alpha, T\right)} \neq S_\alpha\left(\overline{p}, \widetilde{Y}_\alpha, \widetilde{T}\right) \tag{2.36}$$

Different closures have been proposed to model it in the context of large eddy simulation, such as the Eddy Dissipation Concept [47], the flamelet model [48], the Conditional Moment Closure (CMC) [49], thickened flame model [50] and perfectly stirred reactor (PSR)/quasi-laminar (QL) [18]. A review of such methods is presented in Pitsch [51] or Fureby [52].

The Eddy Dissipation Concept relies in an intermittent factor used to weight two measures within the same filtered volume, a fine structure and its surroundings, the latter representing a non-homogeneous inefficient mixing process [32]. Although its use is straightforward, it may heavily depends on constant adjustment that has to be performed case by case. The flamelet model is part of the tabulated chemistry models and, although it has widely been validated, it requires a lookup table based on a fixed flame structured

[53]. The thickened flame model aims to thick the flame front, making it possible to solve it within the mesh size and increasing accuracy. However, it still requires fine parameter tuning to compensate the loss of flame wrinkling. The CMC is of the same category of probability density function methods and it aims to solve statistical properties of a conditional scalar, which can be a limiting factor.

On the other hand, source terms and convective terms can be treated exactly and without the need of specific *ad hoc* models by using probability density function (PDF) methods or, in the context of LES, the filtered density function (FDF). This allows the most important features of the flow to be directly calculated and it is presented on the section 2.4.

2.3.4 Thermodynamic properties

There are several equations of state that can be used to determine the thermodynamic pressure, such as the ideal gas equation or more robust real equation of state models [54, 55, 56]. Although in supersonic combustion conditions the density may not behave as an ideal gas due to the high pressure conditions, it is still the most used equation because of its simplicity and easy coupling with other conservation equations. The ideal gas model for a multicomponent mixture is defined as:

$$p = \rho R_u \left(\sum_{\alpha=1}^{N_s} \frac{Y_\alpha}{M_\alpha} \right) T \tag{2.37}$$

where R_u is the universal gas constant. After applying the filtering operation in Eq. (2.37), it is possible to write:

$$\overline{p} = \overline{\rho} R_u \left(\sum_{\alpha=1}^{N_s} \frac{\widetilde{Y}_\alpha}{M_\alpha} \right) \widetilde{T} + \left(\overline{\rho R_u \left(\sum_{\alpha=1}^{N_s} \frac{Y_\alpha}{M_\alpha} \right) T} - \overline{\rho} R_u \left(\sum_{\alpha=1}^{N_s} \frac{\widetilde{Y}_\alpha}{M_\alpha} \right) \widetilde{T} \right) \tag{2.38}$$

The filtered thermodynamic pressure is therefore not exactly closed even if cast in ideal gas law model. An usual approximation is to calculate the pressure from the filtered values at the node cell, i.e.: $\widetilde{f(x)} \approx f(\widetilde{x})$, neglecting the subgrid mass-fraction and

subgrid temperature correlations:

$$\overline{p} = \overline{\rho} R_u \left(\sum_{\alpha=1}^{N_s} \frac{\widetilde{Y}_\alpha}{M_\alpha} \right) \widetilde{T} \tag{2.39}$$

This approximation has been revisited by Ribert *et al.* [57] and the authors found that the error can be large in high-pressure CH_4-O_2 flames, although for CH_4-air the approximation is well suited. This is because the inert specie N_2 is the major component of the reactive mixture. Equation (2.39) is used in this work when needed.

The diffusion coefficients considered here do not have subgrid scale fluctuations, which means that they are obtained from the node values as well. The individual component viscosity is calculated from the Hirschfelder *et al.* [58] model and the mixture model of Wilke [59] when it is used a multicomponent mixture. It is not investigated here the effects of differential diffusion, which can play a significant role in non-premixed combustion [60, 61], especially with hydrogen. The mass diffusion and thermal conductivity coefficients are not evaluated but obtained from the molecular Prandtl and Schmidt number, which both are assumed to be equal to unity.

2.3.5 Closed filtered transport equations

The final system of equations, represented by Equations (2.16), (2.26), (2.33) and (2.35) together with Eq. (2.39) and a transport model for viscosity are mostly closed:

$$\frac{\partial \overline{\rho}}{\partial t} + \frac{\partial \overline{\rho} \widetilde{u}_i}{\partial x_i} = 0 \tag{2.16}$$

$$\begin{aligned} \frac{\partial \overline{\rho} \widetilde{u}_i}{\partial t} + \frac{\partial \overline{\rho} \widetilde{u}_j \widetilde{u}_i}{\partial x_j} =& - \frac{\partial \overline{p}}{\partial x_i} + \frac{\partial}{\partial x_j} \left[\overline{\rho} \left(\nu + \nu_{sgs} \right) \left(\frac{\partial \widetilde{u}_i}{\partial x_j} + \frac{\partial \widetilde{u}_j}{\partial x_i} - \frac{2}{3} \frac{\partial \widetilde{u}_k}{\partial x_k} \delta_{ij} \right) \right] \\ &+ \frac{\partial}{\partial x_j} \left(\frac{2}{3} \overline{\rho} k_{sgs} \delta_{ij} \right) + \overline{\rho} g_i \end{aligned} \tag{2.26}$$

$$\begin{aligned} \frac{\partial \overline{\rho} \widetilde{e}_t}{\partial t} + \frac{\partial \overline{\rho} \widetilde{u}_i \widetilde{e}_t}{\partial x_i} =& \frac{\partial}{\partial x_i} \left[\overline{\rho} \left(\frac{\nu}{\mathrm{Pr}} + \frac{\nu_{sgs}}{\mathrm{Pr}_{sgs}} \right) \frac{\partial \widetilde{h}}{\partial x_i} \right] - \frac{\partial \overline{p} \widetilde{u}_i}{\partial x_i} + \frac{\partial \widetilde{\tau}_{ij} \widetilde{u}_j}{\partial x_i} + \overline{\rho} g_i \widetilde{u}_i \\ &+ \frac{\partial}{\partial x_i} \left[\overline{\rho} \frac{\nu_{sgs}}{\mathrm{Pr}_{sgs}} \left(\widetilde{u}_j \frac{\partial \widetilde{u}_j}{\partial x_i} + \frac{\partial k_{sgs}}{\partial x_i} \right) \right] \end{aligned} \tag{2.33}$$

$$\frac{\partial \overline{\rho}\widetilde{Y}_\alpha}{\partial t} + \frac{\partial \overline{\rho}\widetilde{u}_i\widetilde{Y}_\alpha}{\partial x_i} = \frac{\partial}{\partial x_i}\left[\overline{\rho}\left(\frac{\nu}{\mathrm{Sc}} + \frac{\nu_{sgs}}{\mathrm{Sc}_{sgs}}\right)\frac{\partial \widetilde{Y}_\alpha}{\partial x_i}\right] + \overline{\rho}\,\widetilde{S_\alpha\left(p, Y_\alpha, T\right)} \tag{2.35}$$

$$\overline{p} = \overline{\rho} R_u \left(\sum_{\alpha=1}^{N_s} \frac{\widetilde{Y}_\alpha}{M_\alpha}\right)\widetilde{T} \tag{2.39}$$

The source term in the filtered mass fraction conservation equation still requires closure, which is addressed in the next section.

2.4 PDF methods

Probability density function (PDF) methods have been used in a wide range of applications related to combustion or not: to model the droplet distribution in a spray [62], soot formation in a combustion system [63], and others [64]. They were introduced in the context of turbulent flows by Lundgren [65] in 1967 and revisited in 1969 [66].

It is presented in this section the two main approaches to deal with PDF methods: one based on the *ensemble average* of Dirac delta functions called *Averaged Probability Density Function*, usually employed within RANS framework. The other PDF approach is based on the *filtering operation* of Dirac delta function called *Filtered Density Function* method and it is used within LES framework. These two methods are reviewed here along with critical mathematical derivations exposed to establish the theoretical underpinning of the developed models in the next chapter.

2.4.1 Averaged Probability Density Function - RANS-PDF

Lundgren [65] defined a one-point PDF $f(\boldsymbol{v}_1; \boldsymbol{x}_1, t)$ for the velocity $\boldsymbol{v}_1$ given by:

$$f(\boldsymbol{v}_1; \boldsymbol{x}_1, t) = \langle \delta \left(\boldsymbol{u} \left(\boldsymbol{x}_1, t \right) - \boldsymbol{v}_1 \right) \rangle \tag{2.40}$$

where the operator $\langle \cdot \rangle$ denotes an ensemble average and $\delta \left(\boldsymbol{u} \left(\boldsymbol{x}_1, t \right) - \boldsymbol{v}_1 \right)$ is the Dirac delta function. The Dirac delta function is also called "fine-grained" PDF. The notation used here is the original from Lundgren [65], in which the subscript "1" indicates the one-point sample at the coordinate $\boldsymbol{x}_1$. The semicolon notation indicates the sample variables included in the PDF[1].

The average operation for a variable $Q(\boldsymbol{u}(\boldsymbol{x}_1, t))$ with random samples $Q(\boldsymbol{v}_1)$ is defined as:

$$\langle Q(\boldsymbol{u}(\boldsymbol{x}_1, t)) \rangle = \int_{-\infty}^{+\infty} Q(\boldsymbol{v}_1) f \left(\boldsymbol{v}_1; \boldsymbol{x}_1, t \right) \mathrm{d}\boldsymbol{v}_1 \tag{2.41}$$

The property shown in Eq.(2.40) can be proved considering $\boldsymbol{u} \left(\boldsymbol{x}_1, t \right) = \boldsymbol{v}_1'$ and using the

[1] This notation would just be introduced later [67], however, to keep the notation consistent it is used in all PDF mentioned in this work.

sifting property of the Dirac delta function [68]:

$$\langle \delta \left(\boldsymbol{u} \left(\boldsymbol{x}_1, t \right) - \boldsymbol{v}_1 \right) \rangle = \int_{-\infty}^{+\infty} \delta \left(\boldsymbol{v}_1' - \boldsymbol{v}_1 \right) f(\boldsymbol{v}_1'; \boldsymbol{x}_1, t) \, \mathrm{d}\boldsymbol{v}_1' = f(\boldsymbol{v}_1; \boldsymbol{x}_1, t) \tag{2.42}$$

In this way $f(\boldsymbol{v}_1; \boldsymbol{x}_1, t) \, \mathrm{d}\boldsymbol{v}_1$ represents the probability that the velocity at the position $\boldsymbol{x}_1$ at time t is within the element $\mathrm{d}\boldsymbol{v}_1$. The Dirac delta can be thought as an ensemble member of the velocity distribution [65]. It is also possible to define a two point distribution function:

$$f_2(\boldsymbol{v}_2, \boldsymbol{v}_1; \boldsymbol{x}_2, \boldsymbol{x}_1, t) = \langle \delta \left(\boldsymbol{u} \left(\boldsymbol{x}_1, t \right) - \boldsymbol{v}_1 \right) \delta \left(\boldsymbol{u} \left(\boldsymbol{x}_2, t \right) - \boldsymbol{v}_2 \right) \rangle \tag{2.43}$$

and multipoint distribution functions can also be defined similarly. However, multipoint functions are usually not employed because of closures issues that are far more complex than for one-point PDFs.

A one point joint distribution can also be defined using Dirac delta functions:

$$f(\boldsymbol{v}_1, \boldsymbol{\psi}_1; \boldsymbol{x}_1, t) = \langle \delta \left(\boldsymbol{u} \left(\boldsymbol{x}_1, t \right) - \boldsymbol{v}_1 \right) \delta \left(\boldsymbol{\phi} \left(\boldsymbol{x}_1, t \right) - \boldsymbol{\psi}_1 \right) \rangle \tag{2.44}$$

The definition of conditional probability is defined for a one point distribution:

$$f(\boldsymbol{\psi}_1 | \boldsymbol{v}_1; \boldsymbol{x}_1, t) = \frac{f(\boldsymbol{v}_1, \boldsymbol{\psi}_1; \boldsymbol{x}_1, t)}{f(\boldsymbol{v}_1; \boldsymbol{x}_1, t)} \tag{2.45}$$

Another important definition is the result of $\langle Q \left(\boldsymbol{x}_1, t \right) \delta \left(\boldsymbol{u} \left(\boldsymbol{x}_1, t \right) - \boldsymbol{v}_1 \right) \rangle$, which is extensively used in PDF methods. For a variable $Q \left(\boldsymbol{x}_1, t \right)$ with a sample space variable ψ_1, this result is presented as follows [68]:

$$\begin{aligned}
\langle Q \left(\boldsymbol{x}_1, t \right) \delta \left(\boldsymbol{u} \left(\boldsymbol{x}_1, t \right) - \boldsymbol{v}_1 \right) \rangle &= \int \int \psi_1 \delta \left(\boldsymbol{v}_1' - \boldsymbol{v}_1 \right) f(\boldsymbol{v}_1', \psi_1; \boldsymbol{x}_1, t) \, \mathrm{d}\boldsymbol{v}_1' \, \mathrm{d}\psi_1 \\
&= \int \psi_1 f(\boldsymbol{v}_1, \psi_1; \boldsymbol{x}_1, t) \, \mathrm{d}\psi_1 \\
&= \int \psi_1 f(\psi_1 | \boldsymbol{v}_1; \boldsymbol{x}_1, t) f(\boldsymbol{v}_1; \boldsymbol{x}_1, t) \, \mathrm{d}\psi_1 \\
&= f(\boldsymbol{v}_1; \boldsymbol{x}_1, t) \int \psi_1 f(\psi_1 | \boldsymbol{v}_1; \boldsymbol{x}_1, t) \, \mathrm{d}\psi_1 \\
&= f(\boldsymbol{v}_1; \boldsymbol{x}_1, t) \left\langle Q \left(\boldsymbol{x}_1, t \right) | \boldsymbol{u} \left(\boldsymbol{x}_1, t \right) = \boldsymbol{v}_1 \right\rangle
\end{aligned} \tag{2.46}$$

where the term $\langle Q(\boldsymbol{x}_1,t)\,|\boldsymbol{u}(\boldsymbol{x}_1,t)=\boldsymbol{v}_1\rangle$ is the conditional expectation of $Q(\boldsymbol{x}_1,t)$ given that $\boldsymbol{u}(\boldsymbol{x}_1,t)=\boldsymbol{v}_1$. It is interesting to note that if a function $Q(\boldsymbol{x}_1,t)$ is independent of $\boldsymbol{u}(\boldsymbol{x}_1,t)$, the conditional expectation is the average value:

$$\langle Q(\boldsymbol{x}_1,t)\,|\boldsymbol{u}(\boldsymbol{x}_1,t)=\boldsymbol{v}_1\rangle=\langle Q(\boldsymbol{x}_1,t)\rangle \tag{2.47}$$

and if a function $Q(\boldsymbol{x}_1,t)$ can be completely defined by $\boldsymbol{u}(\boldsymbol{x}_1,t)$, such as $Q(\boldsymbol{u}(\boldsymbol{x}_1,t))$, then its value is directly [68]:

$$\langle Q(\boldsymbol{u}(\boldsymbol{x}_1,t))\,|\boldsymbol{u}(\boldsymbol{x}_1,t)=\boldsymbol{v}_1\rangle=Q(\boldsymbol{v}_1) \tag{2.48}$$

The consequences of Eq. (2.48) are heavily used in PDF modelling since it allows averaged quantities to be solved exactly. In density variable flows, it is also useful to define a density-weighted (Favre) PDF:

$$\langle f(\boldsymbol{v}_1;\boldsymbol{x}_1,t)\rangle_\rho=\frac{\langle\rho(\boldsymbol{x}_1,t)\delta(\boldsymbol{u}(\boldsymbol{x}_1,t)-\boldsymbol{v}_1)\rangle}{\langle\rho(\boldsymbol{x}_1,t)\rangle} \tag{2.49}$$

For a joint velocity-scalar PDF, the following relations arises if the density can be completely defined from the sample space variables $\boldsymbol{\psi}_1$, such as density, enthalpy and pressure:

$$\langle f(\boldsymbol{v}_1,\boldsymbol{\psi}_1;\boldsymbol{x}_1,t)\rangle_\rho=\frac{\rho(\boldsymbol{\psi})}{\langle\rho(\boldsymbol{x}_1,t)\rangle}f(\boldsymbol{v}_1,\boldsymbol{\psi}_1;\boldsymbol{x}_1,t) \tag{2.50}$$

Having defined the PDF most important properties, a review of some of the most influential works is presented in the following. The transport equations for the PDF and its solution methods proposed are also shown.

Lundgren (1967) [65]:

Lundgren derived a transport equation for $f(\boldsymbol{v}_1;\boldsymbol{x}_1,t)$ using the incompressible form of the momentum equation. He used the continuity equation to express the pressure as an exact solution of a Poisson equation using Green's Theorem:

$$\frac{\partial u_i}{\partial t}+u_j\frac{\partial u_i}{\partial x_j}=-\frac{\partial}{\partial x_i}\left(\frac{1}{4\pi}\int\frac{1}{|x_i-x_i'|}\frac{\partial}{\partial x_i'}\left(u_j(x_i',t)\frac{\partial u_i(x_i',t)}{\partial x_j'}\right)\mathrm{d}x_i'\right)+\nu\frac{\partial^2 u_i}{\partial x_j^2} \tag{2.51}$$

Equation (2.51) respects continuity using the incompressible assumption and depends only on velocity itself. In order to derive a transport equation for $f(\boldsymbol{v}_1; \boldsymbol{x}_1, t)$ it is possible to start with the temporal derivative of it:

$$\begin{aligned} \frac{\partial f}{\partial t} &= \left\langle \frac{\partial}{\partial t} \delta\left(\boldsymbol{u}_1 - \boldsymbol{v}_1\right) \right\rangle \\ &= \left\langle -\frac{\partial \boldsymbol{u}_1}{\partial t} \frac{\partial}{\partial \boldsymbol{v}_1} \delta\left(\boldsymbol{u}_1 - \boldsymbol{v}_1\right) \right\rangle \end{aligned} \tag{2.52}$$

where the derivative property of the Dirac delta function is used [41]. It is now possible to use Eq.(2.51) to express the temporal derivative of velocity (implicitly changing the Einstein summation notation back to vectorial notation):

$$\begin{aligned} &\frac{\partial f}{\partial t} + \left\langle -\boldsymbol{u}_1 \frac{\partial \boldsymbol{u}_1}{\partial \boldsymbol{x}_1} \frac{\partial}{\partial \boldsymbol{v}_1} \delta\left(\boldsymbol{u}_1 - \boldsymbol{v}_1\right) \right\rangle \\ &\quad + \left\langle -\frac{\partial}{\partial \boldsymbol{x}_1} \left(\frac{1}{4\pi} \int \frac{1}{|\boldsymbol{x}_1 - \boldsymbol{x}_2|} \frac{\partial}{\partial \boldsymbol{x}_2} \left(\boldsymbol{u}_2 \frac{\partial \boldsymbol{u}_2}{\partial \boldsymbol{x}_2} \right) \mathrm{d}\boldsymbol{x}_2 \right) \frac{\partial}{\partial \boldsymbol{v}_1} \delta\left(\boldsymbol{u}_1 - \boldsymbol{v}_1\right) \right\rangle \\ &\quad + \left\langle \nu \frac{\partial^2 \boldsymbol{u}_1}{\partial \boldsymbol{x}_1^2} \frac{\partial}{\partial \boldsymbol{v}_1} \delta\left(\boldsymbol{u}_1 - \boldsymbol{v}_1\right) \right\rangle = 0 \end{aligned} \tag{2.53}$$

The main advantage of PDF methods is its ability to treat exactly important unclosed terms, such as the source term $\widetilde{S}_\alpha$ and the convective terms by using the important result shown in Eq. (2.48). The convective term closure is exposed here for Equation (2.53) applying the sifting property of Dirac delta function and using Equation (2.46):

$$\begin{aligned} \left\langle -\boldsymbol{u}_1 \frac{\partial \boldsymbol{u}_1}{\partial \boldsymbol{x}_1} \frac{\partial}{\partial \boldsymbol{v}_1} \delta\left(\boldsymbol{u}_1 - \boldsymbol{v}_1\right) \right\rangle &= \left\langle \boldsymbol{u}_1 \frac{\partial}{\partial \boldsymbol{x}_1} \delta\left(\boldsymbol{u}_1 - \boldsymbol{v}_1\right) \right\rangle \\ &= \frac{\partial}{\partial \boldsymbol{x}_1} \left\langle \boldsymbol{u}_1 \delta\left(\boldsymbol{u}_1 - \boldsymbol{v}_1\right) \right\rangle \\ &= \frac{\partial}{\partial \boldsymbol{x}_1} \left(f(\boldsymbol{v}_1; \boldsymbol{x}_1, t) \left\langle \boldsymbol{u}_1 | \boldsymbol{u}_1 = \boldsymbol{v}_1 \right\rangle \right) \\ &= \frac{\partial}{\partial \boldsymbol{x}_1} \left(f(\boldsymbol{v}_1; \boldsymbol{x}_1, t) \boldsymbol{v}_1 \right) \\ &= \boldsymbol{v}_1 \frac{\partial}{\partial \boldsymbol{x}_1} \left(f(\boldsymbol{v}_1; \boldsymbol{x}_1, t) \right) \end{aligned} \tag{2.54}$$

where the incompressible continuity equation is used on the second and fifth line of Equation (2.54). The critical property of the conditional mean of a function completely

defined by the variables included into the PDF is used.

The pressure term in Equation (2.53) cannot be explicitly solved using a one point distribution. Lundgren used a two point distribution to close it, inserting the integral $\int \delta(\boldsymbol{u}_2 - \boldsymbol{v}_2)\,\mathrm{d}\boldsymbol{v}_2$ into the pressure term:

$$\begin{aligned}
&\left\langle -\frac{\partial}{\partial \boldsymbol{x}_1}\left(\frac{1}{4\pi}\int \frac{1}{|\boldsymbol{x}_1-\boldsymbol{x}_2|}\frac{\partial}{\partial \boldsymbol{x}_2}\left(\boldsymbol{u}_2\frac{\partial \boldsymbol{u}_2}{\partial \boldsymbol{x}_2}\right)\mathrm{d}\boldsymbol{x}_2\right)\frac{\partial}{\partial \boldsymbol{v}_1}\delta\left(\boldsymbol{u}_1-\boldsymbol{v}_1\right)\right\rangle = \\
&\frac{\partial}{\partial \boldsymbol{v}_1}\left\langle -\frac{\partial}{\partial \boldsymbol{x}_1}\left(\frac{1}{4\pi}\int \frac{1}{|\boldsymbol{x}_1-\boldsymbol{x}_2|}\frac{\partial}{\partial \boldsymbol{x}_2}\left(\boldsymbol{u}_2\frac{\partial \boldsymbol{u}_2}{\partial \boldsymbol{x}_2}\right)\mathrm{d}\boldsymbol{x}_2\right)\delta\left(\boldsymbol{u}_1-\boldsymbol{v}_1\right)\right\rangle = \\
&\frac{\partial}{\partial \boldsymbol{v}_1}\left(-\frac{1}{4\pi}\frac{\partial}{\partial \boldsymbol{x}_1}\int\int \frac{1}{|\boldsymbol{x}_1-\boldsymbol{x}_2|}\boldsymbol{v}_2^2\frac{\partial^2 f(\boldsymbol{v}_2,\boldsymbol{v}_1;\boldsymbol{x}_2,\boldsymbol{x}_1,t)}{\partial \boldsymbol{x}_2^2}\,\mathrm{d}\boldsymbol{x}_2\,\mathrm{d}\boldsymbol{v}_2\right)
\end{aligned} \tag{2.55}$$

The remaining viscous term is also reduced with the two-point PDF:

$$\begin{aligned}
\left\langle \nu\frac{\partial^2 \boldsymbol{u}_1}{\partial \boldsymbol{x}_1^2}\frac{\partial}{\partial \boldsymbol{v}_1}\delta\left(\boldsymbol{u}_1-\boldsymbol{v}_1\right)\right\rangle &= \frac{\partial}{\partial \boldsymbol{v}_1}\left\langle \nu\frac{\partial^2 \boldsymbol{u}_1}{\partial \boldsymbol{x}_1^2}\delta\left(\boldsymbol{u}_1-\boldsymbol{v}_1\right)\right\rangle \\
&= \frac{\partial}{\partial \boldsymbol{v}_1}\lim_{\boldsymbol{x}_2\to\boldsymbol{x}_1}\nu\frac{\partial^2}{\partial \boldsymbol{x}_2^2}\left\langle \boldsymbol{u}_2\delta\left(\boldsymbol{u}_1-\boldsymbol{v}_1\right)\right\rangle \\
&= \frac{\partial}{\partial \boldsymbol{v}_1}\lim_{\boldsymbol{x}_2\to\boldsymbol{x}_1}\nu\frac{\partial^2}{\partial \boldsymbol{x}_2^2}\int \boldsymbol{v}_2 f(\boldsymbol{v}_2,\boldsymbol{v}_1;\boldsymbol{x}_2,\boldsymbol{x}_1,t)\,\mathrm{d}\boldsymbol{v}_2
\end{aligned} \tag{2.56}$$

The equation for the one-point PDF is therefore reduced to:

$$\begin{aligned}
&\frac{\partial f}{\partial t} + \boldsymbol{v}_1\frac{\partial}{\partial \boldsymbol{x}_1}\left(f(\boldsymbol{v}_1;\boldsymbol{x}_1,t)\right) \\
&\quad + \frac{\partial}{\partial \boldsymbol{v}_1}\left(-\frac{1}{4\pi}\frac{\partial}{\partial \boldsymbol{x}_1}\int\int \frac{1}{|\boldsymbol{x}_1-\boldsymbol{x}_2|}\boldsymbol{v}_2^2\frac{\partial^2 f(\boldsymbol{v}_2,\boldsymbol{v}_1;\boldsymbol{x}_2,\boldsymbol{x}_1,t)}{\partial \boldsymbol{x}_2^2}\,\mathrm{d}\boldsymbol{x}_2\,\mathrm{d}\boldsymbol{v}_2\right) \\
&\quad + \frac{\partial}{\partial \boldsymbol{v}_1}\lim_{\boldsymbol{x}_2\to\boldsymbol{x}_1}\nu\frac{\partial^2}{\partial \boldsymbol{x}_2^2}\int \boldsymbol{v}_2 f(\boldsymbol{v}_2,\boldsymbol{v}_1;\boldsymbol{x}_2,\boldsymbol{x}_1,t)\,\mathrm{d}\boldsymbol{v}_2 = 0
\end{aligned} \tag{2.57}$$

Equation (2.57) is exact and represents the transport of the one-point PDF, requiring the knowledge of a two-point PDF though. It also possible to derive a transport equation for the two-point PDF, however, it would be required a three-point PDF and so on. This issue is the same as the turbulence closure, where each equation introduces a higher-order variable resulting always in more unknown and than known variables. A closure for the one-point PDF equation is later proposed in Lundgren [66], which solved the PDF equation in many simplified test cases. As the two-point PDF introduces great complexity to the problem, the research groups mainly focused their modelling effort into

closing the one-point PDF equation.

Dopazo (1975) [67]:

An Eulerian one-point PDF equation was also investigated by Dopazo in the 70's [69, 67, 70]. In the work of Dopazo [67] an one-point probability density function for the temperature $f(T_1; \boldsymbol{x}_1, t)$ is considered for modelling an axisymmetric jet of air discharging into still air. The semicolon notation indicates that $f(T_1; \boldsymbol{x}_1, t)$ represents the PDF of T_1 that varies in the space $\boldsymbol{x}_1$ and time t. It satisfies the following transport equation:

$$\begin{aligned} \frac{\partial f(T_1; \boldsymbol{x}_1, t)}{\partial t} + \frac{\partial}{\partial x_i}\left[\langle v | T_1 \rangle \, f(T_1; \boldsymbol{x}_1, t) \right] = \\ -\frac{\partial}{\partial T_1} \lim_{\boldsymbol{x}_2 \to \boldsymbol{x}_1} \alpha \frac{\partial^2}{\partial x_i^2} \int f(T_1, T_2; \boldsymbol{x}_1, \boldsymbol{x}_2, t) T_2 \, \mathrm{d}T_2 \end{aligned} \tag{2.58}$$

where $f(T_1, T_2; \boldsymbol{x}_1, \boldsymbol{x}_2, t)$ is the Eulerian two-point PDF of temperature and α is the thermal diffusivity. Dopazo [67] suggested to model the term on the right-hand side of Eq.(2.58) as a difference between a sample temperature and the average temperature, scaled by the Taylor microscale of the velocity field:

$$-\frac{\partial}{\partial T_1} \lim_{\boldsymbol{x}_2 \to \boldsymbol{x}_1} \alpha \frac{\partial^2}{\partial x_i^2} \int f(T_1, T_2; \boldsymbol{x}_1, \boldsymbol{x}_2, t) T_2 \, \mathrm{d}T_2 \approx \frac{3\nu}{\lambda_t^2} \frac{\partial}{\partial T_1} \left[(T_1 - \langle T_1 \rangle) \, f(T_1; \boldsymbol{x}_1, t) \right] \tag{2.59}$$

where λ_t is the Taylor microscale. This model is very similar to the one developed by Villermaux and Devillon [71] and it is called Interaction by Exchange with the Mean (IEM) micromixing model or Linear Mean-Square Estimation (LMSE) micromixing model [69].

The convective term, in contrast with the model suggested by Lundgren [65], requires modelling and it was closed by assuming it is conditionally Gaussian. The results presented reasonable agreement with experiments, however, they have still shown that the model has several constrains regarding its generalisation.

Pope (1976) [72]:

The work of Pope [72] addressed the issue to model turbulent reacting flows using both a single scalar PDF and a joint scalar PDF. This work has also been evaluated in Pope's subsequent work [73, 74, 75]. The Eulerian one-point joint scalar PDF used by

Pope [72] was defined as the average of a productory of Dirac delta functions:

$$f(\boldsymbol{\psi};\boldsymbol{x},t) = \left\langle \prod_{\alpha=1}^{N_s} \delta\left(\psi_\alpha - \phi_\alpha(\boldsymbol{x},t)\right) \right\rangle \tag{2.60}$$

Using similar techniques of Lundgren [65] and assuming low Mach number it can be obtained a transported equation for the joint scalar PDF:

$$\begin{aligned} \rho(\boldsymbol{\psi})\frac{Df}{Dt} =& \frac{\partial}{\partial x_i}\left[\Gamma\frac{\partial f}{\partial x_i} - \rho(\boldsymbol{\psi}) f \left\langle u_i|\boldsymbol{\psi}\right\rangle\right] \\ & - \sum_{\alpha=1}^{N_s}\frac{\partial}{\partial\psi_\alpha}\left[fS_\alpha(\boldsymbol{\psi}) + \sum_{\beta=1}^{N_s}\frac{\partial}{\partial\psi_\beta}\left(\left\langle \Gamma\frac{\phi_\alpha}{\partial x_i}\frac{\phi_\beta}{\partial x_i}\middle|\boldsymbol{\psi}\right\rangle f\right)\right] \end{aligned} \tag{2.61}$$

where Γ is the species diffusion coefficient. The source term is now properly closed $S_\alpha(\boldsymbol{\psi})$ using similar reasoning presented in Eq.(2.54). Although Pope [72] proposed closures for the single scalar PDF equation, the transport Equation (2.61) for the joint scalar PDF modelling issues had not been addressed yet. The convective term could have been modelled using similar turbulent convection approaches available, however, the molecular mixing term required a more comprehensive approach which was not investigated in his work. This mixing term is known as micromixing and it has been object of extensive research. A micromixing investigation is not the objective of this work, though, and a review on this subject can be found in Fox [76] or Haworth [64].

Pope (1985) [68]:

The seminal paper of Pope [68] highly influenced subsequent proposed models after presenting the Lagrangian-particle formulation to solve a joint scalar PDF or a joint scalar-velocity PDF. The particle formulation was first presented in Pope [77]where two evolution equations were derived, one for the joint scalar PDF and another for the particles. These equations, for the particle and for the PDF, were then coupled to result in only one evolution equation. This equation therefore evolves accordingly to the joint scalar PDF, i.e.: they share the same moments if use the same initial and boundary conditions.

The work in [68] shows a different way to correlate the Lagrangian-particle formulation

and the one-point joint scalar PDF. It presents the PDF transport equation as a Fokker-Planck or forward Kolmogorov equation [78]. Equivalent stochastic differential equations can be therefore used instead of directly solving the PDF transport equation. Pope [68] introduces the Monte-Carlo method to calculate the average values for the variables included in the PDF, firstly proposed by Pope [79] in 1980. The finite difference method had been used in previous works to solve the PDF and it was the most general solution method presented so far [80]. However, because of the high-dimensionality of the PDF the finite difference method becomes unfeasible. The Monte Carlo method, however, does not suffer from this drawback but it has a slower convergence rate. Assuming a random variable ϕ and conducting N experiments with the same initial and boundary conditions to obtain sample values for ϕ, it is possible to calculate the ensemble average of ϕ [68]:

$$\langle \boldsymbol{\phi} \rangle_N = \frac{1}{N} \sum_{n=1}^{N} \phi^n \tag{2.62}$$

where the operator $\langle \cdot \rangle_N$ depicts the ensemble average obtained from N samples. The convergence rate is proportional to the number of samples. Considering a normalised error err:

$$err = \frac{(\langle \boldsymbol{\phi} \rangle_N - \langle \boldsymbol{\phi} \rangle)}{err_N} \tag{2.63}$$

where the err_N is the standard error, the Central Limit theorem shows that the standard error converges following the relation:

$$err_N = \sigma / \sqrt{N} \tag{2.64}$$

where σ here represents the standard deviation of ϕ. The relation presented in Eq.(2.64) indicates the main drawback of the Monte Carlo method. The error decreases only with rate $N^{-0.5}$ and a large number of samples may be required to achieve a certain error threshold.

In Pope [68] it was evaluated a Eulerian fine-grained one-point joint velocity-scalar

PDF:

$$f'(v_i, \phi_\alpha; \boldsymbol{x}, t) = \prod_{i=1}^{3} \delta\left(u_i(\boldsymbol{x}, t) - v_i\right) \prod_{\alpha=1}^{N_s} \delta\left(\phi_\alpha(\boldsymbol{x}, t) - \psi_\alpha\right) \tag{2.65}$$

and using Eq.(2.42) the Eulerian one-point joint velocity-scalar PDF can be obtained:

$$f(v_i, \phi_\alpha; \boldsymbol{x}, t) = \langle f'(v_i, \phi_\alpha; \boldsymbol{x}, t) \rangle \tag{2.66}$$

Using the same techniques presented before, it is also possible to obtain a transported PDF equation for variable density flows, also applying the low Mach number assumption. The derivation for this equation is not presented here however it is thoroughly explained in [68] and [64]. The unclosed transport equation for the one-point joint velocity-scalar PDF is obtained after deriving a transport equation for the fine-grained joint velocity-scalar PDF, using the transport equations for the velocity and chemical species and applying an ensemble average into it, obtaining:

$$\begin{aligned} \rho(\boldsymbol{\phi})\frac{\partial f}{\partial t} + \rho(\boldsymbol{\phi}) v_j \frac{\partial f}{\partial x_j} + \left(\rho(\boldsymbol{\phi}) g_j - \frac{\partial \langle p \rangle}{\partial x_j}\right)\frac{\partial f}{\partial v_j} + \frac{\partial}{\partial \phi_\alpha}\left(\rho(\boldsymbol{\phi}) S_\alpha f\right) = \\ \frac{\partial}{\partial v_j}\left[\left\langle -\frac{\partial \tau_{ij}}{\partial x_i} + \frac{\partial p'}{\partial x_j} \middle| \boldsymbol{v}, \boldsymbol{\psi} \right\rangle f\right] + \frac{\partial}{\partial \psi_\alpha}\left[\left\langle \frac{\partial J_i^\alpha}{\partial x_i} \middle| \boldsymbol{v}, \boldsymbol{\psi} \right\rangle f\right] \end{aligned} \tag{2.67}$$

Equation (2.67) presents the closed terms on the left hand side and the unclosed terms on the right hand side. The pressure has been decomposed in its average and its fluctuation part: $p = \langle p \rangle + p'$. It can be finally seen the convective and source term exactly closed, and they do not require any extra modelling effort. Nonetheless, the RHS needs to be modelled but their influence in a reactive and highly convective flow are supposed to be smaller in comparison to the reactive and convective term, showing the motivation to solve this transport equation.

The idea presented in [68] is to model the unclosed velocity terms by using a Langevin equation, which was originally developed for Brownian motion modelling [81]. The unclosed terms on the scalar part could be modelled using the deterministic Interaction by Exchange with the Mean (IEM) micromixing model [71, 67]. In this way, Eq.(2.67) is

therefore closed using the following assumptions:

$$\frac{\partial}{\partial v_j}\left[\left\langle -\frac{\partial \tau_{ij}}{\partial x_i}+\frac{\partial p'}{\partial x_j}\middle|\boldsymbol{v},\boldsymbol{\psi}\right\rangle f\right]\approx\frac{\partial}{\partial v_j}\left[\langle\rho\rangle\, G_{ij}\left(v_i-\langle u_j\rangle\right) f\right]+\frac{\partial^2}{\partial v_j^2}\left[\frac{1}{2}C_0\epsilon\,\langle\rho\rangle\, f\right] \tag{2.68}$$

$$\frac{\partial}{\partial \psi_\alpha}\left[\left\langle \frac{\partial J_i^\alpha}{\partial x_i}\middle|\boldsymbol{v},\boldsymbol{\psi}\right\rangle f\right]\approx\frac{\partial}{\partial \psi_\alpha}\left[-\frac{1}{2}\langle\rho\rangle\, C_\phi\left(\psi_\alpha-\langle\phi_\alpha\rangle\right) f\right] \tag{2.69}$$

where C_0 is the Langevin constant equal to 2.1, C_ϕ is the micromixing constant equal to 2.0 and ϵ is the rate of dissipation of the turbulent kinetic energy in RANS context. The tensor G_{ij} is defined as isotropic for the simplified Langevin model:

$$G_{ij}=-\frac{\epsilon}{k}\left(\frac{1}{2}+\frac{3}{4}C_0\right)\delta_{ij} \tag{2.70}$$

or anisotropic if the Generalised Langevin model is used [82]:

$$G_{ij}=\frac{\epsilon}{k}\left(\alpha_1\delta_{ij}+\alpha_2 b_{ij}+\alpha_3 b_{ij}^2\right)+H_{ijkl}\frac{\partial\langle u_k\rangle}{\partial x_l} \tag{2.71}$$

where H_{ijkl} is a fourth-order tensor and b_{ij} can account for the normalised anisotropy of the Reynolds-stress tensor. The turbulent kinetic energy can be directly solved since it can be obtained from variables included in the PDF sample space:

$$k=\frac{1}{2}\langle u_i u_i\rangle=\int_{-\infty}^{+\infty}\int_{-\infty}^{+\infty}\frac{1}{2}\left(v_i-\langle u_i\rangle\right)\left(v_i-\langle u_i\rangle\right) f\,\mathrm{d}\boldsymbol{v}\,\mathrm{d}\boldsymbol{\psi} \tag{2.72}$$

However, a model for the turbulent kinetic energy rate of dissipation, ϵ, is still necessary. A model such as Jones and Launder [83], Launder and Spalding [84] is sufficient to calculate it. The full closed equation is therefore:

$$\begin{aligned}\rho(\boldsymbol{\psi})\frac{\partial f}{\partial t}+\rho(\boldsymbol{\psi})v_j\frac{\partial f}{\partial x_j}+\left(\rho(\boldsymbol{\psi})g_j-\frac{\partial\langle p\rangle}{\partial x_j}\right)\frac{\partial f}{\partial v_j}+\frac{\partial}{\partial\psi_\alpha}\left(\rho(\boldsymbol{\psi})S_\alpha f\right)=\\ \frac{\partial}{\partial v_j}\left[\rho(\boldsymbol{\psi})G_{ij}\left(v_i-\langle u_j\rangle\right) f\right]+\frac{\partial^2}{\partial v_j^2}\left[\frac{1}{2}C_0\epsilon\rho(\boldsymbol{\psi})f\right]\\ +\frac{\partial}{\partial\psi_\alpha}\left[-\frac{1}{2}\rho(\boldsymbol{\psi})C_\phi\left(\psi_\alpha-\langle\phi_\alpha\rangle\right) f\right]\end{aligned} \tag{2.73}$$

Equation (2.75) is a variable-density transport equation for the PDF. In this kind of flows a new variable is defined, the mass density function (MDF):

$$\mathscr{F}\left(\boldsymbol{v},\boldsymbol{\psi},\boldsymbol{x};t\right)=\rho\left(\boldsymbol{\psi}\right)f\left(\boldsymbol{v},\boldsymbol{\psi};\boldsymbol{x},t\right) \tag{2.74}$$

The MDF represents the expected mass density in $\boldsymbol{v}-\boldsymbol{\psi}-\boldsymbol{x}$ space and has to respect several properties presented[2] in [68]. For instance, its integral in the whole sample space must result in the averaged density, whereas when multiplied by a function Q and integrated it results in $\langle\rho Q\rangle$. If the MDF is multiplied by ρ^{-1} and integrated, it yields unity. It is critical to notice that the mass density function includes the position in the space $\boldsymbol{x}$ in its sample space, as noticed by the semicolon notation. A new transport equation is finally derived:

$$\begin{gathered}\frac{\partial\mathscr{F}}{\partial t}+\frac{\partial v_j\mathscr{F}}{\partial x_j}+\frac{\partial}{\partial v_j}\left(g_j\mathscr{F}-\frac{1}{\rho(\boldsymbol{\phi})}\frac{\partial\left\langle p\right\rangle}{\partial x_j}\mathscr{F}\right)+\frac{\partial}{\partial\psi_\alpha}\left(S_\alpha\mathscr{F}\right)=\\ \frac{\partial}{\partial v_j}\left[G_{ij}\left(v_i-\left\langle u_j\right\rangle\right)\mathscr{F}\right]+\frac{\partial^2}{\partial v_j^2}\left[\frac{1}{2}C_0\epsilon\mathscr{F}\right]+\frac{\partial}{\partial\psi_\alpha}\left[-\frac{1}{2}C_\phi\left(\psi_\alpha-\left\langle\phi_\alpha\right\rangle\right)\mathscr{F}\right]\end{gathered} \tag{2.75}$$

Equation(2.75) is a Fokker-Planck equation after using the mass density function concept. A general Fokker-Planck equation is used to describe a diffusion process governed by $f\left(\psi_i;t\right)$ and it is given by:

$$\frac{\partial f}{\partial t}=-\frac{\partial}{\partial\psi_i}\left(A_i f\right)+\frac{1}{2}\frac{\partial^2}{\partial\psi_i\partial\psi_j}\left(B_{ik}B_{jk}f\right) \tag{2.76}$$

where A_i is the drift coefficient and B_{ij} is the diffusion tensor. The equivalent stochastic differential equation using Ito interpretation is represented by [78]:

$$\mathrm{d}\phi_i=A_i\,\mathrm{d}t+B_{ij}\,\mathrm{d}W_j \tag{2.77}$$

where $\mathrm{d}W_j$ is a Wiener process. A Wiener process is a class of Markovian process and it is continuous in space and time, however, only differentiable in space. The isotropic

[2] In section 3.3 of [68].

Wiener process, used in this work, have the two following properties:

$$\langle \mathrm{d}W_i \rangle = 0; \qquad \mathrm{d}W_i \, \mathrm{d}W_j = \delta_{ij} \, \mathrm{d}t \tag{2.78}$$

Stochastic differential equations can then be obtained for the variables included in the mass density function $\mathscr{F}$. The n-set of Lagrangian-particle equations is therefore:

$$\mathrm{d}X_i^+ = U_i^+ \, \mathrm{d}t \tag{2.79}$$

$$\mathrm{d}U_i^+ = \left(-\frac{1}{\rho(\boldsymbol{\phi})} \frac{\partial \langle p \rangle}{\partial x_j} + g_j - G_{ij} \left(U_i^+ - \langle u_j \rangle \right) \right) \mathrm{d}t + \sqrt{C_0 \epsilon} \, \mathrm{d}W_t \tag{2.80}$$

$$\mathrm{d}\phi_\alpha^+ = \left(\frac{1}{2} C_\phi \left(\phi_\alpha^+ - \langle \phi_\alpha \rangle \right) + S_\alpha \right) \mathrm{d}t \tag{2.81}$$

This set of Lagrangian equations are equivalent to a discrete MDF Fokker-Planck equation. As proved in [68], this discrete MDF transport equation (not shown here) is equivalent to the original transport Equation (2.75) for the MDF.

This modelling has been investigated in low Mach number [85, 86] and even high Mach number applications [14]. The turbulent kinetic energy k and ϵ are closed using RANS approach, usually in a hybrid Lagrangian/Eulerian approach. If one integrates it in the velocity space it is possible to obtain an one-point joint scalar PDF, however, a closure for the convective term is required [87, 63]. A large compilation of the applications of transported PDF within the Lagrangian framework can be visited in Chapter 9 of Haworth [64].

Kollmann (1992) [88]:

In the context of compressible reacting flows, the pioneer work by Kollmann [88] and Eifler and Kollmann [89] proposed a PDF transport equation aiming the simulation of supersonic hydrogen flames. In order to avoid the low Mach number assumption, one extra thermodynamic variable is included within the Eulerian one-point joint velocity-

scalar PDF:

$$f(\boldsymbol{v}, d, e, \zeta, \eta; \boldsymbol{x}, t) = \langle f'(\boldsymbol{v}, d, e, \zeta, \eta; \boldsymbol{x}, t)\rangle = \\ \langle \delta(\boldsymbol{v} - \boldsymbol{u}(\boldsymbol{x}, t))\delta(d - \rho(\boldsymbol{x}, t))\delta(e - U(\boldsymbol{x}, t))\delta(\zeta - D(\boldsymbol{x}, t))\delta(\eta - \xi(\boldsymbol{x}, t))\rangle \tag{2.82}$$

where d, e, ζ and η are the sample space variables of density $\rho(\boldsymbol{x}, t)$, internal energy $U(\boldsymbol{x}, t)$, velocity divergence $D(\boldsymbol{x}, t) = \partial u_i/\partial x_i$ and mixture fraction $\xi(\boldsymbol{x}, t)$, respectively. The unclosed transported equation for the PDF in non-dimensional form is therefore:

$$\begin{aligned} \frac{\partial f}{\partial t} + v_j \frac{\partial f}{\partial x_j} = \frac{\partial}{\partial d}\left(d^2 \zeta f\right) - \frac{\partial}{\partial v_i}\left(-\left\langle \frac{\partial p}{\partial x_i} f' \right\rangle + \frac{1}{\mathrm{Re}}\left\langle \frac{\partial \tau_{ij}}{\partial x_j} f' \right\rangle + Bd\left\langle f_i f' \right\rangle\right) \\ -\frac{\partial}{\partial e}\left(-\frac{\gamma - 1}{c_v} e d\zeta f + \gamma(\gamma - 1)\frac{\mathrm{Ma}^2}{\mathrm{Re}}\left\langle \boldsymbol{\Psi} f' \right\rangle - \frac{\gamma}{\mathrm{Pe}}\left\langle \frac{\partial q_i}{\partial x_i} f' \right\rangle\right) \\ -\frac{\partial}{\partial \zeta}\left(-\frac{1}{\mathrm{Re}}\left\langle \frac{\partial}{\partial x_i}\left(\frac{1}{\rho}\frac{\partial \tau_{ij}}{\partial x_i}\right) f' \right\rangle - \left\langle \frac{\partial u_i}{\partial x_j}\frac{\partial u_j}{\partial x_i} f' \right\rangle + B\left\langle \frac{\partial f_i}{\partial x_i} f' \right\rangle \right. \\ \left. -\left\langle \frac{\partial}{\partial x_i}\left(\frac{1}{\rho}\frac{\partial p}{\partial x_i}\right) f' \right\rangle\right) - \frac{\partial}{\partial \eta}\left(\left\langle \frac{\partial}{\partial x_i}\left(\rho\Gamma\frac{\partial \zeta}{\partial x_i}\right) f' \right\rangle\right) \end{aligned} \tag{2.83}$$

where B is a dimensionless number associated with the external force f_i, Pe is the Peclet number and Ma is the Mach number. Equation (2.83) was not closed in [89], but it was integrated in the velocity space and closed with mixing models for compressible turbulence. The simulations were validated with experimental data and the authors concluded that compressible reactive PDFs are feasible, although with very complex numerical modelling. The inclusion of the velocity divergence into the PDF sample space results in a sophisticated transport equation for the PDF, which requires extra terms to closure without direct link to physical quantities. This was performed to perfectly close the continuity equation, since the density had also been included into the PDF.

The inclusion of density as a stochastic variable represents a big challenge from the modelling point of view, since it is very difficult to ensure mass conservation. This kind of PDF model would only be revisited by Bakosi and Ristorcelli [90] in 2010 with following works [91, 92]. However, the need to model a stochastic equation for the density still makes this kind of approach an arduous task.

A compressible approach for non-reacting flow was also developed by Welton and Pope

[93] and Welton and Pope [94], which used only an one-point velocity PDF. The focus of these works was to show the coupling the Lagrangian algorithm with a compressible Eulerian one to obtain the average thermodynamic pressure. The extension of this model to consider compressible and reactive flows would be only considered again by Delarue and Pope [20].

Dreeben and Pope (1997) [95]:

The work of Dreeben and Pope [95] proposed a new formulation aimed for high accuracy in near wall regions, and it was also shown in [68]. The idea is to consider part of the viscous effects into the Lagrangian equations instead of fully modelling them, in this way increasing the accuracy in regions of the flow where viscous effects are dominant such as near-wall regions. The Lagrangian equations proposed are:

$$\mathrm{d}X_i^+ = U_i^+ \,\mathrm{d}t + \sqrt{2\nu}\,\mathrm{d}W_i \tag{2.84}$$

$$\begin{aligned}\mathrm{d}U_i^+ = &-\frac{1}{\rho}\frac{\partial \langle p\rangle}{\partial x_i}\,\mathrm{d}t + 2\nu\frac{\partial^2 \left\langle U_i^+\right\rangle}{\partial x_j \partial x_j}\,\mathrm{d}t + \sqrt{2\nu}\frac{\partial \left\langle U_i^+\right\rangle}{\partial x_j}\,\mathrm{d}W_j \\ &+ G_{ij}\left(U_j^+ - \left\langle U_j^+\right\rangle\right)\mathrm{d}t + \sqrt{C_0\epsilon^+}\,\mathrm{d}W_i'\end{aligned} \tag{2.85}$$

The Lagrangian equations are then equivalent to the following Fokker-Planck equation:

$$\begin{aligned}\frac{\partial f_L}{\partial t} + v_i\frac{\partial f_L}{\partial x_i} =&\nu\frac{\partial^2 f_L}{\partial x_i \partial x_i} + \frac{\partial f_L}{\partial v_i}\left(\frac{1}{\rho}\frac{\partial \langle p\rangle}{\partial x_i}\right) - \frac{\partial}{\partial v_i}\left[G_{ij}\left(v_j - \langle U_j\rangle\right) f_L\right] \\ &+ 2\nu\frac{\partial \langle U_j\rangle}{\partial x_i}\frac{\partial^2 f_L}{\partial x_i \partial v_j} + \nu\frac{\partial \langle U_i\rangle}{\partial x_k}\frac{\partial \langle U_j\rangle}{\partial x_k}\frac{\partial^2 f_L}{\partial v_i \partial v_j} + \frac{1}{2}C_0\epsilon\frac{\partial^2 f_L}{\partial v_i \partial v_i}\end{aligned} \tag{2.86}$$

where $f_L(\boldsymbol{v};\boldsymbol{x},t)$ is the Lagrangian one-point PDF. It is also possible to prove that this Fokker-Planck equation is equivalent to the Eulerian counterpart, which is obtained from similar techniques as [68]. The second spatial derivative of the PDF represents the stochastic term in the Lagrangian position X^+ equation. This model therefore accounts for molecular viscosity, which is important in near-wall regions. This kind of modelling has influenced other large eddy simulation works because of the inclusion of molecular

effects and it is revisited by most LES/PDF Lagrangian approaches.

Delarue and Pope (1997) [20]:

Delarue and Pope [20, 96] investigated compressible Lagrangian PDF models including pressure and internal energy as sample variables, along with the velocity, species composition and turbulence frequency in a RANS framework. The developed Eulerian one-point joint velocity-scalar mass density function is:

$$\begin{aligned}\mathscr{F}(\hat{\boldsymbol{u}},\hat{\omega},\hat{e},\hat{p};\boldsymbol{x},t) = \rho(\hat{e},\hat{p})\,\langle\delta(\hat{\boldsymbol{u}}-\boldsymbol{u}(\boldsymbol{x},t))\\ \delta(\hat{\omega}-\omega(\boldsymbol{x},t))\delta(\hat{e}-e(\boldsymbol{x},t))\delta(\hat{p}-p(\boldsymbol{x},t))\rangle\end{aligned} \tag{2.87}$$

The turbulent frequency has been added in order to provide a better closure for the turbulence time-scale, not requiring a priori the solution of transport equations for k and ϵ any more. The Lagrangian equations used in this model are:

$$\mathrm{d}X_i^+ = U_i^+\,\mathrm{d}t \tag{2.88}$$

$$\mathrm{d}U_i^+ = -\frac{1}{\langle\rho\rangle}\frac{\partial\langle p\rangle}{\partial x_i}\,\mathrm{d}t + \frac{1}{2k}\left(\frac{\Pi_d}{\langle\rho\rangle} - \epsilon\left(1+\frac{3}{2}C_0\right)\right)\left(U_i^+ - \langle U_i\rangle\right)\mathrm{d}t + \sqrt{C_0\epsilon}\,\mathrm{d}W_i \tag{2.89}$$

$$\mathrm{d}e^+ = \epsilon\,\mathrm{d}t - p^+\,\mathrm{d}v^+ \tag{2.90}$$

$$\mathrm{d}p^+ = p^+\left(A\,\mathrm{d}t + B\,\mathrm{d}W_t\right) \tag{2.91}$$

$$\mathrm{d}\omega^+ = -\left(\omega^+ - \langle\omega\rangle\right)C_3\Omega\,\mathrm{d}t - \langle\omega\rangle\,\omega^+ S_\omega\,\mathrm{d}t + \sqrt{2\sigma^2\,\langle\omega\rangle\,\omega^+ C_3\Omega}\,\mathrm{d}W \tag{2.92}$$

where v^+ is the specific volume of the stochastic particle related as $p^+v^+ = (\gamma-1)e^+$ and Π_d is the pressure dilatation correction, modelled with the Zeman's model [97]. The turbulence frequency equation, along with a model to obtain the quantity Ω, evolves

according to Jayesh and Pope [98]. The normalised variance σ^2 is defined in Jayesh and Pope [98]. The pressure equation is fully modelled, where A and B are model coefficients. Delarue and Pope [20] did not provide in their work the transport equation for the PDF, however, the equation can be straightforwardly derived using the relation between Eqs.(2.76) and (2.77).

The inclusion of pressure allows the Lagrangian solver to be independent from coupling with a finite volume or finite difference solver in order to obtain the average pressure, a common issue in Lagrangian/particle formulation. The authors therefore could develop a full Lagrangian independent solver, however, the results were only satisfactory in the low-Mach number range. More complex closures would be required, which were computationally prohibited at the time.

Valiño (1998) [19]:

The Eulerian stochastic fields method was developed in 1998. Valiño [19] developed a method to solve the transport equation for the Eulerian PDF using an Eulerian framework technique. In this way, there is no need to develop a new Lagrangian solver within established CFD codes, which increases the popularity of the PDF approach. Also, the Eulerian stochastic differential equations are equivalent to a Eulerian PDF Fokker-Planck transport equation. There is no need a priori to prove the equivalence between a Lagrangian PDF and a Eulerian PDF, one fundamental issue in Lagrangian methods.

The original derivation of Valiño considered a Eulerian one-point scalar PDF $f(\psi;\boldsymbol{x},t) = \langle\delta(\psi-\phi(\boldsymbol{x},t))\rangle$ that evolves according to the following transport equation:

$$\frac{\partial f}{\partial t}+\langle u_i\rangle\frac{\partial f}{\partial x_i}=\frac{\partial}{\partial x_i}\left(\left(\Gamma+\Gamma_t\right)\frac{\partial f}{\partial x_i}\right)+\frac{\partial}{\partial\psi}\left[\frac{\omega}{2}\left(\psi-\langle\phi\rangle\right)f\right]-\frac{\partial}{\partial\psi}\left[S(\psi)f\right] \tag{2.93}$$

where Γ and Γ_t are the molecular and turbulent transport coefficients, respectively, ω is the turbulence frequency and sample and real variables are ψ and $\phi(\boldsymbol{x},t)$, respectively. The method proposed by Valiño to solve Eq.(2.93) is to represent the PDF $f(\psi;\boldsymbol{x},t)$ with

an ensemble of N_f twice differentiable in space Eulerian stochastic fields $\tau^n(\boldsymbol{x},t)$:

$$f_\tau(\psi;\boldsymbol{x},t)=\frac{1}{N_f}\sum_{n=1}^{N_f}\delta\left[\psi-\tau^n(\boldsymbol{x},t)\right]\equiv\left\langle\delta\left[\psi-\tau(\boldsymbol{x},t)\right]\right\rangle \tag{2.94}$$

where the transport equations for $f(\psi;\boldsymbol{x},t)$ and $f_\tau(\psi;\boldsymbol{x},t)$ are the same and have the same moments as well. However, the equation for $f_\tau(\psi;\boldsymbol{x},t)$ can be manipulated to transform Eq.(2.93) into a Fokker-Planck equation in which it is possible to derive Eulerian stochastic equations. For instance, by substituting Eq.(2.94) into Eq.(2.93):

$$\begin{aligned}\frac{\partial\left\langle\delta\left[\psi-\tau(\boldsymbol{x},t)\right]\right\rangle}{\partial t}+\langle u_i\rangle\frac{\partial\left\langle\delta\left[\psi-\tau(\boldsymbol{x},t)\right]\right\rangle}{\partial x_i}=\frac{\partial}{\partial x_i}\left((\Gamma+\Gamma_t)\frac{\partial\left\langle\delta\left[\psi-\tau(\boldsymbol{x},t)\right]\right\rangle}{\partial x_i}\right)\\+\frac{\partial}{\partial\psi}\left[\frac{\omega}{2}\left(\psi-\langle c\rangle\right)\left\langle\delta\left[\psi-\tau(\boldsymbol{x},t)\right]\right\rangle\right]-\frac{\partial}{\partial\psi}\left[S(\psi)\left\langle\delta\left[\psi-\tau(\boldsymbol{x},t)\right]\right\rangle\right]\end{aligned} \tag{2.95}$$

In Eq.(2.95) there are spatial derivatives, which prevent it from being a Fokker-Planck equation if the position $\boldsymbol{x}$ is not into the sample space of the PDF. The convective term can be rewritten as:

$$\begin{aligned}\langle u_i\rangle\frac{\partial\langle\delta\rangle}{\partial x_i}&=\langle u_i\rangle\left\langle\frac{\partial\delta}{\partial x_i}\right\rangle=\langle u_i\rangle\left\langle-\frac{\partial\tau}{\partial x_i}\frac{\partial\delta}{\partial\psi}\right\rangle\\&=-\frac{\partial}{\partial\psi}\left(\langle u_i\rangle\left\langle\frac{\partial\tau}{\partial x_i}\delta\right\rangle\right)=-\frac{\partial}{\partial\psi}\left(\langle u_i\rangle\left\langle\frac{\partial\tau}{\partial x_i}\middle|\psi\right\rangle f_\tau\right)\end{aligned} \tag{2.96}$$

and the diffusive term can be transformed similarly:

$$\begin{aligned}\frac{\partial}{\partial x_i}\left((\Gamma+\Gamma_t)\frac{\partial\langle\delta\rangle}{\partial x_i}\right)&=-\frac{\partial}{\partial x_i}\left((\Gamma+\Gamma_t)\left\langle\frac{\partial\tau}{\partial x_i}\frac{\partial\delta}{\partial\psi}\right\rangle\right)\\&=-\frac{\partial}{\partial\psi}\left[\left\langle\frac{\partial}{\partial x_i}\left((\Gamma+\Gamma_t)\frac{\partial\tau}{\partial x_i}\right)\delta\right\rangle\right.\\&\quad\left.-\left\langle\left((\Gamma+\Gamma_t)\frac{\partial\tau}{\partial x_i}\right)\frac{\partial\delta}{\partial\psi}\frac{\partial\tau}{\partial x_i}\right\rangle\right]\\&=-\frac{\partial}{\partial\psi}\left[\left\langle\frac{\partial}{\partial x_i}\left((\Gamma+\Gamma_t)\frac{\partial\tau}{\partial x_i}\right)\middle|\psi\right\rangle f_\tau\right]\\&\quad+\frac{\partial^2}{\partial\psi^2}\left[\left\langle(\Gamma+\Gamma_t)\frac{\partial\tau}{\partial x_i}\frac{\partial\tau}{\partial x_i}\middle|\psi\right\rangle f_\tau\right]\end{aligned} \tag{2.97}$$

The conditional averages that arise on the convective and diffusive terms are regarded as known terms. This fact derives from the key assumption that the stochastic fields are considered smooth and twice-differentiable in space at the grid level. It should be pointed out that the real scalar field is only differentiable at the Kolmogorov scale. However, the Eulerian stochastic field method is a mathematical representation and does not necessarily have a physical meaning, although it must respect physical properties. The assumption of smoothness only implies that the fields themselves do not include extra subgrid effects that are not already modelled in the PDF transport Equation (2.93). The Fokker-Planck equation can be therefore finally obtained:

$$\begin{aligned}\frac{\partial f_\tau}{\partial t} =& -\frac{\partial}{\partial \psi}\left(-\langle u_i\rangle\left\langle\frac{\partial \tau}{\partial x_i}\middle|\psi\right\rangle f_\tau+\left\langle\frac{\partial}{\partial x_i}\left(\left(\Gamma+\Gamma_t\right)\frac{\partial \tau}{\partial x_i}\right)\middle|\psi\right\rangle f_\tau\right)\\ &-\frac{\partial}{\partial \psi}\left(-\frac{\omega}{2}\left(\psi-\langle c\rangle\right)f_\tau+S(\psi)f_\tau\right)+\frac{\partial^2}{\partial \psi^2}\left(\left\langle\left(\Gamma+\Gamma_t\right)\frac{\partial \tau}{\partial x_i}\frac{\partial \tau}{\partial x_i}\middle|\psi\right\rangle f_\tau\right)\end{aligned} \tag{2.98}$$

The Eulerian stochastic differential equation statistically equivalent to Eq.(2.98) is therefore, taking into consideration that the conditional averages are known:

$$\begin{aligned}\mathrm{d}\tau^n =& -\langle u_i\rangle\frac{\partial \tau^n}{\partial x_i}\,\mathrm{d}t+\frac{\partial}{\partial x_i}\left(\left(\Gamma+\Gamma_t\right)\frac{\partial \tau^n}{\partial x_i}\right)\mathrm{d}t+\sqrt{2\left(\Gamma+\Gamma_t\right)}\frac{\partial \tau^n}{\partial x_i}\,\mathrm{d}W_i^n\\ &-\frac{\omega}{2}\left(\tau^n-\langle c\rangle\right)\mathrm{d}t+S(\tau^n)\,\mathrm{d}t\end{aligned} \tag{2.99}$$

Equation (2.99) represents the evolution of the n^{th} Eulerian stochastic field. This model was originally developed for a single reactive scalar. The work of Hauke and Valiño [99] presents the extension to a multicomponent flow, showing the stochastic fields formulation to solve the one-point joint scalar PDF. However, this method has only become popular after it being extended to the LES framework, which was performed by Mustata *et al.* [100] in 2006. The LES formulation of the stochastic fields is the main subject of this work and it is revised in the next section.

Sabel'nikov and Soulard (2005) [101]:

The work of [101] is regarded as a more rigorous approach to develop Eq. (2.99). It is proved that the smoothness condition is not a necessary condition to obtain the Eulerian stochastic fields. A Favre one-point scalar PDF $f(\psi;\boldsymbol{x},t)$ was considered and

the following transport equation derived:

$$\begin{aligned}\frac{\partial \langle\rho\rangle \langle f\rangle_\rho}{\partial t} + \frac{\partial \langle\rho\rangle \langle u_j\rangle \langle f\rangle_\rho}{\partial x_j} =& \frac{\partial}{\partial x_j}\left(\langle\rho\rangle \Gamma_t \frac{\partial \langle f\rangle_\rho}{\partial x_j}\right) \\ &- \frac{\partial}{\partial \psi}\left(\langle\rho\rangle \mathscr{M} \langle f\rangle_\rho\right) - \frac{\partial}{\partial \psi}\left(\langle\rho\rangle S(\psi) \langle f\rangle_\rho\right)\end{aligned} \tag{2.100}$$

where $\mathscr{M}$ represents here the chosen micromixing model. The idea in this work was to model a Eulerian stochastic partial differential equation (SPDE) equivalent to Eq.(2.100). The proposed SPDE for the evolution of the stochastic field must have the following format:

$$\frac{\partial \tau}{\partial t} + \mathscr{U}_j \frac{\partial \tau}{\partial x_j} = \mathscr{F}(\tau; \boldsymbol{x}, t) \tag{2.101}$$

where τ here is used to represent the stochastic field variable, $\mathscr{F}(\tau; \boldsymbol{x}, t) = -\langle u_j\rangle \partial\tau/\partial x_j + \mathscr{M}(\tau; \boldsymbol{x}, t) + S(\tau; \boldsymbol{x}, t)$ represents the known fluxes and $\mathscr{U}_j$ is the stochastic velocity. The proposed stochastic velocity should preserve the physical meaning of advection and it is not completely random. In fact, the stochastic velocity can be decomposed into two components:

$$\mathscr{U}_j = \mathscr{U}_j^d + \mathscr{U}_j^g \tag{2.102}$$

where $\mathscr{U}_j^d$ is the deterministic drift component and $\mathscr{U}_j^g$ is the Gaussian random component of velocity. In order to preserve its physical meaning, one must use the Stratonovich interpretation of the stochastic integral, as the Stratonovich approach use the same rules as ordinary calculus [78]. The equation for the Eulerian stochastic field is therefore:

$$\frac{\partial \tau}{\partial t} + \mathscr{U}_j^d \frac{\partial \tau}{\partial x_j} + \mathscr{U}_j^g \circ \frac{\partial \tau}{\partial x_j} = \mathscr{F}(\tau; \boldsymbol{x}, t) \tag{2.103}$$

where the symbol $\circ$ means the Stratonovich interpretation of the stochastic term. It is necessary to choose the drift and the Gaussian component of the velocity that makes Eq.(2.103) equivalent to the PDF transport equation. In the original work of Sabel'nikov and Soulard [101], the authors used a characteristic function to derive these components, defined as:

$$\psi_\tau(\lambda, x, t) = e^{i\lambda\tau(x,t)} \tag{2.104}$$

The characteristic function has the convenient property that its average is the Fourier transform of the PDF [41]:

$$\Psi_\tau(\lambda, x, t) = \int_{-\infty}^{+\infty} e^{i\lambda\tau} f(\tau; \boldsymbol{x}, t)\, \mathrm{d}\tau \tag{2.105}$$

and the PDF can be obtained from the inverse Fourier transform of Ψ_τ, making it a Fourier-transform pair:

$$f(\tau; \boldsymbol{x}, t) = \frac{1}{2\pi} \int_{-\infty}^{+\infty} e^{-i\lambda\tau} \Psi_\tau(\lambda, x, t)\, \mathrm{d}\lambda \tag{2.106}$$

It is important at this step to indicate the material derivative of the characteristic function:

$$\mathrm{d}\psi_\tau = \frac{\partial \psi_\tau}{\partial t}\, \mathrm{d}t + \mathrm{d}v_j \circ \frac{\partial \psi_\tau}{\partial x_j}; \quad \mathrm{d}v_j = \langle u_j \rangle\, \mathrm{d}t + \mathscr{U}_j^d\, \mathrm{d}t + \mathscr{U}_j^g\, \mathrm{d}t \tag{2.107}$$

where $\mathrm{d}v_j$ represents all the advection effects of the characteristic function. The material derivative can also be expanded using Taylor series regarding the derivatives in τ:

$$\mathrm{d}\psi_\tau = \frac{\partial \psi_\tau}{\partial \tau}\, \mathrm{d}\tau + \frac{1}{2} \frac{\partial^2 \psi_\tau}{\partial \tau^2}\, \mathrm{d}\tau^2 + ... \tag{2.108}$$

where $\mathrm{d}\tau$ is the source term of the stochastic field equation, defined as:

$$\mathrm{d}\tau = \mathscr{M}(\tau; \boldsymbol{x}, t)\, \mathrm{d}t + S(\tau; \boldsymbol{x}, t)\, \mathrm{d}t = \mathscr{A}(\tau; \boldsymbol{x}, t)\, \mathrm{d}t \tag{2.109}$$

The original work presented the source term using a possible stochastic model for the micromixing. It is considered here a deterministic model for the sake of brevity, although the expansion to a stochastic model can be readily done by considering higher order derivatives on Eq.(2.108). By equating Eqs.(2.107) and (2.108) and using Eq.(2.109), it is possible to derive a transport equation for the characteristic function:

$$\frac{\partial \psi_\tau}{\partial t}\, \mathrm{d}t + \mathrm{d}v_j \circ \frac{\partial \psi_\tau}{\partial x_j} = \frac{\partial \psi_\tau}{\partial \tau} \mathscr{A}(\tau; \boldsymbol{x}, t)\, \mathrm{d}t = i\lambda \psi_\tau \mathscr{A}\, \mathrm{d}t \tag{2.110}$$

and by taking the Fourier transform:

$$\frac{\partial \Psi_\tau}{\partial t}\,\mathrm{d}t + \left\langle \mathrm{d}v_j \circ \frac{\partial \psi_\tau}{\partial x_j} \right\rangle = i\lambda \left\langle \psi_\tau \mathscr{A} \right\rangle \mathrm{d}t \tag{2.111}$$

The average advection term needs to be defined. It should be highlighted that, in contrast to the Ito interpretation, the convective term does not have the no-correlation property. In order to obtain an expression for it, it is necessary to convert it to the Ito interpretation. The portability between the Ito and Stratonovich interpretations can be performed using the simple relation [78]:

$$X \circ \mathrm{d}W = X\,\mathrm{d}W + \frac{1}{2}\,\mathrm{d}X\,\mathrm{d}W \tag{2.112}$$

By applying this relation, the convective term can be rewritten as:

$$\begin{aligned} \mathrm{d}v_j \circ \frac{\partial \psi_\tau}{\partial x_j} &= \mathrm{d}v_j \frac{\partial \psi_\tau}{\partial x_j} + \frac{1}{2}\,\mathrm{d}\left(\frac{\partial \psi_\tau}{\partial x_j}\right)\mathrm{d}v_j \\ &= \mathrm{d}v_j \frac{\partial \psi_\tau}{\partial x_j} + \frac{1}{2}\frac{\partial}{\partial x_j}\left(\mathrm{d}\psi_\tau\,\mathrm{d}v_j\right) - \frac{1}{2}\,\mathrm{d}\psi_\tau \frac{\partial\,\mathrm{d}v_j}{\partial x_j} \end{aligned} \tag{2.113}$$

The derivative $\mathrm{d}\psi_\tau$ is different than the previous one, since it is not the material derivative of ψ_τ. It is, however, a derivative obtained recasting Equation (2.110) into stochastic differential form [101]:

$$\mathrm{d}\psi_\tau = -\,\mathrm{d}v_k \frac{\partial \psi_\tau}{\partial x_k} + i\lambda \psi_\tau \mathscr{A}\,\mathrm{d}t \tag{2.114}$$

Abusing the notation, since the Ito interpretation is being casted on the right hand side of Eq.(2.113), $\mathrm{d}\psi_\tau$ is written here using the Ito interpretation. Equation (2.113) is therefore recast as:

$$\mathrm{d}v_j \circ \frac{\partial \psi_\tau}{\partial x_j} = \mathrm{d}v_j \frac{\partial \psi_\tau}{\partial x_j} - \frac{1}{2}\frac{\partial}{\partial x_j}\left(\mathrm{d}v_k \frac{\partial \psi_\tau}{\partial x_k}\,\mathrm{d}v_j\right) + \frac{1}{2}\,\mathrm{d}v_k \frac{\partial \psi_\tau}{\partial x_k}\frac{\partial\,\mathrm{d}v_j}{\partial x_j} \tag{2.115}$$

where high order terms like $\mathrm{d}t\,\mathrm{d}v_j$ can be neglected. The average of the convective term

can be therefore obtained and the transport equation for Ψ_α is written as:

$$\frac{\partial \Psi_\tau}{\partial t}\,\mathrm{d}t + \left(\langle \mathrm{d}v_j\rangle + \frac{1}{2}\left\langle \mathrm{d}v_j \frac{\partial\, \mathrm{d}v_k}{\partial x_k}\right\rangle\right)\frac{\partial \Psi_\tau}{\partial x_j} = \frac{\partial}{\partial x_j}\left(\frac{1}{2}\left\langle \mathrm{d}v_j\, \mathrm{d}v_k\right\rangle \frac{\partial \Psi_\tau}{\partial x_k}\right) + i\lambda \left\langle \psi_\tau \mathscr{A}\right\rangle \mathrm{d}t \tag{2.116}$$

and by taking the inverse Fourier transform, one can finally obtain:

$$\frac{\partial f}{\partial t} + \left(\frac{\langle \mathrm{d}v_j\rangle}{\mathrm{d}t} + \frac{1}{2\,\mathrm{d}t}\left\langle \mathrm{d}v_j \frac{\partial\, \mathrm{d}v_k}{\partial x_k}\right\rangle\right)\frac{\partial f}{\partial x_j} = \frac{\partial}{\partial x_j}\left(\frac{1}{2}\frac{\langle \mathrm{d}v_j\, \mathrm{d}v_k\rangle}{\mathrm{d}t}\frac{\partial f}{\partial x_k}\right) - \frac{\partial}{\partial \tau}\left(\mathscr{A} f\right) \tag{2.117}$$

At last, for Equation (2.117) to be equal to Eq.(2.100), the following equalities must be respected:

$$\frac{1}{2}\left\langle \mathrm{d}v_j\, \mathrm{d}v_k\right\rangle = \Gamma_t \delta_{jk}\,\mathrm{d}t \tag{2.118}$$

$$\langle \mathrm{d}v_j\rangle + \frac{1}{2}\left\langle \mathrm{d}v_j \frac{\partial\, \mathrm{d}v_k}{\partial x_k}\right\rangle = \langle u_i\rangle\,\mathrm{d}t - \frac{1}{\langle\rho\rangle}\frac{\partial \langle\rho\rangle}{\partial x_j}\Gamma_t\,\mathrm{d}t \tag{2.119}$$

which gives the constrains to the drift and Gaussian component of the velocity:

$$\frac{1}{2}\left\langle \mathscr{U}_i^g \mathscr{U}_j^g\right\rangle \mathrm{d}t = \Gamma_t \delta_{ij} \tag{2.120}$$

$$\mathscr{U}_j^d = -\frac{1}{2}\left\langle \frac{\partial \mathscr{U}_i^g}{\partial x_i}\mathscr{U}_j^g\right\rangle \mathrm{d}t - \frac{1}{\langle\rho\rangle}\frac{\partial \langle\rho\rangle}{\partial x_j}\Gamma_t \tag{2.121}$$

These constrains can be derived by substituting $\mathrm{d}v_j = \langle u_j\rangle\,\mathrm{d}t + \mathscr{U}_j^d\,\mathrm{d}t + \mathscr{U}_j^g\,\mathrm{d}t$ into the equalities and using the fact that only the Gaussian component is random and therefore $\mathscr{U}_i^g \mathscr{U}_j^g \sim \mathrm{d}t$. Sabel'nikov and Soulard [101] demonstrated that a possible solution, but not the only one, for the velocity components of Eq. (2.103) is:

$$\mathscr{U}_i^d = -\frac{1}{2}\frac{\partial \Gamma_t}{\partial x_i} - \frac{1}{\langle\rho\rangle}\frac{\partial \langle\rho\rangle}{\partial x_i}\Gamma_t \tag{2.122}$$

$$\mathscr{U}_i^g = -\sqrt{2\Gamma_t} \circ \frac{\mathrm{d}W_i}{\mathrm{d}t} \tag{2.123}$$

A minus signal has been introduced on Eq.(2.123) here for clarity, which is different than the original solution of Sabel'nikov and Soulard [101]. This does not change the Wiener term behaviour and it is still a possible solution that preserves the constrains. Finally, the equation for the Eulerian stochastic field can be obtained:

$$\begin{aligned}\frac{\partial \tau}{\partial t} + \left(\langle u_j \rangle - \frac{1}{2}\frac{\partial \Gamma_t}{\partial x_i} - \frac{1}{\langle \rho \rangle}\frac{\partial \langle \rho \rangle}{\partial x_i}\Gamma_t \right) \frac{\partial \tau}{\partial x_j} = \\ \sqrt{2\Gamma_t}\frac{\partial \tau}{\partial x_j} \circ \frac{\mathrm{d}W_i}{\mathrm{d}t} + \mathscr{M}(\tau; \boldsymbol{x}, t) + S(\tau; \boldsymbol{x}, t)\end{aligned} \tag{2.124}$$

Equation (2.124) was derived using no assumption regarding the smoothness of the stochastic field. However, it is still written in Stratonovich interpretation, which may be numerically inconvenient to be used in an explicit solver as it requires the information in the middle of the time-step, not only at the beginning, as in the Ito integral. In order to use the Ito interpretation, the relation shown in Equation (2.112) can be applied:

$$\begin{aligned}\frac{\partial \tau}{\partial t} + \langle u_j \rangle \frac{\partial \tau}{\partial x_j} - \frac{1}{2}\frac{\partial \Gamma_t}{\partial x_i}\frac{\partial \tau}{\partial x_j} - \frac{1}{\langle \rho \rangle}\frac{\partial}{\partial x_i}\left(\langle \rho \rangle \Gamma_t \frac{\partial \tau}{\partial x_j} \right) + \frac{\partial}{\partial x_j}\left(\Gamma_t \frac{\partial \tau}{\partial x_j} \right) = \\ \sqrt{2\Gamma_t}\frac{\partial \tau}{\partial x_j}\frac{\mathrm{d}W_i}{\mathrm{d}t} + \frac{1}{2}\sqrt{2\Gamma_t}\frac{\partial \tau}{\partial x_j}\frac{\partial}{\partial \tau}\left(\sqrt{2\Gamma_t}\frac{\partial \tau}{\partial x_j} \right) + \mathscr{M}(\tau; \boldsymbol{x}, t) + S(\tau; \boldsymbol{x}, t)\end{aligned} \tag{2.125}$$

and by using the relation $\partial\tau/\partial x_j \partial/\partial\tau = \partial/\partial x_j$ [101] it is possible to obtain the Eulerian stochastic field equation:

$$\begin{aligned}\frac{\partial \tau}{\partial t} + \langle u_j \rangle \frac{\partial \tau}{\partial x_j} = &\frac{1}{\langle \rho \rangle}\frac{\partial}{\partial x_i}\left(\langle \rho \rangle \Gamma_t \frac{\partial \tau}{\partial x_j} \right) + \sqrt{2\Gamma_t}\frac{\partial \tau}{\partial x_j}\frac{\mathrm{d}W_i}{\mathrm{d}t} \\ &+ \mathscr{M}(\tau; \boldsymbol{x}, t) + S(\tau; \boldsymbol{x}, t)\end{aligned} \tag{2.126}$$

which is the essentially the same as Equation (2.99), although in partial differential equation form. Both equations are equivalent to the one-point scalar PDF, however, the later is derived with less restrictives assumptions. Equation (2.126) can also be derived from the Lagrangian equations, such as those shown in Pope [68], by considering them the characteristic equations of the SPDE shown in Eq. (2.126), also proved in [101].

If molecular viscosity has to be taken into account, such as close to wall and in LES context, the stochastic equations obtained in [101] cannot be interpreted as advection-

reaction equations any more according to Valiño *et al.* [102]. The resultant equations must have advection, diffusion and reactive terms, behaving as a parabolic system, not as a hyperbolic one as claimed by Sabel'nikov and Soulard [101]. However, as explained in [101], the diffusion term is misleading in Eq.(2.126) because the Ito interpretation of the Wiener term does not have the same interpretation as in classical calculus. It is the sum of the diffusion-like term and the stochastic term that results in in the advection Wiener term, as shown in Equation (2.124). Only by using the Stratonovich interpretation that it is possible to obtain the same physical meaning as in ordinary calculus. The equations derived in [102] therefore rely on the assumption of the smoothness of the Eulerian fields.

Soulard and Sabel'nikov (2006) [103]:

The characteristic interpretation of the Lagrangian equations is the starting point of the model developed by Soulard and Sabel'nikov [103], which was the first attempt to solve a joint velocity-scalar PDF using Eulerian stochastic equations. The following incompressible transport equation for the one point velocity PDF $f(\boldsymbol{v};\boldsymbol{x},t)$ was considered:

$$\frac{\partial f}{\partial t}+v_j\frac{\partial f}{\partial x_j}=-\frac{\partial}{\partial v_j}\left[\left(-\frac{1}{\rho}\frac{\partial\langle p\rangle}{\partial x_j}+G_{ij}\left(v_j-\langle u_j\rangle\right)\right)f\right]+\frac{1}{2}C_0\epsilon\frac{\partial^2 f}{\partial v_j\partial v_j} \tag{2.127}$$

where the simplified Langevin model is used to model the tensor G_{ij} and ϵ is the turbulent energy dissipation. The Lagrangian stochastic equations equivalent to the PDF Fokker-Planck equation are [68]:

$$\mathrm{d}X_j^+=U_j^+\,\mathrm{d}t \tag{2.128}$$

$$\mathrm{d}U_j^+=\left(-\frac{1}{\rho}\frac{\partial\langle p\rangle}{\partial x_j}+G_{ij}\left(U_j^+-\langle u_j\rangle\right)\right)\mathrm{d}t+\sqrt{C_0\epsilon}\,\mathrm{d}W_j \tag{2.129}$$

It is also useful to define a stochastic density to ensure mass conservation of the Eulerian equations. This stochastic density is r^+ is different than the physical density ρ, which is assumed constant, but is related to it through $\langle r^+\rangle=\rho$. Therefore, the following equation has been proposed:

$$\mathrm{d}r^+=-r^+\frac{\partial U_j^+}{\partial x_j}\,\mathrm{d}t \tag{2.130}$$

And by considering the Lagrangian equations the characteristics of a system of stochastic partial differential equations, it possible to recast the Lagrangian equations into Eulerian framework:

$$\frac{\partial r}{\partial t} + U_j \frac{\partial r}{\partial x_j} = -r \frac{\partial U_j}{\partial x_j} \tag{2.131}$$

$$\frac{\partial U_i}{\partial t} + U_j \frac{\partial U_i}{\partial x_j} = -\frac{1}{\rho} \frac{\partial \langle p \rangle}{\partial x_j} + G_{ij} \left(U_j - \langle u_j \rangle \right) + \sqrt{C_0 \epsilon} \frac{\mathrm{d}W_j}{\mathrm{d}t} \tag{2.132}$$

which can be recast in the conservative form:

$$\frac{\partial r}{\partial t} + \frac{\partial r U_j}{\partial x_j} = 0 \tag{2.133}$$

$$\frac{\partial r U_i}{\partial t} + \frac{\partial r U_j U_i}{\partial x_j} = -\frac{r}{\rho} \frac{\partial \langle p \rangle}{\partial x_j} + r G_{ij} \left(U_j - \langle u_j \rangle \right) + r \sqrt{C_0 \epsilon} \frac{\mathrm{d}W_j}{\mathrm{d}t} \tag{2.134}$$

In this derivation the Ito interpretation has been used for the Wiener term of the Langevin model. Soulard and Sabel'nikov [103] provides further elements of proof for the relation $\langle r^+ \rangle = \rho$ and the equivalence of the Equations (2.133) and (2.134) to the transport PDF equation. On this formulation there is no need to include a model for the turbulent viscosity, as the convective terms are already closed. This model has been further validated in Soulard and Sabel'nikov [104], where a set of validation tests has been performed.

However, the set of Eulerian stochastic field equations developed presented a major issue, which was pointed out in the work of Petrova [105]. The momentum equation is a non-linear hyperbolic equation (Burgers' equation), which is multi-valued and can produce shocks. The shocks can be physical but the numerical solutions can lead to numerical and artificial shocks, which can be prevented by using a specific discretisation scheme based on the parametrised graph solution of Eqs.(2.133) and (2.134) [105, 106].

Azarnykh *et al.* (2016) [107]:

The work of Azarnykh *et al.* [107] presented an approach to solve the stochastic partial differential equation for the velocity using a weakly compressible Langevin model. The authors also investigated several different discretisation schemes that can be used to

solve the stochastic equations with accuracy and stability. In their work, the momentum equation does not behave like a Burgers' equation, as the pressure can be completely defined from the density because of the weakly compressible approach. The following equations are obtained considering an one-dimensional configuration:

$$\frac{\partial \rho(x,t)}{\partial t} + \frac{\partial \rho(x,t)u(x,t)}{\partial x} = 0 \tag{2.135}$$

$$\begin{aligned} &\frac{\partial \rho(x,t)u(x,t)}{\partial t} + \frac{\partial \rho(x,t)u(x,t)u(x,t)}{\partial x} = -\frac{\partial p(x,t)}{\partial x} \\ &-\gamma_a \rho(x,t)\left(u(x,t) - u_0(x,t)\right) + \sqrt{\rho(x,t) D \gamma_a}\,\zeta(x,t) \end{aligned} \tag{2.136}$$

$$p(x,t) = \rho(x,t) c_s^2 \tag{2.137}$$

where $\zeta(x,t)$ is a Gaussian white noise, c_s is the isothermal speed of sound and D and γ_a correspond to fluctuation and dissipation coefficients, respectively, of the notional particles of the flow. The pressure $p(x,t)$ on the momentum equation is not the average pressure as in Eq.(2.134). Therefore the equation does not behave as a Burgers' equation and, in this way, the numerical shocks are avoided. In fact, the solution presented by Azarnykh *et al.* [107] is the precursor of the Eulerian stochastic equations developed in this work to solve the transport equation for a Eulerian one-point one-time joint velocity-scalar PDF.

Table 2.1 summarises some of the most influential works using the PDF method, stating its closures and solution method proposed.

Reference	PDF model	Closures	Solution
Lundgren [65] (1967)	Velocity	Two point PDF	-
Lundgren [66] (1969)	Velocity	Pressure relaxation	Analytical
Dopazo [67] (1975)	Scalar	IEM	Analytical
Pope [72] (1976)	Scalar	Mixing length	Analytical
Janicka *et al.* [80] (1978)	Scalar	Integral model	Finite diff.
Pope [77] (1979)	Scalar	Conditionally Gaussian	Lagrangian eq.
Pope [79] (1981)	Scalar	Curl's model	Lagrangian MC
Pope [68](1985)	Velocity-Scalar	IEM/Langevin model	Lagrangian MC
Kollmann [88] (1992)	Compressible VS	Integral model	Lagrangian MC
Delarue and Pope [20] (1997)	Compressible VS	IEM/Langevin model	Lagrangian MC
Dreeben and Pope [95] (1997)	VPDF Near-wall	Langevin model	Lagrangian MC
Valiño [19] (1998)	Scalar	IEM	Eulerian MC
Hauke and Valiño [99] (2004)	Scalar	IEM	Eulerian MC
Sabel'nikov and Soulard [101] (2005)	Scalar	IEM	Eulerian MC
Soulard and Sabel'nikov [103] (2006)	Velocity	Langevin	Eulerian MC
Petrova [105] (2015)	Velocity	Langevin	Eulerian MC
Valiño *et al.* [102] (2016)	SPDF Near-wall	IEM	Eulerian MC
Azarnykh *et al.* [107] (2016)	Velocity	Langevin	Eulerian MC

Table 2.1: Influential PDF works, where MC stands for Monte-Carlo method.

2.4.2 Filtered Density Function (FDF) - LES-PDF

The averaged transport equations for the PDF have been visited in the last section. However, because of the increasing popularity and the large computational power now available, the large eddy simulation has been chosen as the standard method for combustion studies. The modelling of a filtered PDF equation in a LES framework is therefore of critical importance to extend its advantages to a more accurate environment.

The application of a PDF method in large eddy simulation was first suggested by Givi [108]. Pope [109] presented the concept of a filtered density function (FDF) to be used in a LES framework, while Gao and O'Brien [17] developed a transport equation for it. The one-point one-time fine-grained Eulerian joint scalar filtered density function is defined as:

$$f'(\boldsymbol{\psi};\boldsymbol{x},t)=\prod_{\alpha=1}^{N_s}\delta(\phi_\alpha(\boldsymbol{x},t)-\psi_\alpha) \tag{2.138}$$

The filtered density function or spatially filtered fine-grained PDF is defined by applying the filtering operation to the fine-grained FDF:

$$\overline{f}(\boldsymbol{\psi};\boldsymbol{x},t)=\int_{-\infty}^{+\infty}G(\boldsymbol{x}-\boldsymbol{x'},\Delta)\prod_{\alpha=1}^{N_s}\delta(\phi_\alpha(\boldsymbol{x'},t)-\psi_\alpha)\,\mathrm{d}\boldsymbol{x'} \tag{2.139}$$

The filtered density function is very similar to the originally developed PDF. However, it is derived from a different concept. While the PDF $f(\psi;\boldsymbol{x},t)$ is derived from the ensemble average of the fine-grained PDF, the FDF $\overline{f}(\psi;\boldsymbol{x},t)$ is obtained from the filtering operation. It can be thought that the filter function $G(\boldsymbol{x}-\boldsymbol{x'},\Delta)$ is the PDF of the Dirac delta function within the subgrid scale element $\mathrm{d}\boldsymbol{x'}$. In fact, their relationship is defined as [109]:

$$f(\boldsymbol{\psi};\boldsymbol{x},t)=\lim_{\Delta\to 0}\left\langle\overline{f}(\boldsymbol{\psi};\boldsymbol{x},t)\right\rangle \tag{2.140}$$

As concluded by Wang [110], the FDF represents samples taken surrounding the element $\mathrm{d}\boldsymbol{x'}$ centred at $\boldsymbol{x'}$ and time t. In contrast, the PDF represents several samples taken the same time and position in different experiments. This concept is very useful in Lagrangian approaches because the FDF is constructed from the particles surrounding an Eulerian

volume [64]. Nonetheless, the portability between Lagrangian FDF to Eulerian FDF is not trivial and still subject to discussion [110, 51, 64]. In this work, the filtered PDF/LES-PDF nomenclature is used when the Eulerian stochastic fields method is used and FDF if the Lagrangian approach is chosen.

The FDF/LES-PDF also respects the following property:

$$\begin{aligned}\int_{-\infty}^{+\infty} \overline{f}(\boldsymbol{\psi};\boldsymbol{x},t)\,\mathrm{d}\boldsymbol{\psi} &= \int_{-\infty}^{+\infty}\int_{-\infty}^{+\infty} G(\boldsymbol{x}-\boldsymbol{x'},\Delta)\prod_{\alpha=1}^{N_s}\delta(\phi_\alpha(\boldsymbol{x'},t)-\psi_\alpha)\,\mathrm{d}\boldsymbol{x'}\,\mathrm{d}\boldsymbol{\psi}\\ &= \int_{-\infty}^{+\infty} G(\boldsymbol{x}-\boldsymbol{x'},\Delta)\int_{-\infty}^{+\infty}\prod_{\alpha=1}^{N_s}\delta(\phi_\alpha(\boldsymbol{x'},t)-\psi_\alpha)\,\mathrm{d}\boldsymbol{\psi}\,\mathrm{d}\boldsymbol{x'}\\ &= \int_{-\infty}^{+\infty} G(\boldsymbol{x}-\boldsymbol{x'},\Delta)\,\mathrm{d}\boldsymbol{x'} = 1\end{aligned} \tag{2.141}$$

where from the second line to the third line of the previous equation the integral property of the Dirac delta function has been used. The filtered variables are obtained by taking the average operation using the FDF. For instance, for a variable $\boldsymbol{\phi}(\boldsymbol{x},t)$:

$$\begin{aligned}\int_{-\infty}^{+\infty} \boldsymbol{\psi}\overline{f}(\boldsymbol{\psi};\boldsymbol{x},t)\,\mathrm{d}\boldsymbol{\psi} &= \int_{-\infty}^{+\infty}\boldsymbol{\psi}\int_{-\infty}^{+\infty} G(\boldsymbol{x}-\boldsymbol{x'},\Delta)\prod_{\alpha=1}^{N_s}\delta(\phi_\alpha(\boldsymbol{x'},t)-\psi_\alpha)\,\mathrm{d}\boldsymbol{x'}\,\mathrm{d}\boldsymbol{\psi}\\ &= \int_{-\infty}^{+\infty} G(\boldsymbol{x}-\boldsymbol{x'},\Delta)\int_{-\infty}^{+\infty}\boldsymbol{\psi}\prod_{\alpha=1}^{N_s}\delta(\phi_\alpha(\boldsymbol{x'},t)-\psi_\alpha)\,\mathrm{d}\boldsymbol{\psi}\,\mathrm{d}\boldsymbol{x'}\\ &= \int_{-\infty}^{+\infty} G(\boldsymbol{x}-\boldsymbol{x'},\Delta)\boldsymbol{\phi}(\boldsymbol{x'},t)\,\mathrm{d}\boldsymbol{x'} = \overline{\boldsymbol{\phi}}(\boldsymbol{x},t)\end{aligned} \tag{2.142}$$

The Favre-filtered PDF is defined similarly:

$$\widetilde{f}(\boldsymbol{\psi};\boldsymbol{x},t) = \frac{\displaystyle\int_{-\infty}^{+\infty}\rho\,(\boldsymbol{x'},t)\,G(\boldsymbol{x}-\boldsymbol{x'},\Delta)\prod_{\alpha=1}^{N_s}\delta(\phi_\alpha(\boldsymbol{x'},t)-\psi_\alpha)\,\mathrm{d}\boldsymbol{x'}}{\displaystyle\int_{-\infty}^{+\infty}\rho\,(\boldsymbol{x'},t)\,G(\boldsymbol{x}-\boldsymbol{x'},\Delta)\,\mathrm{d}\boldsymbol{x'}} \tag{2.143}$$

and it is also important to define the conditional Favre-filtering operation of a function

$Q(\boldsymbol{x},t)$:

$$\widetilde{Q(\boldsymbol{x},t)|\boldsymbol{\psi}} = \frac{\displaystyle\int_{-\infty}^{+\infty} \rho\left(\boldsymbol{x'},t\right) Q(\boldsymbol{x'},t) f'(\boldsymbol{\psi};\boldsymbol{x'},t) G(\boldsymbol{x}-\boldsymbol{x'},\Delta)\,\mathrm{d}\boldsymbol{x'}}{\displaystyle\int_{-\infty}^{+\infty} \rho\left(\boldsymbol{x'},t\right) f'(\boldsymbol{\psi};\boldsymbol{x'},t) G(\boldsymbol{x}-\boldsymbol{x'},\Delta)\,\mathrm{d}\boldsymbol{x'}} = \frac{\widetilde{Qf}}{\widetilde{f}} \tag{2.144}$$

The conditional filtering operation can be defined likewise. The unclosed conditional filtered term $\widetilde{Q(\boldsymbol{x},t)|\boldsymbol{\psi}}$ also shares the critical property of the conditional average counterpart. It is closed if the function $Q(\boldsymbol{x},t)$ can be completely defined by the variables included into the PDF sample space. This can be demonstrated by considering a function $Q(\boldsymbol{\phi}\left(\boldsymbol{x},t\right))$, applying the filtering operation and using the sifting property of the Dirac delta function [41]:

$$\begin{gathered}\int_{-\infty}^{+\infty} \rho\left(\boldsymbol{x'},t\right) Q(\boldsymbol{\phi}\left(\boldsymbol{x'},t\right)) f'(\boldsymbol{\psi};\boldsymbol{x'},t) G(\boldsymbol{x}-\boldsymbol{x'},\Delta)\,\mathrm{d}\boldsymbol{x'} = \\ \int_{-\infty}^{+\infty} \rho\left(\boldsymbol{x'},t\right) Q(\boldsymbol{\psi}) f'(\boldsymbol{\psi};\boldsymbol{x'},t) G(\boldsymbol{x}-\boldsymbol{x'},\Delta)\,\mathrm{d}\boldsymbol{x'} = \\ Q(\boldsymbol{\psi}) \int_{-\infty}^{+\infty} \rho\left(\boldsymbol{x'},t\right) f'(\boldsymbol{\psi};\boldsymbol{x'},t) G(\boldsymbol{x}-\boldsymbol{x'},\Delta)\,\mathrm{d}\boldsymbol{x'} = Q(\boldsymbol{\psi})\overline{\rho}\widetilde{f}\end{gathered} \tag{2.145}$$

Therefore the filtered source term can also be exactly closed if the sample space includes variables such as the chemical mass fractions, enthalpy and pressure. Likewise, the convective term is closed if the sample space includes the velocity components.

Colucci *et al.* (1998) [13]:

Colucci *et al.* [13] were the first to perform reactive LES simulations using the Lagrangian method to solve a FDF equation. They considered a one-point one-time Eulerian joint scalar FDF. The transport equation derivation is shown here for this model and similar reasoning can be applied for the several other Lagrangian FDF approaches. A starting point for the transport equation for the FDF is to take the temporal derivative of the fine-grained scalar FDF $f'(\boldsymbol{\psi};\boldsymbol{x},t)$ and apply the filtering operation:

$$\begin{aligned}\overline{\frac{\partial f'}{\partial t}} &= -\overline{\frac{\partial \phi_\alpha}{\partial t}\frac{\partial f'}{\partial \psi_\alpha}} \\ \frac{\partial \overline{f}}{\partial t} &= -\frac{\partial}{\partial \psi_\alpha}\left(\overline{\frac{\partial \phi_\alpha}{\partial t} f'}\right)\end{aligned} \tag{2.146}$$

the temporal derivative for ϕ_α can be obtained from its transport equation, resulting in:

$$\begin{aligned}\frac{\partial \overline{f}}{\partial t} &= -\frac{\partial}{\partial \psi_\alpha}\left(\overline{\left(-u_j\frac{\partial \phi_\alpha}{\partial x_j}+\frac{\partial J_i^\alpha}{\partial x_i}+S(\boldsymbol{\phi})\right)f'}\right)\\ &= -\frac{\partial}{\partial \psi_\alpha}\left(\overline{-u_j\frac{\partial \phi_\alpha}{\partial x_j}\middle|\boldsymbol{\psi}}\,\overline{f}+\overline{\frac{\partial J_i^\alpha}{\partial x_i}\middle|\boldsymbol{\psi}}\,\overline{f}+S(\boldsymbol{\psi})\overline{f}\right)\\ &= -\frac{\partial \overline{u_j|\boldsymbol{\psi}}\;\overline{f}}{\partial x_j}-\frac{\partial}{\partial \psi_\alpha}\left(\overline{\frac{\partial J_i^\alpha}{\partial x_i}\middle|\boldsymbol{\psi}}\,\overline{f}+S(\boldsymbol{\psi})\overline{f}\right)\end{aligned} \tag{2.147}$$

Equation (2.147) is unclosed and the conditional filtered term require modelling. It is common in LES modelling to simply add a large scale (known) term and subtract it along with the unclosed subgrid term. This difference is at the small scales level and therefore subject to a smaller error. The unclosed diffusion term can also be rewritten using similar reasoning as in Eq.(2.97). For instance, Eq.(2.147) can be recast as:

$$\begin{aligned}\frac{\partial \overline{f}}{\partial t} =& -\frac{\partial \overline{u}_j\overline{f}}{\partial x_j}+\left(\frac{\partial \overline{u}_j\overline{f}}{\partial x_j}-\frac{\partial \overline{u_j|\boldsymbol{\psi}}\;\overline{f}}{\partial x_j}\right)\\ &+\frac{\partial}{\partial x_j}\left(\Gamma\frac{\partial \overline{f}}{\partial x_j}\right)-\frac{\partial}{\partial \psi_\alpha}\left(S(\boldsymbol{\psi})\overline{f}\right)-\frac{\partial^2}{\partial \psi_\alpha\partial\psi_\beta}\left(\overline{\Gamma\frac{\partial \phi_\alpha}{\partial x_j}\frac{\partial \phi_\beta}{\partial x_j}\middle|\boldsymbol{\psi}}\,\overline{f}\right)\end{aligned} \tag{2.148}$$

where Γ is the molecular diffusion coefficient. The convective unclosed term can be modelled with a traditional LES approach, as demonstrated in Section 2.3:

$$\frac{\partial \overline{u}_j\overline{f}}{\partial x_j}-\frac{\partial \overline{u_j|\boldsymbol{\psi}}\;\overline{f}}{\partial x_j}=\frac{\partial}{\partial x_j}\left(\Gamma_{sgs}\frac{\partial \overline{f}}{\partial x_j}\right) \tag{2.149}$$

where Γ_{sgs} is the subgrid viscosity and requires modelling. The second derivative on Eq.(2.148) can be closed using a micromixing model as in RANS framework. The IEM micromixing model is chosen [71]:

$$-\frac{\partial^2}{\partial \psi_\alpha\partial\psi_\beta}\left(\overline{\Gamma\frac{\partial \phi_\alpha}{\partial x_j}\frac{\partial \phi_\beta}{\partial x_j}\middle|\boldsymbol{\psi}}\,\overline{f}\right)\approx\frac{\partial}{\partial \psi_\alpha}\left(\omega_{sgs}\left(\psi_\alpha-\overline{\phi}_\alpha\right)\overline{f}\right) \tag{2.150}$$

where ω_{sgs} is the subgrid turbulence frequency. The closed FDF transport equation is

therefore:

$$\frac{\partial \overline{f}}{\partial t} + \frac{\partial \overline{u}_j \overline{f}}{\partial x_j} = \frac{\partial}{\partial x_j}\left(\left(\Gamma + \Gamma_{sgs}\right) \frac{\partial \overline{f}}{\partial x_j} \right) - \frac{\partial}{\partial \psi_\alpha}\left(-\omega_{sgs}\left(\psi_\alpha - \overline{\phi}_\alpha\right)\overline{f} + S(\boldsymbol{\psi})\overline{f} \right) \tag{2.151}$$

To solve the FDF equation, Colucci *et al.* [13] proposed Lagrangian stochastic equations:

$$\mathrm{d}X_i^+ = \left[\overline{u}_i + \frac{\partial\left(\Gamma + \Gamma_{sgs}\right)}{\partial x_i} \right] \mathrm{d}t + \sqrt{2\left(\Gamma + \Gamma_{sgs}\right)}\, \mathrm{d}W_i \tag{2.152}$$

$$\mathrm{d}\phi_\alpha^+ = -\omega_{sgs}\left(\phi_\alpha^+ - \overline{\phi}_\alpha\right)\mathrm{d}t + S_\alpha\, \mathrm{d}t \tag{2.153}$$

The Lagrangian stochastic equations are equivalent to a Lagrangian Fokker-Planck equation, but can be proved to be equivalent to the Eulerian transport Equation (2.151). The work of Colucci *et al.* [13] concluded that the FDF approach, although more computationally expensive than the pure LES approach, it is more accurate and comparable to the DNS results, which demands much higher computational power. They concluded that the subgrid fluctuations of the source term have considerable influence and neglecting it may result in overprediction of the reaction rate.

The work of Jaberi *et al.* [111] introduced the Eulerian filtered mass density function (FMDF), similar to the MDF developed in RANS framework to deal with variable density flows:

$$\overline{\mathscr{F}\left(\boldsymbol{\psi}; \boldsymbol{x}, t\right)} = \int_{-\infty}^{+\infty} \rho\left(\boldsymbol{x}', t\right) \prod_{\alpha=1}^{N_s} \delta(\phi_\alpha(\boldsymbol{x}', t) - \psi_\alpha) G\left(\boldsymbol{x} - \boldsymbol{x}', \Delta\right) \mathrm{d}\boldsymbol{x}' \tag{2.154}$$

The transport equation for $\mathscr{F}\left(\boldsymbol{\psi}; \boldsymbol{x}, t\right)$ is very similar to Eq.(2.151) and can be obtained using the same techniques, but also including the Favre-filtering and conditional Favre-filtering:

$$\begin{aligned} \frac{\partial \widetilde{\mathscr{F}}}{\partial t} + \frac{\partial \widetilde{u}_i \widetilde{\mathscr{F}}}{\partial x_i} = & \frac{\partial}{\partial x_i}\left[\left(\Gamma + \Gamma_{sgs}\right) \frac{\partial(\widetilde{\mathscr{F}}/\overline{\rho})}{\partial x_i} \right] \\ & + \frac{\partial}{\partial \psi_\alpha}\left(\omega_{sgs}\left(\psi_\alpha - \widetilde{\phi}_\alpha\right)\widetilde{\mathscr{F}} \right) - \frac{\partial}{\partial \psi_\alpha}\left(S_\alpha \widetilde{\mathscr{F}} \right) \end{aligned} \tag{2.155}$$

Lagrangian stochastic equations similar to those developed in Colucci *et al.* [13] were proposed in order to solve Eq. (2.155). The feasibility of the FMDF method is also proved by investigating spatial and temporally mixing layer and a planar jet.

The modelling of Lagrangian stochastic equations to solve a one-point one-time joint scalar MFDF has intensively been used to simulate low Mach number turbulent reactive flows [112, 113, 114, 115, 116, 117, 118, 119, 120, 121]. The accuracy of the LES to solve the filtered momentum equations combined with the exact solution of the source term for the reactive scalars represents a very powerful approach.

Gicquel *et al.* (2002) [122]:

A filtered velocity PDF is also an object of interest for large eddy simulation of highly convective flows. It can potentially eliminate the main source of numerical error, since the convective term is treated exactly. The work of Gicquel *et al.* [122] was the first to develop a velocity FDF, still considering an incompressible approach though. Two transport equations of the evolution of the velocity FDF $\overline{f}(\boldsymbol{v};\boldsymbol{x},t)$ were derived, each one with a particular advantage:

$$\begin{aligned}\frac{\partial \overline{f}}{\partial t}+v_k\frac{\partial \overline{f}}{\partial x_k} =& -\frac{\partial}{\partial x_k}\left[\left(v_k-\overline{u}_k\right)\overline{f}\right]+\frac{\partial \overline{p}}{\partial x_i}\frac{\partial \overline{f}}{\partial v_i}+\nu\frac{\partial^2 \overline{f}}{\partial x_k\partial x_k}+\nu\frac{\partial \overline{u}_i}{\partial x_k}\frac{\partial \overline{u}_j}{\partial x_k}\frac{\partial^2 \overline{f}}{\partial v_i\partial v_j}\\ &+2\nu\frac{\partial \overline{u}_i}{\partial x_k}\frac{\partial^2 \overline{f}}{\partial x_k\partial v_i}-\frac{\partial}{\partial v_i}\left[G_{ij}\left(v_j-\overline{u}_j\right)\overline{f}\right]+\frac{1}{2}C_0\epsilon_{sgs}\frac{\partial^2 \overline{f}}{\partial v_i\partial v_i}\end{aligned} \tag{2.156}$$

$$\begin{aligned}\frac{\partial \overline{f}}{\partial t}+v_k\frac{\partial \overline{f}}{\partial x_k} =& -\frac{\partial}{\partial x_k}\left[\left(v_k-\overline{u}_k\right)\overline{f}\right]+\frac{\partial \overline{p}}{\partial x_i}\frac{\partial \overline{f}}{\partial v_i}-\frac{\partial \overline{\tau}_{ik}}{\partial x_k}\frac{\partial \overline{f}}{\partial v_i}\\ &-\frac{\partial}{\partial v_i}\left[G_{ij}\left(v_j-\overline{u}_j\right)\overline{f}\right]+\frac{1}{2}C_0\epsilon_{sgs}\frac{\partial^2 \overline{f}}{\partial v_i\partial v_i}\end{aligned} \tag{2.157}$$

where the Langevin model has been used to jointly model all unclosed terms. The Langevin equations in a LES framework are modelled using similar equations to those in RANS:

$$G_{ij}=-\omega_{sgs}\left(\frac{1}{2}+\frac{3}{4}C_0\right)\delta_{ij};\quad \epsilon_{sgs}=C_\epsilon k_{sgs}^{3/2}/\Delta;\quad \omega_{sgs}=\epsilon_{sgs}/k_{sgs} \tag{2.158}$$

In the LES context, k_{sgs} and ϵ_{sgs} are the subgrid kinetic energy and the dissipation of the subgrid kinetic energy, respectively. It is interesting to note that the subgrid kinetic energy can also be exactly obtained with the velocity-scalar PDF, such as in Eq.(2.72) for RANS models:

$$k_{sgs} = \frac{1}{2}\overline{u_i u_i} - \overline{u}_i\overline{u}_i = \frac{1}{2}\int_{-\infty}^{+\infty} (v_i - \overline{u}_i)\,(v_i - \overline{u}_i)\,\overline{f}\,\mathrm{d}\boldsymbol{v} \tag{2.159}$$

The model for ϵ_{sgs} is a classical approach for LES modelling [42] and it does not require an extra transport equation. It assumes that the production is equal to the dissipation of k_{sgs}, in an equilibrium approach.

The first equation has extra viscous terms because it is possible to expand the viscous tensor, $\overline{\tau}_{ik}$, to generate extra terms, such as the second spatial derivative, the second derivative with respect to $\boldsymbol{v}_i$ and the cross derivative of the FDF. The presence of these extra terms results in higher accuracy in regions of the flow dominated by viscous effects, since the molecular dissipation of the FDF is taken into account. The Lagrangian equations equivalent to the first transport equation are:

$$\mathrm{d}X_i^+ = U_i^+\,\mathrm{d}t + \sqrt{2\nu}\,\mathrm{d}W_i^x \tag{2.160}$$

$$\mathrm{d}U_i^+ = \left[-\frac{\partial\overline{p}}{\partial x_i} + 2\nu\frac{\partial^2\overline{u}_i}{\partial x_k\partial x_k} + G_{ij}\left(U_j^+ - \overline{u}_j\right)\right]\mathrm{d}t + \sqrt{C_0\epsilon_{sgs}}\,\mathrm{d}W_i^u + \sqrt{2\nu}\frac{\partial\overline{u}_i}{\partial x_j}\,\mathrm{d}W_j^x \tag{2.161}$$

where the Lagrangian stochastic equation for velocity presents two Wiener terms, one that arises from the $\mathrm{d}X_i^+$ equation and the other derived from the Langevin model. These equations are very similar to those derived by Dreeben and Pope [95] in a RANS framework. The Lagrangian equations equivalent to the second transport equation for the velocity FDF are:

$$\mathrm{d}X_i^+ = U_i^+\,\mathrm{d}t \tag{2.162}$$

$$\mathrm{d}U_i^+ = \left[-\frac{\partial \overline{p}}{\partial x_i} + \frac{\partial \overline{\tau}_{ik}}{\partial x_k} + G_{ij}\left(U_j^+ - \overline{u}_j\right)\right]\mathrm{d}t + \sqrt{C_0 \epsilon_{sgs}}\,\mathrm{d}W_i^u \tag{2.163}$$

It should be notice the absence of the Wiener term weighted by the molecular viscosity in the $\mathrm{d}X_i^+$ equation. The viscous effects are entirely modelled at the large eddy scale and only resolved viscous effects are being taken into account. This is the drawback of Eq.(2.156) in comparison to Eq. (2.157). Gicquel *et al.* [122] investigated both equations using also a mixing layer and a planar jet and concluded that the velocity FDF model can also generate accurate results in comparison to DNS data.

Sheikhi *et al.* (2003) [123]:

The joint velocity-scalar can be straightforwardly derived by combining the scalar and the velocity FDFs. This model is able to treat both convective and reactive terms in a large eddy simulation environment, although still using the low Mach number assumption. This was firstly performed in [123] considering a constant density approach, in which a Eulerian fine-grained one-point one-time joint velocity-scalar FDF is defined:

$$f'\left(\boldsymbol{v}, \boldsymbol{\psi}; \boldsymbol{x}, t\right) = \prod_{i=1}^{3} \delta\left(v_i - u_i\left(\boldsymbol{x}, t\right)\right) \prod_{\alpha=1}^{N_s} \delta\left(\psi_\alpha - \phi_\alpha\left(\boldsymbol{x}, t\right)\right) \tag{2.164}$$

and the respective FDF is obtained after applying the filtering operation:

$$\overline{f}\left(\boldsymbol{v}, \boldsymbol{\psi}; \boldsymbol{x}, t\right) = \int_{-\infty}^{+\infty} G(\boldsymbol{x} - \boldsymbol{x'}, \Delta) \prod_{i=1}^{3} \delta\left(v_i - u_i\left(\boldsymbol{x'}, t\right)\right) \prod_{\alpha=1}^{N_s} \delta\left(\psi_\alpha - \phi_\alpha\left(\boldsymbol{x'}, t\right)\right) \mathrm{d}\boldsymbol{x'} \tag{2.165}$$

The mathematical derivation of the transport equation of the FDF followed a different route than usual in this work. Instead of first obtaining a Fokker-Planck equation and then model the unclosed terms, Sheikhi *et al.* [123] proceeded to derive the unclosed transport equation and then generate closed Lagrangian equations. They derived the Fokker-Planck equation equivalent to the closed Lagrangian stochastic equations. They proceeded finally by comparing the two Fokker-Planck equations and writing the assumptions required to close the original transport equations and obtain the desired Lagrangian stochastic equations. The assumptions are similar to those of Pope [68], whereas the un-

closed terms of the Fokker-Planck equation, derived from the viscous and pressure parts, must be jointly modelled by the Langevin and a micromixing model.

The unclosed equation can be obtained using very similar techniques as present in the predecessor works [13, 122]:

$$\begin{aligned}\frac{\partial \overline{f}}{\partial t}+\frac{\partial \overline{f}}{\partial x_k} =&\nu\frac{\partial^2 \overline{f}}{\partial x_k \partial x_k}+\frac{\partial \overline{p}}{\partial x_k}\frac{\partial \overline{f}}{\partial x_k}-\frac{\partial}{\partial \psi_\alpha}\left[S_\alpha\left(\boldsymbol{\psi}\right)\overline{f}\right]\\ &+\frac{\partial}{\partial v_k}\left[\left(\overline{\frac{\partial p}{\partial x_k}\middle|\boldsymbol{v},\boldsymbol{\psi}}-\frac{\partial \overline{p}}{\partial x_k}\right)\overline{f}\right]-\frac{\partial^2}{\partial v_i \partial v_j}\left[\overline{\nu\frac{\partial u_i}{\partial x_k}\frac{\partial u_j}{\partial x_k}\middle|\boldsymbol{v},\boldsymbol{\psi}}\,\overline{f}\right]\\ &-2\frac{\partial^2}{\partial v_i \partial \psi_\alpha}\left[\overline{\nu\frac{\partial u_i}{\partial x_k}\frac{\partial \phi_\alpha}{\partial x_k}\middle|\boldsymbol{v},\boldsymbol{\psi}}\,\overline{f}\right]-\frac{\partial^2}{\partial \psi_\alpha \partial \psi_\beta}\left[\overline{\nu\frac{\partial \phi_\alpha}{\partial x_k}\frac{\partial \phi_\beta}{\partial x_k}\middle|\boldsymbol{v},\boldsymbol{\psi}}\,\overline{f}\right]\end{aligned} \tag{2.166}$$

The desired Lagrangian equations must present several properties, such as the realisability of the scalar field and must yield a Fokker-Planck equation that possess the same moments as the original unclosed equations. The proposed Lagrangian equations, using the Langevin model and the IEM micromixing model are:

$$\mathrm{d}X_i^+ = U_i^+\,\mathrm{d}t+\sqrt{2\nu}\,\mathrm{d}W_i^x \tag{2.167}$$

$$\mathrm{d}U_i^+ = \left[-\frac{\partial \overline{p}}{\partial x_i}+2\nu\frac{\partial^2 \overline{u}_i}{\partial x_k \partial x_k}+G_{ij}\left(U_j^+-\overline{u}_j\right)\right]\mathrm{d}t+\sqrt{C_0\epsilon_{sgs}}\,\mathrm{d}W_i^u+\sqrt{2\nu}\frac{\partial \overline{u}_i}{\partial x_j}\,\mathrm{d}W_j^x \tag{2.168}$$

$$\mathrm{d}\phi_\alpha^+ = \left[-C_\phi\omega\left(\phi_\alpha^+-\overline{\phi}_\alpha\right)+S_\alpha\right]\mathrm{d}t \tag{2.169}$$

and the Fokker-Planck equation obtained through the Lagrangian equations are:

$$\begin{aligned}\frac{\partial \overline{f}}{\partial t}+\frac{\partial}{\partial x_k}\left(v_k\overline{f}\right) =&\frac{\partial \overline{p}}{\partial x_i}\frac{\partial \overline{f}}{\partial v_i}-\frac{\partial}{\partial v_i}\left[G_{ij}\left(v_j-\overline{u}_j\right)\overline{f}\right]+\frac{\partial}{\partial \psi_\alpha}\left[C_\phi\omega\left(\psi_\alpha-\overline{\phi}_\alpha\right)\overline{f}\right]\\ &-\frac{\partial}{\partial \psi_\alpha}\left[S_\alpha\left(\boldsymbol{\psi}\right)\overline{f}\right]+\nu\frac{\partial^2 \overline{f}}{\partial x_k \partial x_k}+2\nu\frac{\partial \overline{u}_j}{\partial x_i}\frac{\partial^2 \overline{f}}{\partial x_i \partial v_j}\\ &+\nu\frac{\partial \overline{u}_i}{\partial x_k}\frac{\partial \overline{u}_j}{\partial x_k}\frac{\partial^2 \overline{f}}{\partial v_i \partial v_j}+\frac{1}{2}C_0\epsilon_{sgs}\frac{\partial^2 \overline{f}}{\partial v_k \partial v_k}\end{aligned} \tag{2.170}$$

This is already a closed equation, where all unclosed terms originally presented in Eq. (2.166) are jointly modelled using the Langevin model and the IEM micromixing.

The authors used the same approaches for the models' constants and to specified ϵ_{sgs} as in [13, 122]. The simulation of incompressible non-reacting mixing layers were then performed to assess the developed model and the Lagrangian Monte-Carlo algorithm. This algorithm was coupled with a finite difference LES solver to obtain the filtered pressure field, a common approach when solving the velocity field using stochastic particles. The results of the work were very promising, achieving good agreement with DNS data.

The extension of the joint velocity-scalar FDF model to variable density flows was carried on the work of Sheikhi *et al.* [124]. The transport equation for the Eulerian one-point one-time joint velocity-scalar FMDF is directly derived using the same techniques presented for the scalar FMDF in Jaberi *et al.* [111]. The velocity-scalar FMDF is defined as:

$$\begin{aligned}\overline{\mathscr{F}\left(\boldsymbol{v},\boldsymbol{\psi};\boldsymbol{x},t\right)} = \int_{-\infty}^{+\infty} \rho\left(\boldsymbol{x'},t\right) \prod_{i=1}^{3} \delta\left(v_i - u_i\left(\boldsymbol{x'},t\right)\right) \prod_{\alpha=1}^{N_s} \delta(\psi_\alpha - \phi_\alpha(\boldsymbol{x'},t)) \\ \times G\left(\boldsymbol{x}-\boldsymbol{x'},\Delta\right) \mathrm{d}\boldsymbol{x'}\end{aligned} \tag{2.171}$$

The Lagrangian stochastic equations are very similar to those of [123], however accounting for extra density terms:

$$\mathrm{d}X_i^+ = U_i^+ \,\mathrm{d}t + \sqrt{\frac{2\mu}{\overline{\rho}}}\,\mathrm{d}W_i^x \tag{2.172}$$

$$\begin{aligned}\mathrm{d}U_i^+ = \Bigg[-\frac{1}{\overline{\rho}}\frac{\partial \overline{p}}{\partial x_i} + \frac{2}{\overline{\rho}}\frac{\partial}{\partial x_j}\left(\mu\frac{\partial \widetilde{u}_i}{\partial x_j}\right) + \frac{1}{\overline{\rho}}\frac{\partial}{\partial x_j}\left(\mu\frac{\partial \widetilde{u}_j}{\partial x_i}\right) - \frac{2}{3}\frac{1}{\overline{\rho}}\frac{\partial}{\partial x_i}\left(\mu\frac{\partial \widetilde{u}_j}{\partial x_j}\right) \\ + G_{ij}\left(U_j^+ - \widetilde{u}_j\right)\Bigg]\mathrm{d}t + \sqrt{C_0\epsilon_{sgs}}\,\mathrm{d}W_i^u + \sqrt{\frac{2\mu}{\overline{\rho}}}\frac{\partial \widetilde{u}_i}{\partial x_j}\,\mathrm{d}W_j^x\end{aligned} \tag{2.173}$$

$$\mathrm{d}\phi_\alpha^+ = \left[-C_\phi\omega_{sgs}\left(\phi_\alpha^+ - \widetilde{\phi}_\alpha\right) + S_\alpha\right]\mathrm{d}t \tag{2.174}$$

where the same modelling used in Gicquel *et al.* [122] can be applied:

$$G_{ij} = -\omega \left(\frac{1}{2} + \frac{3}{4} C_0 \right) \delta_{ij}; \quad \epsilon_{sgs} = C_\epsilon k_{sgs}^{3/2} / \Delta; \quad \omega_{sgs} = \epsilon_{sgs} / k_{sgs} \tag{2.175}$$

The fully closed FMDF transport equation is therefore obtained:

$$\begin{aligned} \frac{\partial \widetilde{\mathscr{F}}}{\partial t} + \frac{\partial v_i \widetilde{\mathscr{F}}}{\partial x_i} =& \frac{1}{\overline{\rho}} \frac{\partial \overline{p}}{\partial x_i} \frac{\partial \widetilde{\mathscr{F}}}{\partial v_i} - \frac{2}{\overline{\rho}} \frac{\partial}{\partial x_j} \left(\mu \frac{\partial \widetilde{u}_i}{\partial x_j} \right) \frac{\partial \widetilde{\mathscr{F}}}{\partial v_i} - \frac{1}{\overline{\rho}} \frac{\partial}{\partial x_j} \left(\mu \frac{\partial \widetilde{u}_j}{\partial x_i} \right) \frac{\partial \widetilde{\mathscr{F}}}{\partial v_i} \\ &+ \frac{2}{3} \frac{1}{\overline{\rho}} \frac{\partial}{\partial x_i} \left(\mu \frac{\partial \widetilde{u}_j}{\partial x_j} \right) \frac{\partial \widetilde{\mathscr{F}}}{\partial v_i} - \frac{\partial}{\partial v_i} \left(G_{ij} \left(v_j - \widetilde{u}_j \right) \widetilde{\mathscr{F}} \right) \\ &+ \frac{\partial}{\partial x_j} \left(\mu \frac{\partial \left(\widetilde{\mathscr{F}} / \overline{\rho} \right)}{\partial x_j} \right) + \frac{\partial}{\partial x_j} \left(\frac{2\mu}{\overline{\rho}} \frac{\partial \widetilde{u}_j}{\partial x_j} \frac{\partial \widetilde{\mathscr{F}}}{\partial v_i} \right) \\ &+ \frac{\mu}{\overline{\rho}} \frac{\partial \widetilde{u}_i}{\partial x_k} \frac{\partial \widetilde{u}_j}{\partial x_k} \frac{\partial^2 \widetilde{\mathscr{F}}}{\partial v_i \partial v_j} + \frac{1}{2} C_0 \epsilon_{sgs} \frac{\partial^2 \widetilde{\mathscr{F}}}{\partial v_i \partial v_i} \\ &+ \frac{\partial}{\partial \psi_\alpha} \left(C_\phi \omega_{sgs} \left(\psi_\alpha - \widetilde{\phi}_\alpha \right) \widetilde{\mathscr{F}} \right) - \frac{\partial}{\partial \psi_\alpha} \left(S_\alpha \left(\boldsymbol{\psi} \right) \widetilde{\mathscr{F}} \right) \end{aligned} \tag{2.176}$$

The authors used temporally and spatially developing mixing layers to validate this approach, also comparing their results to DNS data. The results presented good agreement and the computational expense was about 100 times cheaper than DNS, although 15 times heavier than pure LES simulation using the same mesh size. The results using the velocity-scalar FMDF were more accurate, though.

Despite its elegant formulation, the Lagrangian solver for velocity and the scalars still needs to be coupled with a Eulerian one to calculate the filtered pressure, which makes it a very complex numerical approach. This numerical approach is difficult to implement and prone to interpolation error. Because of this the Lagrangian velocity-scalar FMDF has not been so popular as the scalar FMDF, although it was used by Nik *et al.* [125] to validate it using a Sandia D flame.

Mustata *et al.* (2006) [100]:

The Eulerian stochastic fields formulation developed by Valiño [19] was extended to the large eddy simulation framework in the work of Mustata *et al.* [100]. The Eulerian

one-point one-time joint scalar Favre-filtered PDF is:

$$\widetilde{f}(\boldsymbol{\psi};\boldsymbol{x},t)=\frac{\displaystyle\int_{-\infty}^{+\infty}\rho\left(\boldsymbol{x}',t\right)G(\boldsymbol{x}-\boldsymbol{x}',\Delta)\prod_{\alpha=1}^{N_s}\delta(\phi_\alpha(\boldsymbol{x}',t)-\psi_\alpha)\,\mathrm{d}\boldsymbol{x}'}{\displaystyle\int_{-\infty}^{+\infty}\rho\left(\boldsymbol{x}',t\right)G(\boldsymbol{x}-\boldsymbol{x}',\Delta)\,\mathrm{d}\boldsymbol{x}'} \tag{2.143}$$

The transport equation can be obtained using the same techniques as in RANS framework. The filtered transport equation for the PDF is:

$$\begin{aligned}\overline{\rho}\frac{\partial\widetilde{f}}{\partial t}+\overline{\rho}\widetilde{u}_j\frac{\partial\widetilde{f}}{\partial x_j}-\frac{\partial}{\partial\psi_\alpha}\left(\overline{\rho}S_\alpha(\boldsymbol{\psi})\widetilde{f}\right)=&\frac{\partial}{\partial x_i}\left(\overline{\rho}\frac{\nu}{\mathrm{Sc}}\frac{\partial\widetilde{f}}{\partial x_i}\right)-\frac{\partial}{\partial x_i}\left[\left(\overline{\rho}\,\widetilde{\overline{u_i|\boldsymbol{\psi}}}-\overline{\rho}\widetilde{u}_i\right)\widetilde{f}\right]\\&-\frac{\partial^2}{\partial\psi_\alpha\partial\psi_\beta}\left[\overline{\rho}\,\widetilde{\frac{\nu}{\mathrm{Sc}}\frac{\partial\phi_\alpha}{\partial x_i}\frac{\partial\phi_\beta}{\partial x_i}\middle|\boldsymbol{\psi}}\,\widetilde{f}\right]\end{aligned} \tag{2.177}$$

where the unclosed terms on the right-hand side of the transport equation requires modelling. The Smagorinsky model was used to close the convective term and the IEM micromixing model is also used to close the molecular diffusion term. The closed equation is therefore:

$$\begin{aligned}\overline{\rho}\frac{\partial\widetilde{f}}{\partial t}+\overline{\rho}\widetilde{u}_j\frac{\partial\widetilde{f}}{\partial x_j}-\frac{\partial}{\partial\psi_\alpha}\left(\overline{\rho}S_\alpha(\boldsymbol{\psi})\widetilde{f}\right)=&\frac{\partial}{\partial x_i}\left(\overline{\rho}\left(\frac{\nu}{\mathrm{Sc}}+\frac{\nu_{sgs}}{\mathrm{Sc}_{sgs}}\right)\frac{\partial\widetilde{f}}{\partial x_i}\right)\\&-\frac{\partial}{\partial\psi_\alpha}\left(-\frac{\overline{\rho}}{2\tau_{sgs}}\left(\psi_\alpha-\widetilde{\phi}_\alpha\right)\widetilde{f}\right)\end{aligned} \tag{2.178}$$

where τ_{sgs} is the subgrid timescale and requires modelling. In order to solve the closed filtered transport equation, the idea of Mustata *et al.* [100] were very similar to Valiño [19], but using LES framework. The Favre-filtered PDF can be represented by smooth Eulerian stochastic fields $\xi_\alpha^n\left(\boldsymbol{x},t\right)$:

$$\widetilde{f}\left(\boldsymbol{\psi};\boldsymbol{x},t\right)=\frac{1}{N_f}\sum_{n=1}^{N_f}\prod_{\alpha=1}^{N_s}\delta\left(\psi_\alpha-\xi_\alpha^n\left(\boldsymbol{x},t\right)\right) \tag{2.179}$$

It is interesting to point out that it is the average operation of samples on the same position $\boldsymbol{x}$ and time t that constructs the Eulerian PDF. On the Lagrangian formulation, these samples are taken into the same Eulerian volume, however, not at the same point $\boldsymbol{x}$

and the portability to the Eulerian PDF is not trivial. On the Eulerian stochastic fields methods, the filtered PDF is directly obtained. Using similar mathematical reasoning as in [19], it is possible to obtain the following n^{th} stochastic field equation:

$$\begin{aligned}\overline{\rho}\,\mathrm{d}\xi_\alpha^n = &-\overline{\rho}\widetilde{u}_i\frac{\partial\xi_\alpha^n}{\partial x_i}\,\mathrm{d}t + \frac{\partial}{\partial x_i}\left(\overline{\rho}\left(\frac{\nu}{\mathrm{Sc}}+\frac{\nu_{sgs}}{\mathrm{Sc}_{sgs}}\right)\frac{\partial\xi_\alpha^n}{\partial x_i}\right)\mathrm{d}t + \overline{\rho}S_\alpha^n\,\mathrm{d}t \\ &+\overline{\rho}\sqrt{2\left(\frac{\nu}{\mathrm{Sc}}+\frac{\nu_{sgs}}{\mathrm{Sc}_{sgs}}\right)}\frac{\partial\xi_\alpha^n}{\partial x_i}\,\mathrm{d}W_i^n - \frac{\overline{\rho}}{2\tau_{sgs}}\left(\xi_\alpha^n-\widetilde{\phi}_\alpha\right)\mathrm{d}t\end{aligned} \tag{2.180}$$

A possible choice for the subgrid timescale is:

$$\frac{1}{\tau_{sgs}} = C_\phi\frac{(\nu+\nu_{sgs})}{\Delta^2} \tag{2.181}$$

where the constant C_ϕ is equal to 2. Mustata *et al.* [100] validated this approach by simulating a low Mach number Sandia D flame. Also, they compared the results of 8 and 16 fields simulations and due to the small difference concluded that 8 fields were enough to obtain convergence of the first moments.

The Eulerian stochastic fields method to solve a filtered transport equation for the PDF has become since a very popular strategy. This is mainly due to its simplicity to be coupled with traditional CFD codes and good compromised between accuracy and computational cost. This method has been widely used in combustion applications, although the majority of them are based in low Mach number solvers [62, 126, 127, 128, 129, 130, 131, 132, 133, 134, 29, 135, 136].

The use of Eulerian stochastic fields to solve a joint scalar PDF using a compressible formulation was firstly proposed by Gong *et al.* [29]. In their work, they added a energy correction in the enthalpy equation to account for part of the compressible effects, although without explicitly adding the total derivative of pressure into the enthalpy equation. This approach also has a drawback pointed by Gerlinger [137]. As the sample space do not include an extra thermodynamic variable, such as density or pressure, the compressible effects on the source term are also neglected. Nevertheless the authors validated their method by simulating the DLR scramjet and obtaining good agreement with

experiments.

Nik (2012) [16]:

The work of Nik [16] was largely based on Delarue and Pope [20], although using LES techniques. Their work was also published in [21] and revisited in Nouri *et al.* [138]. It presents a filtered mass density function Lagrangian formulation aiming reactive and high-Mach number flows, again independent from a external solver. The FMDF includes the velocity components, species composition, internal energy and pressure (EPVS-FMDF):

$$\begin{aligned}\widetilde{\mathscr{F}\left(\boldsymbol{v},\boldsymbol{\psi},\theta,\eta;\boldsymbol{x},t\right)} = \int_{-\infty}^{+\infty} \rho\left(\boldsymbol{x'},t\right) \prod_{i=1}^{3} \delta\left(v_i - u_i\left(\boldsymbol{x'},t\right)\right) \prod_{\alpha=1}^{N_s} \delta(\psi_\alpha - \phi_\alpha(\boldsymbol{x'},t)) \\ \times \delta\left(\theta - e(\boldsymbol{x'},t)\right)\right) \delta\left(\eta - p(\boldsymbol{x'},t)\right) G\left(\boldsymbol{x}-\boldsymbol{x'},\Delta\right) \mathrm{d}\boldsymbol{x'}\end{aligned} \tag{2.182}$$

A transport equation for the $\widetilde{\mathscr{F}}$ can be obtained using very similar techniques to Sheikhi *et al.* [124]. The Lagrangian equations are therefore obtained employing similar closure to Delarue and Pope [20]:

$$\mathrm{d}X_i^+ = U_i^+ \,\mathrm{d}t + \sqrt{\frac{2\mu}{\overline{\rho}}}\,\mathrm{d}W_i \tag{2.183}$$

$$\begin{aligned}\mathrm{d}U_i^+ = \Bigg[-\frac{1}{\overline{\rho}}\frac{\partial \overline{p}}{\partial x_i} + \frac{2}{\overline{\rho}}\frac{\partial}{\partial x_j}\left(\mu\frac{\partial \widetilde{u}_i}{\partial x_j}\right) + \frac{1}{\overline{\rho}}\frac{\partial}{\partial x_j}\left(\mu\frac{\partial \widetilde{u}_j}{\partial x_i}\right) - \frac{2}{3}\frac{1}{\overline{\rho}}\frac{\partial}{\partial x_i}\left(\mu\frac{\partial \widetilde{u}_j}{\partial x_j}\right) \\ + G_{ij}\left(U_j^+ - \widetilde{u}_j\right)\Bigg]\mathrm{d}t + \sqrt{C_0\epsilon_{sgs}}\,\mathrm{d}W_i^u + \sqrt{\frac{2\mu}{\overline{\rho}}}\frac{\partial \widetilde{u}_i}{\partial x_j}\,\mathrm{d}W_j^x\end{aligned} \tag{2.184}$$

$$\mathrm{d}\phi_\alpha^+ = -C_\phi\omega_{sgs}\left(\phi_\alpha^+ - \widetilde{\phi}_\alpha\right)\mathrm{d}t \tag{2.185}$$

$$\begin{aligned}\mathrm{d}E^+ = \left(-\frac{C_e\omega_{sgs}}{\gamma}\left(E^+ - \widetilde{e}\right) + \frac{1}{\gamma}\left(\frac{\epsilon_{sgs}}{\rho^+} + \frac{\widetilde{\tau}_{ij}}{\rho^+}\frac{\partial \widetilde{u}_i}{\partial x_j}\right) + \frac{\gamma-1}{\gamma}E^+\left(A - \frac{B^2}{\gamma}\right)\right)\mathrm{d}t \\ + \frac{\gamma-1}{\gamma}E^+ B\,\mathrm{d}W^p\end{aligned} \tag{2.186}$$

$$\mathrm{d}P^+ = P^+\left(A\,\mathrm{d}t + B\,\mathrm{d}W^p\right) \tag{2.187}$$

where the required proposed closures are:

$$G_{ij} = \frac{\Pi_d}{2k_{sgs}\overline{\rho}} - \omega_{sgs}\left(\frac{1}{2} + \frac{3}{4}C_0\right)\delta_{ij} \tag{2.188}$$

$$k_{sgs} = \frac{1}{2}\left\langle \left(U_i^+ - \widetilde{u}_i\right)\left(U_i^+ - \widetilde{u}_i\right)\right\rangle_{lf} \tag{2.189}$$

$$\epsilon_{sgs} = \overline{\rho}C_e\frac{k_{sgs}^{3/2}}{\Delta} \tag{2.190}$$

$$\omega_{sgs} = \frac{1}{\overline{\rho}}\frac{\epsilon_{sgs}}{k_{sgs}} \tag{2.191}$$

$$\Pi_d = C_\Pi\left(\left\langle \overline{p}\frac{\partial \widetilde{u}_i}{\partial x_i}\right\rangle_l - \langle\overline{p}\rangle_l\frac{\partial\left\langle\widetilde{u}_i\right\rangle_{lf}}{\partial x_i}\right) \tag{2.192}$$

$$\begin{aligned} A = &-\frac{C_e\omega_{sgs}}{E^+}\left(E^+ - \widetilde{e}\right) + \frac{1}{E^+}\left(\frac{\epsilon_{sgs}}{\rho^+} + \frac{1}{\rho^+}\widetilde{\tau}_{ij}\frac{\partial\widetilde{u}_i}{\partial x_j}\right) - \gamma\frac{\Pi_d\left(P^+ - \overline{p}\right)}{\left\langle\left(P^+ - \overline{p}\right)\left(P^+ - \overline{p}\right)\right\rangle_l} \\ &-\gamma\frac{\partial\widetilde{u}_i}{\partial x_i} - \frac{\gamma}{\gamma-1}\frac{1}{\rho^+E^+}\left(\frac{\partial\widetilde{q}_i}{\partial x_i} + \frac{\partial}{\partial x_i}\left(\mu\frac{\partial\widetilde{e}}{\partial x_i}\right)\right) \end{aligned} \tag{2.193}$$

$$B = 0 \tag{2.194}$$

where the operations $\langle\cdot\rangle_l$ and $\langle\cdot\rangle_{lf}$ represent the average and Favre-average, respectively, using the Lagrangian particles, which is used to exactly obtain filtered values.

This formulation exactly closes the source term without using the low Mach number assumption. However, the excessive complexity of the stochastic system still prevents its use in more challenging simulations. Nik [16] presented results for a three-dimensional non-reactive mixing layer using the EPVS-FMDF model. However, it still lacks validation on a supersonic combustion system.

There have been some effort though to bring other Lagrangian attempts to compressible environment using a joint scalar FMDF. It is worth mention the works of [15, 139]

that expanded the FMDF into compressible flows by correcting the enthalpy equation and accounting for the total derivative of pressure. Irannejad *et al.* [140] has presented a formulation applicable to high-speed two-phases flows. The work of Gerlinger [137] also solves a scalar FMDF in a compressible environment and it highlights the fact that it is necessary one more thermodynamic variable to completely obtain the source term. Nonetheless, Gerlinger propose to use the Lagrangian particles to obtain the pressure and feed it into the Eulerian solver. In this way, depending on the equation of state, the pressure can be exactly obtained and there is no need to model subgrid pressure terms, an idea that it is also employed in this work. Zhang *et al.* [141] developed a energy-consistency-preserving approach for the joint scalar FMDF, also fixing the compressible source term on the enthalpy equation and validating it using a shock-tube and a temporally developing mixing layer.

Table 2.2 summarises some of the works mentioned using the LES-PDF/FDF method. The proposed solution methods have been mostly the Lagrangian or the Eulerian Monte-Carlo approaches, however there are other PDF-based methods such as the already mentioned Conditional Moment Closure (CMC) [49] and quadrature-based moment method [9, 37]. Nonetheless, the Monte-Carlo approach is the one with less restrictive assumptions.

Reference	FDF model	Closures	Solution
Gao and O'Brien [17] (1993)	$\rho = \text{cte}$, Scalar	IEM	-
Colucci *et al.* [13] (1998)	$\rho = \text{cte}$, Scalar	IEM	Lagrangian MC
Jaberi *et al.* [111] (1999)	$\rho(\boldsymbol{\psi})$, Scalar	IEM	Lagrangian MC
Gicquel *et al.* [122] (2002)	$\rho = \text{cte}$, Velocity	Langevin	Lagrangian MC
Sheikhi *et al.* [123] (2003)	$\rho = \text{cte}$, Velocity-Scalar	IEM/Langevin	Lagrangian MC
Mustata *et al.* [100] (2006)	$\rho(\boldsymbol{\psi})$, Scalar	IEM	Eulerian MC
Sheikhi *et al.* [124] (2007)	$\rho(\boldsymbol{\psi})$, Velocity-Scalar	IEM/Langevin	Lagrangian MC
Jones *et al.* [62] (2011)	$\rho(\boldsymbol{\psi})$, Spray, Scalar	IEM	Eulerian MC
Banaeizadeh *et al.* [15] (2011)	$\rho(\boldsymbol{\psi})$, Comp. Scalar	IEM	Lagrangian MC
Jones *et al.* [128] (2012)	$\rho(\boldsymbol{\psi})$, Scalar	IEM	Eulerian MC
Nik [16] (2012)	$\rho(\boldsymbol{\psi})$, Energy-Pressure VS	IEM/Langevin	Lagrangian MC
Gong *et al.* [29] (2017)	$\rho(\boldsymbol{\psi})$, Comp. Scalar	IEM	Eulerian MC
Gerlinger [137] (2017)	$\rho(\boldsymbol{\psi})$, Comp. Scalar	IEM	Lagrangian MC
Zhang *et al.* [141] (2018)	$\rho(\boldsymbol{\psi})$, Comp. Scalar	IEM	Lagrangian MC

Table 2.2: Influential LES-PDF/FDF works, where MC stands for Monte-Carlo method.

2.5 Summary

The probability density function methods presented in this chapter form the groundwork of this thesis. The supersonic combustion phenomena is challenging to numerically reproduce using the current mathematical tools available and a specific new combustion model is necessary. The usage of PDF methods applied to supersonic combustion has been recently investigated, although not fully explored and developed. A PDF method dedicated to simulate high-speed and reacting flows can reduce the number of uncertainties from the traditional modelling by closing exactly the velocity and/or reactive terms.

The solution method for the PDF transport equation has been mainly the stochastic Lagrangian and the Eulerian approaches. Whereas the Lagrangian formulation dominates the PDF solution methods, the Eulerian methods have become popular amongst researchers because of its simple portability to well-established CFD codes. The Eulerian stochastic fields method was first introduced by Valiño [19], where instead of a sample of stochastic particles, a sample of stochastic fields is used to represent the PDF. It is important to highlight that the fields do not represent a particular realisation of the flow. However, the stochastic fields and the real flow evolve with the same PDF and share the same moments.

The Eulerian stochastic fields method therefore constitutes a convenient approach to solve the PDF equation with reasonable computational effort. In the next chapter two new formulations aiming the solution of supersonic combustion are presented. These formulations have been developed under the scope of this work. Its limitations along with its advantages are also described. Numerical implementation techniques are exposed to provide an accurate algorithm to solve the LES-PDF transport equation in a compressible solver.

Chapter 3

LES-PDF modelling for supersonic reacting flows

3.1 Introduction

Two PDF models are proposed here to be applied to supersonic combustion. This chapter has been partially published in Almeida and Navarro-Martinez [142]. The models are designed to operate within the large eddy simulation framework. The joint scalar LES-PDF is presented first and a new joint velocity-scalar is shown afterwards. The Eulerian stochastic fields method is employed to solve both LES-PDF transport equation, and equations are derived using the same method as Valiño [19] and Sabel'nikov and Soulard [101]. The new models are implemented in CompReal, an in-house Fortran-based compressible code developed to solve complex flows, described in Section 3.4.

3.2 Joint scalar PDF (SPDF)

The joint scalar fine-grained Eulerian probability density function (PDF) is defined as:

$$f'(\eta, \boldsymbol{Z}; \boldsymbol{x}, t) = \delta(h(\boldsymbol{x}, t) - \eta) \times \prod_{\alpha=1}^{N_s} \delta(Y_\alpha(\boldsymbol{x}, t) - Z_\alpha) \tag{3.1}$$

where η, Z_α are the sample enthalpy and mass fractions, $h(\boldsymbol{x}, t)$ and $Y_\alpha(\boldsymbol{x}, t)$ are the real enthalpy and mass fractions, respectively. The LES-PDF is defined by applying a spatial filter to Eq.(3.1):

$$\overline{f} = \int_{-\infty}^{+\infty} f'(\boldsymbol{\psi}; \boldsymbol{x'}, t) G(\boldsymbol{x} - \boldsymbol{x'}, \Delta) \, \mathrm{d}\boldsymbol{x'} \tag{3.2}$$

where $\boldsymbol{\psi} = [\eta, Z_\alpha]$. The LES-PDF must also respect the following property:

$$\int_{-\infty}^{+\infty} \overline{f}(\boldsymbol{\psi}; \boldsymbol{x}, t) \, \mathrm{d}\boldsymbol{\psi} = 1 \tag{3.3}$$

which limits the choice of the filter. For the purpose of this application, the filter has to be always positive and the box or top-hat filter can be used:

$$G(\boldsymbol{x} - \boldsymbol{x'}, \Delta) = \begin{cases} \dfrac{1}{\Delta^3}, & \text{if } |\boldsymbol{x} - \boldsymbol{x'}| \leq \dfrac{\Delta}{2} \\ 0, & \text{otherwise} \end{cases} \tag{3.4}$$

where Δ is the cut-off scale in space, taken by the cubic root of the volume of the cell in the mesh, $\Delta = (\Delta x_1 \Delta x_2 \Delta x_3)^{1/3}$. As previously mentioned, this filter satisfies the normalisation condition and it is also considered that the filtering operation commutes with spatial differentiation.

The respective Favre filtered density function is:

$$\overline{\rho}\widetilde{f} = \int_{-\infty}^{+\infty} \rho f'(\boldsymbol{\psi}; \boldsymbol{x'}, t) G(\boldsymbol{x} - \boldsymbol{x'}, \Delta) \, \mathrm{d}\boldsymbol{x'} \tag{3.5}$$

For completeness, a conditional filtering operation of a function $Q(\boldsymbol{x}, t)$ is also presented

here:

$$\widetilde{Q \mid \boldsymbol{\psi}} = \frac{\displaystyle\int_{-\infty}^{+\infty} \rho\left(\boldsymbol{x'},t\right) Q(\boldsymbol{x'},t) f'(\boldsymbol{\psi};\boldsymbol{x'},t) G(\boldsymbol{x}-\boldsymbol{x'},\Delta)\,\mathrm{d}\boldsymbol{x'}}{\displaystyle\int_{-\infty}^{+\infty} \rho\left(\boldsymbol{x'},t\right) f'(\boldsymbol{\psi};\boldsymbol{x'},t) G(\boldsymbol{x}-\boldsymbol{x'},\Delta)\,\mathrm{d}\boldsymbol{x'}} = \frac{\overline{\rho}\widetilde{Qf}}{\overline{\rho}\widetilde{f}} \tag{3.6}$$

The LES-PDF equation therefore can be obtained by deriving a transport equation for f' and applying a spatial filter [64].

The non-closed equation obtained is:

$$\begin{aligned}
&\frac{\partial \overline{\rho}\widetilde{f}}{\partial t} + \frac{\partial \overline{\rho}\widetilde{u}_i\widetilde{f}}{\partial x_i} = \frac{\partial}{\partial x_i}\left(\Gamma \frac{\partial \widetilde{f}}{\partial x_i}\right) \\
&- \frac{\partial}{\partial Z_\alpha}\left(\overline{\rho}\widetilde{S_\alpha \mid \boldsymbol{\psi}}\,\widetilde{f}\right) + \frac{\partial}{\partial x_i}\left(\overline{\rho}\widetilde{u}_i\widetilde{f} - \overline{\rho}\widetilde{u_i \mid \boldsymbol{\psi}}\,\widetilde{f}\right) \\
&- \frac{\partial}{\partial \eta}\left(\overline{\rho}\,\widetilde{\frac{1}{\rho}\frac{Dp}{Dt}\middle|\boldsymbol{\psi}}\,\widetilde{f} + \overline{\rho}\,\widetilde{\frac{\tau_{ij}}{\rho}\frac{\partial u_i}{\partial x_j} \mid \boldsymbol{\psi}}\,\widetilde{f}\right) \\
&+ \frac{\partial}{\partial x_i}\left(\overline{\rho}\Gamma\widetilde{\frac{\partial f'}{\partial x_i}} - \overline{\rho}\Gamma\frac{\partial \widetilde{f}}{\partial x_i}\right) \\
&- \frac{\partial^2}{\partial \psi_\alpha \partial \psi_\beta}\left(\overline{\rho}\Gamma\widetilde{\frac{\partial \phi_\alpha}{\partial x_i}\frac{\partial \phi_\beta}{\partial x_i} \mid \boldsymbol{\psi}}\,\widetilde{f}\right)
\end{aligned} \tag{3.7}$$

where $\Gamma = \mu/\mathrm{Sc}$ is the molecular transport coefficient, which is assumed the same for all species and enthalpy, as required in a joint-scalar PDF model shown in Chapter 2. The Smagorinsky model is chosen to close the convective terms. More sophisticate models can be used such as the Germano dynamic model [43, 44] and in theory the same LES models described in the previous chapter can be used. However, the Smagorinsky model, which assumes isotropy at the subgrid scales, is retained here because of its simplicity and adequate accuracy:

$$\frac{\partial}{\partial x_i}\left(\overline{\rho}\widetilde{u}_i\widetilde{f} - \overline{\rho}\widetilde{u_i \mid \boldsymbol{\psi}}\,\widetilde{f}\right) \approx \frac{\partial}{\partial x_i}\left(\frac{\mu_{sgs}}{\mathrm{Sc}_{sgs}}\frac{\partial \widetilde{f}}{\partial x_i}\right) \tag{3.8}$$

It is important to highlight that the source term in this model is not completely closed. The proposed LES-PDF equation relies on the assumption that the reactive source term is a function of the sample variables and the filtered pressure. The source term is therefore

partially modelled as $\widetilde{S}_\alpha \approx S_\alpha\left(\overline{p}, \boldsymbol{\psi}\right)$.

This assumption has been applied by several authors [14, 15, 29, 137] in order to avoid the inclusion of one more thermodynamic variable into the LES-PDF equation. It differs from the traditional low-Mach number assumption because the pressure is not a reference pressure, but the same pressure that is used along with the compressible flow solver. However, as pointed out by Gerlinger [137], no investigation have been performed yet to evaluate the magnitude of possible errors resulting from this assumption.

In this work the (IEM) micromixing model [71] is employed to close remaining terms:

$$\begin{aligned}
&-\frac{\partial}{\partial\eta}\left(\overline{\rho}\,\widetilde{\frac{1}{\rho}\frac{Dp}{Dt}\middle|\boldsymbol{\psi}}\,\widetilde{f}+\overline{\rho}\,\widetilde{\frac{\tau_{ij}}{\rho}\frac{\partial u_i}{\partial x_j}\mid\boldsymbol{\psi}}\,\widetilde{f}\right)+\frac{\partial}{\partial x_i}\left(\overline{\rho}\,\Gamma\widetilde{\frac{\partial f'}{\partial x_i}}-\overline{\rho}\Gamma\frac{\partial\widetilde{f}}{\partial x_i}\right)\\
&-\frac{\partial^2}{\partial\psi_\alpha\partial\psi_\beta}\left(\overline{\rho}\,\Gamma\widetilde{\frac{\partial\phi_\alpha}{\partial x_i}\frac{\partial\phi_\beta}{\partial x_i}\mid\boldsymbol{\psi}}\,\widetilde{f}\right)\approx-\frac{\partial}{\partial\eta}\left(\frac{D\overline{p}}{Dt}\widetilde{f}+\widetilde{\tau}_{ij}\frac{\partial\widetilde{u}_i}{\partial x_j}\widetilde{f}\right)\\
&-\frac{\partial}{\partial Z_\alpha}\left(-\frac{1}{2}\frac{C_{Y_\alpha}}{\tau_{sgs}}\overline{\rho}\left(Z_\alpha-\widetilde{Y}_\alpha\right)\widetilde{f}\right)-\frac{\partial}{\partial\eta}\left(-\frac{1}{2}\frac{C_h}{\tau_{sgs}}\overline{\rho}\left(\eta-\widetilde{h}\right)\widetilde{f}\right)
\end{aligned}\tag{3.9}$$

where the subgrid timescale, τ_{sgs}, is defined using the model of Jones *et al.* [128]:

$$\tau_{sgs}=\left(\frac{\mu+\mu_{sgs}}{\overline{\rho}\Delta^2}\right)^{-1}\left(1-\exp(-\mathscr{R}^2)\right)\tag{3.10}$$

where $\mathscr{R}$ is a subgrid scale turbulence Reynolds number defined as μ_{sgs}/μ. It should be noticed that the correction term τ_{sgs} should tend to zero in a DNS simulation, as $\Delta\to 0$ in this case. The term $(1-\exp(-\mathscr{R}^2))$ corrects the micromixing timescale by imposing the limiting behaviour $\tau_{sgs}\to 0$ as $\mu_{sgs}\to 0$. The closed LES-PDF equation is therefore:

$$\begin{aligned}
&\frac{\partial\overline{\rho}\widetilde{f}}{\partial t}+\frac{\partial\overline{\rho}\widetilde{u}_i\widetilde{f}}{\partial x_i}=\frac{\partial}{\partial x_i}\left(\Gamma'\frac{\partial\widetilde{f}}{\partial x_i}\right)\\
&-\frac{\partial}{\partial Z_\alpha}\left(\overline{\rho}S_\alpha\left(\overline{p},\boldsymbol{\psi}\right)\widetilde{f}-\frac{1}{2}\frac{C_{Y_\alpha}}{\tau_{sgs}}\overline{\rho}\left(Z_\alpha-\widetilde{Y}_\alpha\right)\widetilde{f}\right)\\
&-\frac{\partial}{\partial\eta}\left(\frac{D\overline{p}}{Dt}\widetilde{f}+\widetilde{\tau}_{ij}\frac{\partial\widetilde{u}_i}{\partial x_j}\widetilde{f}-\frac{1}{2}\frac{C_h}{\tau_{sgs}}\overline{\rho}\left(\eta-\widetilde{h}\right)\widetilde{f}\right)
\end{aligned}\tag{3.11}$$

where $\Gamma' = \mu/\mathrm{Sc} + \mu_{sgs}/\mathrm{Sc}_{sgs}$ is the total diffusion coefficient. The Schmidt number Sc and its subgrid equivalent Sc_{sgs} are equal to unity, like the Prandtl numbers (see Chapter 2). The constants C_{Y_α} and C_h are equal to 2, same value used in previous works [62, 128]. In Equation (3.11), differential diffusion is also neglected. The Smagorinsky model is used to obtain the subgrid dynamic viscosity[1]:

$$\mu_{sgs} = \overline{\rho}\left(C_\mu \Delta\right)^2 ||\widetilde{S}_{ij}||; \quad \widetilde{S}_{ij} = \frac{1}{2}\left(\frac{\partial \widetilde{u}_i}{\partial x_j} + \frac{\partial \widetilde{u}_j}{\partial x_i}\right) \tag{3.12}$$

where the constant C_μ is equal to 0.15, unless stated otherwise. A value between 0.1 and 0.2 is usually set, and here the value of 0.15 is chosen following other supersonic combustion LES simulations [18].

In order to solve Eq. (3.11), Eulerian stochastic differential equations are derived for the mass fractions and enthalpy. These equations are then obtained using the same method as Sabel'nikov and Soulard [101], employing a different function for $\mathscr{M}(\boldsymbol{\psi}; \boldsymbol{x}, t)$ in Eq.(2.100) to make it equivalent to Eq. (3.11).

The equations for the n^{th}-set of Eulerian stochastic fields are therefore:

$$\begin{aligned} &\frac{\partial \overline{\rho}\mathscr{Y}_\alpha^n}{\partial t} + \frac{\partial \overline{\rho}\widetilde{u}_i \mathscr{Y}_\alpha^n}{\partial x_i} = \frac{\partial}{\partial x_i}\left(\Gamma' \frac{\partial \mathscr{Y}_\alpha^n}{\partial x_i}\right) + \overline{\rho} S_\alpha^n\left(\overline{p}, \boldsymbol{\psi}\right) \\ &- \frac{1}{2}\frac{C_{Y_\alpha}}{\tau_{sgs}}\overline{\rho}\left(\mathscr{Y}_\alpha^n - \widetilde{Y}_\alpha\right) + \left(2\overline{\rho}\Gamma'\right)^{1/2} \frac{\partial \mathscr{Y}_\alpha^n}{\partial x_i}\frac{\mathrm{d}W_i^n}{\mathrm{d}t} \end{aligned} \tag{3.13}$$

$$\begin{aligned} &\frac{\partial \overline{\rho}\mathscr{H}^n}{\partial t} + \frac{\partial \overline{\rho}\widetilde{u}_i \mathscr{H}^n}{\partial x_i} = \frac{\partial}{\partial x_i}\left(\Gamma' \frac{\partial \mathscr{H}^n}{\partial x_i}\right) + \frac{D\overline{p}}{Dt} + \widetilde{\tau}_{ij}\frac{\partial \widetilde{u}_i}{\partial x_j} \\ &- \frac{1}{2}\frac{C_H}{\tau_{sgs}}\overline{\rho}\left(\mathscr{H}^n - \widetilde{h}\right) + \left(2\overline{\rho}\Gamma'\right)^{1/2} \frac{\partial \mathscr{H}^n}{\partial x_i}\frac{\mathrm{d}W_i^n}{\mathrm{d}t} \end{aligned} \tag{3.14}$$

where $\mathscr{Y}_\alpha^n(\boldsymbol{x}, t)$ and $\mathscr{H}^n(\boldsymbol{x}, t)$ are the stochastic fields for mass fractions and enthalpy, respectively. Favre-filtered quantities are calculated from the average of the stochastic fields as:

$$\widetilde{Q} = \langle Q \rangle = \frac{1}{N_f}\sum_{n=1}^{N_f} Q^n \tag{3.15}$$

[1]This is also described in Chapter 2.

It is useful to point out that in conventional LES the filtered pressure field has a subgrid part. For the ideal gas equation of state, the filtered pressure can be recasted into a resolved and subgrid part, as in the following:

$$\overline{p} = \overline{\rho} R_u \left(\sum_{\alpha=1}^{N_s} \frac{\widetilde{Y}_\alpha}{M_\alpha} \right) \widetilde{T} + \left(\overline{\rho} R_u \overline{\left(\sum_{\alpha=1}^{N_s} \frac{Y_\alpha}{M_\alpha} \right) T} - \overline{\rho} R_u \left(\sum_{\alpha=1}^{N_s} \frac{\widetilde{Y}_\alpha}{M_\alpha} \right) \widetilde{T} \right) \tag{3.16}$$

where the term on the right hand side is usually neglected. In the present work, the filtered pressure field is solved exactly when applying the ideal gas law:

$$\overline{p} = \overline{\rho \widetilde{RT}} \approx \overline{\rho} R_u \left[\frac{1}{N_F} \sum_{n=1}^{N_F} \left(\sum_{\alpha=1}^{N_s} \frac{\mathscr{Y}_\alpha^n}{MW_\alpha} \right) T^n \right] \tag{3.17}$$

where R_u is the gas universal constant and MW_α is the molecular weight of the chemical specie α. In this manner, no subgrid contribution is neglected and the stochastic fields will affect the momentum equations.

Finally, the Eulerian stochastic fields equations are coupled with a LES compressible solver to calculate the remaining variables such as density, velocity and total energy. It is also useful to define a total resolved enthalpy variable to solve the enthalpy equation within the compressible framework:

$$\mathscr{H}_t^n = \mathscr{H}^n + \widetilde{K} \tag{3.18}$$

where $\widetilde{K} = \frac{1}{2}\widetilde{u}_i \widetilde{u}_i$ is the resolved kinetic energy. The transport equation for the resolved kinetic energy is:

$$\frac{\partial \overline{\rho} \widetilde{K}}{\partial t} + \frac{\partial \overline{\rho} \widetilde{u}_i \widetilde{K}}{\partial x_i} = \frac{\partial}{\partial x_i} \left(\Gamma' \frac{\partial \widetilde{K}}{\partial x_i} \right) - \widetilde{u}_i \frac{\partial \overline{p}}{\partial x_i} + \widetilde{u}_j \frac{\partial \widetilde{\tau}_{ij}}{\partial x_j} \tag{3.19}$$

and the total enthalpy equation can be obtained by adding Eq. (3.19) to Eq. (3.14):

$$\begin{aligned} &\frac{\partial \overline{\rho} \mathscr{H}_t^n}{\partial t} + \frac{\partial \overline{\rho} \widetilde{u}_i \mathscr{H}_t^n}{\partial x_i} = \frac{\partial}{\partial x_i} \left(\Gamma' \frac{\partial \mathscr{H}_t^n}{\partial x_i} \right) + \frac{\partial \overline{p}}{\partial t} + \frac{\partial \widetilde{\tau}_{ij} \widetilde{u}_i}{\partial x_j} \\ &- \frac{1}{2} \frac{C_H}{\tau_{sgs}} \overline{\rho} \left(\mathscr{H}^n - \widetilde{h} \right) + \left(2 \overline{\rho} \Gamma' \right)^{1/2} \frac{\partial \mathscr{H}^n}{\partial x_i} \frac{\mathrm{d}W_i^n}{\mathrm{d}t} \end{aligned} \tag{3.20}$$

The total enthalpy formulation has the advantage of not requiring the calculation of spatial gradients of pressure, as previous demanded if the total derivative of pressure was to be obtained. This reduces potential numerical error from the spatial discretisation of pressure, which can be large in sharp gradient regions.

3.3 Joint velocity-scalar PDF (VSPDF)

The joint velocity-scalar fine-grained Eulerian probability density function (PDF) is defined as:

$$\begin{aligned} f'(d,\boldsymbol{v},\zeta,\boldsymbol{Z};\boldsymbol{x},t) =& \delta(\rho(\boldsymbol{x},t)-d)\prod_{i=1}^{3}\delta(u_i(\boldsymbol{x},t)-v_i)\times \\ & \delta(e_t(\boldsymbol{x},t)-\zeta)\prod_{\alpha=1}^{N_s}\delta(Y_\alpha(\boldsymbol{x},t)-Z_\alpha) \end{aligned} \tag{3.21}$$

where d, v_i, ζ and Z_α are the sample density, velocity, total energy and mass fraction, while $\rho(\boldsymbol{x},t)$, $u_i(\boldsymbol{x},t)$, $e_t(\boldsymbol{x}$ and $Y_\alpha(\boldsymbol{x},t)$ are the respective real fields. The Favre-filtered joint velocity-scalar PDF is defined likewise:

$$\overline{\rho}\widetilde{f} = \int_{-\infty}^{+\infty} \rho f'(\boldsymbol{\Psi};\boldsymbol{x'},t)G(\boldsymbol{x}-\boldsymbol{x'},\Delta)\,\mathrm{d}\boldsymbol{x'} \tag{3.22}$$

where $\boldsymbol{\Psi} = [d,\boldsymbol{v},\zeta,\boldsymbol{Z}]$. It is possible to obtain a LES-PDF equation using the same method for the joint scalar PDF, by deriving a transport equation for f' and applying the spatial filtering operation. This derivation is presented here because it is not so common as the joint scalar counterpart. The temporal derivative of f' is:

$$\rho\frac{\partial f'}{\partial t} = -\frac{\partial}{\partial d}\left(\rho f'\frac{\partial \rho}{\partial t}\right) - \frac{\partial}{\partial v_i}\left(\rho f'\frac{\partial u_i}{\partial t}\right) - \frac{\partial}{\partial \zeta}\left(\rho f'\frac{\partial e_t}{\partial t}\right) - \frac{\partial}{\partial Z_\alpha}\left(\rho f'\frac{\partial Y_\alpha}{\partial t}\right) \tag{3.23}$$

and considering the following the unfiltered equations, neglecting the momentum body forces:

$$\frac{\partial \rho}{\partial t} + \frac{\partial \rho u_i}{\partial x_i} = 0 \tag{3.24}$$

$$\rho\frac{\partial \rho}{\partial t} = -\rho u_i\frac{\partial \rho}{\partial x_i} - \rho^2\frac{\partial u_i}{\partial x_i} \tag{3.25}$$

$$\rho\frac{\partial u_i}{\partial t} = -\rho u_j\frac{\partial u_i}{\partial x_j} - \frac{\partial p}{\partial x_i} + \frac{\partial \tau_{ij}}{\partial x_j} \tag{3.26}$$

$$\rho\frac{\partial e_t}{\partial t} = -\rho u_i\frac{\partial e_t}{\partial x_i} + \frac{\partial q_i}{\partial x_i} - \frac{\partial p u_i}{\partial x_i} + \frac{\partial \tau_{ij}u_j}{\partial x_i} \tag{3.27}$$

$$\rho\frac{\partial Y_\alpha}{\partial t} = -\rho u_i\frac{\partial Y_\alpha}{\partial x_i} + \frac{\partial J_{\alpha,i}}{\partial x_i} + \rho S_\alpha \tag{3.28}$$

The transport equation for f' can be obtained by using the previous equations and inserting them into Equation (3.23):

$$\begin{aligned}\frac{\partial \rho f'}{\partial t} + \frac{\partial \rho u_i f'}{\partial x_i} =& -\frac{\partial}{\partial d}\left(-\rho^2\frac{\partial u_i}{\partial x_i}f'\right)\\ &-\frac{\partial}{\partial Z_\alpha}\left(\frac{\partial J_{\alpha,i}}{\partial x_i}f' + \rho S_\alpha f'\right)\\ &-\frac{\partial}{\partial v_i}\left(-\frac{\partial p}{\partial x_i}f' + \frac{\partial \tau_{ij}}{\partial x_j}f'\right)\\ &-\frac{\partial}{\partial \zeta}\left(\frac{\partial q_i}{\partial x_i}f' - \frac{\partial p u_i}{\partial x_i}f' + \frac{\partial \tau_{ij}u_j}{\partial x_i}f'\right)\end{aligned} \tag{3.29}$$

By filtering Equation (3.29), it is possible to obtain the unclosed filtered equation for the joint velocity-scalar PDF:

$$\begin{aligned}&\frac{\partial \overline{\rho}\widetilde{f}}{\partial t} + \frac{\partial \overline{\rho}v_i\widetilde{f}}{\partial x_i} = -\frac{\partial}{\partial d}\left(-\overline{\rho}^2\frac{\partial \widetilde{u}_i}{\partial x_i}\widetilde{f}\right) - \frac{\partial}{\partial Z_\alpha}\left(\frac{\partial \widetilde{J}_{\alpha,i}}{\partial x_i}\widetilde{f} + \overline{\rho}S_\alpha(\mathbf{\Psi})\widetilde{f}\right)\\ &-\frac{\partial}{\partial v_i}\left(-\frac{\partial \overline{p}}{\partial x_i}\widetilde{f} + \frac{\partial \widetilde{\tau}_{ij}}{\partial x_i}\widetilde{f}\right) - \frac{\partial}{\partial \zeta}\left(\frac{\partial \widetilde{q}_i}{\partial x_i}\widetilde{f} - \frac{\partial \overline{p}\widetilde{u}_i}{\partial x_i}\widetilde{f} + \frac{\partial \widetilde{\tau}_{ij}\widetilde{u}_j}{\partial x_i}\widetilde{f}\right)\\ &-\frac{\partial}{\partial v_i}\left(-\overline{\rho}\,\overline{\frac{1}{\rho}\frac{\partial p}{\partial x_i}\middle|\mathbf{\Psi}}\,\widetilde{f} + \frac{\partial \overline{p}}{\partial x_i}\widetilde{f} + \overline{\rho}\,\overline{\frac{1}{\rho}\frac{\partial \tau_{ij}}{\partial x_i}\middle|\mathbf{\Psi}}\,\widetilde{f} - \frac{\partial \widetilde{\tau}_{ij}}{\partial x_i}\widetilde{f}\right)\\ &-\frac{\partial}{\partial \zeta}\left(\overline{\rho}\,\overline{\frac{1}{\rho}\frac{\partial q_i}{\partial x_i}\middle|\mathbf{\Psi}}\,\widetilde{f} - \frac{\partial \widetilde{q}_i}{\partial x_i}\widetilde{f} - \overline{\rho}\,\overline{\frac{1}{\rho}\frac{\partial p u_i}{\partial x_i}\middle|\mathbf{\Psi}}\,\widetilde{f} + \frac{\partial \overline{p}\widetilde{u}_i}{\partial x_i}\widetilde{f}\right.\\ &\left.+\overline{\rho}\,\overline{\frac{1}{\rho}\frac{\partial \tau_{ij}u_j}{\partial x_i}\middle|\mathbf{\Psi}}\,\widetilde{f} - \frac{\partial \widetilde{\tau}_{ij}\widetilde{u}_j}{\partial x_i}\widetilde{f}\right)\\ &-\frac{\partial}{\partial d}\left(-\overline{\rho}\,\overline{\rho\frac{\partial u_i}{\partial x_i}\middle|\mathbf{\Psi}}\,\widetilde{f} + \overline{\rho}^2\frac{\partial \widetilde{u}_i}{\partial x_i}\widetilde{f}\right) - \frac{\partial}{\partial Z_\alpha}\left(\overline{\rho}\,\overline{\frac{1}{\rho}\frac{\partial J_{\alpha,i}}{\partial x_i}\middle|\mathbf{\Psi}}\,\widetilde{f} - \frac{\partial \widetilde{J}_{\alpha,i}}{\partial x_i}\widetilde{f}\right)\end{aligned} \tag{3.30}$$

It should be highlighted that the source term here is exactly closed together with the convective term. No approximation is performed for these closures, as the PDF sample

space variables allow to determine the entire source and convective terms. The unclosed conditional terms still require modelling though. The simplified Langevin model [68] is used to close the unknown terms for the velocity and density part:

$$\begin{aligned}
&-\frac{\partial}{\partial v_i}\left(-\overline{\rho}\,\overline{\frac{1}{\rho}\frac{\partial p}{\partial x_i}\middle|\boldsymbol{\Psi}}\;\widetilde{f}+\frac{\partial \overline{p}}{\partial x_i}\widetilde{f}+\overline{\rho}\,\overline{\frac{1}{\rho}\frac{\partial \tau_{ij}}{\partial x_i}\middle|\boldsymbol{\Psi}}\;\widetilde{f}-\frac{\partial \widetilde{\tau}_{ij}}{\partial x_i}\widetilde{f}\right)\\
&-\frac{\partial}{\partial d}\left(-\overline{\rho}\,\overline{\rho\frac{\partial u_i}{\partial x_i}\middle|\boldsymbol{\Psi}}\;\widetilde{f}+\overline{\rho}^2\frac{\partial \widetilde{u}_i}{\partial x_i}\widetilde{f}\right)\approx\\
&-\frac{\partial}{\partial v_i}\left(\overline{\rho}G_{ij}\left(v_j-\widetilde{u}_j\right)\widetilde{f}\right)+\frac{\partial^2}{\partial v_i\partial v_i}\left(\frac{1}{2}C_0\epsilon_{sgs}\widetilde{f}\right)
\end{aligned}\tag{3.31}$$

The Langevin model of Delarue and Pope [20] could be used to improve the accuracy and account for extra effects of compressibility, such as in the density part. However, the simplified Langevin model has been chosen because of its simple implementation and widespread use within combustion. The tensor G_{ij} is then defined as:

$$G_{ij}=-\frac{\epsilon_{sgs}}{k_{sgs}}\left(\frac{1}{2}+\frac{3}{4}C_0\right)\delta_{ij}\tag{3.32}$$

where k_{sgs} and ϵ_{sgs} are the subgrid kinetic energy and the dissipation of the subgrid kinetic energy, respectively. The IEM micromixing model [71] is selected to close the remaining unknown terms on the total energy and mass fractions part:

$$\begin{aligned}
&-\frac{\partial}{\partial \zeta}\left(\overline{\rho}\,\overline{\frac{1}{\rho}\frac{\partial q_i}{\partial x_i}\middle|\boldsymbol{\Psi}}\;\widetilde{f}-\frac{\partial \widetilde{q}_i}{\partial x_i}\widetilde{f}-\overline{\rho}\,\overline{\frac{1}{\rho}\frac{\partial p u_i}{\partial x_i}\middle|\boldsymbol{\Psi}}\;\widetilde{f}+\frac{\partial \overline{p}\widetilde{u}_i}{\partial x_i}\widetilde{f}\right.\\
&\left.+\overline{\rho}\,\overline{\frac{1}{\rho}\frac{\partial \tau_{ij}u_j}{\partial x_i}\middle|\boldsymbol{\Psi}}\;\widetilde{f}-\frac{\partial \widetilde{\tau}_{ij}\widetilde{u}_j}{\partial x_i}\widetilde{f}\right)-\frac{\partial}{\partial Z_\alpha}\left(\overline{\rho}\,\overline{\frac{1}{\overline{\rho}}\frac{\partial J_{\alpha,i}}{\partial x_i}\middle|\boldsymbol{\Psi}}\;\widetilde{f}-\frac{\partial \widetilde{J}_{\alpha,i}}{\partial x_i}\widetilde{f}\right)\approx\\
&-\frac{\partial}{\partial \zeta}\left(-\frac{1}{2}C_{e_t}\frac{\epsilon_{sgs}}{k_{sgs}}\overline{\rho}\left(\zeta-\widetilde{e}_t\right)\widetilde{f}\right)-\frac{\partial}{\partial Z_\alpha}\left(-\frac{1}{2}C_{Y_\alpha}\frac{\epsilon_{sgs}}{k_{sgs}}\overline{\rho}\left(Z_\alpha-\widetilde{Y}_\alpha\right)\widetilde{f}\right)
\end{aligned}\tag{3.33}$$

and the closed LES-PDF transport equation is therefore:

$$\begin{aligned}
&\frac{\partial \overline{\rho}\widetilde{f}}{\partial t} + \frac{\partial \overline{\rho} v_i \widetilde{f}}{\partial x_i} = -\frac{\partial}{\partial d}\left(-\overline{\rho}^2 \frac{\partial \widetilde{u}_i}{\partial x_i}\widetilde{f}\right) \\
&- \frac{\partial}{\partial Z_\alpha}\left(\frac{\partial \widetilde{J}_{\alpha,i}}{\partial x_i}\widetilde{f} + \overline{\rho} S_\alpha\left(\mathbf{\Phi}\right)\widetilde{f} - \frac{1}{2} C_{Y_\alpha}\frac{\epsilon}{k}\overline{\rho}\left(Z_\alpha - \widetilde{Y}_\alpha\right)\widetilde{f}\right) \\
&- \frac{\partial}{\partial v_i}\left(-\frac{\partial \overline{p}}{\partial x_i}\widetilde{f} + \frac{\partial \widetilde{\tau}_{ij}}{\partial x_i}\widetilde{f} + \overline{\rho} G_{ij}\left(v_j - \widetilde{u}_j\right)\widetilde{f}\right) + \frac{\partial^2}{\partial v_i \partial v_i}\left(\frac{1}{2} C_0 \epsilon_{sgs}\widetilde{f}\right) \\
&- \frac{\partial}{\partial \zeta}\left(\frac{\partial \widetilde{q}_i}{\partial x_i}\widetilde{f} - \frac{\partial \overline{p}\widetilde{u}_i}{\partial x_i}\widetilde{f} + \frac{\partial \widetilde{\tau}_{ij}\widetilde{u}_j}{\partial x_i}\widetilde{f} - \frac{1}{2} C_{e_t}\frac{\epsilon_{sgs}}{k_{sgs}}\overline{\rho}\left(\zeta - \widetilde{e}_t\right)\widetilde{f}\right)
\end{aligned} \tag{3.34}$$

The chosen solution method is also the Eulerian stochastic fields. The equations are derived using the characteristics method for the Lagrangian formulation, as in Soulard and Sabel'nikov [103]. Equation (3.34) is recast using the filtered mass density function definition $\widetilde{\mathscr{F}}(d, \boldsymbol{v}, \zeta, \boldsymbol{Z}, \boldsymbol{x}; t) = \overline{\rho}(\boldsymbol{x}, t)\widetilde{f}(d, \boldsymbol{v}, \zeta, \boldsymbol{Z}; \boldsymbol{x}, t)$ [111]:

$$\begin{aligned}
&\frac{\partial \widetilde{\mathscr{F}}}{\partial t} + \frac{\partial v_i \widetilde{\mathscr{F}}}{\partial x_i} = -\frac{\partial}{\partial d}\left(-\overline{\rho}\frac{\partial \widetilde{u}_i}{\partial x_i}\widetilde{\mathscr{F}}\right) \\
&- \frac{\partial}{\partial Z_\alpha}\left(\frac{1}{\overline{\rho}}\frac{\partial \widetilde{J}_{\alpha,i}}{\partial x_i}\widetilde{\mathscr{F}} + S_\alpha\left(\mathbf{\Phi}\right)\widetilde{\mathscr{F}} - \frac{1}{2} C_{Y_\alpha}\frac{\epsilon_{sgs}}{k_{sgs}}\left(Z_\alpha - \widetilde{Y}_\alpha\right)\widetilde{\mathscr{F}}\right) \\
&- \frac{\partial}{\partial v_i}\left(-\frac{1}{\overline{\rho}}\frac{\partial \overline{p}}{\partial x_i}\widetilde{\mathscr{F}} + \frac{1}{\overline{\rho}}\frac{\partial \widetilde{\tau}_{ij}}{\partial x_i}\widetilde{\mathscr{F}} + G_{ij}\left(v_j - \widetilde{u}_j\right)\widetilde{\mathscr{F}}\right) + \frac{\partial^2}{\partial v_i \partial v_i}\left(\frac{1}{2}\frac{C_0 \epsilon_{sgs}}{\overline{\rho}}\widetilde{\mathscr{F}}\right) \\
&- \frac{\partial}{\partial \zeta}\left(\frac{1}{\overline{\rho}}\frac{\partial \widetilde{q}_i}{\partial x_i}\widetilde{\mathscr{F}} - \frac{1}{\overline{\rho}}\frac{\partial \overline{p}\widetilde{u}_i}{\partial x_i}\widetilde{\mathscr{F}} + \frac{1}{\overline{\rho}}\frac{\partial \widetilde{\tau}_{ij}\widetilde{u}_j}{\partial x_i}\widetilde{\mathscr{F}} - \frac{1}{2} C_{e_t}\frac{\epsilon_{sgs}}{k_{sgs}}\left(\zeta - \widetilde{e}_t\right)\widetilde{\mathscr{F}}\right)
\end{aligned} \tag{3.35}$$

The Lagrangian stochastic equations equivalent to the Fokker-Planck Equation (3.35) are directly obtained:

$$\mathrm{d}X^+ = U_i^+ \,\mathrm{d}t \tag{3.36}$$

$$\mathrm{d}\rho^+ = -\overline{\rho}\frac{\partial \widetilde{u}_i}{\partial x_i}\,\mathrm{d}t \tag{3.37}$$

$$\mathrm{d}U_i^+ = -\frac{1}{\overline{\rho}}\frac{\partial \overline{p}}{\partial x_i}\,\mathrm{d}t + \frac{1}{\overline{\rho}}\frac{\partial \widetilde{\tau}_{ij}}{\partial x_i}\,\mathrm{d}t + G_{ij}\left(U_j^+ - \widetilde{u}_j\right)\mathrm{d}t + \sqrt{C_0\frac{\epsilon_{sgs}}{\overline{\rho}}}\,\mathrm{d}W_i \tag{3.38}$$

$$\mathrm{d}Y_\alpha^+ = \frac{1}{\overline{\rho}}\frac{\partial \widetilde{J}_{\alpha,i}}{\partial x_i}\,\mathrm{d}t + S_\alpha\left(\mathbf{\Psi}\right)\mathrm{d}t - \frac{1}{2} C_{Y_\alpha}\frac{\epsilon_{sgs}}{k_{sgs}}\left(Y_\alpha^+ - \widetilde{Y}_\alpha\right)\mathrm{d}t \tag{3.39}$$

$$\mathrm{d}e_t^+ = \frac{1}{\overline{\rho}}\frac{\partial \widetilde{q}_i}{\partial x_i}\,\mathrm{d}t - \frac{1}{\overline{\rho}}\frac{\partial \overline{p}\widetilde{u}_i}{\partial x_i}\,\mathrm{d}t + \frac{1}{\overline{\rho}}\frac{\partial \widetilde{\tau}_{ij}\widetilde{u}_j}{\partial x_i}\,\mathrm{d}t - \frac{1}{2}C_{e_t}\frac{\epsilon_{sgs}}{k_{sgs}}\left(e_t^+ - \widetilde{e}_t\right)\mathrm{d}t \tag{3.40}$$

The previous equations results in the following Fokker-Planck equation for the Lagrangian FMDF $\mathscr{F}^*(d, \boldsymbol{v}, \zeta, \boldsymbol{Z}, \boldsymbol{x}; t)$:

$$\begin{aligned}
&\frac{\partial \mathscr{F}^*}{\partial t} + \frac{\partial v_i \mathscr{F}^*}{\partial x_i} = -\frac{\partial}{\partial d}\left(-\overline{\rho}\frac{\partial \widetilde{u}_i}{\partial x_i}\mathscr{F}^*\right) \\
&- \frac{\partial}{\partial Z_\alpha}\left(\frac{1}{\overline{\rho}}\frac{\partial \widetilde{J}_{\alpha,i}}{\partial x_i}\mathscr{F}^* + S_\alpha\left(\boldsymbol{\Psi}\right)\mathscr{F}^* - \frac{1}{2}C_{Y_\alpha}\frac{\epsilon_{sgs}}{k_{sgs}}\left(Z_\alpha - \widetilde{Y}_\alpha\right)\mathscr{F}^*\right) \\
&- \frac{\partial}{\partial v_i}\left(-\frac{1}{\overline{\rho}}\frac{\partial \overline{p}}{\partial x_i}\mathscr{F}^* + \frac{1}{\overline{\rho}}\frac{\partial \widetilde{\tau}_{ij}}{\partial x_i}\mathscr{F}^* + G_{ij}\left(v_j - \widetilde{u}_j\right)\mathscr{F}^*\right) + \frac{\partial^2}{\partial v_i \partial v_i}\left(\frac{1}{2}C_0\frac{\epsilon_{sgs}}{\overline{\rho}}\mathscr{F}^*\right) \\
&- \frac{\partial}{\partial \zeta}\left(\frac{1}{\overline{\rho}}\frac{\partial \widetilde{q}_i}{\partial x_i}\mathscr{F}^* - \frac{1}{\overline{\rho}}\frac{\partial \overline{p}\widetilde{u}_i}{\partial x_i}\mathscr{F}^* + \frac{1}{\overline{\rho}}\frac{\partial \widetilde{\tau}_{ij}\widetilde{u}_j}{\partial x_i}\mathscr{F}^* - \frac{1}{2}C_{e_t}\frac{\epsilon_{sgs}}{k_{sgs}}\left(\zeta - \widetilde{e}_t\right)\mathscr{F}^*\right)
\end{aligned} \tag{3.41}$$

where the FMDF can be recovered throught the average of $\mathscr{F}^*$:

$$\widetilde{\mathscr{F}}(r, v_i, \zeta, Z_\alpha, \boldsymbol{x}; t) = \langle \mathscr{F}^*(r, v_i, \zeta, Z_\alpha, \boldsymbol{x}; t)\rangle \tag{3.42}$$

In order to solve using Eulerian stochastic equations, the Lagrangian equations can be seen as the stochastic characteristics of the Eulerian stochastic partial differential equations (SPDEs) [103]. The n^{th}-set of Eulerian stochastic fields is:

$$\frac{\partial \varrho^n}{\partial t} + \mathscr{U}_i^n\frac{\partial \varrho^n}{\partial x_i} = -\overline{\rho}\frac{\partial \widetilde{u}_i}{\partial x_i} \tag{3.43}$$

$$\frac{\partial \mathscr{U}_i^n}{\partial t} + \mathscr{U}_j^n\frac{\partial \mathscr{U}_i^n}{\partial x_j} = -\frac{1}{\overline{\rho}}\frac{\partial \overline{p}}{\partial x_i} + \frac{1}{\overline{\rho}}\frac{\partial \widetilde{\tau}_{ij}}{\partial x_i} + G_{ij}\left(\mathscr{U}_j^n - \widetilde{u}_j\right) + \sqrt{C_0\frac{\epsilon_{sgs}}{\overline{\rho}}}\frac{\mathrm{d}W_i^n}{\mathrm{d}t} \tag{3.44}$$

$$\frac{\partial \mathscr{Y}_\alpha^n}{\partial t} + \mathscr{U}_i^n\frac{\partial \mathscr{Y}_\alpha^n}{\partial x_i} = \frac{1}{\overline{\rho}}\frac{\partial \widetilde{J}_{\alpha,i}}{\partial x_i} + S_\alpha\left(\boldsymbol{\Psi}\right) - \frac{1}{2}C_{Y_\alpha}\frac{\epsilon_{sgs}}{k_{sgs}}\left(\mathscr{Y}_\alpha^n - \widetilde{Y}_\alpha\right) \tag{3.45}$$

$$\frac{\partial \mathscr{E}_t^n}{\partial t} + \mathscr{U}_i^n\frac{\partial \mathscr{E}_t^n}{\partial x_i} = \frac{1}{\overline{\rho}}\frac{\partial \widetilde{q}_i}{\partial x_i} - \frac{1}{\overline{\rho}}\frac{\partial \overline{p}\widetilde{u}_i}{\partial x_i} + \frac{1}{\overline{\rho}}\frac{\partial \widetilde{\tau}_{ij}\widetilde{u}_j}{\partial x_i} - \frac{1}{2}C_{e_t}\frac{\epsilon_{sgs}}{k_{sgs}}\left(\mathscr{E}_t^n - \widetilde{e}_t\right) \tag{3.46}$$

where $\varrho^n(\boldsymbol{x},t)$, $\mathscr{U}_i{}^n(\boldsymbol{x},t)$, $\mathscr{Y}_\alpha^n(\boldsymbol{x},t)$ and $\mathscr{E}_t^n(\boldsymbol{x},t)$ are the stochastic density, velocity, mass fraction and total energy of the n^{th} set of Eulerian stochastic fields. However, these set of equations does not ensure that each realisation respects continuity. In addition, as depicted in Petrova [105], the characteristics of these equations may cross, which results in numerical shocks if a conventional numerical scheme is used. Two further approximations are proposed in this work. The first is to substitute the pressure terms by the stochastic pressure field, $\mathscr{P}(\boldsymbol{x},t)$, instead of the filtered pressure, $\overline{p}$, neglecting subgrid pressure fluctuations. This results in a different momentum equation from the Burgers' equation, preventing the occurrence of numerical shocks. The stochastic pressure can be directly obtained from stochastic variables $\mathscr{P} \equiv \mathscr{P}(\varrho, \mathscr{U}_i, \mathscr{E}_t, \mathscr{Y}_\alpha)$ and present the same properties of the real pressure field.

The other approximation used is to neglect the stochastic difference on the right hand side of the continuity equation if written on conservative form, so it can ensure mass conservation for all set of stochastic fields. This approximation does not affect the first-moments and is exact if the density is constant. Although this approximation can be avoided in a Lagrangian framework, the stochastic PDEs are aimed to be coupled with a Eulerian solver. This numerical approximation can be understood as an additional force to prevent the fields from severe separation by "adding" or "removing" stochastic density. The proposed set of Eulerian stochastic PDEs is:

$$\frac{\partial \varrho^n}{\partial t} + \mathscr{U}_i{}^n \frac{\partial \varrho^n}{\partial x_i} = -\varrho^n \frac{\partial \mathscr{U}_i^n}{\partial x_i} \tag{3.47}$$

$$\frac{\partial \mathscr{U}_i^n}{\partial t} + \mathscr{U}_j{}^n \frac{\partial \mathscr{U}_i^n}{\partial x_j} = -\frac{1}{\varrho^n}\frac{\partial \mathscr{P}^n}{\partial x_i} + \frac{1}{\overline{\rho}}\frac{\partial \widetilde{\tau}_{ij}}{\partial x_i} + G_{ij}\left(\mathscr{U}_j^n - \widetilde{u}_j\right) + \sqrt{C_0 \frac{\epsilon_{sgs}}{\overline{\rho}}}\frac{\mathrm{d}W_i^n}{\mathrm{d}t} \tag{3.48}$$

$$\frac{\partial \mathscr{Y}_\alpha^n}{\partial t} + \mathscr{U}_i{}^n \frac{\partial \mathscr{Y}_\alpha^n}{\partial x_i} = \frac{1}{\overline{\rho}}\frac{\partial \widetilde{J}_{\alpha,i}}{\partial x_i} + S_\alpha\left(\boldsymbol{\Psi}\right) - \frac{1}{2}C_{Y_\alpha}\frac{\epsilon_{sgs}}{k_{sgs}}\left(\mathscr{Y}_\alpha^n - \widetilde{Y}_\alpha\right) \tag{3.49}$$

$$\frac{\partial \mathscr{E}_t^n}{\partial t} + \mathscr{U}_i{}^n \frac{\partial \mathscr{E}_t^n}{\partial x_i} = \frac{1}{\overline{\rho}}\frac{\partial \widetilde{q}_i}{\partial x_i} - \frac{1}{\overline{\rho}}\frac{\partial \overline{p}\widetilde{u}_i}{\partial x_i} + \frac{1}{\overline{\rho}}\frac{\partial \widetilde{\tau}_{ij}\widetilde{u}_j}{\partial x_i} - \frac{1}{2}C_{e_t}\frac{\epsilon_{sgs}}{k_{sgs}}\left(\mathscr{E}_t^n - \widetilde{e}_t\right) \tag{3.50}$$

The stochastic PDEs can be recast in a conservative formulation:

$$\frac{\mathrm{d}\varrho^n}{\mathrm{d}t} + \frac{\partial \varrho^n \mathscr{U}_i^n}{\partial x_i} = 0 \tag{3.51}$$

$$\frac{\mathrm{d}\varrho^n \mathscr{U}_i^n}{\mathrm{d}t} + \frac{\partial \varrho^n \mathscr{U}_j^n \mathscr{U}_i^n}{\partial x_j} = -\frac{\partial \mathscr{P}^n}{\partial x_i} + \frac{\varrho^n}{\overline{\rho}}\frac{\partial \widetilde{\tau}_{ij}}{\partial x_i} + \varrho^n G_{ij}\left(\mathscr{U}_j^n - \widetilde{u}_j\right) + \varrho^n \sqrt{C_0 \frac{\epsilon_{sgs}}{\overline{\rho}}}\frac{\mathrm{d}W_i^n}{\mathrm{d}t} \tag{3.52}$$

$$\frac{\mathrm{d}\varrho^n \mathscr{Y}_\alpha^n}{\mathrm{d}t} + \frac{\partial \varrho^n \mathscr{U}_i^n \mathscr{Y}_\alpha^n}{\partial x_i} = \frac{\varrho^n}{\overline{\rho}}\frac{\partial \widetilde{J}_{\alpha,i}}{\partial x_i} + \varrho^n S_\alpha\left(\mathbf{\Psi}\right) - \frac{1}{2} C_{Y_\alpha}\frac{\epsilon_{sgs}}{k_{sgs}}\varrho^n\left(\mathscr{Y}_\alpha^n - \widetilde{Y}_\alpha\right) \tag{3.53}$$

$$\frac{\mathrm{d}\varrho^n \mathscr{E}_t^n}{\mathrm{d}t} + \frac{\partial \varrho^n \mathscr{U}_i^n \mathscr{E}_t^n}{\partial x_i} = \frac{\varrho^n}{\overline{\rho}}\frac{\partial \widetilde{q}_i}{\partial x_i} - \frac{\varrho^n}{\overline{\rho}}\frac{\partial \overline{p}\widetilde{u}_i}{\partial x_i} + \frac{\varrho^n}{\overline{\rho}}\frac{\partial \widetilde{\tau}_{ij}\widetilde{u}_j}{\partial x_i} - \frac{1}{2} C_{e_t}\frac{\epsilon_{sgs}}{k_{sgs}}\varrho^n\left(\mathscr{E}_t^n - \widetilde{e}_t\right) \tag{3.54}$$

The employed closure relation for the dissipation of the subgrid kinetic energy, ϵ_{sgs}, is the following[2]:

$$\epsilon_{sgs} = C_\epsilon k_{sgs}^{3/2}/\Delta; \tag{3.55}$$

where the constant C_ϵ is equal to 1.05. The micromixing constants C_{Y_α} and C_{e_t} are equal to 2 and the Langevin constant is set to 2.1. The subgrid kinetic energy, k_{sgs}, can be directly obtained from the stochastic fields information:

$$k_{sgs} = \frac{1}{2}\left(\frac{1}{N_f}\sum_{n=1}^{N_f}(\mathscr{U}_i^n - \widetilde{u}_i)^2\right) \tag{3.56}$$

Depending on the initial condition, all velocity fields may share the same initial value, and the subgrid kinetic energy would be zero and the dissipation as well. The Yoshizawa model, Eq.(2.29) can be used to obtain a modelled k_{sgs} at $t = 0$ and trigger turbulence. Alternatively, the fields may possess variance as a initial condition, therefore imposing different values for each field. The energy spectra can also be imposed for a determined

[2]See in Chapter 2.

flow field with initial subgrid reproduced by the stochastic fields.

At last, the filtered variables can be obtained from the average of the Eulerian stochastic fields. For a variable $Q(\boldsymbol{x}, t)$, it is possible to recover the filtered and the Favre-filtered values:

$$\overline{Q} = \frac{1}{N_f} \sum_{n=1}^{N_f} Q^n; \qquad \widetilde{Q} = \frac{\sum_{n=1}^{N_f} \varrho^n Q^n}{\sum_{n=1}^{N_f} \varrho^n} \tag{3.57}$$

The developed Eulerian stochastic differential equations are equivalent to Eq.(3.34) with mild assumptions. The continuity and momentum equations resemble those of Azarnykh *et al.* [107]. This set of equations also does not generate the numerical shocks predicted in Petrova [105] if a conventional discretisation scheme is employed. Most important, the convective and source terms are closed and do not require any modelling, improving the numerical accuracy of supersonic combustion and other high-speed reacting flows.

3.4 CompReal solver

The proposed equations have been implemented in CompReal, an in-house Fortran-based DNS finite-difference compressible code. In the development of this work, the code has been extended to large eddy simulation and reactive flows environment. The stochastic equations have been implemented within CompReal solution algorithm and are summarised in the following sections.

3.4.1 Discretisation schemes

Accurate discretisation schemes are of considerable importance in compressible solvers. The spatial discretisation schemes employed in CompReal are derived from two families of schemes. One is the dispersion-relation-preserving (DRP) scheme [143], which in CompReal is set to fourth order of accuracy while using a 13-point stencil (unless stated otherwise). The DRP scheme is a high-order, low dispersive and low dissipative explicit scheme [144]. The classical finite difference uses the following approximation on the node l, considering M values of f to the right and N values to the left:

$$\left(\frac{\partial f}{\partial x}\right)_l \approx \frac{1}{\Delta x}\sum_{j=-N}^{M} a_j f_{l+j} \tag{3.58}$$

The coefficients a_j are usually determined by expanding the derivative in Taylor series. The main idea of the DRP discretisation is to minimise the error between the Fourier transforms of the analytical derivative and the numerical one by optimising the finite-difference coefficients. By taking the Fourier transform of Eq.(3.58):

$$\begin{aligned}\int_{-\infty}^{+\infty}\left(\frac{\partial f}{\partial x}\right)_l e^{-i\lambda x}\,\mathrm{d}x &\approx \int_{-\infty}^{+\infty}\frac{1}{\Delta x}\sum_{j=-N}^{M} a_j f_{l+j} e^{-i\lambda x}\,\mathrm{d}x \\ i\lambda f(\lambda) &\approx \left(\frac{1}{\Delta x}\sum_{j=-N}^{M} a_j e^{-i\lambda j\Delta x}\right) f(\lambda) = i\kappa f(\lambda)\end{aligned} \tag{3.59}$$

where the quantity κ is equal to:

$$\kappa = \frac{-i}{\Delta x} \sum_{j=-N}^{M} a_j e^{-ij\lambda\Delta x} \tag{3.60}$$

and must be set as close as the real λ as possible. The integrated error therefore must be minimised:

$$\mathscr{E} = \int_{-\pi/2}^{\pi/2} |\lambda\Delta x - \kappa\Delta x|^2 \, \mathrm{d}(\lambda\Delta x) \tag{3.61}$$

and appropriate coefficients a_j arise to minimise the function $\mathscr{E}$. The coefficients depend on the chosen discretisation order and a few examples can be found on [143] and [144]. The scheme therefore preserves the low dissipation of the centred difference schemes. It is also low dispersive, since the wave speeds of the numerical discretisation are preserved the most in comparison to the wave speed of the analytical partial derivative.

The DRP scheme is used to discretise the convective derivatives. The modelling of acoustics is not the main focus of this work although it is useful to employ a spatial discretisation scheme that reduces the spurious numerical oscillations that may be introduced by the high-order DRP scheme.

The Harten-Lax-van Leer-Contact total variation diminishing (HLLC-TVD) solver of Toro *et al.* [145] is also employed in CompReal for the convective terms in regions of sharp gradients to reduce the instability and increase the robustness of the code. The HLLC solver recasts the differential equations into convective form. For instance, considering the Euler equations for an one-dimensional and single component flow:

$$\frac{\partial \boldsymbol{U}}{\partial t} + \frac{\partial \boldsymbol{F}(\boldsymbol{U})}{\partial x} = 0 \tag{3.62}$$

where $\boldsymbol{U}$ represent the conserved variables and $\boldsymbol{F}(\boldsymbol{U})$ the respective fluxes:

$$\boldsymbol{U} = [\rho, \rho u, \rho e_t]^T ; \qquad \boldsymbol{F}(\boldsymbol{U}) = \left[\rho u, \rho u^2, \rho u(e_t + p)\right]^T \tag{3.63}$$

The integral form is:

$$\oint \left(\boldsymbol{U}\, \mathrm{d}x - \boldsymbol{F}(\boldsymbol{U})\, \mathrm{d}t \right) = 0 \tag{3.64}$$

By considering a time-marching procedure in a control volume of dimensions Δx and Δt, the integral over this volume centred in the point i is:

$$\boldsymbol{U}_i^{n+1} = \boldsymbol{U}_i^n - \frac{\Delta t}{\Delta x} \left(\boldsymbol{F}_{i+1/2} - \boldsymbol{F}_{i-1/2} \right) \tag{3.65}$$

and it is necessary to define the fluxes $\boldsymbol{F}_{i+1/2}$ and $\boldsymbol{F}_{i-1/2}$. These fluxes are determined from the Harten-Lax-van Leer contact solver, which is a improvement to the HLL solver by considering the contact surface into the wave pattern [145]. The second order total variation diminishing (TVD) limiter scheme is used to calculate the values at $i+1/2$ and $i-1/2$ necessary to obtain the fluxes.

The convective terms are therefore discretised through a hybrid DRP/HLLC-TVD scheme. The coupling is perfomed using a sensor similar to the one of Ferrer [26]. Considering a function $Q \in [0, \infty)$ centred at a node i on x-direction, the sensor $\mathscr{S}$ returns two possible values:

$$\mathscr{S} = \begin{cases} 1, & \text{if } |Q_{i+1} - Q_{i-1}| > C_{Hy} Q_i \\ 0, & \text{otherwise} \end{cases} \tag{3.66}$$

where C_{Hy} is a coefficient that needs to be specified, usually taken as 0.15. This condition is searched in density, pressure and mass fractions. If the condition is met for any of these properties, then the sensor is activated. If $\mathscr{S} = 1$, then a sharp gradient is detected and the HLLC-TVD discretisation is employed. Otherwise, the DRP discretisation is used:

$$\left(\frac{\partial f}{\partial x} \right)_i \approx \mathscr{S} \frac{1}{\Delta x} \left(f(Q)_{i+1/2} - f(Q)_{i-1/2} \right) + (1 - \mathscr{S}) \frac{1}{\Delta x} \sum_{j=-N}^{M} a_j f_{i+j} \tag{3.67}$$

This scheme is therefore second order accurate in sharp gradient regions and at least fourth order accurate in regions without shocks.

The remaining spatial derivatives are discretised with a fourth order classical central differences, as in Eq.(3.58). This discretisation is employed mostly in viscous terms,

where it is expected to introduce stability and not to play a major role in supersonic combustion at high Reynolds number.

The temporal integration is performed using a third order accurate explicit deterministic Runge-Kutta multistep. This low-storage scheme requires only two storage locations and uses three inner steps to advance to the next time step. For each inner step, the following algorithm is executed [146]:

$$\begin{aligned} (\boldsymbol{U})_2^n &= (\boldsymbol{U})_1^n \\ (\boldsymbol{U})_1^{n+1} &= (\boldsymbol{U})_1^n + C_2^n \Delta t \boldsymbol{R}\,(\boldsymbol{U})_1^n \\ (\boldsymbol{U})_2^{n+1} &= (\boldsymbol{U})_2^n + C_1^n \Delta t \boldsymbol{R}\,(\boldsymbol{U})_1^n \end{aligned} \tag{3.68}$$

where the subindex 1 and 2 mean the different storage positions and $\boldsymbol{R}\,(\boldsymbol{U})$ is the vector representing all the terms on the right-hand side of the Eulerian stochastic equations. The constants C_1^n and C_2^n are chosen to be 2/3 and 1/4 for the first inner step, 5/12 and 3/20 for the second and 3/5 and 3/5 for the third, respectively.

The use of a third-order deterministic Runge-Kutta time scheme does not ensure the same accuracy when applied to stochastic differential partial equations. In fact, there are extra derivatives that must be considered because of the Wiener term, which are not considered here. The scheme is therefore as accurate as a weak first order scheme and strong 0.5 order for the stochastic equations, but keeps the third-order accuracy for the deterministic equations. For this approach to be consistent, the Wiener term $\mathrm{d}W_i/\,\mathrm{d}t$ remains constant within the inner steps of the Runge-Kutta integrator, i.e.: the random numbers are only generated at the beginning of the time step.

The Euler-Maruyama scheme is an explicit stochastic first order temporal integrator that has been usually employed with the stochastic fields approach in low Mach number solvers [62, 128]. However, this discretisation is unconditional unstable if applied to all equation terms and must be coupled with other stable integrator at least for the deterministic terms to prevent spurious oscillations. The chosen explicit Runge-Kutta method is conditionally stable and if applied to the stochastic term it reverts to the Euler-Maruyama scheme in terms of accuracy.

In order to remove grid-to-grid oscillations, a selective explicit filter is also applied [144]. The explicit filter is applied only in regions where the DRP discretisation is used, to prevent over-dissipation when the HLLC-TVD is employed. The filtering scheme implemented in CompReal uses a 13-point stencil and it is eighth order accurate.

3.4.2 Reaction term

The chemical mechanism is a very stiff system and requires implicit integration to be solved even using small time steps to retain stability. The Newton-Raphson method is used to obtain the reaction terms $S(\overline{p}, \boldsymbol{\psi})$ and $S(\boldsymbol{\Psi})$ for the joint scalar PDF and velocity-scalar PDF, respectively. By definition, the source term is a temporal derivative of the chemical species and it can be rewritten in vectorial format to include all species:

$$\frac{\partial \boldsymbol{Y}}{\partial t} = \boldsymbol{S}; \quad \boldsymbol{Y} = [\mathscr{Y}_1, \mathscr{Y}_2, ..., \mathscr{Y}_{N_s}]^T \tag{3.69}$$

and to solve this equation using an implicit approach, it is possible to use:

$$\boldsymbol{Y}^{n+1} = \boldsymbol{Y}^n + \boldsymbol{S}\Delta t \tag{3.70}$$

where n is the index for the inner time step and $\boldsymbol{S} = \boldsymbol{S}\left(\boldsymbol{Y}^{n+1}, \mathscr{H}^n, \overline{p}^n\right)$ for the scalar PDF and $\boldsymbol{S} = \boldsymbol{S}\left(\boldsymbol{Y}^{n+1}, \mathscr{H}^n, \mathscr{P}^n\right)$ for the velocity scalar PDF, where the enthalpy is obtained from the total energy and velocity. Since the variables to be integrated are the chemical species mass fractions, they are the only ones that need to be advanced in time. The enthalpy and pressure therefore are taken constant within Eq.(3.70).

Therefore, the evaluation of the source term requires the calculation of $\boldsymbol{Y}^{n+1}$. The Newton-Raphson method is used to to figure out the composition $\boldsymbol{Y}$ in the inner time step $n+1$ by defining the following function $f\colon \boldsymbol{Y} \mapsto \boldsymbol{Y}$:

$$f\left(\boldsymbol{Y}^{n+1}\right) = \boldsymbol{S}\left(\boldsymbol{Y}^{n+1}, ...\right) - \left(\frac{\boldsymbol{Y}^{n+1} - \boldsymbol{Y}^n}{\Delta t}\right) = \boldsymbol{0} \tag{3.71}$$

The idea of the Newton-Raphson method is to find which $\boldsymbol{Y}^{n+1}$ gives the root of $f\left(\boldsymbol{Y}^{n+1}\right)$.

The search through the values of $\boldsymbol{Y}^{n+1}$ is performed using the Taylor approximation on the function f:

$$f\left(\boldsymbol{Y}^{n+1}+\delta\boldsymbol{Y}^{n+1}\right)=f\left(\boldsymbol{Y}^{n+1}\right)+\frac{\partial f\left(\boldsymbol{Y}^{n+1}\right)}{\partial\boldsymbol{Y}^{n+1}}\delta\boldsymbol{Y}^{n+1} \tag{3.72}$$

where $\delta\boldsymbol{Y}^{n+1}$ is the differential increment in $\boldsymbol{Y}^{n+1}$ space and $\partial f\left(\boldsymbol{Y}^{n+1}\right)/\partial\boldsymbol{Y}^{n+1}$ is the Jacobian matrix:

$$\boldsymbol{J}=\frac{\partial f\left(\boldsymbol{Y}^{n+1}\right)}{\partial\boldsymbol{Y}^{n+1}}=\frac{\partial\boldsymbol{S}\left(\boldsymbol{Y}^{n+1},...\right)}{\partial\boldsymbol{Y}^{n+1}}-\frac{1}{\Delta t}\boldsymbol{I} \tag{3.73}$$

Knowing that $\delta\boldsymbol{Y}^{n+1}=\boldsymbol{Y}_{j+1}^{n+1}-\boldsymbol{Y}_{j}^{n+1}$, where the index j represents the Newton-Raphson step, it is possible to obtain the next value $j+1$ by setting Eq. (3.72) equals to zero:

$$\boldsymbol{Y}_{j+1}^{n+1}=\boldsymbol{Y}_{j}^{n+1}-\boldsymbol{J}_{j}^{-1}f\left(\boldsymbol{Y}_{j}^{n+1}\right) \tag{3.74}$$

The Jacobian matrix requires inversion which is done using linear algebra algorithms. Once $\boldsymbol{Y}^{n+1}$ is found, Equation 3.70 is used to obtain the reactive term on all the stochastic equations. The temporal integration is therefore partially explicit, since the reactive term is obtained implicitly. This does not affect, however, the accuracy of the Runge-Kutta solver, as it is still a deterministic term.

3.4.3 LES-PDF algorithm

The discretisation procedures described previously are coupled with the stochastic equations. For all Wiener processes, the derivative $\mathrm{d}W_i^n$ is approximated by $\mathrm{d}t^{1/2}\gamma$, where $\gamma=\{-1,1\}$ is a dichotomic vector [19], ensuring that $\langle\mathrm{d}W_i\rangle=0$. The dichotomic vector could be Gaussian, although it would require a large number of fields to guarantee that $\langle\mathrm{d}W_i\rangle=0$ and $\langle\mathrm{d}W_i\,\mathrm{d}W_j\rangle=\delta_{ij}\,\mathrm{d}t$.

The joint scalar PDF algorithm procedure is presented in Figure 3.1. It describes how the multi-step Runge-Kutta integration is performed. This algorithm is then executed three times, one for each inner Runge-Kutta step, to advance to the next time step. It should be highlighted the role of the LES solver, that solves Eqs.(2.16), (2.26), (2.33),

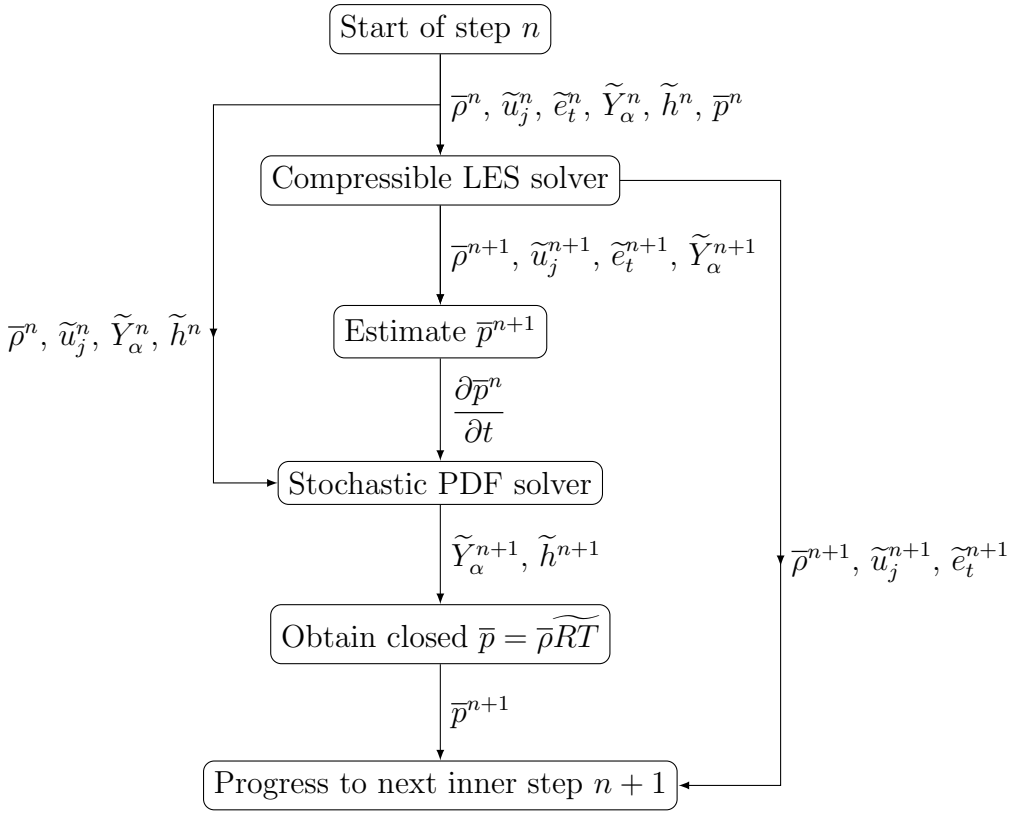

Figure 3.1: Algorithm proposed to couple the stochastic fields equations of the joint scalar PDF model with the compressible LES solver.

(2.35) and (2.39). This part generates a first estimate of the filtered pressure $\overline{p}^{n+1}$ neglecting the subgrid terms, which is crucial to obtain the temporal derivative of pressure required in the stochastic total enthalpy equation. The LES solver also generates the filtered density and velocity fields, used as input for the stochastic equations. The total energy equation, although redundant, is therefore solved here.

The stochastic PDF solver is responsible to advance the Runge-Kutta inner step for all stochastic equations. In this case, the stochastic PDEs for mass fractions, Eq. (3.13), and total enthalpy, Eq.(3.20). It also generates the filtered values $\widetilde{Y}_\alpha$ and $\widetilde{h}$ by taking the average of the stochastic fields. The filtered pressure $\overline{p}$ is recalculated afterwards without neglecting the subgrid part this time through $\overline{p} = \widetilde{\overline{\rho}RT}$.

The algorithm to solve the stochastic equations for the joint velocity-scalar PDF is simpler than for the joint scalar PDF. This is because of the Equations (3.51), (3.52), (3.53) and (3.54) do not require coupling from an external LES solver. Figure 3.2 presents this algorithm, where the stochastic PDF solver is responsible for integrating the stochas-

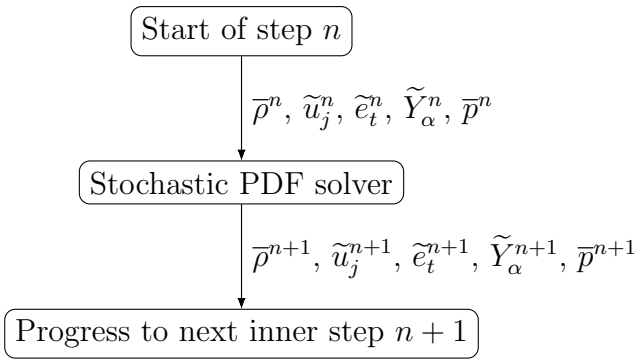

Figure 3.2: Algorithm proposed to solve the stochastic fields equations of the joint velocity-scalar PDF model.

tic equations and obtain the filtered and Favre-filtered variables at the end of each step.

3.4.4 Boundary conditions

For supersonic inlets, the boundary conditions can be completely specified. For zero-gradient configurations, the halo cells (auxiliary cells that extend the original domain beyond the boundary to ensure the conditions) are set equal to the first point on the mesh. The Navier-Stokes Characteristics Boundary Conditions (NSCBC) method, developed by Poinsot and Lele [147], has been the first choice for compressible reactive flows recently [26, 18] and is also implemented in CompReal. The NSCBC are very important for acoustics analysis and present an useful capability of damping unwanted pressure reflections for far-field boundary conditions.

However, the modelling of acoustics is not evaluated in this work. The first order boundary conditions are more robust and present higher stability than the NSCBC. They do not have a specific treatment to deal with pressure reflections, though. In CompReal the HLLC-TVD is specified to regions close to the boundaries, i.e.: the first and last 5% of the domain size in the direction of interest. In this way, spurious numerical oscillations and reflections are damped through the dissipative nature of the HLLC-TVD scheme.

For adiabatic wall boundaries, the velocity is specified and the remaining variables are set to zero gradients. Close to the wall the HLLC-TVD is used for the convective

terms, as it is a near-boundary region. The remaining derivatives, which are discretised with fourth order central differences, decrease their order as approaching to the wall, remaining centred. At the last node, first-order one-sided derivatives are employed.

3.4.5 Mesh generation and complex geometries

At the current state of the code, the mesh generation algorithm in CompReal allows structured meshes only. The meshes can be non-uniform though, using different functions to distribute the grid points accordingly. For instance, a exponential function ca be used to describe the x-coordinate points distribution, increasing the mesh density close to walls or to the center of the domain, or a combination of both, as shown in Figure 3.3.

The simulation of complex geometries, such as a scramjet, can be performed using the Immersed Boundary Condition (IBC) method [148]. In this method an arbitrary geometry is immersed into a structured mesh and the points close to boundary requires special

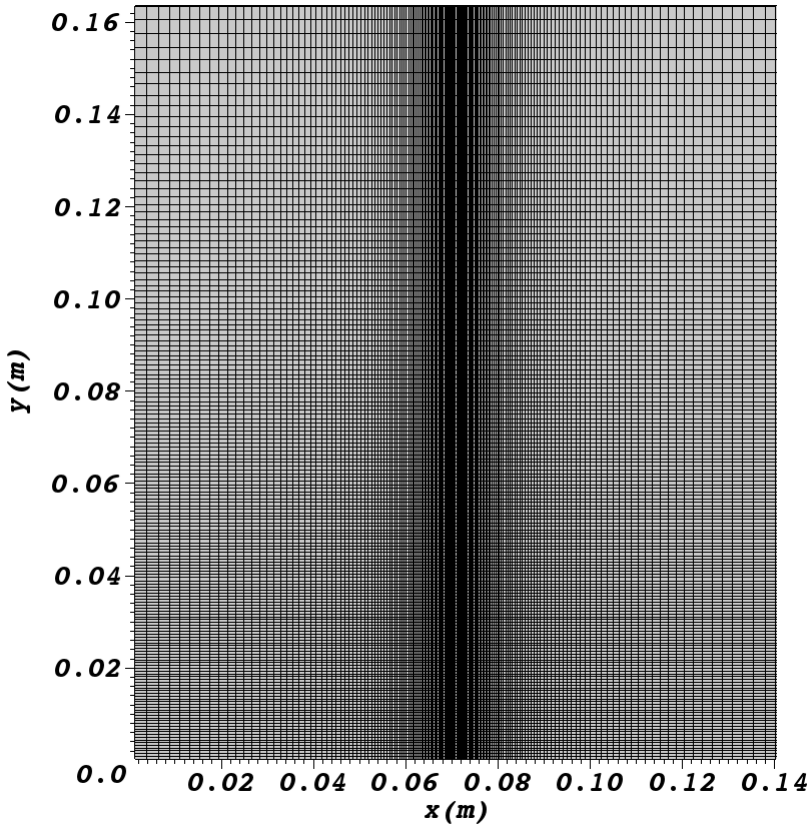

Figure 3.3: Example of mesh used in burners configurations. The centre of x-coordinate concentrate more points as well as the base of the geometry, y-coordinate, and near the burner.

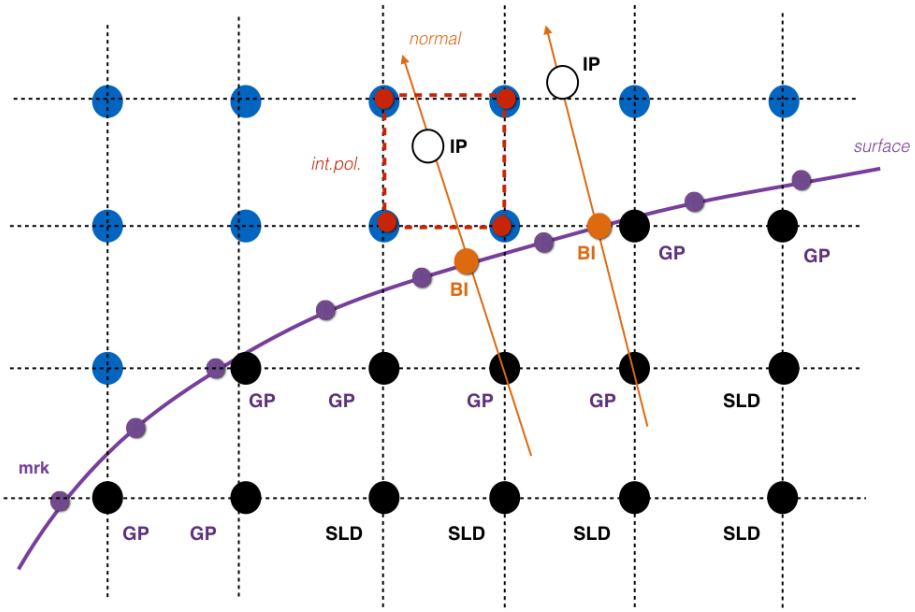

Figure 3.4: Immersed Boundary conditions method - Figure extracted from CompReal User & Developer manual [149].

treatment to reproduce the geometry surface. Figure 3.4 presents a surface immersed into an uniform grid. The method consists in the projection of the ghost points (GP) into the fluid region. The projected IP point requires interpolation from the resolved neighbor points to generate a value, and then calculate the boundary points (BI). The interpolated values are calculated using also a a second order TVD reconstruction scheme with the Van Leer limiter.

At last, the complex geometries are read in CompReal using the GNU Triangulated Surface (GTS) Library. This library transforms CAD/STL geometries into GTS files. These GTS files are used in CompReal to define the surfaces employed by the immersed boundary method. Therefore, complex geometries can be simulated using structured and Cartesian coordinates.

3.5 Summary

This chapter presents the derivation and formulation of the two set of Eulerian stochastic equations able to solve the joint scalar and joint velocity-scalar LES-PDF transport equation. The joint scalar approach has been developed in the recent literature for compressible flows using the approximation $S(\boldsymbol{\psi}, \overline{p})$. The developed formulation calculates the exact filtered pressure, which for this kind of PDF models had been only performed in Lagrangian framework. This potentially increases the accuracy of the joint scalar model, which may compensate the approximation on the source term. An algorithm has been developed to couple the Eulerian stochastic equations into a compressible LES solver.

The developed joint velocity-scalar PDF model is a new formulation, including the density and the total energy as sample variables, along with the velocity and mass fractions. The LES-PDF transport equation is solved using the Eulerian stochastic fields method, where the equations have been derived using the Lagrangian approach and the method of characteristics. Mild assumptions are considered for the stochastic characteristics not to cross and generate numerical shocks. A stochastic pressure, that has the same properties as the real pressure field, is proposed and used in the momentum equation, instead of the filtered pressure. The stochastic continuity equation also neglects possible stochastic mass source terms, which are purely numerical. This approximation can be interpreted as the inclusion of a non-specified additional model to compensate this source terms and ensure mass conservation.

The in-house finite-difference compressible code CompReal has also been presented, with its main capabilities described. The temporal integrator is the third order Runge-Kutta that reverts to a strong 0.5-order and weak first order because the high-order Wiener terms are not included. The conditionally stability of the Runge-Kutta schemes are preserved, though. The convective fluxes discretisation is performed using a hybrid fourth/second order DRP/HLLC-TVD scheme and remaining spatial derivatives are discretised using a fourth order centred differences model. An explicit filter employing a 13-point stencil and eighth order accurate is used in the DRP regions. The methods presented in this chapter are verified and validated in the next chapter.

Chapter 4

Numerical verification and validation

4.1 Introduction

The numerical verification performed aims the investigation of the discretisation schemes employed in CompReal and the implemented LES-PDF models. In this chapter the classical test case of homogeneous isotropic turbulence (HIT) is evaluated, in which kinetic energy spectra are calculated along with other turbulent variables such as enstrophy. The HIT configuration is inspired in the setup of Garnier *et al.* [150]. This test case has been proposed to assess the numerical behaviour of the code and the LES coupling.

The proposed LES-PDF models are further investigated by using the reactive shock tube of Fedkiw *et al.* [151]. This one-dimensional test case allows the investigation of the LES-PDF accuracy in comparison to DNS and the convergence of the stochastic partial differential equations. Because of its simple geometry, a large number of stochastic fields can be employed and their statistical behaviour, such as the moments, are evaluated.

The simulation of reactive mixing layers, both two and three-dimensional, is performed within the same configuration of Ferrer [26]. The results are then compared with DNS data [26] and an analysis of its performance and accuracy is exposed.

At last, the simulation of supersonic burners are performed to conduct the validation of the code. The experimental data of the burners of Evans *et al.* [152] and Cheng *et al.* [7] are classical benchmarks for reacting and compressible codes and have previously inves-

tigated in the literature. Therefore, these two three-dimensional test cases are simulated here to evaluate CompReal performance under harsh and real burners configuration.

4.2 Homogeneous isotropic turbulence

The freely decaying homogeneous isotropic turbulence (HIT) test case is a classical benchmark for compressible code performance evaluation. Although being challenging to reproduce it experimentally, the HIT is simple to set numerically and its results have major theoretical importance. It has been used extensively in the literature for numerical discretisation and large-eddy simulation evaluation [153, 150, 154].

The HIT chosen configuration is the same as used by Garnier *et al.* [150]. The single component non-reactive inviscid (infinite Reynolds number) equations are solved in non-dimensional form. The initial density is uniform and equals to unity in the whole domain. The initial random divergence-free velocity field is calculated using a Gaussian PDF noise and imposing the spectra of $E(k) \sim k^4 e^{-2(k^2/k_0^2)}$ with $k_0 = 2$. The initial pressure field is therefore calculated by solving a Poisson equation providing a divergence-free velocity field. The temperature is then evaluated using the relation:

$$\frac{p}{\rho} = \frac{T}{\gamma \mathrm{Ma}_{rms}^2} \tag{4.1}$$

where γ is set constant and equal to 1.4. The initial rms Mach number, Ma_{rms}, is chosen equal to 0.2 or 1.0, depending on the case. The domain size is 2π and it is discretised using 64^3 nodes. The boundary conditions are periodic. All simulations are performed up to $t = 10$ non-dimensional units, which allows $10/\pi$ initial eddy-turnover times [150].

4.2.1 Discretisation performance

In this section the DRP discretisation scheme is evaluated together with the HLLC-TVD and the hybrid scheme described previously for the convective term. Each scheme is also investigated when used in conjunction with the Smagorinsky model. The boundaries are periodic, so the discretisations schemes are freely applied without being specified to be the HLLC-TVD scheme.

The kinetic energy spectrum is a valuable tool to check if the schemes can reproduce the Kolmogorov 4/5 law [155], which means that the energy spectrum presents a -5/3

slope in the inertial range in low-Mach number conditions. The energy spectra is defined as:

$$E(k) = \frac{1}{2}\left(\mathbf{u}(\mathbf{k}) \cdot \mathbf{u}^*(\mathbf{k})\right) \tag{4.2}$$

where $k = |\mathbf{k}| = \sqrt{k_1^2 + k_2^2 + k_3^2}$ and $\mathbf{u}(\mathbf{k})$ is the velocity $\mathbf{u}(\boldsymbol{x})$ in the Fourier space obtained through the three-dimensional Fourier transform:

$$u_1(\mathbf{k}) = \frac{1}{(2\pi)^3}\int_{-\infty}^{+\infty} e^{-ik_3x_3}\int_{-\infty}^{+\infty} e^{-ik_2x_2}\int_{-\infty}^{+\infty} e^{-ik_1x_1}u_1(\boldsymbol{x})\,\mathrm{d}x_1\,\mathrm{d}x_2\,\mathrm{d}x_3 \tag{4.3}$$

$$u_2(\mathbf{k}) = \frac{1}{(2\pi)^3}\int_{-\infty}^{+\infty} e^{-ik_3x_3}\int_{-\infty}^{+\infty} e^{-ik_2x_2}\int_{-\infty}^{+\infty} e^{-ik_1x_1}u_2(\boldsymbol{x})\,\mathrm{d}x_1\,\mathrm{d}x_2\,\mathrm{d}x_3 \tag{4.4}$$

$$u_3(\mathbf{k}) = \frac{1}{(2\pi)^3}\int_{-\infty}^{+\infty} e^{-ik_3x_3}\int_{-\infty}^{+\infty} e^{-ik_2x_2}\int_{-\infty}^{+\infty} e^{-ik_1x_1}u_3(\boldsymbol{x})\,\mathrm{d}x_1\,\mathrm{d}x_2\,\mathrm{d}x_3 \tag{4.5}$$

The energy spectra for the different simulations with $Ma_{rms} = 0.2$ is shown in Figure 4.1 at the last time step. It can be seen that the hybrid scheme generates at the final time step a spectra which is very similar to those generated by the DRP simulations. This result is expected, since the sensor in the hybrid scheme would be mostly off in an incompressible simulation without shocks. It should be pointed out the better spectra achieved by using the Smagorinsky model for the DRP/hybrid models, which reproduce the -5/3 slope in the inertial range between $k = 5$ and $k = 16$. The HLLC-TVD, in contrast, is very dissipative and both results, with and without the Smagorinsky model, do not reproduce accurately the Kolmogorov law. At high-wave numbers, all schemes seem to achieve same level of numerical dissipation because of the explicit filter influence.

The spectra for all discretisation schemes using $\mathrm{Ma}_{rms} = 1.0$ is reproduced in Figure 4.2. It is possible now to notice the influence of the hybrid scheme into the DRP scheme. The results are slightly more dissipative and energy is lost faster with the hybrid, mainly because of the shocks generated. Although the initial condition presents supersonic speeds, at the last time step the flow is predominantly at low Mach number condition because of the dissipation effects, so the -5/3 slope has to be reproduced.

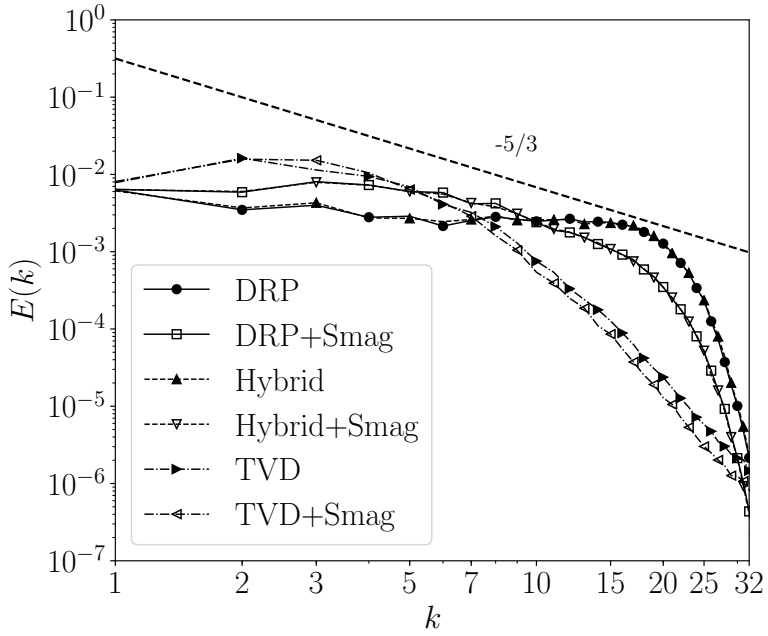

Figure 4.1: Spectrum of kinetic energy - $\mathrm{Ma}_{rms} = 0.2$ case at $t = 10$.

Again, the DRP and the hybrid schemes with the aid of the Smagorinsky model better reproduce this behaviour. The HLLC-TVD scheme is the most stable, however, it introduces considerable numerical dissipation, which reduces the accuracy of the compressible LES simulation, especially if used alone.

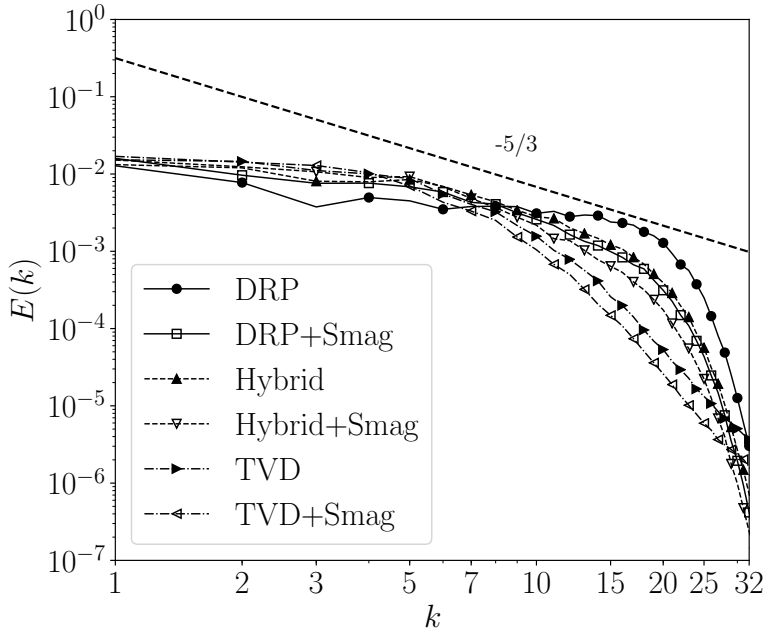

Figure 4.2: Spectrum of kinetic energy - $\mathrm{Ma}_{rms} = 1.0$ case at $t = 10$.

Figure 4.3 shows the flow development for the hybrid discretisation with and without the Smagorinsky model for the $\mathrm{Ma}_{rms} = 1.0$ case. It can be noticed the shocks and sharp gradients present at $t = 2$ but in $t = 6$ and $t = 10$ they are dissipated. The usage of the Smagorinsky model increased the dissipation and provides a smoother flow development. This is an expected behaviour and also reproduced in the literature [150]. The shock-capturing ability of the hybrid scheme is essential for stable simulations of complex physics as supersonic flows.

Figure 4.4 and 4.5 present the temporal evolution of the spatial averaged enstrophy for the $\mathrm{Ma}_{rms} = 0.2$ and $\mathrm{Ma}_{rms} = 1.0$ cases, respectively. The figures depict how more dissipative schemes prevent the growth of enstrophy by damping small turbulence structures [150]. As exposed in the kinetic energy spectrum, the hybrid and DRP schemes show the same result for the incompressible case whereas in the compressible case the hybrid scheme introduces higher numerical dissipation. In all schemes evaluated, the Smagorinsky subgrid model increases the numerical damping even further. Nevertheless, the LES model preserves the self-similarity of the results within the same discretisation scheme.

Another interesting result is the temporal evolution of the spatial averaged kinetic energy shown in Figure 4.6 and Figure 4.7. The kinetic energy begins to be dissipated very early in the simulation, which happens before the enstrophy decay for all schemes. Figure 4.6 depicts the incompressible case in which the kinetic energy is preserved for longer mainly for the DRP discretisation. However, the compressible case exposed in Figure 4.7 indicates a sharp dissipation in the beginning of the simulation which is due to the presence of the strong shocks, as shown in Figure 4.3.

Another important tool to evaluate the flow development is the analysis of the maximum and minimum density ratio within the domain, also performed by Garnier *et al.* [150]. Figure 4.8 exposes this result and shows how the shocks quickly develop for all discretisation schemes, with peak around $t \sim [1, 1.5]$ for the $Ma_{rms} = 1.0$ case. The results for the incompressible case are not shown as the ratio keeps close to unity in all cases. It can be seen in Figure 4.8 that the Smagorinsky model and the HLLC-TVD

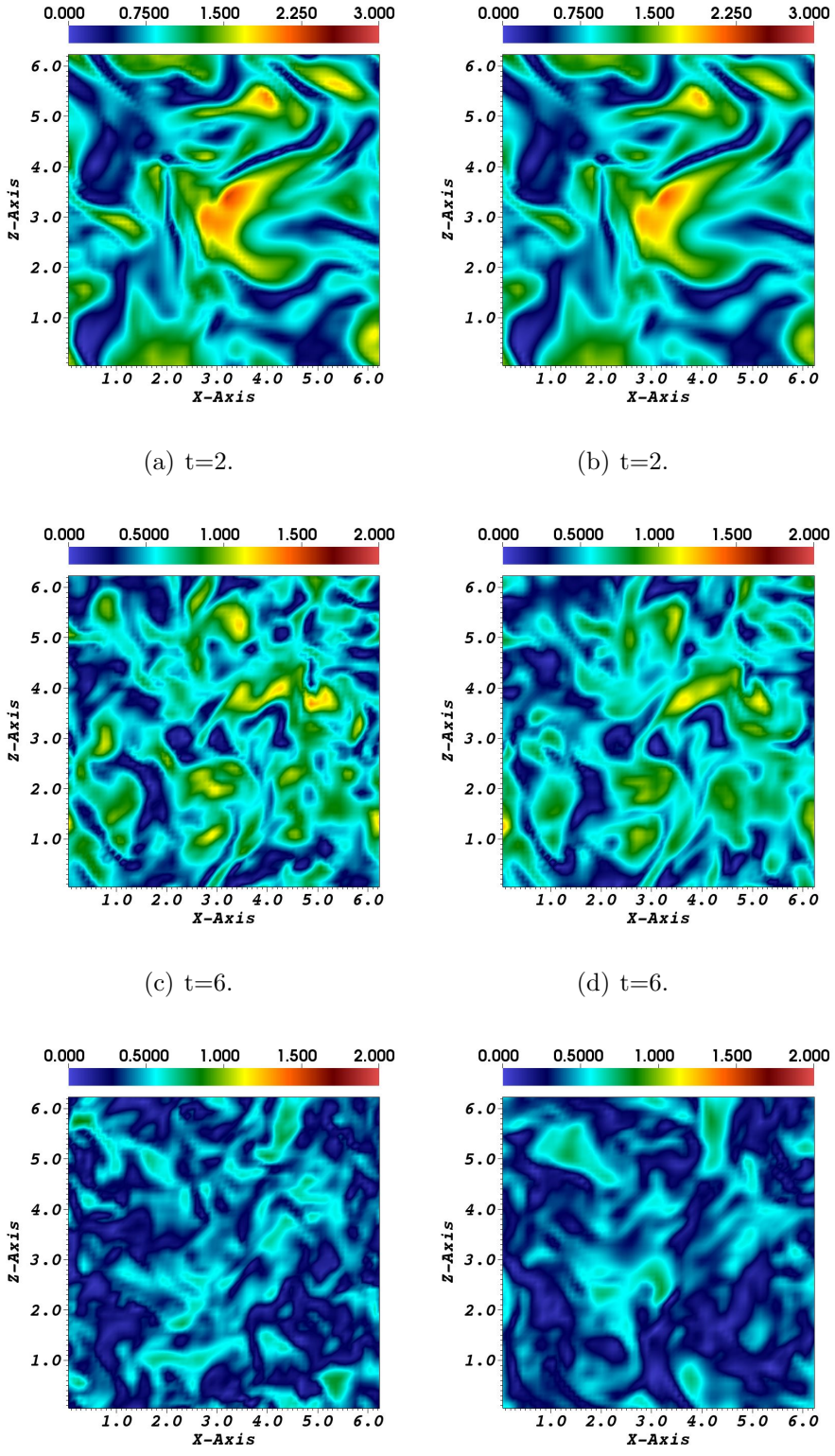

(a) t=2. (b) t=2.

(c) t=6. (d) t=6.

(e) t=10. (f) t=10.

Figure 4.3: Mach number contour plot for the $\mathrm{Ma}_{rms} = 1.0$ case. On the left, hybrid discretisation without LES modelling. On the right, hybrid with LES modelling.

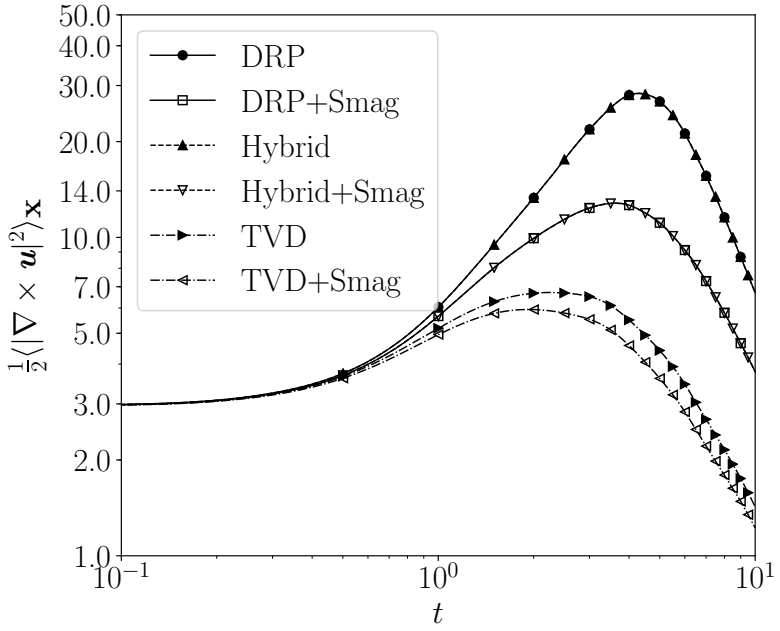

Figure 4.4: Enstrophy temporal evolution - $\mathrm{Ma}_{rms} = 0.2$ case.

heavily damp the shocks, preventing another peak occurrence which happens in $t = 4$ and $t = 5$ for the DRP and hybrid schemes, respectively.

The results shown in this section describe the numerical discretisation behaviour and accuracy. Although the DRP schemes seem to be the most accurate, their instability in

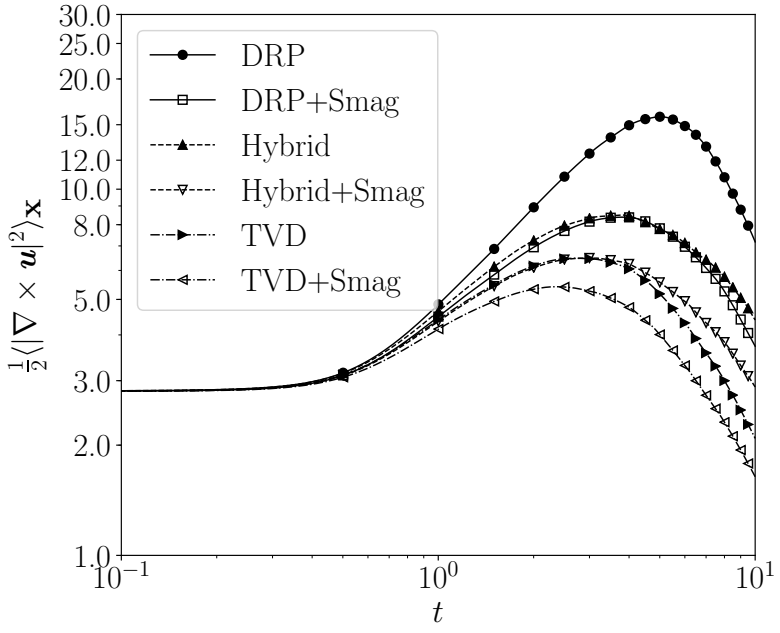

Figure 4.5: Enstrophy temporal evolution - $\mathrm{Ma}_{rms} = 1.0$ case.

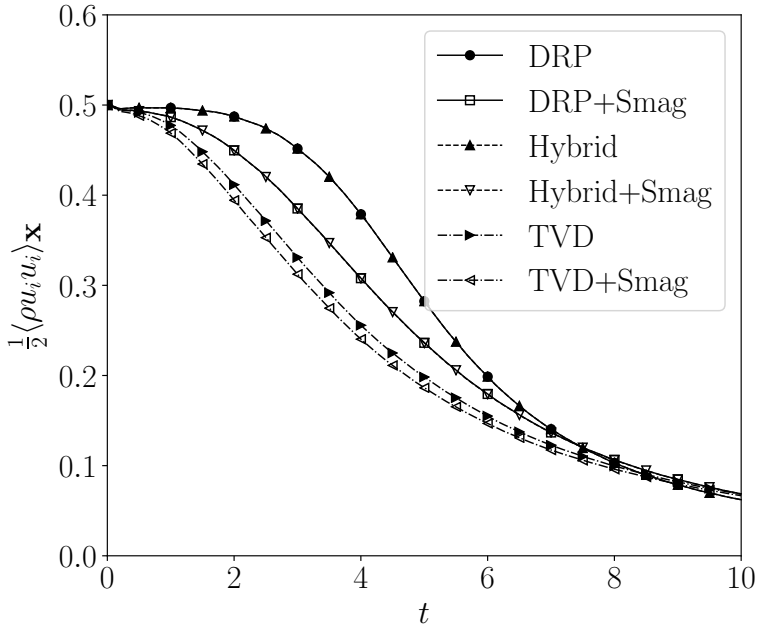

Figure 4.6: Kinetic energy temporal evolution - Ma = 0.2 case.

more challenging simulations might prevent their full usage unless in conjunction with a large explicit filtering technique. On the other hand, the HLLC-TVD heavily damps turbulence and small structures. The implemented CompReal hybrid scheme is good compromise between accuracy and stability, acting also as a shock-capturing scheme and

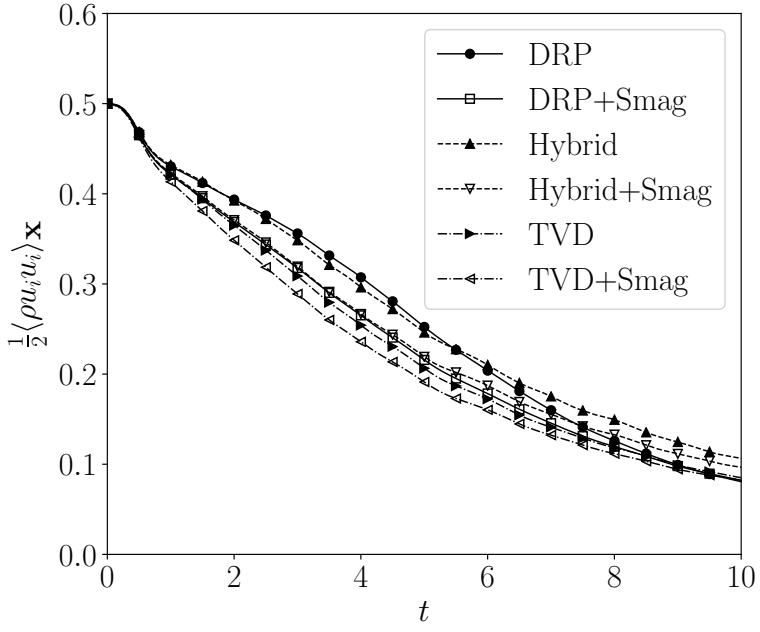

Figure 4.7: Kinetic energy temporal evolution - Ma = 1.0 case.

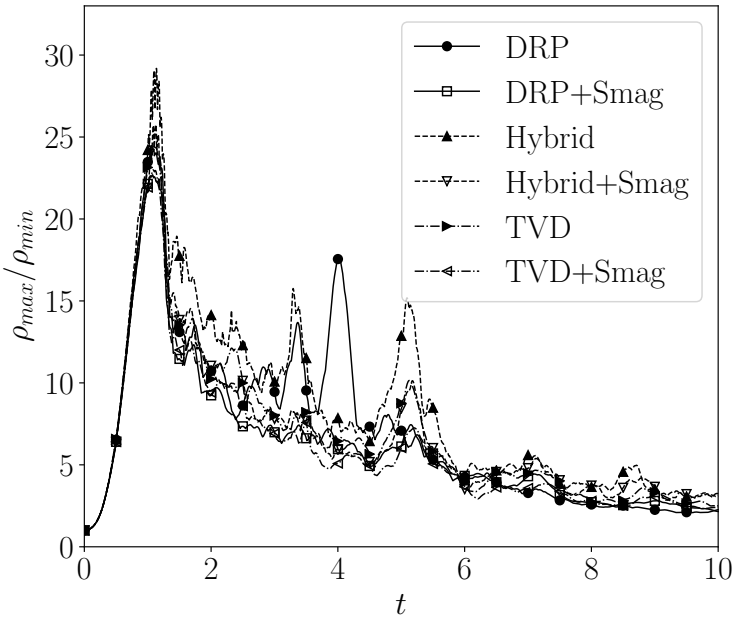

Figure 4.8: Maximum and minimum density in the whole domain ratio temporal evolution - $\mathrm{Ma}_{rms} = 1.0$ case.

preserving the accuracy of the DRP scheme to an extent.

Because of the stochastic nature of the differential equations used to solve the developed LES-PDF equations, numerical stability is one the major issues associated with their solution. A robust scheme such as the hybrid one presented here introduces numerical diffusion only locally in sharp gradient regions and preserve accuracy in other regions of the flow. Its usage is a good compromise for simulations of stochastic differential equations.

4.2.2 LES-PDF analysis

This section investigates the joint scalar PDF and joint velocity-scalar PDF models still using the HIT canonical configuration. It is considered a reactive scalar with initial value of $y = 0.5$ in the whole domain, employing the same initial conditions used in the test case with $\mathrm{Ma}_{rms} = 1.0$. The one-step reaction mechanism is described by the following reaction:

$$S = \begin{cases} A\left[2\left(Y_s - 0.5\right) - \left(2\left(Y_s - 0.5\right)\right)^3\right], & \text{if } Y_s > 0.5 \\ 0, & \text{otherwise} \end{cases} \tag{4.6}$$

where $1/A$ is the chemical time scale. The above mechanism means that the reactive scalar concentration remains at 0.5 throughout the simulation, as $S(0.5) = 0$. However, if there are subgrid scale fluctuations, $Y_s \to 1$ as $t \to \infty$.

The use of the Eulerian stochastic fields or the Lagrangian particles, however, allows the description of the same initial value of 0.5 but with stochastic variance. The variance value of 0.01 was chosen and two fields are employed in this simulation, as in an initial bi-modal PDF. One field therefore starts with 0.4 and the other with 0.6 scalar concentration, uniform in the whole domain. The SPDF model is used here but the results can be reproduced using the VSPDF as well. The IEM micromixing model results in an attraction force towards the mean, so the field with 0.4 concentration will increase to 0.5 just by micromixing effect. The field 2 with concentration 0.6 will react and increase until 1.0, also pushing the average value close to 0.7.

Here it is introduced the Damköhler number definition of $Da = \pi/(1/A)$, in which π is the time scale of the HIT. The hybrid discretisation is employed and 6 test cases are performed following the configuration presented on Table 4.1. The results are shown in Figure 4.9.

For the case 1, the average mass fraction immediately jumps to 0.7 and steadily increases to 0.75 until the $t = 2$. This occurs because one stochastic field with initial value of 0.6 reacts and the average concentration quickly goes to 1.0. The other field with initial value of 0.4 does not react, however, the micromixing model acts as a source term driving the concentration towards the mean value of 0.7. When this field reaches a value

Case	Da	Model
1	$\pi/0.001$	SPDF
2	$\pi/0.1$	SPDF
3	$\pi/1$	SPDF
4	$\pi/10$	SPDF
5	$\pi/100$	SPDF
6	$\pi/1$	No Model (NM)

Table 4.1: Test cases for the joint scalar LES-PDF. Cases 1-3 and 6, Da > 1; cases 4-5, Da < 1.

greater than 0.5, what happens at $t = 2$, it reacts as well and its concentration increases to 1.0.

As the Damköhler number reduces by increasing the chemical time scale, the average concentration takes more time to increase to 1.0, and for the cases 4 ($Da = \pi/10$) and 5 ($Da = \pi/100$) it does not reach 1.0 after 10 time units. Case 6, which does not include the SPDF model, in contrast, even with $Da = \pi/1$, does not change the concentration and conserves the constant value of 0.5.

Figure 4.10 demonstrates the behaviour for case 3, also showing the particular Eulerian stochastic fields evolution. The first field starts with 0.6 and reacts until 1.0 concentration. The second field with starting 0.4 concentration changes by micromixing effects and at

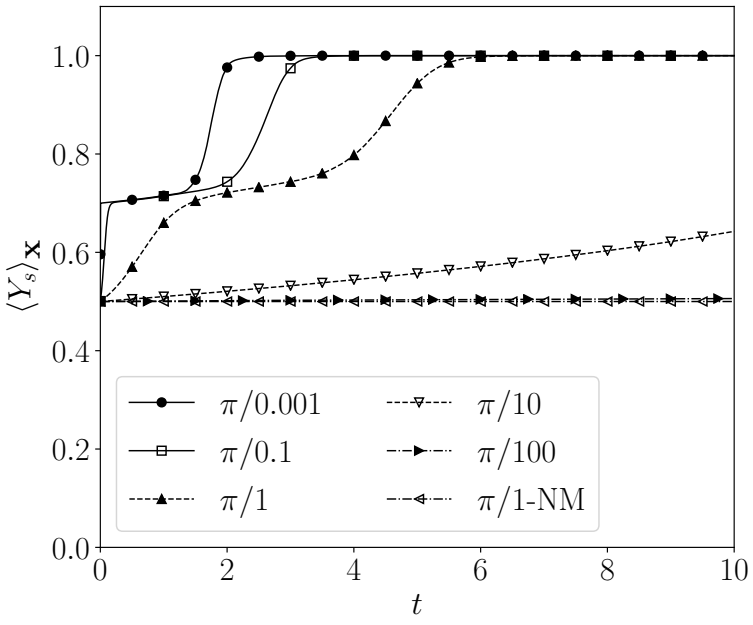

Figure 4.9: Temporal evolution of spatial average reactive scalar.

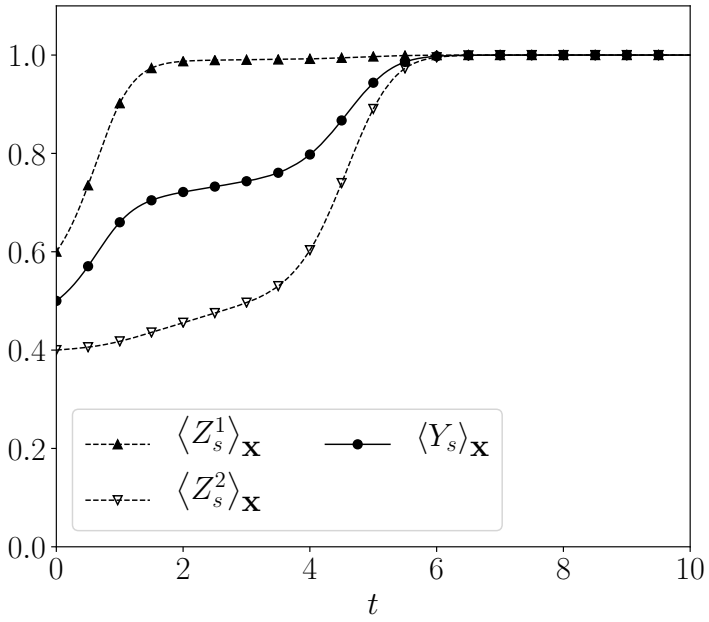

Figure 4.10: Temporal evolution of spatial average reactive scalar including the stochastic fields for the case 3.

$t = 4$ begins to react.

This effect can only be captured by probabilistic models, such as the LES-PDF, and models that do not rely only on large scale gradients. The stochastic solution approach like the Eulerian fields or the Lagrangian particles are suitable to capture this effect [68, 112, 141, 137, 14]. Other probabilistic modelling techniques such as the CMC can also reproduce it [156, 157], however, models that do not rely on a LES-PDF equation may not capture it.

The developed joint velocity-scalar LES-PDF model is evaluated by assessing the enstrophy and kinetic energy. This is performed using the $Ma_{rms} = 1.0$ test case and with the hybrid discretisation. All VSPDF simulations are performed with 8 fields and all fields share the same initial condition. Figure 4.11 presents the kinetic energy spectra for the VSPDF, Smagorinsky and no turbulent model. All simulations present similar spectra at the final step, where supersonic effects have vanished and the spectra should follow the -5/3 slope in the inertial range. The VSPDF slightly dissipates more energy than the Smagorinsky model. This happens because of its stochastic random noise that adds or subtracts momentum in gradient regions. In the case of adding momentum, the

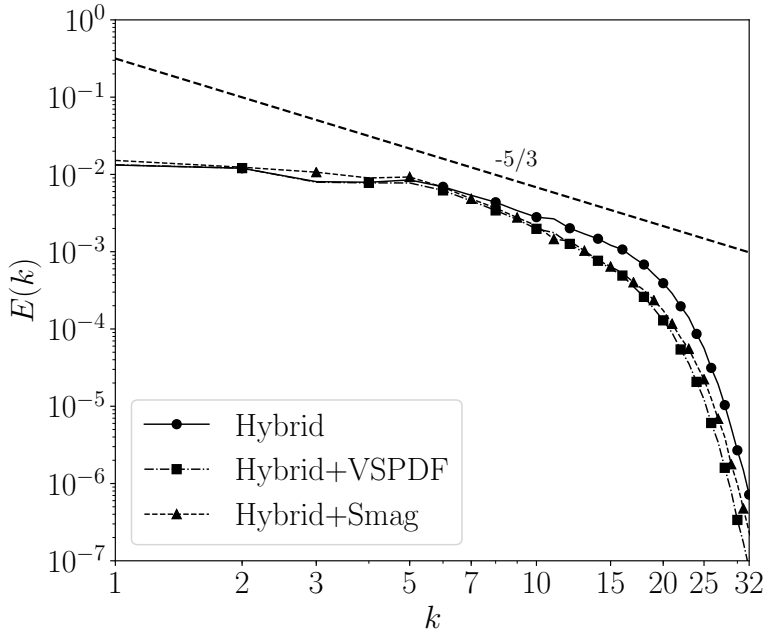

Figure 4.11: Kinetic energy spectra at $t = 10$ - Ma $= 1.0$ case.

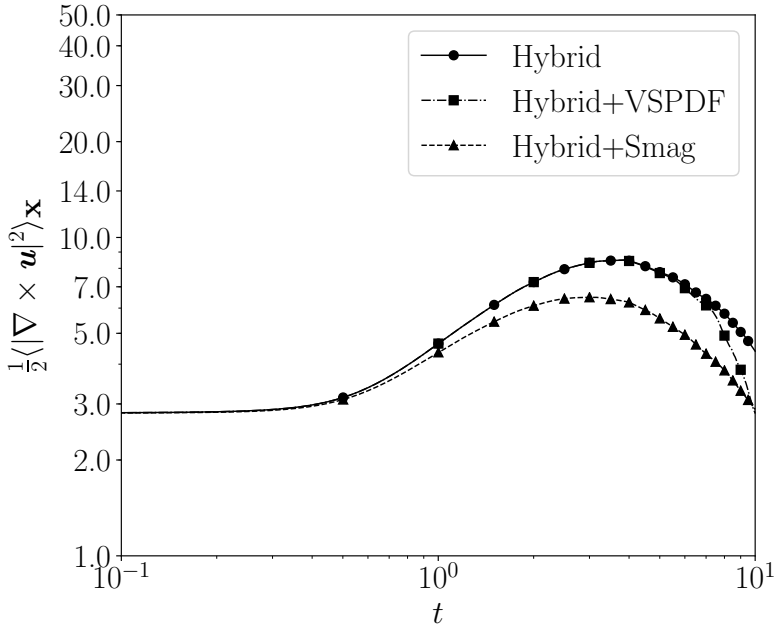

Figure 4.12: Temporal spatial average enstrophy evolution - Ma $= 1.0$ case.

hybrid scheme acts and more energy is dissipated. In contrast, the Smagorinsky model dissipates energy for including extra viscosity.

The enstrophy evolution is shown in Figure 4.12. The hybrid with no model and the VSPDF evolve very similarly until $t = 5$. In this moment the rate of destruction of enstrophy for the VSPDF is higher. The Smagorinsky model dissipates more than both

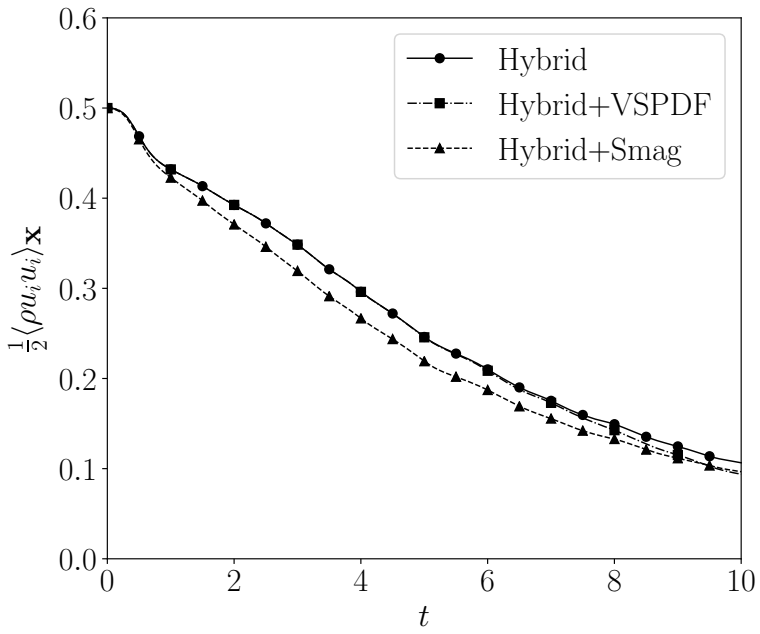

Figure 4.13: Temporal spatial average kinetic energy evolution - Ma = 1.0 case.

simulations but preserves the self-similarity with the no model approach. The VSPDF do not preserve the statistical self-similarity, though. The growth of small scales to large, which occurs until $t = 4$, is the same as with employing no model, however, it destroys the large turbulent structures faster than the Smagorinsky model.

The kinetic energy temporal evolution is presented in Figure 4.13. The initial kinetic energy is only dissipated within the domain, and the VSPDF and the hybrid no model simulation present very similar evolution until $t = 6$. The same issue presented in Figure 4.12 is also shown here. From $t = 6$ to $t = 10$ the VSPDF dissipates more energy in a faster rate than the Smagorinsky model. This can be possibly caused by the stronger separation of the stochastic fields or an incomplete modelling able to preserve the large structures.

As shown in Figure 4.14, from $t = 6$ the simulation is dominated by subsonic effects. Therefore the VSPDF faster rate of enstrophy and kinetic energy destruction is not related to the presence of shocks. It occurs when the stochastic Eulerian fields are more distance apart, which increases the stochastic term within the Langevin model. A possible approach to fix this issue would be a better calibration for the Langevin model constant. As originally proposed by Pope [68], the Langevin model does not model pos-

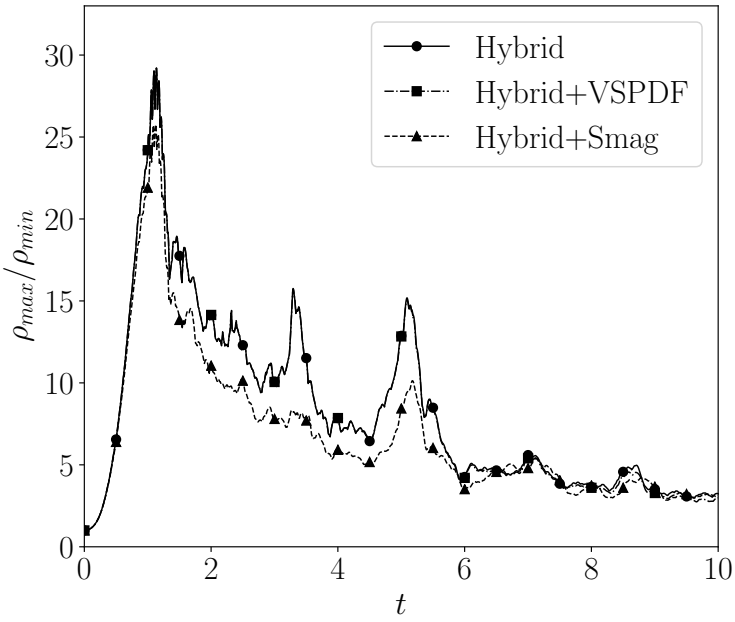

Figure 4.14: Temporal spatial average density ratio evolution - Ma = 1.0 case.

sible stochastic pressure fluctuations, but only mean/filtered pressure quantities. This new calibration, however, is not performed in this work.

4.3 Reactive shock tube

The reactive shock tube is an one-dimensional test case to assess the performance of the code and the LES-PDF models using a real chemistry mechanism. The use of this test case is also performed by Ferrer [26] to verify the accuracy of the code. The test case, originally proposed by Fedkiw *et al.* [151], is a one-dimensional reactive shock tube with initial mole fraction ratio of 2/1/7 for $H_2/O_2/Ar$ in the whole domain. The hydrogen combustion mechanism of [158], with 9 species and 18 reactions is employed. The shock tube has length $l_x = 0.12\ m$ and the following initial configuration:

$$(\rho, u_x, p) = \begin{cases} 0.072\ kg/m^3, 0.00\ m/s, 7173\ Pa, & \text{if } x \leq l_x/2 \\ 0.18075\ kg/m^3, -487.34\ m/s, 35594\ Pa, & \text{otherwise} \end{cases} \tag{4.7}$$

The initial Mach number is 0.89 at $x > l_x/2$. The left boundary is a wall and zero gradient is applied to the boundary condition at the right. The hybrid spatial discretisation is employed in all test cases for the convective term. Remaining spatial derivatives are discretised using fourth order finite differences. Temporal integration is performed using an explicit third order Runge-Kutta scheme. The shock wave will travel to the left, hit the wall, increase pressure and temperature and the flame ignites, generating a reaction wave towards the right. It is a weak deflagration wave, where a pressure wave is moving and it is not a low Mach number regime.

The first test performed aims to verify if the Smagorinsky model, the LES-PDF and DNS simulations have similar behaviour after achieving mesh convergence. As in all LES simulations, as the mesh size tends to Kolmogorov scales, the simulation should reproduce DNS results. The LES models are being evaluated in an one-dimensional test, which may pose some limitations in accuracy. On this test, all models should therefore converge to the same DNS solution when mesh convergence is achieved. Simulations using from 50 to 6400 elements on x-direction have been performed. For the mesh convergence test, 8 fields are used on both SPDF and VSPDF models. A stochastic convergence test is also performed using 400 elements and employing from 2 to 8192 stochastic fields for the

SPDF and VSPDF.

4.3.1 Model accuracy investigation

Figure 4.15 shows instantaneous results for the $N_x = 6400$ simulation, when mesh convergence is achieved. As expected, all results converge to the same 1D-DNS solution. It is also possible to see from Figure 4.15 that the premixed flame behaves as a weak detonation instead of a constant pressure flame. At $t = 160\mu s$, the flame has already ignited and the reaction wave is traveling from the left to the right at the position of $x = 0.025m$ and the shock is positioned at $x = 0.04m$, approximately. At $t = 230\mu s$ the reaction wave has already overtaken the shock wave. It is possible to see, from left to the right, a rarefaction wave, a contact discontinuity and a detonation wave [151]. This test case ensures that the models have consistent behaviour as the mesh size increases.

Figure 4.16 presents results using 400 elements, keeping the 6400 elements result for the 1D-DNS though. The SPDF model evaluated in this test case do not present the subgrid time scale correction for low Reynolds and premixed flames approach of Jones *et al.* [128]. The SPDF without subgrid correction generates excessive viscous effects, which overly accelerates the premixed flame. The Smagorinsky and the 1D-DNS simulations present similar results, which infer that the Smagorinsky model does not play a critical role using this mesh size.

The VSPDF flame presents results very similar to the 6400 elements simulation. The solution do not change dramatically by increasing the number of stochastic fields beyond 8, confirming that the solution also presents stochastic convergence. This shows the ability of the VSPDF model to capture the correct solution using fewer elements than the Smagorinsky, SPDF and even coarse mesh 1D-DNS. It is also interesting to highlight that the same numerical scheme has been employed in all cases. The VSPDF therefore presents the same discretisation limitations as the Smagorinsky and the 1D-DNS simulations. However, the usage of the Eulerian stochastic fields including velocity in the sample space results in a more accurate representation of the flame.

After the inclusion of the subgrid scale correction mentioned in Eq. (3.10), the SPDF

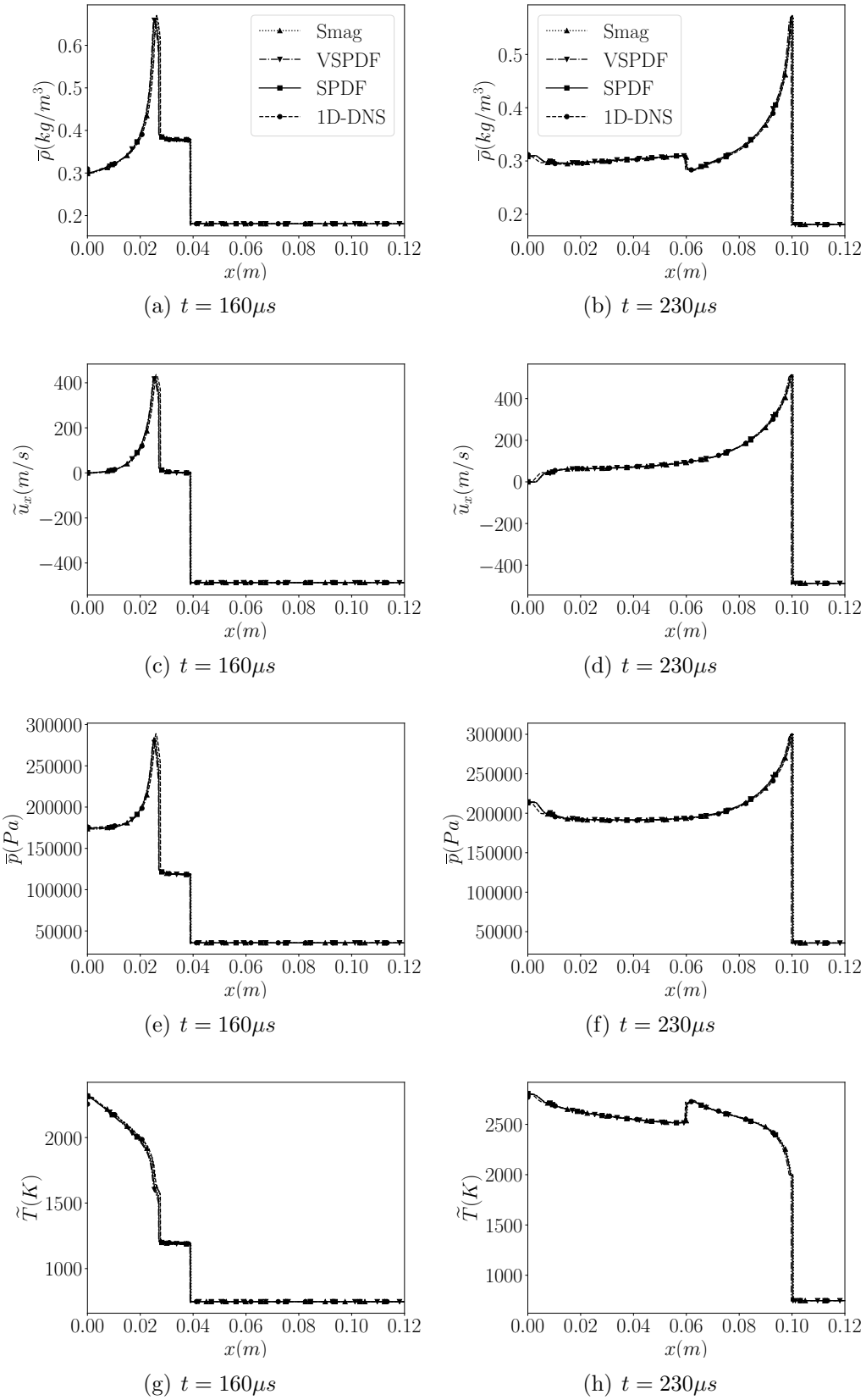

(a) $t = 160\mu s$ (b) $t = 230\mu s$

(c) $t = 160\mu s$ (d) $t = 230\mu s$

(e) $t = 160\mu s$ (f) $t = 230\mu s$

(g) $t = 160\mu s$ (h) $t = 230\mu s$

Figure 4.15: Results for reactive shock tube using 6400 elements.

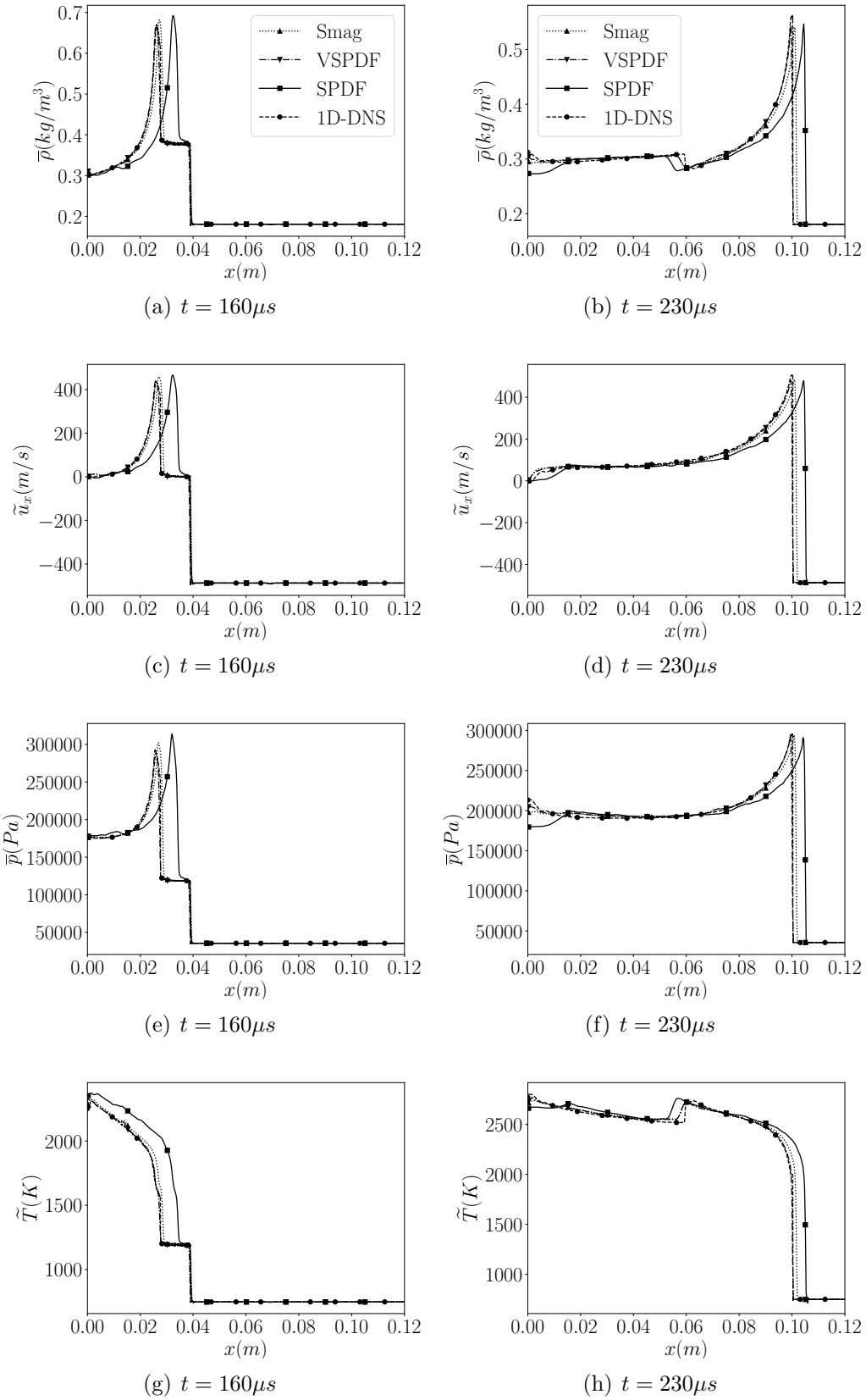

(a) $t = 160\mu s$ (b) $t = 230\mu s$

(c) $t = 160\mu s$ (d) $t = 230\mu s$

(e) $t = 160\mu s$ (f) $t = 230\mu s$

(g) $t = 160\mu s$ (h) $t = 230\mu s$

Figure 4.16: Results for reactive shock tube using 400 elements. SPDF without subgrid correction. 1D-DNS simulation has 6400 elements.

model is able to return a solution similar to the Smagorinsky and 1D-DNS simulations, as shown in Figure 4.17. It can be seen that the correction is of critical importance to the accurate modelling of the joint scalar PDF. Without the correction, this model captures wrong flame speed unless using a very fine mesh. By using the correction, the SPDF model yields results as accurate as the Smagorinsky model, as expected since the SPDF still also uses the Smagorinsky model to close the convective terms. Valiño *et al.* [102] presents a different correction to ensure consistent behaviour at low Reynolds number. The main idea is to ensure that the stochastic term vanishes and the stochastic field equation returns to the deterministic conservation equation Eq. (2.10). This has not been investigated here since the correction seems to be already accurate enough.

Another important aspect of the stochastic Eulerian fields modeling is the ability to capture several different composition spaces. Figure 4.18 shows several stochastic chemical species using a 4096 fields SPDF simulation and 400 elements. There are several different flame fronts that contribute to the average value. Picciani *et al.* [135] investigated a premixed flame with several stochastic fields and took into account the many different flame positions to model a thickened stochastic fields approach, which is potentially more accurate than the traditional SPDF for low Mach number formulation. This method, however, has not been implemented in this work.

Figure 4.19 presents four scatter plots for the simulation of 4096 fields and SPDF using 400 elements. They show instantaneous results at the flame front and $t = 230\mu s$ for pressure, temperature, hydrogen and OH as function of H_2O. It can be seen the strong correlation presented for the H_2O production and increase of temperature and pressure. It can also be noticed the correlation between production of H_2O and consumption of H_2 and OH. The stochastic pressure is not defined for the SPDF model and it is not used in the resolution algorithm. However, it can be easily defined as a function of the stochastic mass fraction and temperature:

$$p^n = \overline{\rho} R^n T^n \tag{4.8}$$

for a n^{th} stochastic field.

The VSPDF scatter plots are shown in Figure 4.20. The number of 4096 stochastic

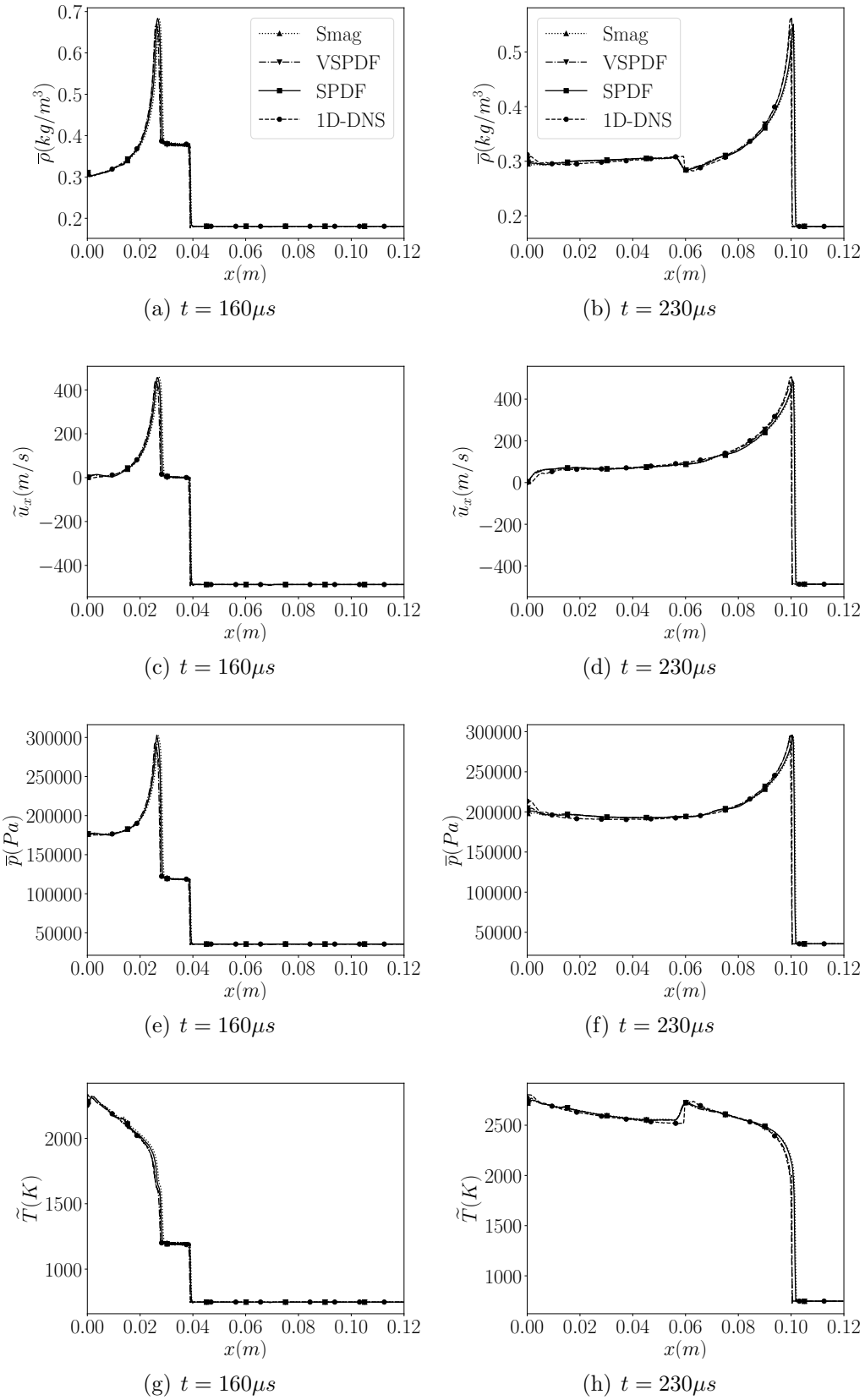

(a) $t = 160\mu s$ (b) $t = 230\mu s$

(c) $t = 160\mu s$ (d) $t = 230\mu s$

(e) $t = 160\mu s$ (f) $t = 230\mu s$

(g) $t = 160\mu s$ (h) $t = 230\mu s$

Figure 4.17: Results for reactive shock tube using 400 elements. SPDF with subgrid correction. 1D-DNS simulation has 6400 elements.

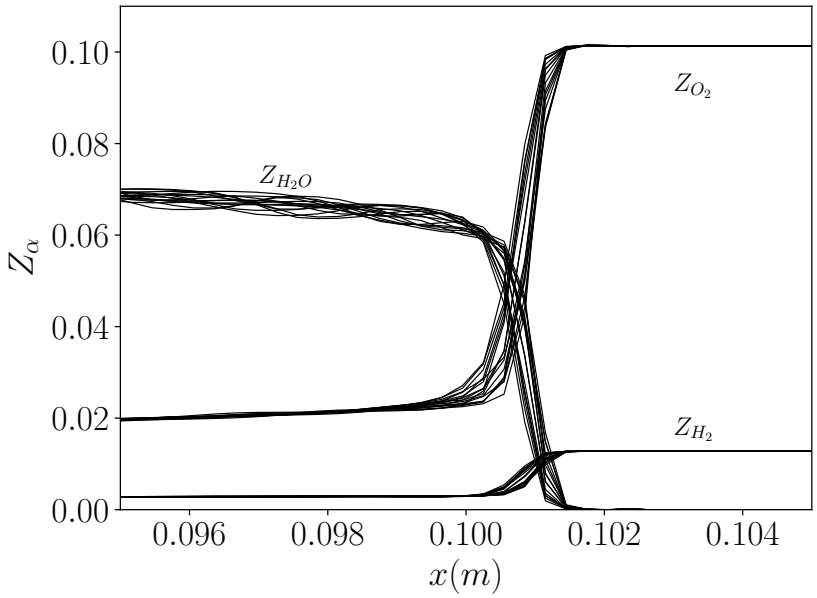

Figure 4.18: Stochastic fields at the flame front for the SPDF model at $t = 230\mu s$.

fields is also used. Although the scatter plots are also shown at the same flame front

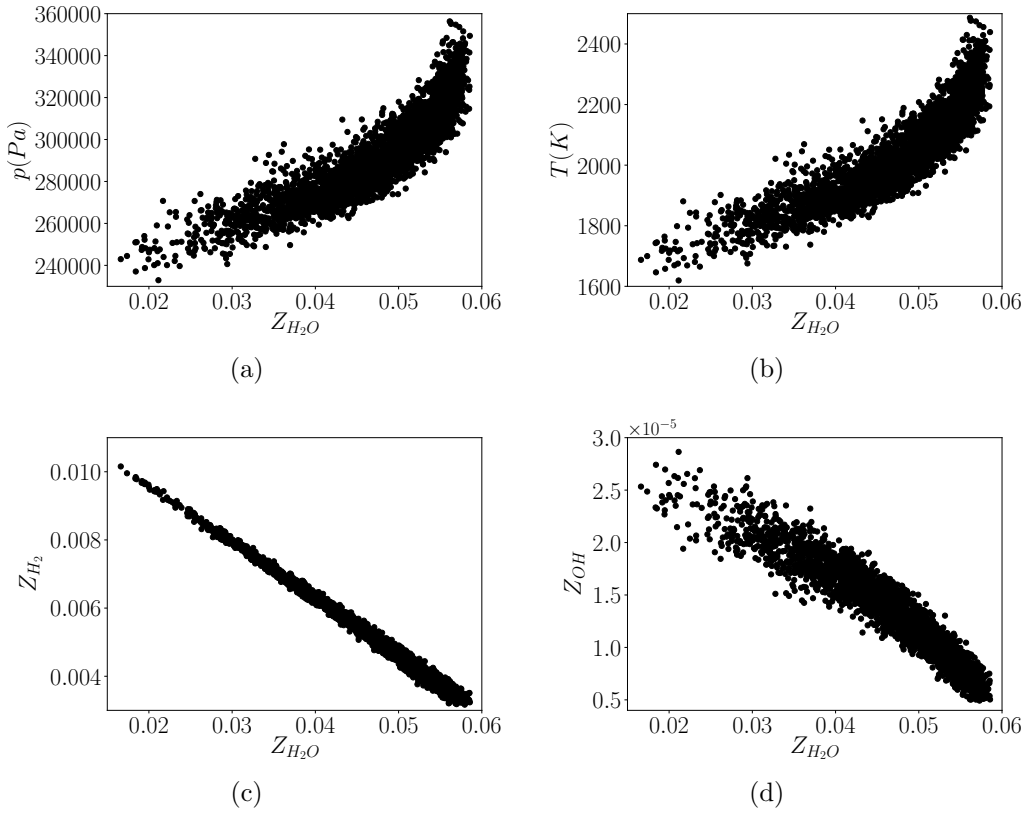

Figure 4.19: Instantaneous scatter plots at the flame front position for the SPDF model at $t = 230\mu s$.

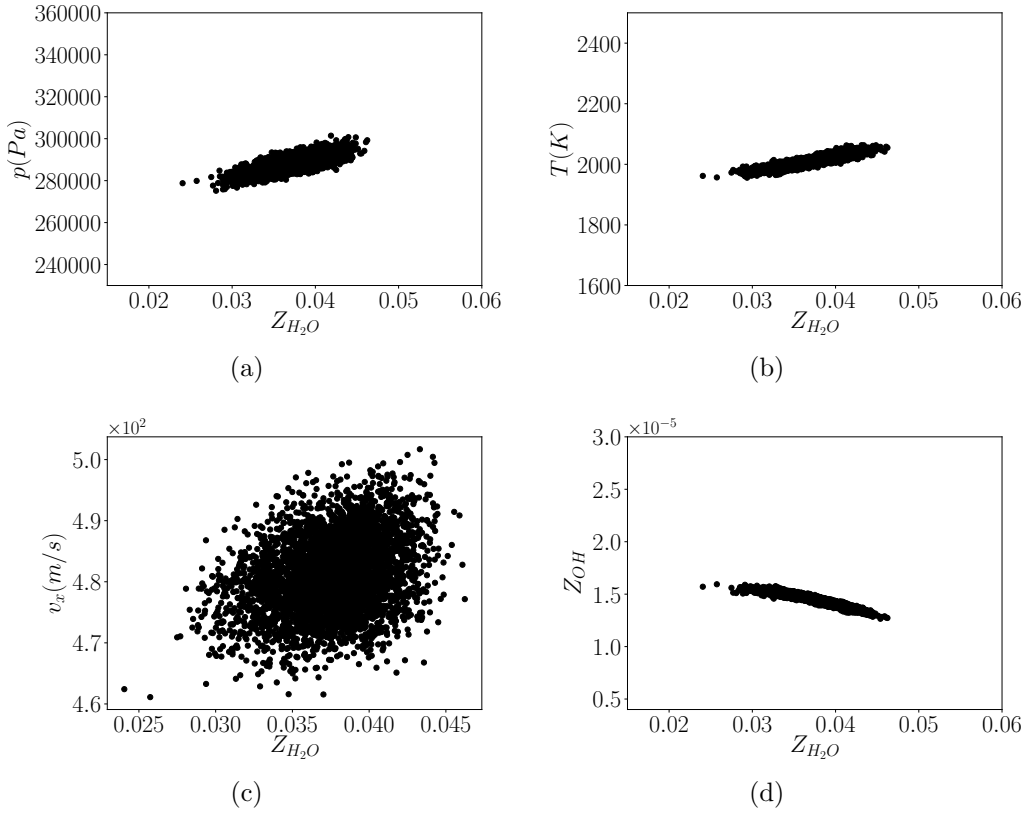

Figure 4.20: Instantaneous scatter plots at the flame front position for the VSPDF model at $t = 230\mu s$.

position, the VSPDF has a smaller variance than the SPDF model. The temperature varies from 1960K to 2060K in the VSPDF, while using the SPDF it varies from 1600K to 2500K. The fields are kept closer in the VSPDF, which may pose an issue in more complex simulations where access to different combustion composition space is critical to accuracy. The velocity scatter plot is also shown and a weak correlation can be noticed between the production of H_2O and the increasing in momentum.

4.3.2 Stochastic convergence

Simulations using 400 elements and ranging from 2 to 8192 stochastic fields are employed in order to evaluate the stochastic convergence. It is therefore important to first define the moments used. The first moment is defined as:

$$\boldsymbol{\mu}_1(\boldsymbol{x}, t) = \int_{-\infty}^{+\infty} \boldsymbol{\Psi} \widetilde{f}(\boldsymbol{\Psi}; \boldsymbol{x}, t) \, \mathrm{d}\boldsymbol{\Psi} \tag{4.9}$$

where $\boldsymbol{\mu}_1 = \left[\widetilde{Y}_1, \widetilde{Y}_2, ..., \widetilde{Y}_{N_s}, \widetilde{h}\right]^T$ for the SPDF and $\boldsymbol{\mu}_1 = \left[\overline{\rho}, \overline{p}, \widetilde{u}_1, \widetilde{Y}_1, \widetilde{Y}_2, ..., \widetilde{Y}_{N_s}, \widetilde{e}_t\right]^T$ for the VSPDF. It is approximated as:

$$\boldsymbol{\mu}_1^{N_f}(\boldsymbol{x}, t) = \frac{1}{N_f} \sum_{n=1}^{N_f} \boldsymbol{\xi}^n(\boldsymbol{x}, t) \underset{N_f \to \infty}{=} \boldsymbol{\mu}_1(\boldsymbol{x}, t) \tag{4.10}$$

where $\boldsymbol{\xi}^n(\boldsymbol{x}, t)$ represents the stochastic field variable and $\boldsymbol{\mu}_1^{N_f}(\boldsymbol{x}, t)$ is the approximated moment obtained through N_f fields. The centred moment is used to investigate the remaining moments. It is defined as:

$$\boldsymbol{\mu}_i(\boldsymbol{x}, t) = \int_{-\infty}^{+\infty} (\boldsymbol{\Psi} - \boldsymbol{\mu}_1(\boldsymbol{x}, t))^i \widetilde{f}(\boldsymbol{\Psi}; \boldsymbol{x}, t) \, \mathrm{d}\boldsymbol{\Psi} \tag{4.11}$$

where i indicates the i^{th}-centred moment. It is also approximated as:

$$\boldsymbol{\mu}_i^{N_f}(\boldsymbol{x}, t) = \frac{1}{N_f} \sum_{n=1}^{N_f} \left(\boldsymbol{\xi}^n(\boldsymbol{x}, t) - \boldsymbol{\mu}_1^{N_f}(\boldsymbol{x}, t)\right)^i \underset{N_f \to \infty}{=} \boldsymbol{\mu}_i(\boldsymbol{x}, t) \tag{4.12}$$

With the exception of the first moment, all the other moments investigated are centred moments. Two different kinds of numerical error are therefore evaluated, a local relative error and a spatially averaged relative error. The spatial average of the i^{th}-moment is defined as:

$$I\boldsymbol{\mu}_i(t) = \frac{\int_{\mathbf{0}}^{\boldsymbol{L}} \boldsymbol{\mu}_i(\boldsymbol{x}, t) \, \mathrm{d}\boldsymbol{x}}{\int_{\mathbf{0}}^{\boldsymbol{L}} \mathrm{d}\boldsymbol{x}} \tag{4.13}$$

The numerical error of the Monte-Carlo method should decrease with slope $N_f^{-0.5}$. In order to evaluate the slope of the several moments, the solution obtained with 8192 is considered the reference value. The local relative error in comparison to 8192 fields for the i^{th}-moment is then defined as:

$$\boldsymbol{\epsilon}_i^{N_f}(\boldsymbol{x}, t) = abs\left(\frac{\boldsymbol{\mu}_i^{N_f}(\boldsymbol{x}, t) - \boldsymbol{\mu}_i^{8192}(\boldsymbol{x}, t)}{\boldsymbol{\mu}_i^{8192}(\boldsymbol{x}, t)}\right) \tag{4.14}$$

where the error is evaluated at $x = 0.10m$ and $t = 230\mu s$. The spatially averaged relative

error is therefore:

$$I\boldsymbol{\epsilon}_i^{N_f}(t) = abs\left(\frac{I\boldsymbol{\mu}_i^{N_f}(t) - I\boldsymbol{\mu}_i^{8192}(t)}{I\boldsymbol{\mu}_i^{8192}(t)}\right) \tag{4.15}$$

where it is also evaluated at the time of $t = 230\mu s$. The spatially averaged relative error generates more reliable solutions as it takes into account samples from the whole domain.

Figure 4.21 presents the local relative error for the SPDF model, while Figure 4.22 shows the spatially averaged relative error. For the SPDF it is presented the convergence rate for the $1^{st} - 6^{th}$-moment of the species H_2, O_2 and H_2O. Overall, the convergence rate for the local error is slightly slower than the predicted $N_f^{-0.5}$ theoretical slope. For the first moment and second moment the local error presents a uniform behaviour. As the centred moments increase the deviation increases as well. This presents the challenge for capturing high moments with a small number of stochastic fields, as it is required at least 200 fields for the $3^{rd} - 6^{th}$-moment to converge.

The spatially averaged relative error has smaller variance since it has $400 \times N_f$ more samples. The moments also converge with slightly smaller rate than the theoretical one. The fifth moment of H_2O presents a very slow convergence rate, although the sixth moment converges with rate close to the theoretical one for all species.

By checking the first moment convergence in Figures 4.21 and 4.22 it is possible to infer that 8 fields is already enough to achieve statistical error less than 1% for the SPDF model. Although this test represents a premixed flame, a non-premixed flame would also present strong gradients in the same position, at the flame front. The statistically convergence is therefore likely to be the same, since it is the gradients that increase the stochastic term in Eq. (3.13). The number of 8 fields is also widely used in the literature [100, 126, 62, 128]. Henceforth, the number of 8 fields for the SPDF is used unless stated otherwise.

Figure 4.23 shows the local relative error convergence for the VSPDF model. The radicals H_2O, H_2 and the velocity convergence rate are presented. The first moment convergence rate has double the rate of the theoretical value. Overall, the convergence rate is close to $N_f^{-1.0}$. The convergence rate for the chemical species do not present a clear figure from the second moment to the sixth one. It is, on average, for both H_2O

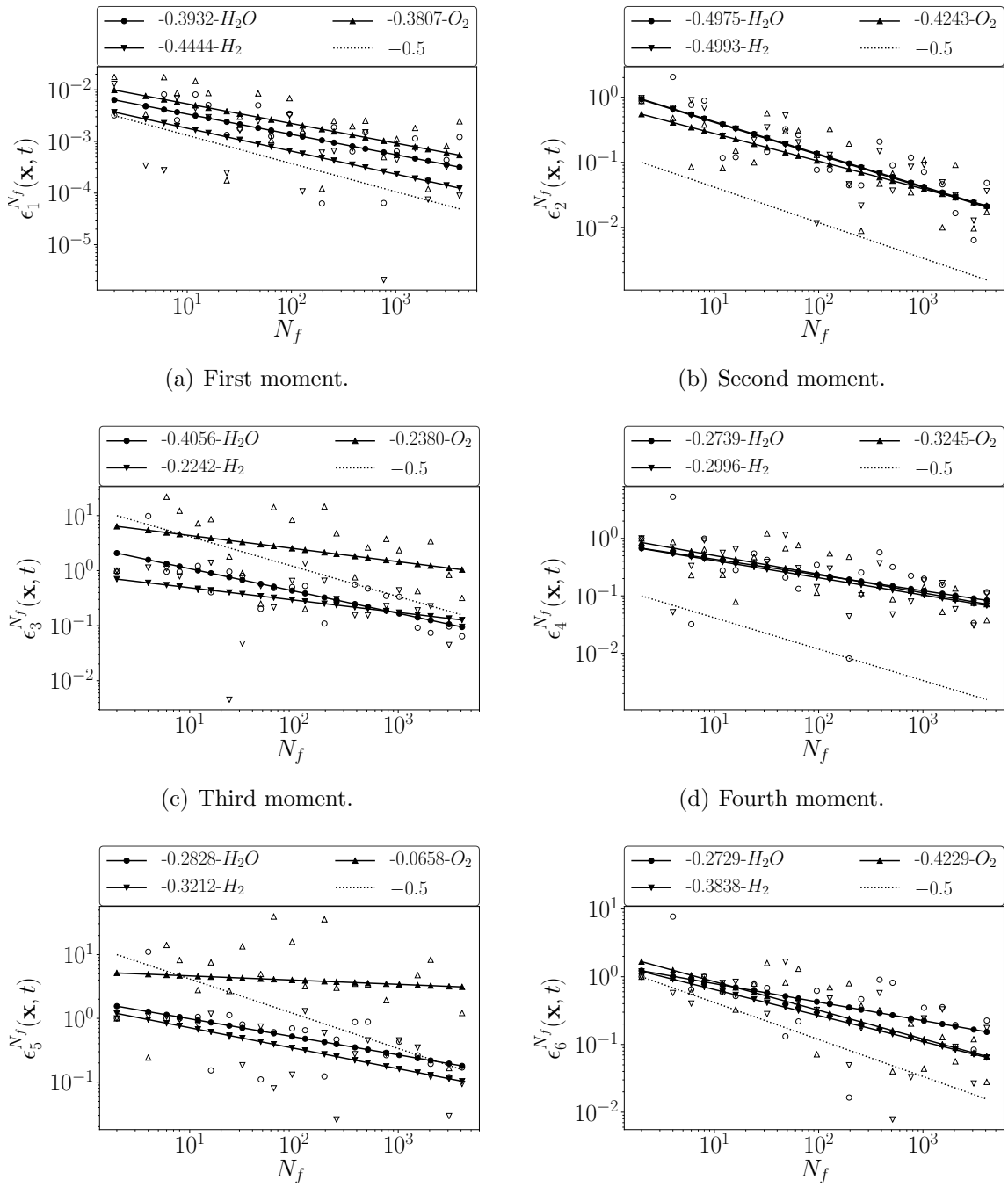

(a) First moment.

(b) Second moment.

(c) Third moment.

(d) Fourth moment.

(e) Fifth moment.

(f) Sixth moment.

Figure 4.21: Convergence rate for local moments at $x = 0.10m$ and $t = 230\mu s$ for the SPDF model. Slope for the trend lines indicated for each stochastic variable along with the theoretical -0.5 slope. Unfilled markers indicate the actual values.

and H_2 around $N_f^{-1/4}$ and also present high variance. The relative error can be large at this position, in contrast to the SPDF.

The calculated first moment obtained using 8192 fields for H_2O is 1.214×10^{-4}, for the H_2 is 1.277×10^{-2} and for the velocity is 477.75 m/s. The number of 1000 fields can

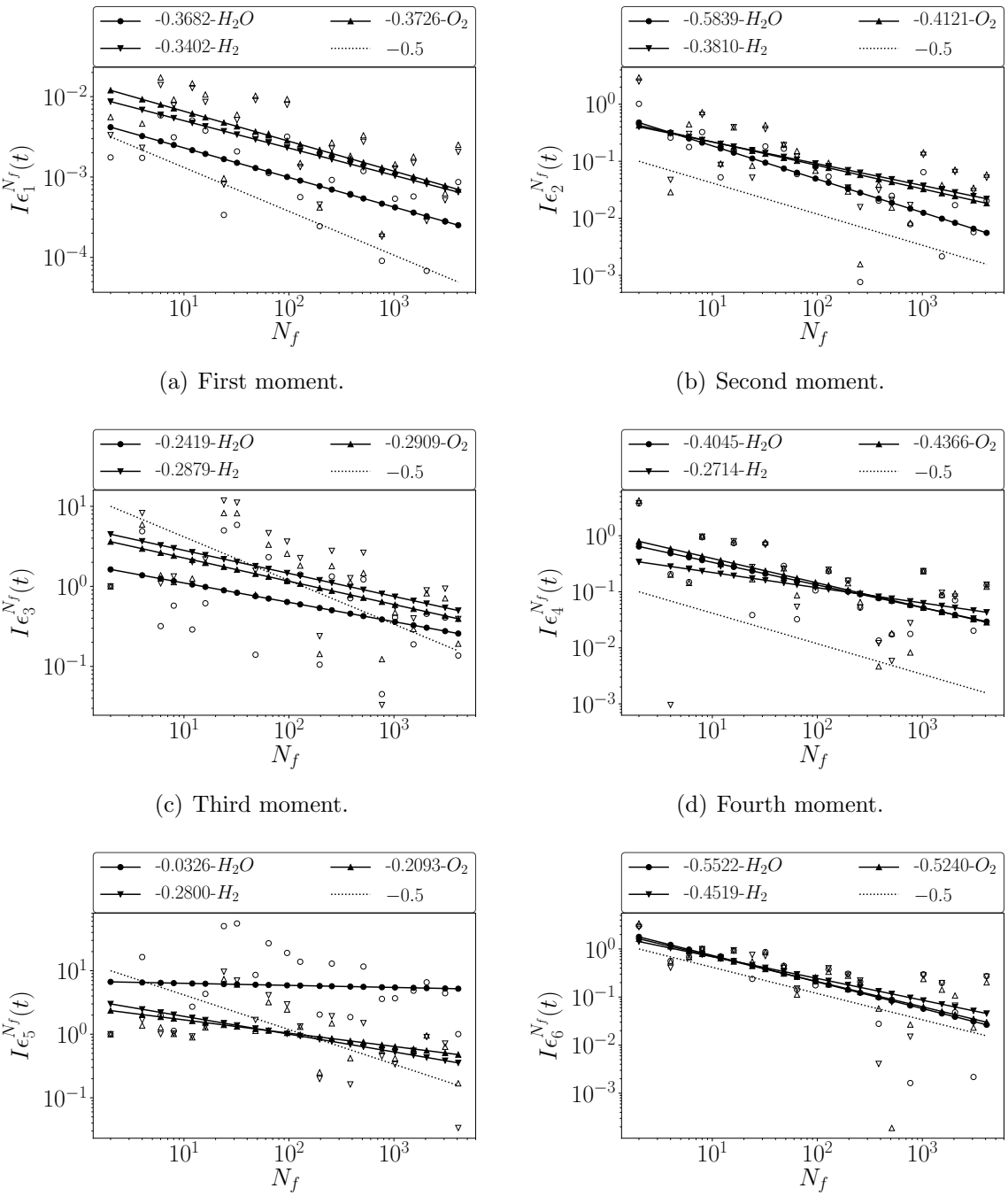

Figure 4.22: Convergence rate for spatially averaged moments at $x = 0.10m$ and $t = 230\mu s$ for the SPDF model. Slope for the trend lines indicated for each stochastic variable along with the theoretical -0.5 slope. Unfilled markers indicate the actual values.

be necessary to statistically achieve relative error less than 1%. The selected position, however, can potentially have large variance and the spatially averaged error presents a well-behaved trend.

The results for the spatially averaged relative error is shown in Figure 4.24. The

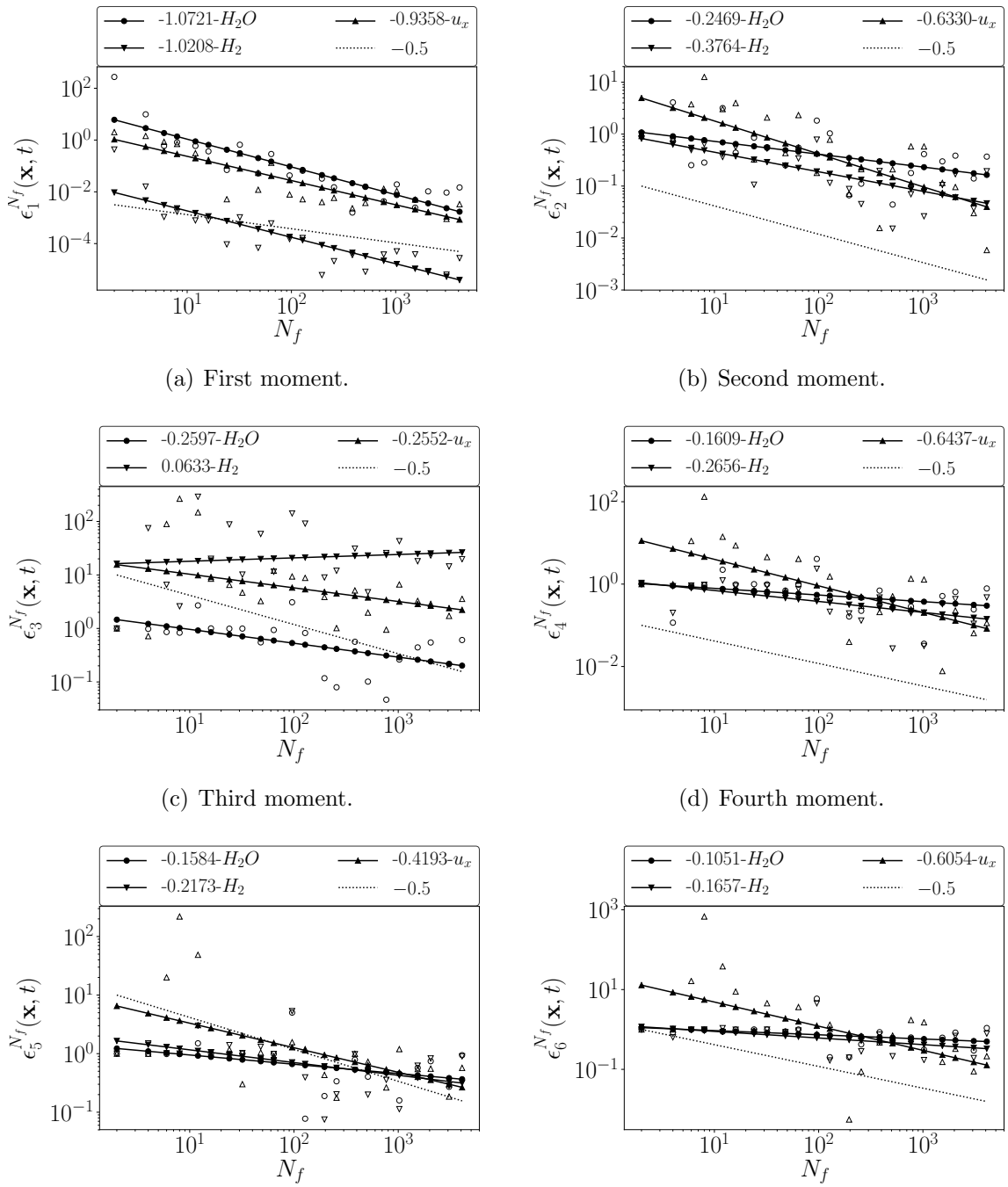

(a) First moment.

(b) Second moment.

(c) Third moment.

(d) Fourth moment.

(e) Fifth moment.

(f) Sixth moment.

Figure 4.23: Convergence rate for local moments at $x = 0.10m$ and $t = 230\mu s$ for the VSPDF model. Slope for the trend lines indicated for each stochastic variable along with the theoretical -0.5 slope. Unfilled markers indicate the actual values.

convergence rate is closer to $N_f^{-0.5}$, being higher for the first and second moment and smaller for the others moments. The relative error is still large is comparison to the SPDF, presented in Figure 4.22. The velocity first moment is statistically smaller then 5% when used 8 fields and it requires 150 fields to achieve 1% error. The remaining

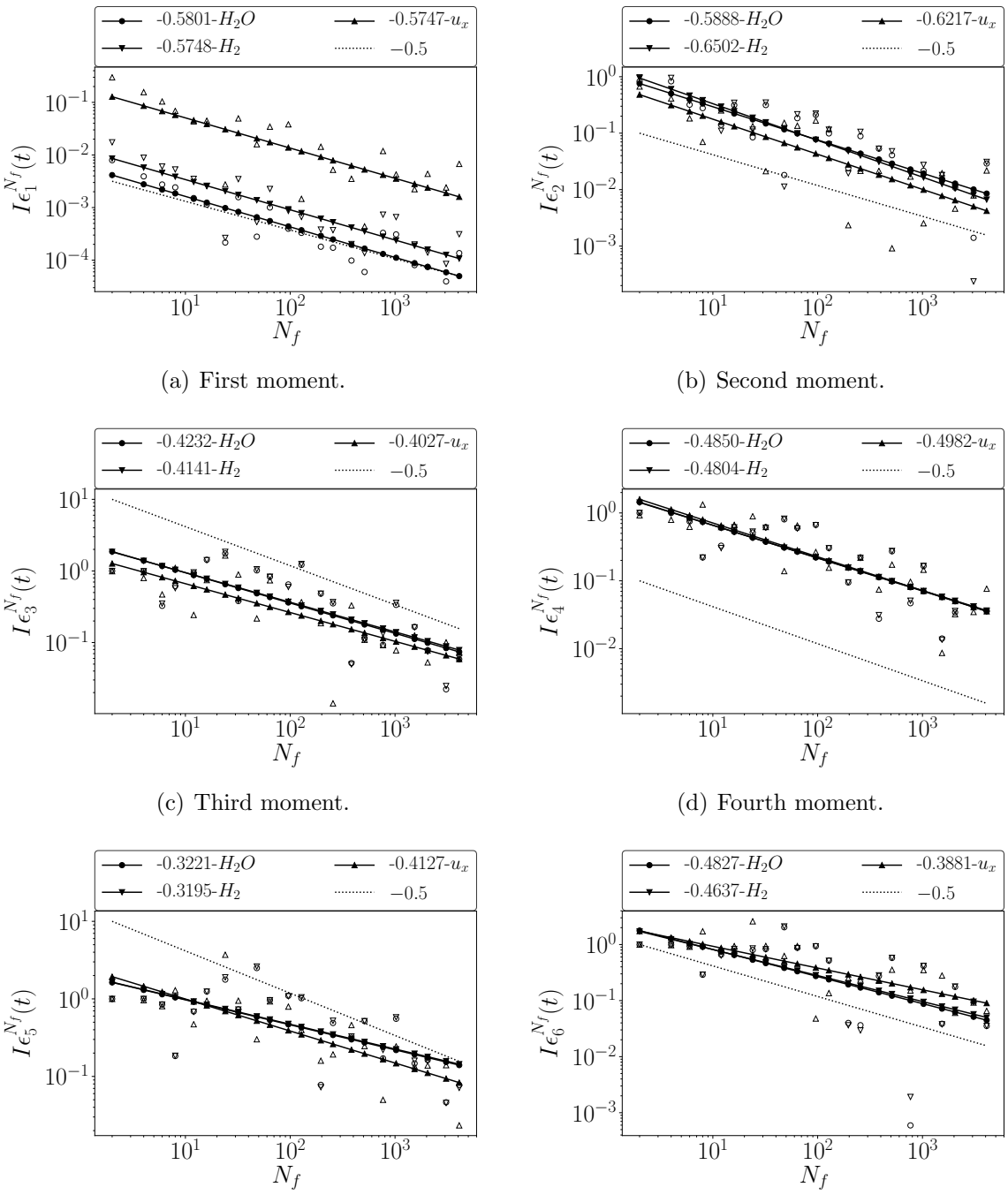

(a) First moment.

(b) Second moment.

(c) Third moment.

(d) Fourth moment.

(e) Fifth moment.

(f) Sixth moment.

Figure 4.24: Convergence rate for spatially averaged moments at $x = 0.10m$ and $t = 230\mu s$ for the VSPDF model. Slope for the trend lines indicated for each stochastic variable along with the theoretical -0.5 slope. Unfilled markers indicate the actual values.

chemical species show relative error smaller than 1% for 8 fields as well. Therefore, the number of 8 fields will be used, although the momentum error can be up to 5% in flows with strong gradients like the detonation wave presented in the reactive shock tube.

The last convergence test result is the construction of the probability density function from the Eulerian stochastic fields simulation. The PDFs using 512, 1024, 2048 and 4096 fields simulations for the scalar PDF model are shown in Figure 4.25 along with Gaussian approximations for the 4096 fields simulation. The PDFs for H_2, O_2, H and H_2O are exposed. The stochastic model captures different PDF shapes for the SPDF, unlike presumed PDF approaches. The converged solution of the 4096 fields simulation does resemble a traditional Gaussian PDF for the VSPDF, though.

Figure 4.26 presents the obtained PDFs using the VSPDF model. The converged 4096 fields simulation this time presents a very similar behaviour to the Gaussian approximation. The PDFs for H_2, O_2, H_2O and u_x are shown. The low variance for the chemical species of the VSPDF model in comparison to the SPDF model, which is firstly shown in Figure 4.20, is also noted in Figure 4.26 mainly in the PDFs for O_2 and H_2O. The PDFs have also higher values, which results from sharp transition and fewer spaces

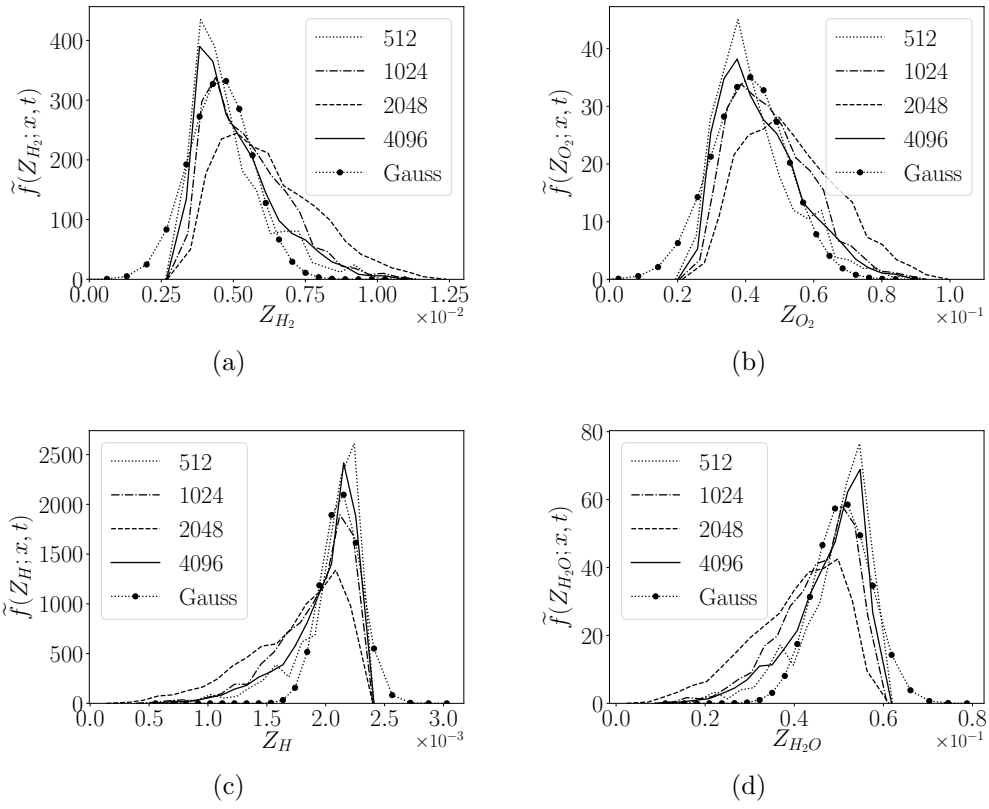

Figure 4.25: Instantaneous PDFs constructed from stochastic fields from the SPDF simulation.

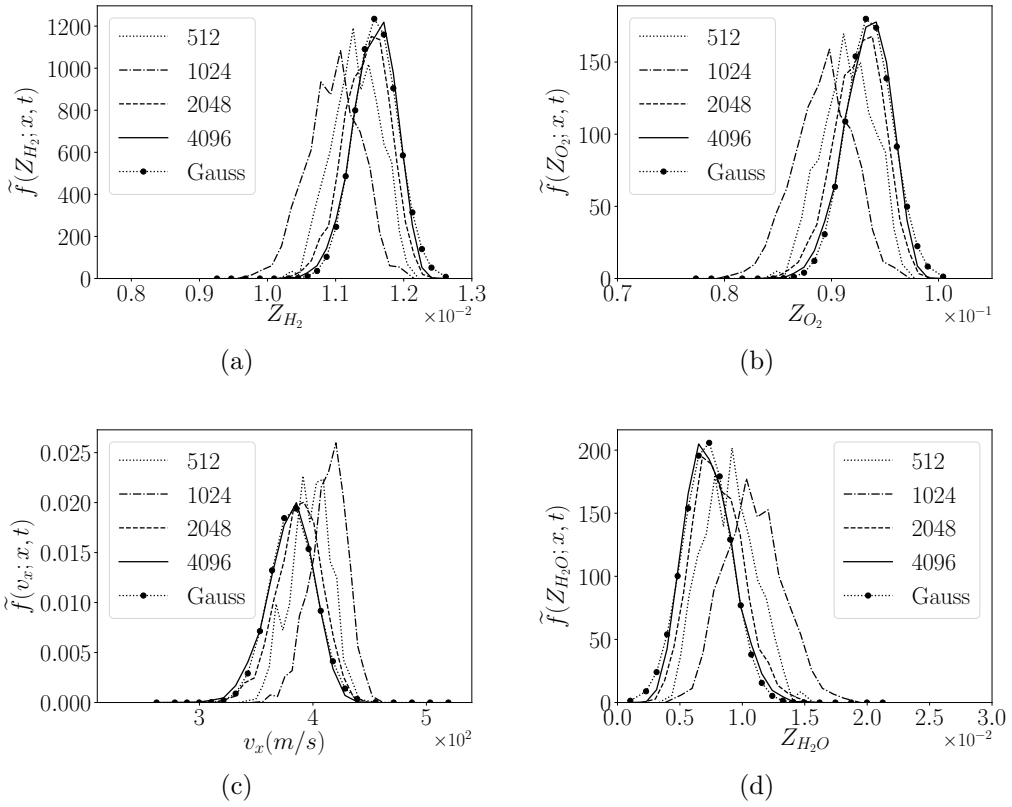

Figure 4.26: Instantaneous PDFs constructed from stochastic fields from the VSPDF simulation.

being accessed. The velocity, however, has expected higher variance and ranges from 300 to $450 m/s$. This reflects from the absence of Wiener terms in the stochastic conservation equation for the chemical species.

The reactive shock tube of Fedkiw *et al.* [151] has been throughly investigated using the SPDF and the VSPDF models. The VSPDF converges faster to the accurate solution, although it may require a much higher number of fields than in comparison to the SPDF on average. However, by investigating the scatter plots and the PDF behaviour of the generated data, the SPDF model represents more meaningful results than the VSPDF. The velocity-scalar PDF model generates narrow and Gaussian-like PDFs and scatter plots with low variance. This could be consequence of the absence of a pressure correction term, which is not included in this work.

4.4 Reactive mixing layer

The investigated reactive mixing layer is the one proposed by Ferrer [26] and later published in [159, 160]. It is a supersonic reactive mixing layer, in which two streams of cold fuel and hot air mix, described in Figure 4.27. The results in this section have been submitted to publication in the *Flow, Turbulence and Combustion* journal.

The composition of the streams at the inlet is shown in Table 4.2. The hot air stream has inlet velocity of $U_1 = 1151.6\ m/s$ (Ma = 1.5) and temperature of 1475 K while the cold fuel has inlet velocity of $U_2 = 669.1\ m/s$ (Ma=1.1) and temperature of 545 K. The thermodynamic pressure on both streams is 94232.25 Pa.

Two cases have been evaluated, a two-dimensional and three-dimensional with the same inlet configuration. The obtained results are then compared with the DNS solution of Ferrer [26]. The convective Mach number is defined as:

$$M_c = \frac{\Delta U}{c_1 + c_2} \tag{4.16}$$

Table 4.2: Mass fractions at the inlet [26].

Specie	Fuel	Oxidizer
Y_{H_2}	0.05	0
Y_{O_2}	0	0.278
Y_{H_2O}	0	0.17
Y_H	0	5.60×10^{-7}
Y_O	0	1.55×10^{-4}
Y_{OH}	0	1.83×10^{-3}
Y_{HO_2}	0	5.10×10^{-6}
$Y_{H_2O_2}$	0	2.50×10^{-7}
Y_{N_2}	0.95	0.55

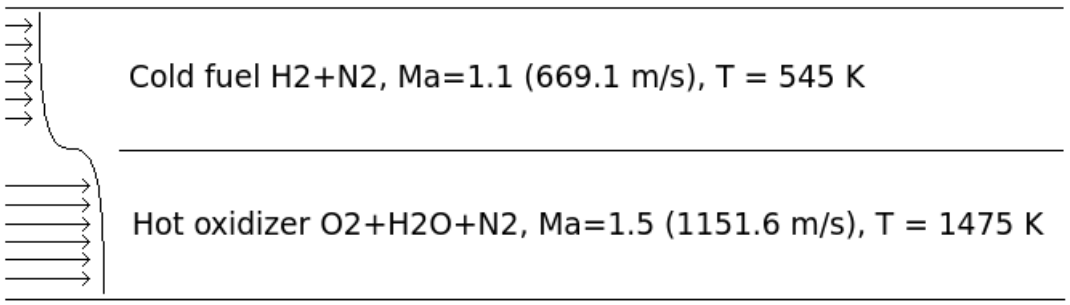

Figure 4.27: Investigated supersonic reactive mixing layer of Ferrer [26].

where $\Delta U = U_1 - U_2$ and c_1 and c_2 represent the speed of sound of the hot air and the cold fuel stream, respectively. The convective Mach number of the test cases is 0.35, which indicates presence of weak compressible effects. It is also useful to define the vorticity thickness growth:

$$\delta_w = \frac{U_1 - U_2}{|\partial \widetilde{u}_1 / \partial x_2|_{max,2}} \tag{4.17}$$

where $|\cdot|_{max,2}$ indicates the maximum of the function at the crosswise coordinate y. The streamwise velocity profile is initialised using a hyperbolic tangent function [26]:

$$u_1 = \frac{U_1 + U_2}{2} + \frac{U_1 - U_2}{2} \tanh\left(\frac{2x_2}{\delta_{w,0}}\right) \tag{4.18}$$

where $\delta_{w,0}$ is the initial vorticity thickness. At last, a perturbation is introduced at the crosswise component of velocity, in similar fashion as Ferrer [26], for the two-dimensional case:

$$u_{2,p} = \varepsilon_1 \alpha U_c \exp\left(-\frac{(x_1 - x_{1,0})^2 + (x_2 - x_{2,0})^2}{\delta_{w,0}^2}\right) \tag{4.19}$$

and for the three-dimensional case:

$$u_{2,p} = \varepsilon_1 \alpha U_c \exp\left(-\frac{(x_1 - x_{1,0})^2 + (x_2 - x_{2,0})^2}{\delta_{w,0}^2}\right) \cos\left(\frac{2\pi(x_3 - x_{3,0})N_p}{L_3} + \varepsilon_2 \pi\right) \tag{4.20}$$

where ε_1 and ε_2 are random numbers between -1 and $+1$, α is the amplitude of the perturbation. The lengths of the domain L_1, L_2 and L_3 are defined accordingly for each test case. The reference initial coordinates $(x_{1,0}, x_{2,0}, x_{3,0})$ are equal to $(0, L_2/2, 0)$. In order to allow at least three complete periods for the perturbation at the spanwise x_3-direction an appropriate value for N_p is chosen. The definition of a convective velocity for the large structures of the flow, U_c, is proposed by Papamoschou and Roshko [161] and also used by Ferrer [26]:

$$U_c = \frac{c_1 U_1 + c_2 U_2}{c_1 + c_2} \tag{4.21}$$

Simulations with the VSPDF, SPDF and Smagorinsky models are therefore performed and compared with the DNS results of Ferrer [26], which used 641691 cells (1739×369) for the two-dimensional case and around 88 millions cells ($1517 \times 325 \times 179$) for the

three-dimensional case.

4.4.1 Two-dimensional case

This test case has been performed using 8 stochastic fields for both VSPDF and SPDF. The number of 8 fields is justified from the reactive shock tube test case. The domain length used is $L_x = 350\delta_{w,0}$ and $L_2 = 80\delta_{w,0}$. A mesh size of 36 thousand cells (360×108) is employed, using a stretching grid that increases the mesh elements density towards the centre line. An initial vorticity thickness value of $\delta_{w,0} = 1.98 \times 10^{-4}\ m$ is used. The amplitude of the perturbation is set to $\alpha = 1.0 \times 10^{-1}$.

The hybrid discretisation is used in all models, employing a 13-point stencil and 8^{th} order accuracy for the DRP and using the second order HLLC-TVD scheme for the sharp gradient regions. Remaining spatial derivatives are also discretised with a fourth order finite difference method. The model constants are set to $C_s = 0.15$, $C_y = 0.0066$ and $Pr_{sgs} = Sc_{sgs} = 1.0$, which are the same as before. A time step of $5.0 \times 10^{-9}\ s$ is employed to ensure that the acoustic Courant number does not increase above 0.2. The combustion mechanism used is the one of Yetter *et al.* [162], using 9 chemical species and 19 reactions. The simulations are run for 1.5 ms that equals to 25 residence times to ensure time convergence. First order zero-gradient boundary conditions are used at the outlets, with a specified boundary at the inlet.

Figure 4.28 shows a contour plot of mass fraction of the radical OH for the SPDF simulation. In this figure it is possible to notice the growth of the vortical structure of the mixing layer, along with the combustion and generation of OH. The results show the slow growth of the edges and big structures using the Smagorinsky model, which is possibly due to a heavy turbulence damp. The SPDF model, in contrast, generates proper mixing levels. The pressure exactly solution on Eq. (3.17) increases the growth of vorticity thickness and the level of combustion.

The VSPDF, however, seems to overly generates turbulence in this test case. The vortices in the VSPDF model seem more disturbed than the SPDF and the generation of OH is not high. The excessive turbulence levels presented in the VSPDF simulation

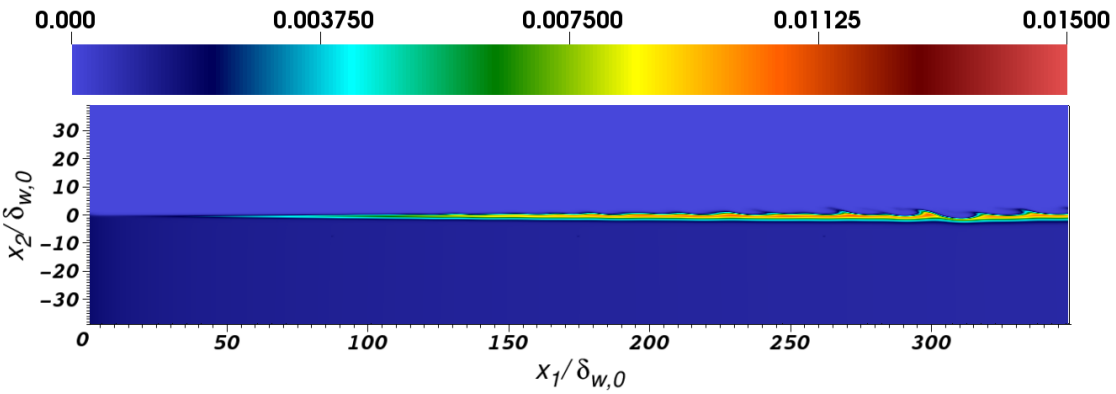

(a) Smagorinsky.

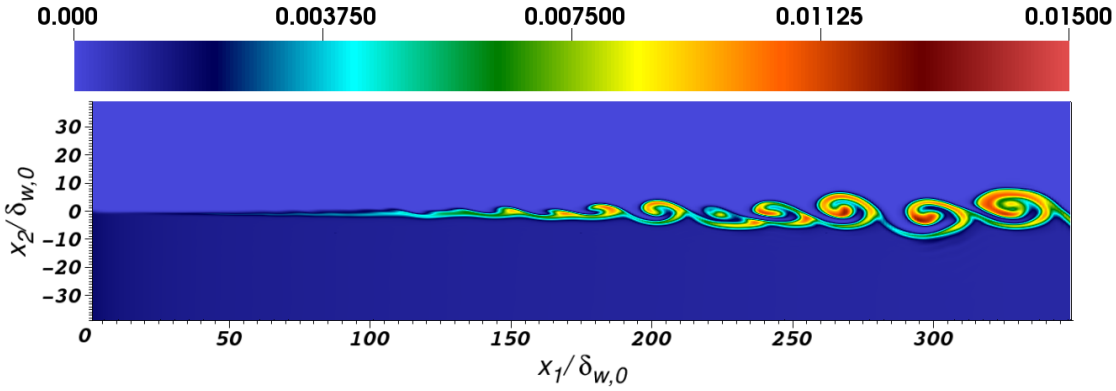

(b) SPDF.

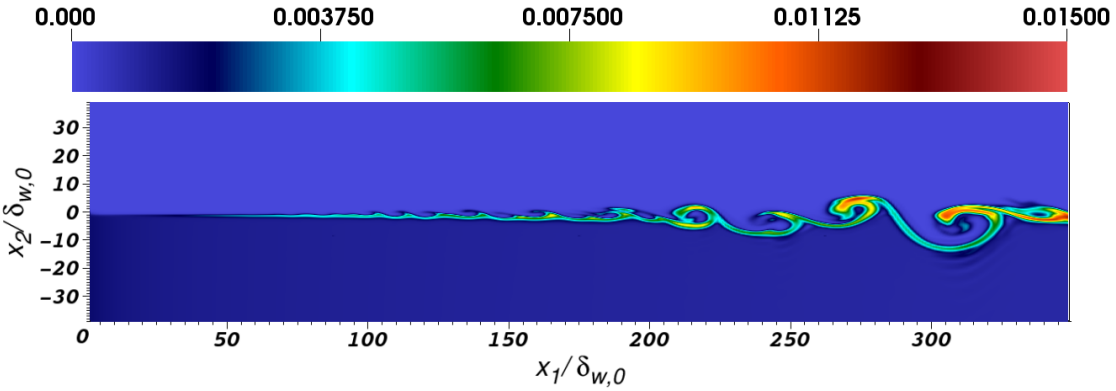

(c) VSPDF.

Figure 4.28: $\widetilde{Y}_{OH}$ radical at $t = 250\mu s$.

does not allow enough time for combustion to occur.

The normalised vorticity thickness growth results are shown in Figure 4.29, where $\eta = (U_1 - U_2)/(U_1 + U_2)$. The mixing layer vorticity thickness growth present asymptotic linear behaviour, as predicted by theory [163]. However, the models present different growth rate, with the SPDF being the closest to the DNS values. The Smagorinsky

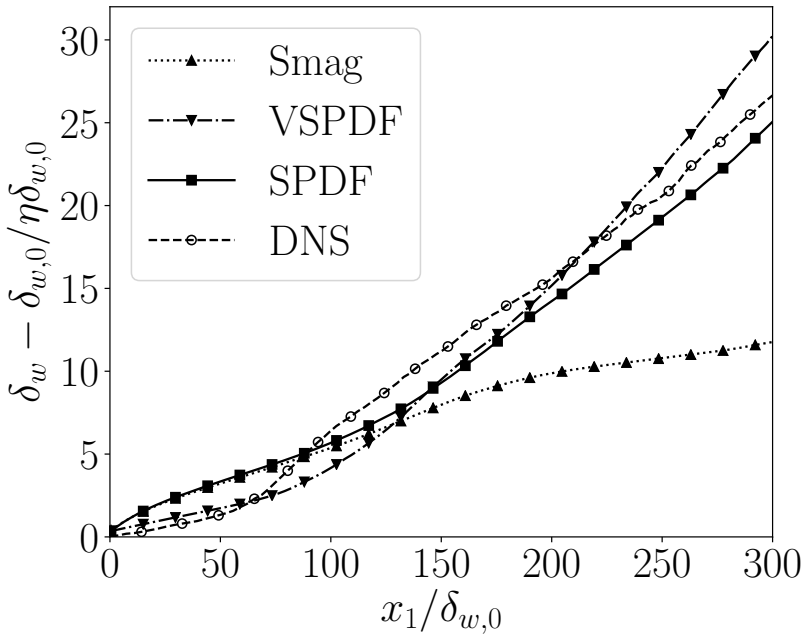

Figure 4.29: Vorticity thickness growth.

model and the SPDF present a very similar growth rate until $x_1/\delta_{w,0} = 125$ when the combustion starts to play a major role. From this point on, the SPDF growth rate shifts to the same value as the DNS one, while the Smagorinsky damps it and prevent the expansion of it. It should be highlighted that the vorticity thickness is a flow property and the SPDF captures it, even if the subgrid model employed for the momentum equations is the Smagorinsky model. The VSPDF, which has no convective subgrid modelling, presents similar growth as the DNS until $x_1/\delta_{w,0} = 60$. Downstream this position the early stages of combustion are sufficient and the mixing layer starts to detach, setting the growth rate to a higher value than the DNS one.

Figure 4.30 shows the normalised averaged axial velocity at several positions. It is possible to see the dominant self-similarity of the velocity profiles, although the VSPDF model presents slightly higher lost of momentum. The momentum for the VSPDF model steadily changes from the streamwise to the crosswise direction at a faster rate than its counterparts. Momentum lost also occurs because of the reaction, but as it can be seen in Figure 4.28, the combustion is not as strong in the VSPDF simulation as in comparison to the SPDF model.

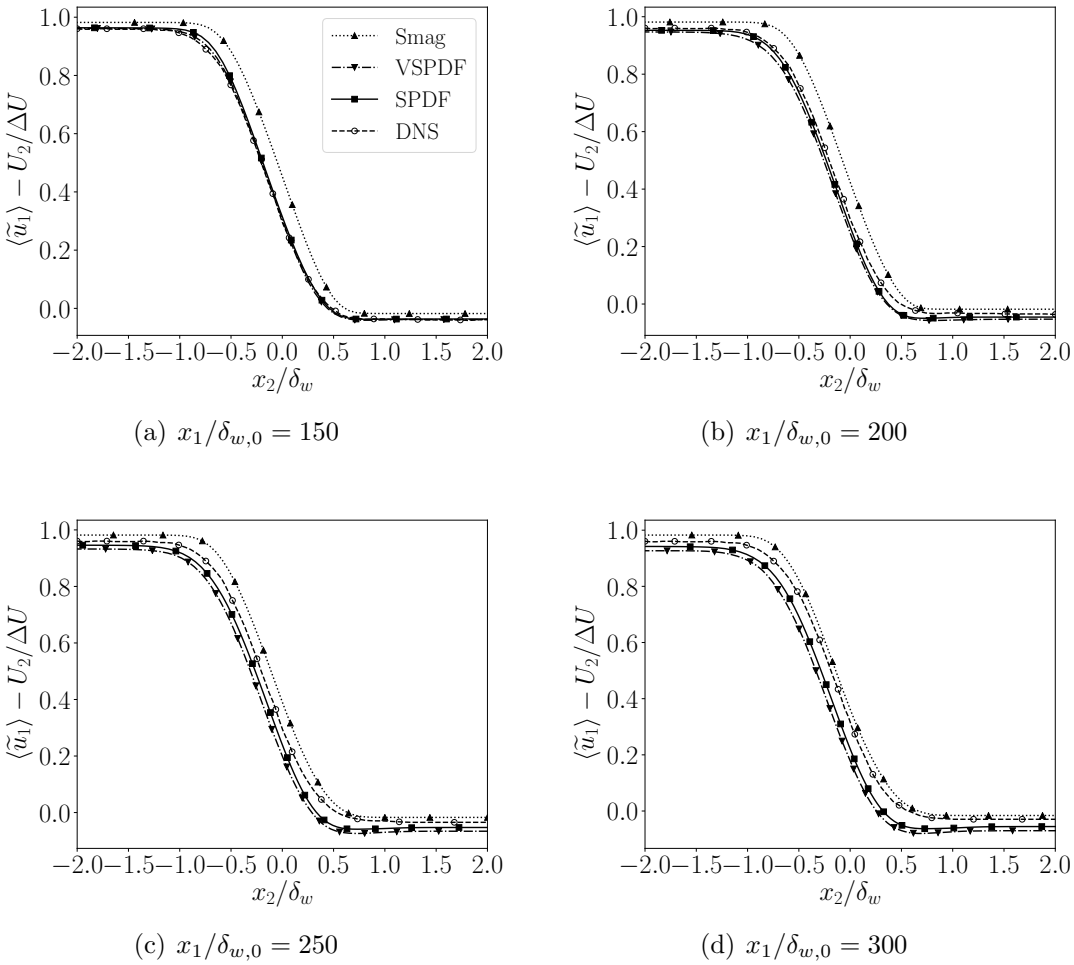

(a) $x_1/\delta_{w,0} = 150$ (b) $x_1/\delta_{w,0} = 200$

(c) $x_1/\delta_{w,0} = 250$ (d) $x_1/\delta_{w,0} = 300$

Figure 4.30: Normalised temporal averaged axial velocity.

The SPDF model is also the closest one to the DNS results. The accurate combustion description without adding extra stochastic noise on the momentum equation allows an accurate description of the flow using a smaller mesh size. At the positions of $x_1/\delta_{w,0} = 250$ and $x_1/\delta_{w,0} = 300$ the SPDF has a non-negligible difference to the DNS results close to $x_2/\delta_w = 0.5$, where the SPDF presents smaller axial velocity. It is useful to highlight that this position is the flame front. The reactive mechanism employed by Ferrer [26] is the O'Conaire *et al.* [164] one, while here it is used the Yetter *et al.* [162] mechanism, which may have influenced this small difference. The O'Conaire *et al.* [164] mechanism also uses 9 species, however, employs 21 reactions instead of 19 reactions of the Yetter *et al.* [162] mechanism.

The Smagorinsky model, as also shown in Figure 4.29, presents very small momen-

tum changes and remains mostly undisturbed throughout the domain. The traditional Smagorinsky model which models the convective part by adding subgrid viscosity is not enough to simulate accurately the two-dimensional mixing layer unless more points are used to trigger turbulence.

Figure 4.31 presents the normalised root mean square of the axial velocity fluctuation u_1''. It is obtained through:

$$\left\langle u_i'' u_j'' \right\rangle = \langle \widetilde{u}_i \widetilde{u}_j \rangle - \langle \widetilde{u}_i \rangle \langle \widetilde{u}_j \rangle ; \quad \widetilde{u}_i = \langle \widetilde{u}_i \rangle + u_i'' \tag{4.22}$$

where the superscript $''$ means temporal fluctuation. The Smagorinsky model, as expected, yields non-accurate results. This arises from the fact that the entire subgrid convective part is modelled and the individual components of the subgrid Reynolds tensor are modelled as a whole. The fluctuations levels are therefore expectedly low.

The SPDF and the VSPDF present very good qualitative agreement with the DNS data with both models showing reasonable levels of self-similarity. The VSPDF does not present perfect agreement with temporal averaged velocity data, however, the fluctuations levels are in good agreement and are slightly below the DNS results. The SPDF shows smaller velocity fluctuation but still closer to DNS and better than the Smagorinsky model.

Figure 4.32 presents the crosswise velocity fluctuation root mean square. Self-similar results are also obtained. For the crosswise velocity the VSPDF presented a better agreement with DNS data than the SPDF model, which in general shows a smaller fluctuation level than the other models. The Smagorinsky model presents very small turbulence levels also in the crosswise direction.

Figure 4.33 shows the averaged cross-correlation of the velocity components. The PDF models present good agreement with DNS data. The VSPDF generates slightly better results in comparison to the SPDF. The VSPDF model, which solves exactly the convective term, represents better the velocity fluctuations overall. The Smagorinsky model requires a finer resolution and a combustion model to reproduce the DNS with accuracy.

Figure 4.34 presents the chemical species temporal average profiles for the Smagorinsky, SPDF and VSPDF models. The DNS results are not included here because they are not shown in Ferrer [26] for the two-dimensional case. It is interesting to notice that both models provide a good mixing level and the profiles are more spread than the Smagorinsky model. The H_2 and O_2 profiles of the SPDF and the VSPDF models are similar, noting that the hydrogen has been more consumed in the SPDF model. The H_2O profile is interesting because shows that the combustion on the Smagorinsky model occurs, however, it remains constrained to the centreline since there is a very small turbulent behaviour. The SPDF and VSPDF models generate moderated levels of H_2O, with the SPDF generating more.

The N_2 profiles also represent the mixing level of each case, being very similar for

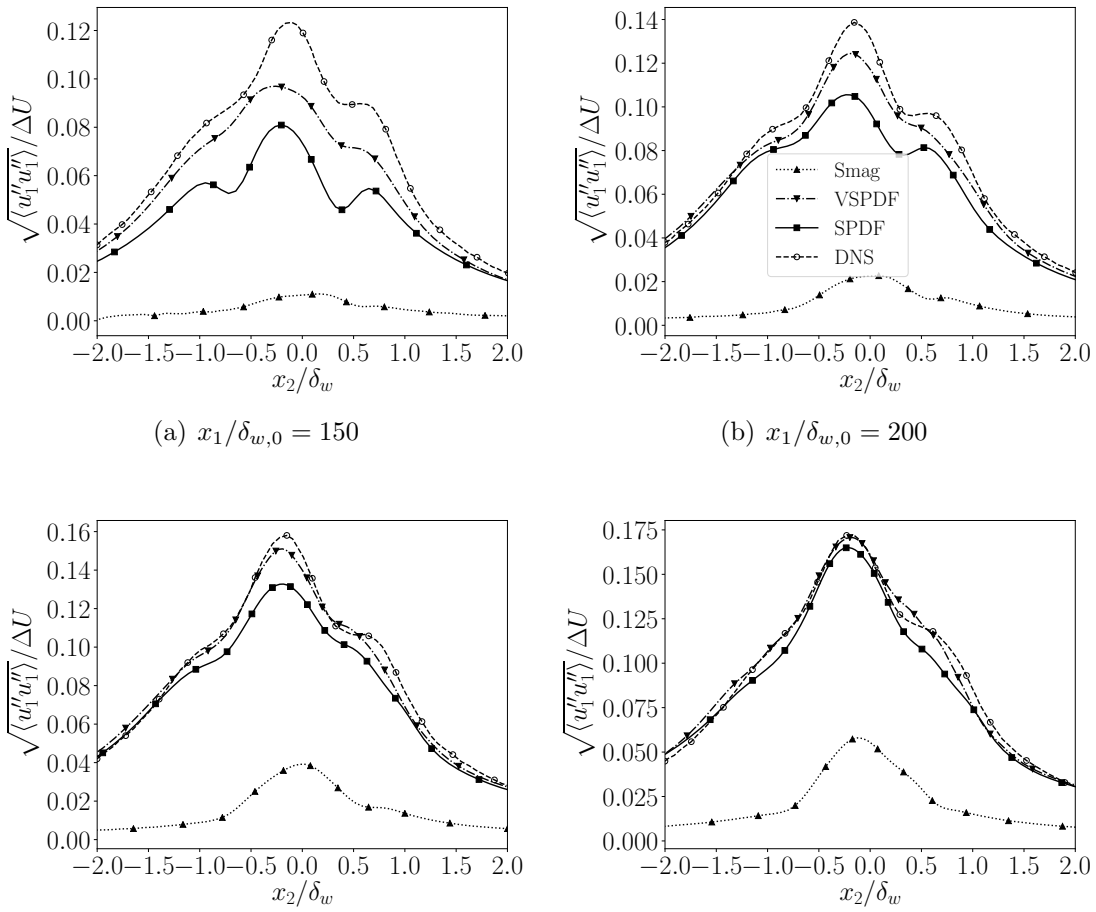

(a) $x_1/\delta_{w,0} = 150$

(b) $x_1/\delta_{w,0} = 200$

(c) $x_1/\delta_{w,0} = 250$

(d) $x_1/\delta_{w,0} = 300$

Figure 4.31: Normalised temporal averaged axial velocity fluctuation rms.

the SPDF and VSPDF. These profiles are also more spread than the Smagorinsky one, like the H_2 and O_2 profiles. The OH and HO_2 also present interesting results. Such as the H_2O profile, the Smagorinsky model generates higher concentration of combustion intermediate radicals, which is mostly due to the reaction being concentrated at the flame front and not expanding to the surroundings. The SPDF have smaller mass fraction of intermediates in comparison to the VSPDF, however, the final product H_2O concentration is higher.

The two-dimensional reactive mixing layer summarises interesting results. It shows the ability of the stochastic models to simulate supersonic flows in a challenging environment and using a complex chemical mechanism for the hydrogen combustion. The SPDF improves the combustion levels while also increases turbulence for this test case. The

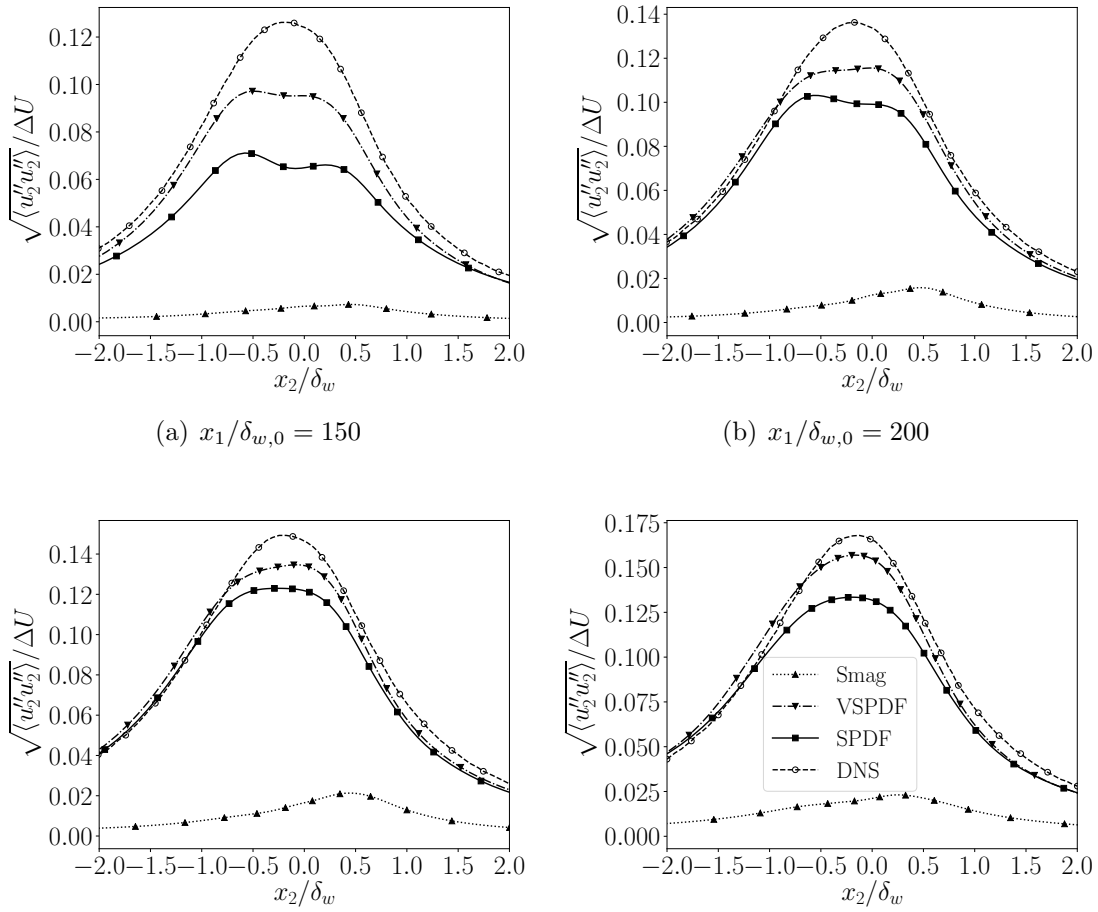

(a) $x_1/\delta_{w,0} = 150$

(b) $x_1/\delta_{w,0} = 200$

(c) $x_1/\delta_{w,0} = 250$

(d) $x_1/\delta_{w,0} = 300$

Figure 4.32: Normalised temporal averaged crosswise velocity fluctuation rms.

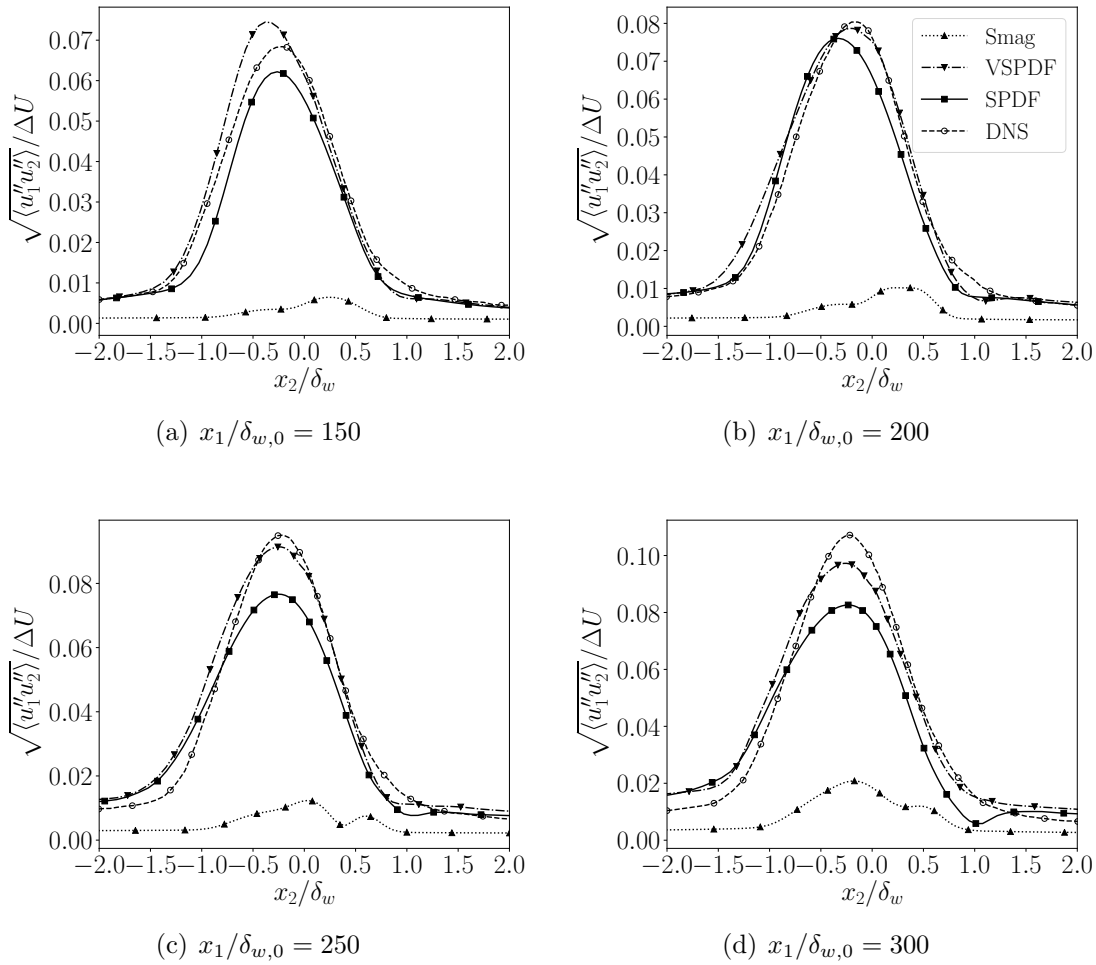

(a) $x_1/\delta_{w,0} = 150$ (b) $x_1/\delta_{w,0} = 200$

(c) $x_1/\delta_{w,0} = 250$ (d) $x_1/\delta_{w,0} = 300$

Figure 4.33: Normalised temporal averaged cross-correlation velocity fluctuation rms.

VSPDF can reproduce adequate levels of momentum fluctuation but the combustion is not fast enough, which is possibly a numerical consequence of the absence of stochastic terms in the chemical species equation, or a too strong micromixing effect. The Smagorinsky model could not generate good results, probably due to the lacking of enough mesh resolution or the inadequacy of this model in a challenging but non three-dimensional environment.

4.4.2 Three-dimensional case

The three-dimensional simulations have similar configuration to the two-dimensional case, presented in Figure 4.27. Eight stochastic fields have been used for the VSPDF and SPDF. The three-dimensional domain size is $L_x = 350\delta_{w,0}$, $L_2 = 80\delta_{w,0}$ and $L_3 = 40\delta_{w,0}$. The

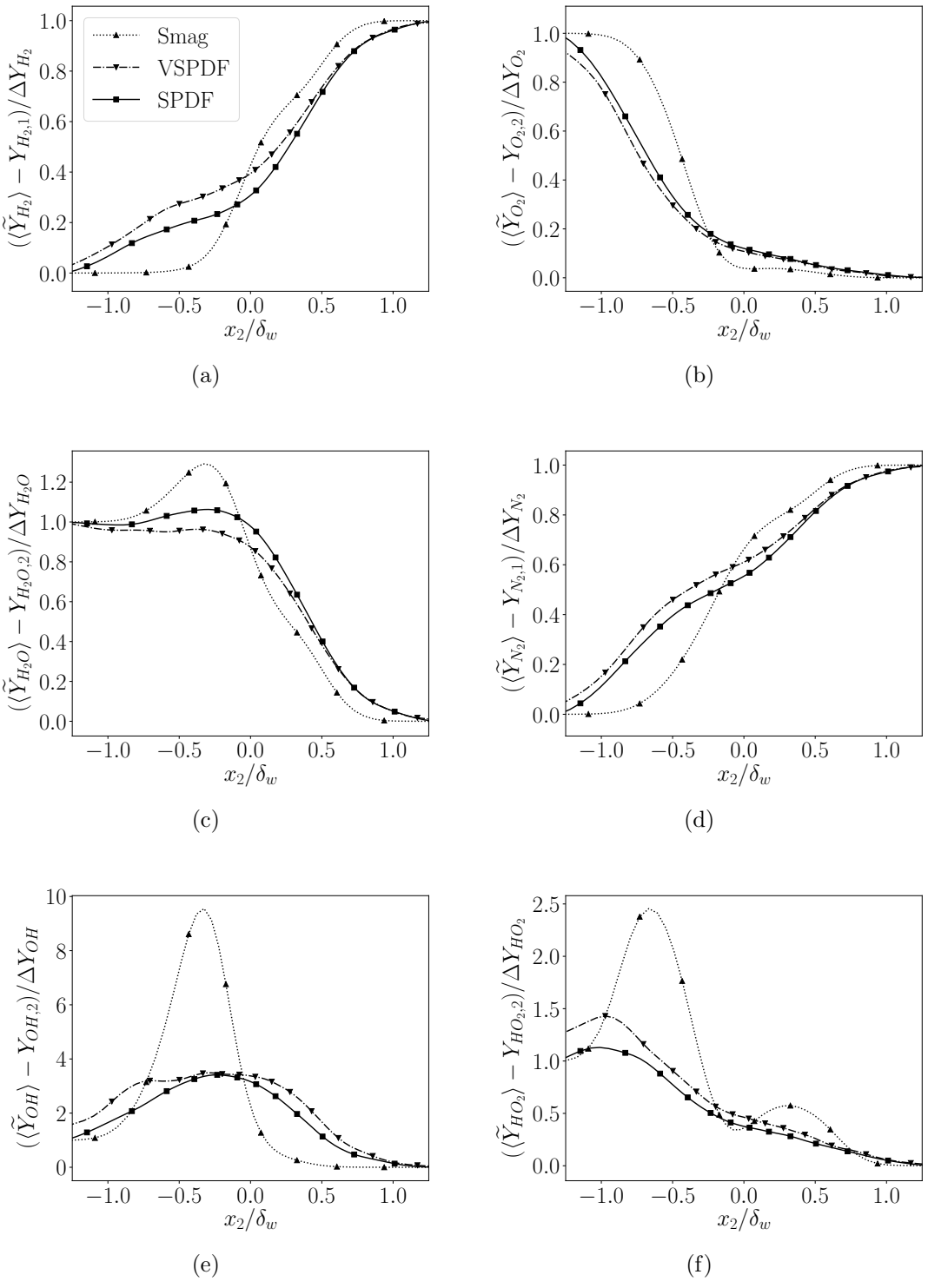

Figure 4.34: Normalised averaged chemical species concentration at $x_1/\delta_{w,0} = 300$.

mesh size for all simulation is of 2.5 millions ($360 \times 108 \times 64$), also applying a stretching grid with more elements at the centreline. The vorticity thickness value used here is the same as in the two-dimensional case, $\delta_{w,0} = 1.98 \times 10^{-4} m$. The amplitude of the

perturbation is $\alpha = 1.0$, a higher value than the one used by Ferrer [26] to compensate for the smaller mesh size.

The same numerical methods that have been employed in the two-dimensional simulation have been used in this case. The simulations ran for 0.6ms, equivalent to approximately 10 residence times to ensure statistical convergence. The LES parameters are the same used before and the Yetter *et al.* [162] chemical mechanism is used to model the hydrogen combustion. First order zero-gradient boundary conditions are also used here similarly to the two-dimensional case.

Figure 4.35 shows isocontours of the instantaneous mass fraction of OH radical. As in the two-dimensional case, the SPDF presents a slightly larger and well defined vortical growth in comparison to the Smagorinsky model. However, the Smagorinsky model, now in a three-dimensional environment, presents better results than the two-dimensional counterpart. The VSPDF model presents a more turbulent behaviour, mostly due to the stochastic term present in the momentum equation and the absence of turbulent viscosity to model the convective terms.

The vorticity thickness growth is shown in Figure 4.36. The DNS results of Ferrer [26], which used 88 millions cells, presented a regular growth rate from $x_1/\delta_{w,0} = 100$ onwards. The SPDF and the Smagorinsky models presents similar growth rate until $x_1/\delta_{w,0} = 150$, when combustion occurs more intensively and the results differ. The SPDF presents a slower rate than the Smagorinsky one, although closer to the DNS. The VSPDF presents a growth rate well above the DNS value from $x_1/\delta_{w,0} = 125$ onwards. This excessive growth is already present in the two-dimensional case to a lesser extent. In the three-dimensional case, however, it is higher and indicates that the VSPDF requires further modelling on the Langevin model or micromixing part.

The averaged axial velocity are shown in Figure 4.37 for the position of $x_1/\delta_{w,0} = 300$. This figure also shows experimental data for non-reacting cases. The reacting cases present momentum losses, which is caused by the combustion. The Smagorinsky model in this case presents higher velocity at the end of the domain, mostly because the combustion is delayed. The SPDF and the VSPDF presents results similar to the DNS. It

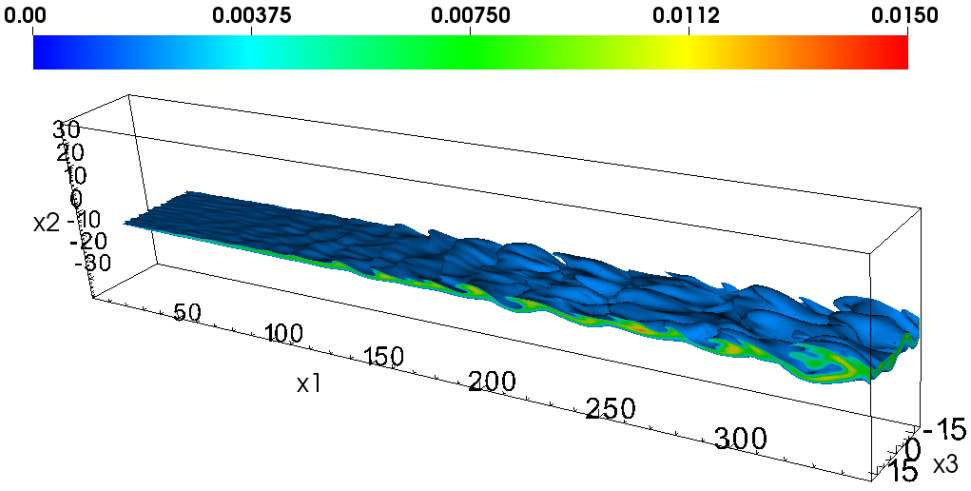

(a) Smagorinsky model.

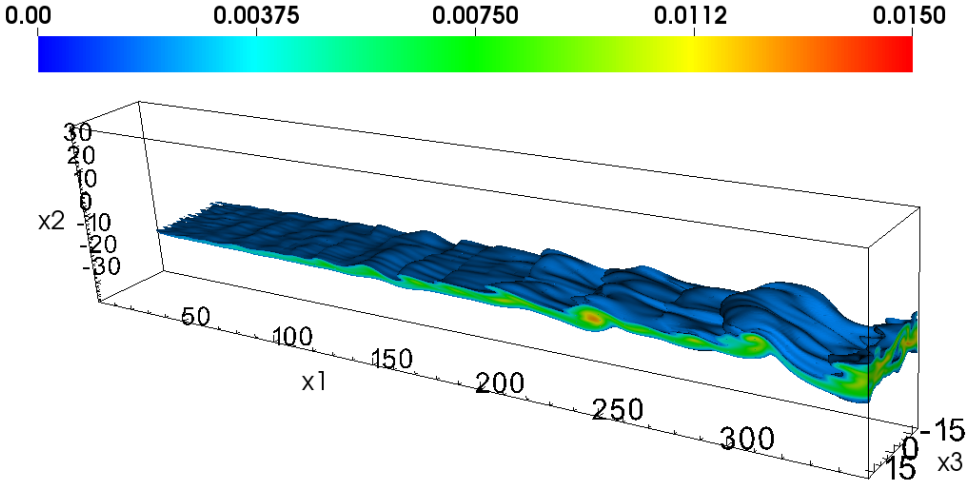

(b) SPDF model.

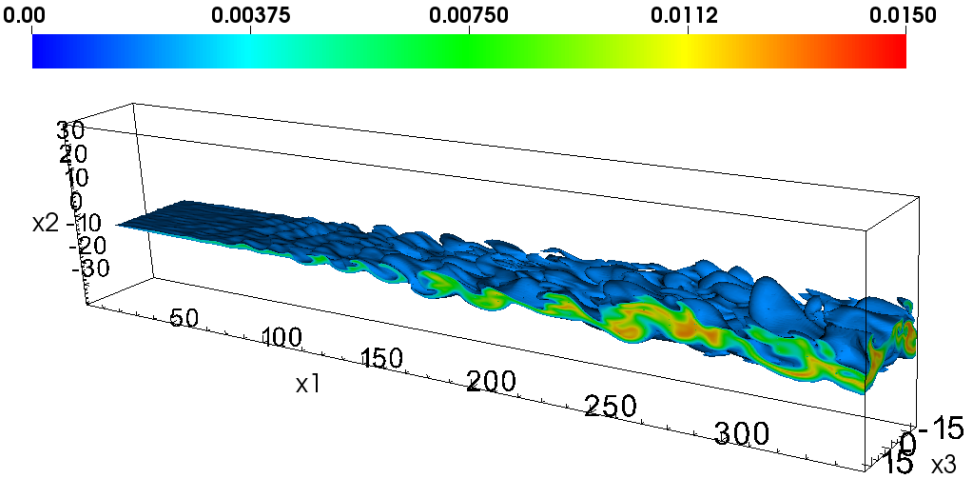

(c) VSPDF model.

Figure 4.35: Isocontours of instantaneous $\widetilde{Y}_{OH}$. Coordinates are normalised by $\delta_{w,0}$.

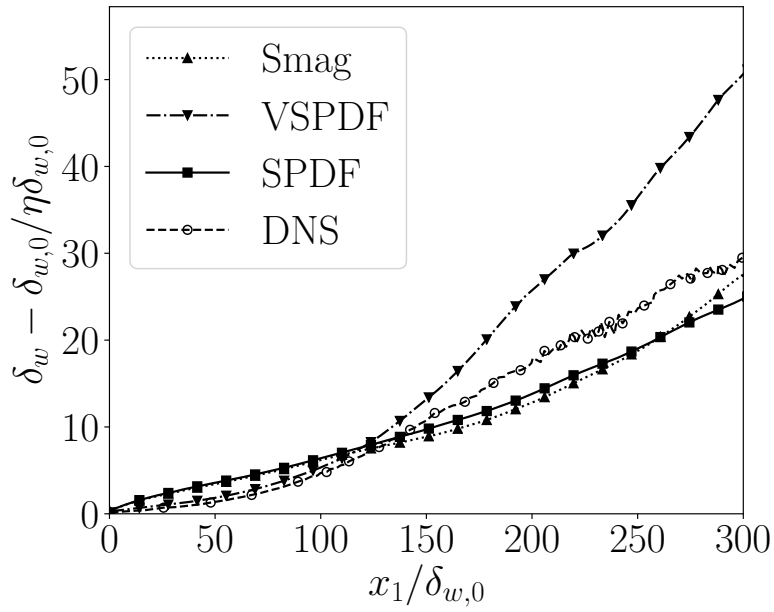

Figure 4.36: Vorticity thickness growth.

should also be highlighted that the SPDF model, although presenting the same sub-grid closure for the convective term as the Smagorinsky model, is still able to capture better momentum statistics. This occurs because of the filtered pressure coupling and better subgrid combustion capturing.

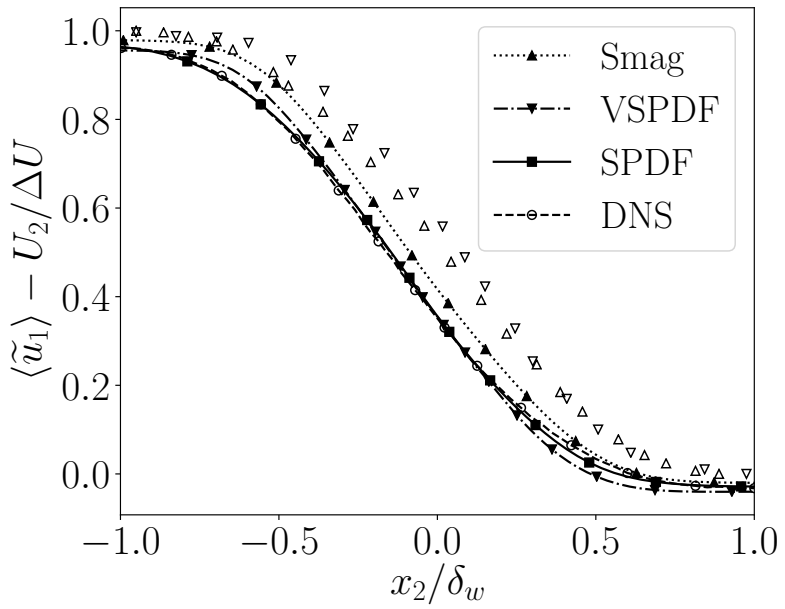

Figure 4.37: Normalised averaged axial velocity at $x_1/\delta_{w,0} = 300$. Experimental data for non-reacting mixing layer of Bell and Mehta [163] ($\triangle$) and Spencer and Jones [165] ($\triangledown$).

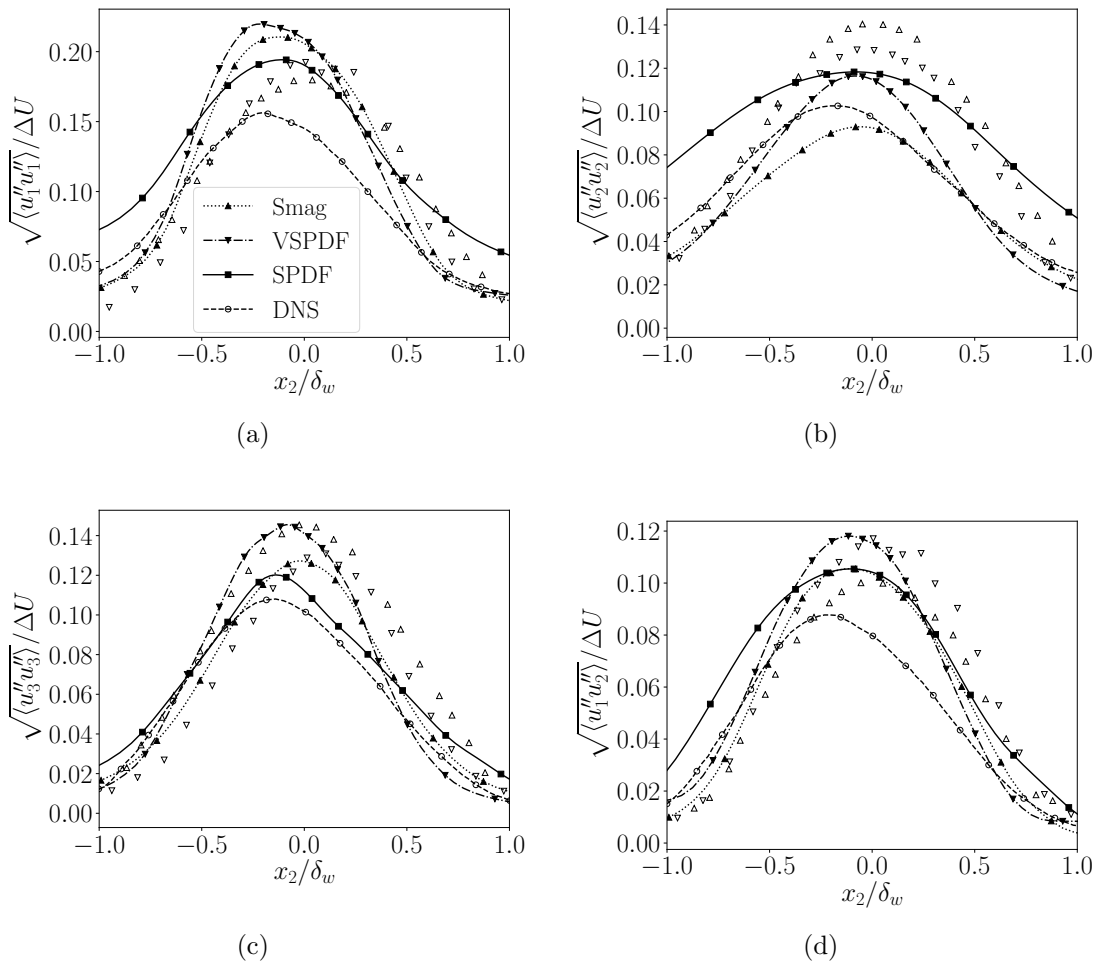

Figure 4.38: Normalised averaged velocity rms at $x_1/\delta_{w,0} = 300$. Experimental data for non-reacting mixing layer of Bell and Mehta [163] ($\triangle$) and Spencer and Jones [165] ($\triangledown$).

Figure 4.38 shows the normalised averaged velocity rms, also at $x_1/\delta_{w,0} = 300$. Results for the Smagorinsky model are better than in comparison to its two-dimensional counterpart. All models in this simulation show reasonable qualitative and quantitative agreement with the DNS data. The VSPDF generates higher fluctuation levels and the SPDF shows wider profiles. The results are also close to the experimental non-reacting data, showing that for this case the combustion and the fluctuations levels do not present strong correlation [26].

The last results are the average mass fractions, shown in Figure 4.39 and their respective fluctuations, presented in Figure 4.40. The comparison in this case can be difficult, since the DNS data was generated using the O'Conaire *et al.* [164] mechanism. Overall, the SPDF presents more diffusive profiles, with less H_2 and O_2 and more H_2O in

comparison to the VSPDF and Smagorinsky simulations.

The mass fraction of N_2 also indicates a higher mixing for the SPDF. The VSPDF and Smagorinsky showed a somewhat similar behaviour, with the VSPDF closer to the DNS data for this radical. The OH profiles show that the SPDF and VSPDF models generate a thicker flame than the DNS results. The HO_2 radical DNS profile could not be reproduced by any model, which can be related to the different chemical mechanism used here.

The mass fractions fluctuation profiles presents some interesting profiles. As expected, the SPDF shows more diffusive behaviour overall, also shown in the averaged mass fraction results. The fluctuations levels for H_2, O_2, H_2O and N_2 for all models are slightly higher than the DNS values, however, with good qualitative agreement.

The SPDF N_2 fluctuation profile, though, presents two peaks, possibly because of the higher mixing level on both streams. The OH and HO_2 fluctuations are somewhat different from the DNS results, which is also expected because of the different combustion model. The results, however, are of the same order of magnitude and also comparable to the DNS data.

Overall, the SPDF and VSPDF results are capable of reproducing DNS data with some limitations. The three-dimensional simulations are challenging and includes many physical phenomena that are difficult to simulate. The Smagorinsky model and the implicit/quasi-laminar approach to deal with the combustion performs better in a three-dimensional domain.

The developed stochastic models to solve the SPDF and the VSPDF also show reasonable results. They are able to reproduce average and fluctuation DNS levels to an extent. The SPDF through the pressure coupling improves momentum and other flow variables. It is a very consistent model and generates good results using one-dimension to three-dimensional domains.

The VSPDF, however, misses extra closures related to the approximations to deal with numerical shocks, such as the inclusion of a stochastic pressure for each field. Although its results are reasonable, the excessive momentum growth rate, also presented in the two-

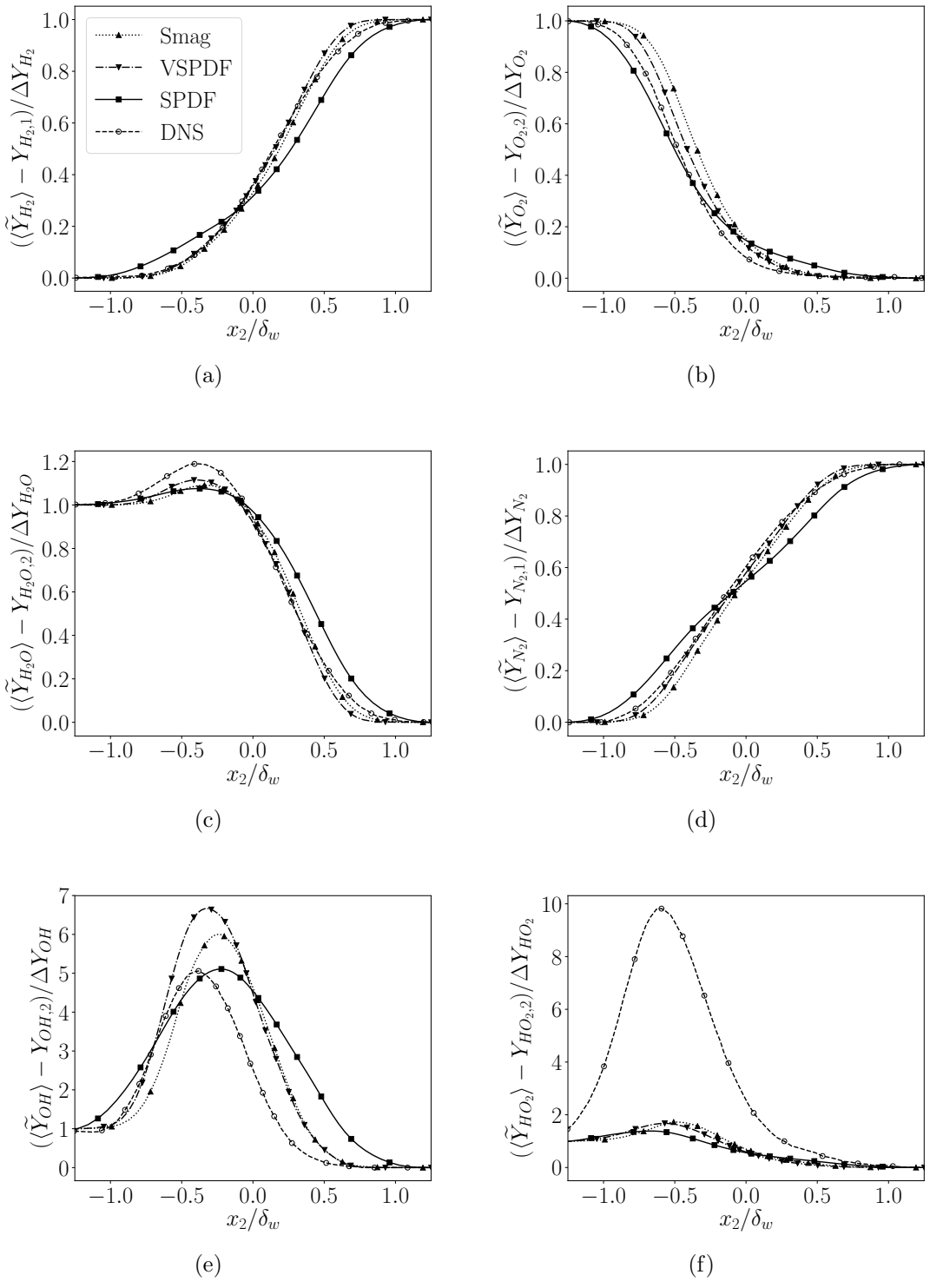

Figure 4.39: Normalised chemical species mass fractions at $x_1/\delta_{w,0} = 300$.

dimensional simulation, shows that the Langevin model must be improved. The inclusion of an extra micromixing term or another constant optimisation can be performed to deal with this matter. Further investigation is therefore required to be used in highly complex

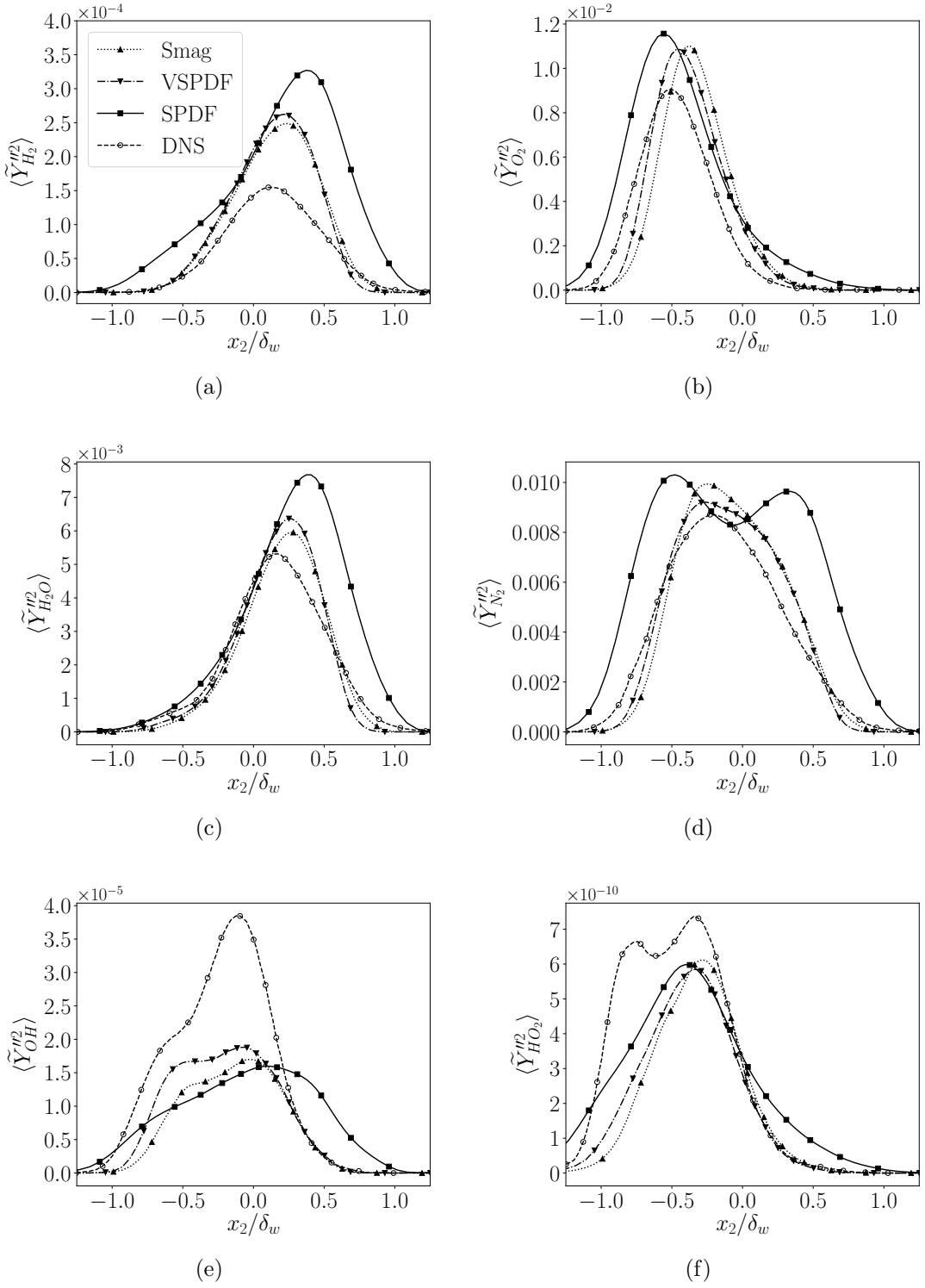

Figure 4.40: Averaged chemical species mass fractions fluctuations at $x_1/\delta_{w,0} = 300$.

simulations.

4.5 Supersonic burners

The numerical verification has been performed through the HIT test case, the one-dimensional reactive shock tube and the two and three-dimensional mixing layers. These simulations have been conducted to assess the reliability of the models and the developed code. After this step, a numerical validation against experimental data is still necessary to assess the accuracy of the models in real cases.

Two supersonic burners with canonical configuration have been chosen to evaluate the code. The supersonic burner of Cheng *et al.* [7] offers plenty of data for mole fraction of species and velocity. It has therefore been consistently used in the literature for investigation of supersonic phenomena and model evaluation [14, 166, 32, 18]. It is a lifted supersonic hydrogen flame with a co-flow of vitiated air, presenting a daunting task under the numerical modelling point of view.

The other supersonic burner used is the one of Evans *et al.* [152], which is similar to the configuration of the Cheng's burner. However, its data set is older and more limited, presenting only the pitot-pressure data instead of the velocity field and few chemical species mass fractions. Nevertheless, it has also been used in several numerical studies [167, 14, 9] for code assessment and validation.

The two burners have been simulated with coarse and fine mesh. Part of the Cheng's burner assessment has been published in Almeida and Navarro-Martinez [142]. The VSPDF model evaluation performed by [142] corroborates what has been verified in the numerical studies. The VSPDF needs further closures and reliability before being used in a heavy simulation. Therefore, because of the higher computational power demanded only the Smagorinsky and the SPDF models are evaluated henceforth.

4.5.1 Cheng's burner

The Cheng's burner configuration is presented on Table 4.3. It consists of a pure injection of hydrogen at Ma = 1, resulting in a transonic and very unstable flow. The co-flow of vitiated air is injected at Ma = 2 and high temperature, resulting in a self-ignited flame.

Table 4.3: Supersonic burner configuration of Cheng *et al.* [7].

Dimensions	
Nozzle exit inner diameter	17.78 mm
Fuel injector inner diameter	2.36 mm
Fuel injector outer diameter	3.81 mm
Vitiated air exit conditions	
Pressure	107 kPa
Temperature	1250 K
Mach number	2.0
Velocity	1420 m/s
O_2 mole fraction	0.201
N_2 mole fraction	0.544
H_2O mole fraction	0.255
Fuel exit conditions	
Pressure	112 kPa
Temperature	540 K
Mach number	1.0
Velocity	1780 m/s
H_2 mole fraction	1.0

A domain size of $70D \times 60D \times 60D$ is used, where D is the injector inner diameter equals to 2.36 mm.

Two meshes have been employed, also using a stretching grid formulation allowing more points towards the centre and close to the burner injection, as presented in Figure 3.3. A mesh of $168 \times 168 \times 168$ - 4.7 millions - points (MESH1) is used to perform Smagorinsky and SPDF simulations, the latter including eight stochastic fields. A second mesh with $336 \times 336 \times 336$ - 37.9 millions - points (MESH2) is also used to perform a Smagorinsky simulation. In this way, the Smagorinsky model with the quasi-laminar approach should present results as accurate as the SPDF with 8 fields. Simulations with the fine mesh have been performed using ARCHER, the UK National Supercomputing Service under the UK Turbulent Reacting Flows Consortium (UKCTRF).

The discretisation parameters are the same as used in the previous section. A time-step of 1.0×10^{-8} s is used for the coarse mesh and 5.0×10^{-9} s for the finer one, keeping the CFL number < 0.2. Ten resident times are simulated on the coarse mesh case and five on the finer mesh, with both cases achieving statistical convergence.

The LES parameters are the same as used in the three-dimensional reactive mixing

layer described in the previous section. Prescribed boundary conditions are employed at both injector inlets, while a constant inflow of air at $20m/s$ is specified at the remaining bottom boundary. Synthetic turbulence is included using a digital filter [168] in the fuel and co-flow injector, with 18% and 22% of the axial velocity value, as in Bouheraoua *et al.* [18]. Zero-gradient is set in the remaining boundaries. The simulations are performed also using the Yetter *et al.* [162] hydrogen mechanism of 9 species and 19 reactions.

Figure 4.41 shows contour plots of the instantaneous temperature for the MESH1 case. The flame seems better connected on the SPDF case, although the general flame shape is very similar. Overall, both flames present poor combustion when compared to other numerical studies [166, 18]. The diffusion levels presented are not enough to mix the reactants fast enough, which can be an issue of the Yetter *et al.* [162] mechanism for this test case.

The contour plots for instantaneous pressure and temperature for the MESH2 case are shown in Figure 4.42. It is possible to see in the pressure contour the shock waves present close to the burner inlet, in regions of fast transition of high and low pressure. It

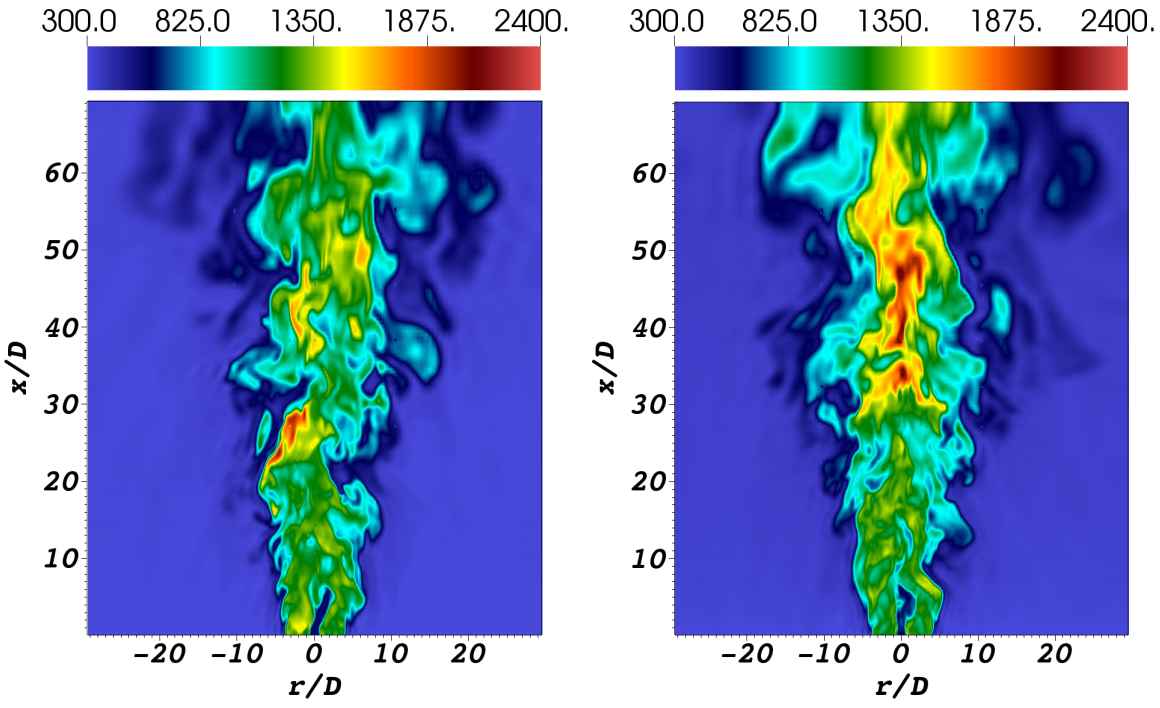

(a) Smagorinsky. (b) SPDF.

Figure 4.41: $\widetilde{T}(K)$ at an instantaneous time for the MESH1 case.

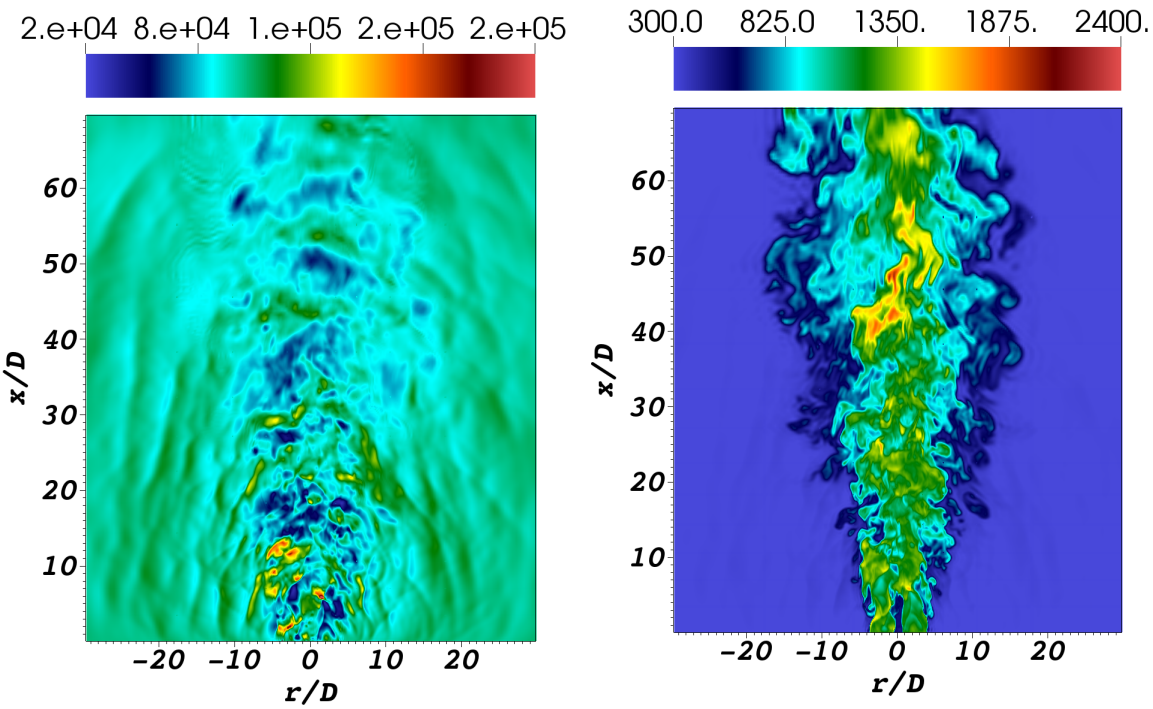

(a) $\overline{p}$(Pa). (b) $\widetilde{T}$(K).

Figure 4.42: Smagorinsky simulation instantaneous contour plots for the MESH2 case (Smag2).

should be noticed on the temperature contour plot that the flame is not well connected either, despite the high resolution of the test case. The vitiated air co-flow jet mixes more with the ambient air in comparison to the one of Bouheraoua *et al.* [18], although the turbulence levels at the inlet are set the same.

The radial profile results are obtained through the azimuthal average of the temporal mean values. In this way a faster convergence is achieved. The results for the axial velocity are presented in Figure 4.43. For the position closer to the burner, $x/D = 0.85$, the velocity profile of the vitiated air co-flow does not seem to fit the experimental inlet conditions. In fact, Cheng *et al.* [7] state that the velocity of the co-flow can be 10-20% lower than the values specified on Table 4.3. The specified boundary condition, however, has been used in the literature for numerical simulations [166, 18] and it is kept here for the purposes of comparison. All models presented somewhat a higher diffusion level than the experimental one and there are no remarkable differences between them. Only at the farther downstream position of $x/D = 43.1$ that the results of Smagorinsky and MESH2 (Smag2) present a better fit to the experimental data than the SPDF and Smagorinsky

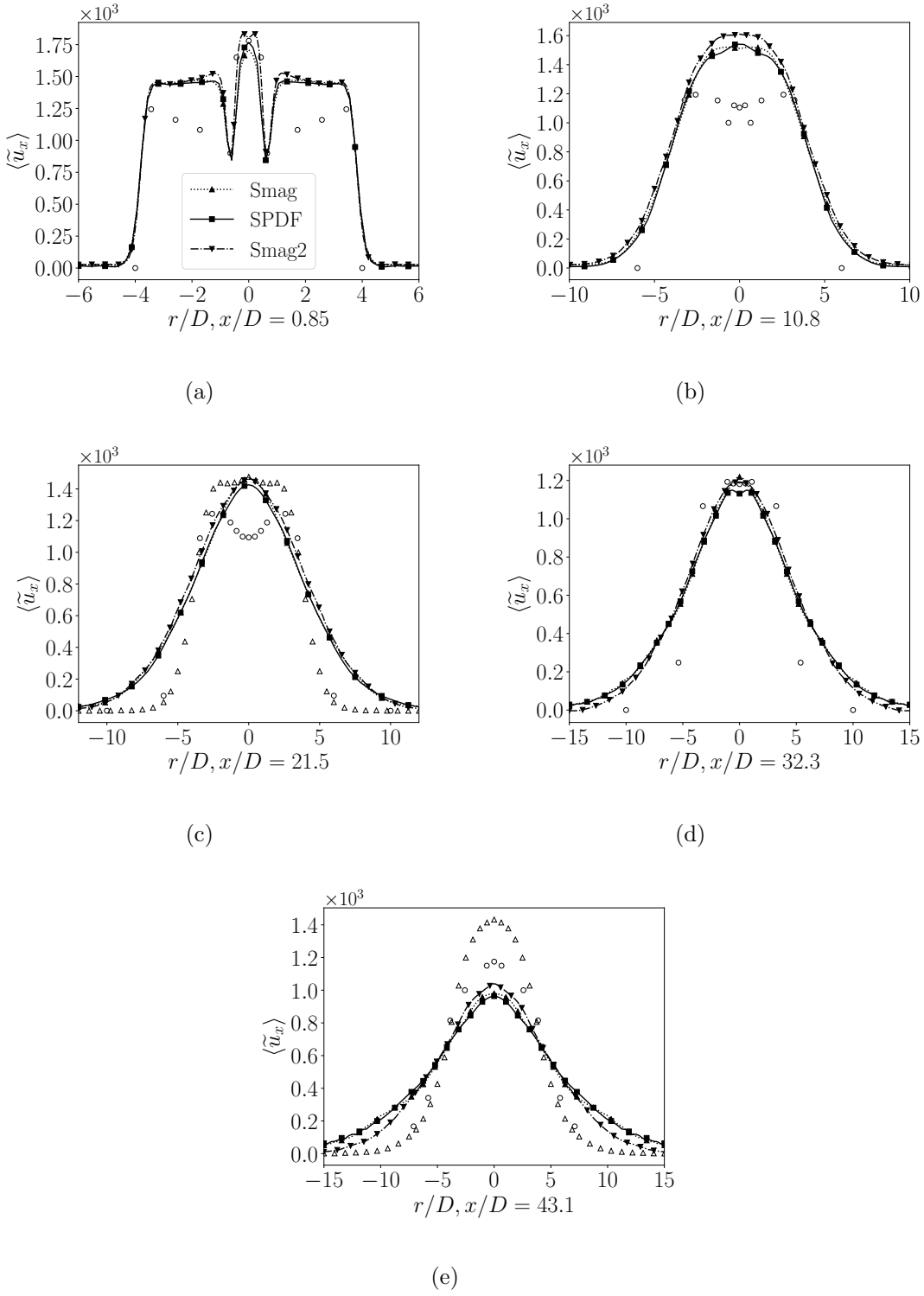

Figure 4.43: Averaged axial velocity (m/s) results. Experimental data of Cheng *et al.* [7] (○) and numerical SPDF data of Almeida and Navarro-Martinez [142] (△).

models.

The results of Almeida and Navarro-Martinez [142] are included for the positions of $x/D = 21.5$ and $x/D = 43.1$ and presents better agreement. These results are obtained

a coarse mesh of 0.2 millions points, which highly increases the viscosity and amplified the SPDF model. This indicates that a better constant adjustment to the micromixing model may be necessary, allowing extra stochastic effects.

Figure 4.44 and Figure 4.45 present the averaged mole fractions and temperature, and their rms counterparts, respectively, at the position $x/D = 0.85$. It is interesting to note that the boundary conditions are mostly well reproduced by all simulations, including the rms levels of temperature. As expected, all simulations could accurate reproduce the data close to the burner. The OH radical is present on the experimental data because it is formed on the vitiated air, which is not specified in these simulations.

Figure 4.46 and Figure 4.47 show the results at $x/D = 10.8$. At this position the results are still fairly similar, although the SPDF simulation presents slightly higher temperature and production of OH radical. The rms of OH, shown in Figure 4.47, presents a better agreement to the experimental data. The averaged experimental data indicate a poor mixing, in which the O_2 and N_2 are not completely mixed with the fuel jet. In the numerical simulations, both O_2 and N_2 radicals are in higher concentrations for all models than the experiment. The rms data, overall, seems more sparse and also more diffusive.

The results at $x/D = 21.5$ are presented in Figures 4.48 and 4.49, where the differences between the models start to become more evident. The SPDF model with MESH1 shows better agreement with experimental values. Nevertheless, the Smagorinsky model shows similar qualitative behaviour. Both meshes used for the Smagorinsky model generate quite similar results, which has also been the case for Bouheraoua *et al.* [18]. Figure 4.48 includes the SPDF results of [142], with a mesh of 0.2 millions. The simulation presented similar levels of air entrainment in comparison to the experimental data. The rms profiles are similar overall, with the SPDF simulation presenting higher agreement for the O_2 and OH mole fractions.

Figures 4.50 and 4.51 shown the results at $x/D = 32.3$. The presence of the radical OH indicates that for all cases, on average, the flame has already ignited. The SPDF model, although with a coarser mesh, is able to better reproduce the experimental data.

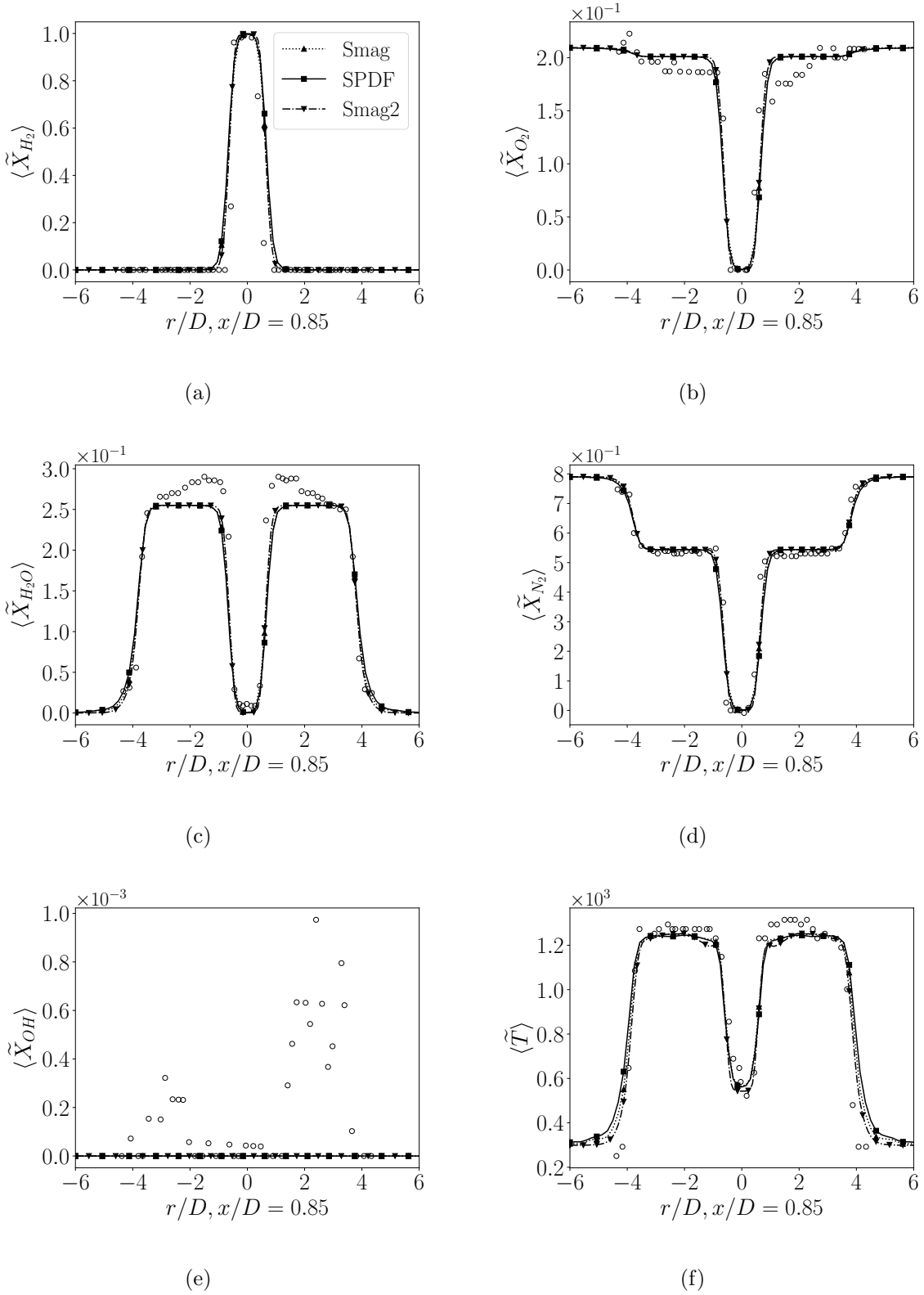

Figure 4.44: Averaged results for mole fractions and temperature. Experimental data of Cheng *et al.* [7] (○).

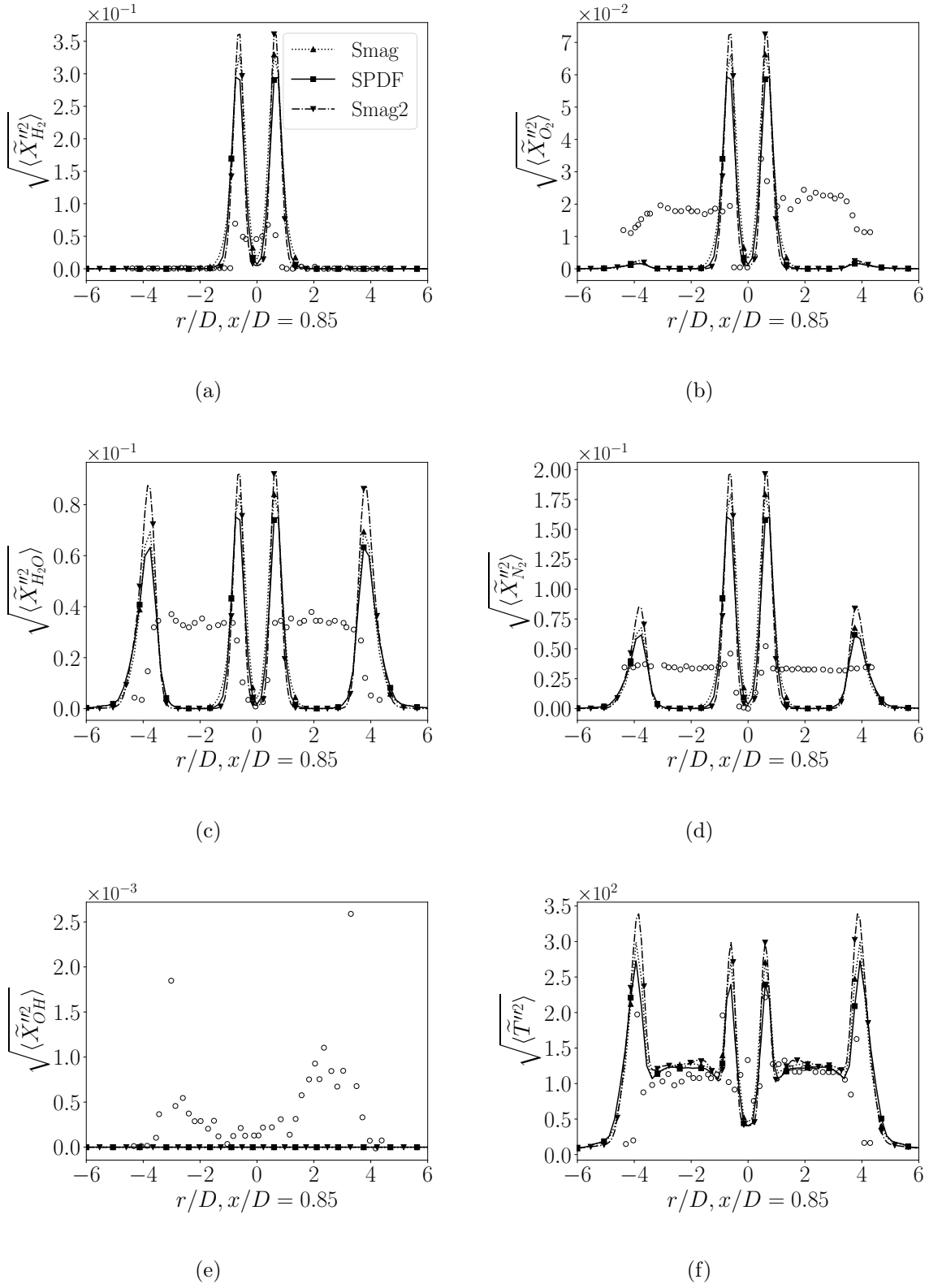

Figure 4.45: Averaged mole fractions and temperature rms results. Experimental data of Cheng *et al.* [7] (○).

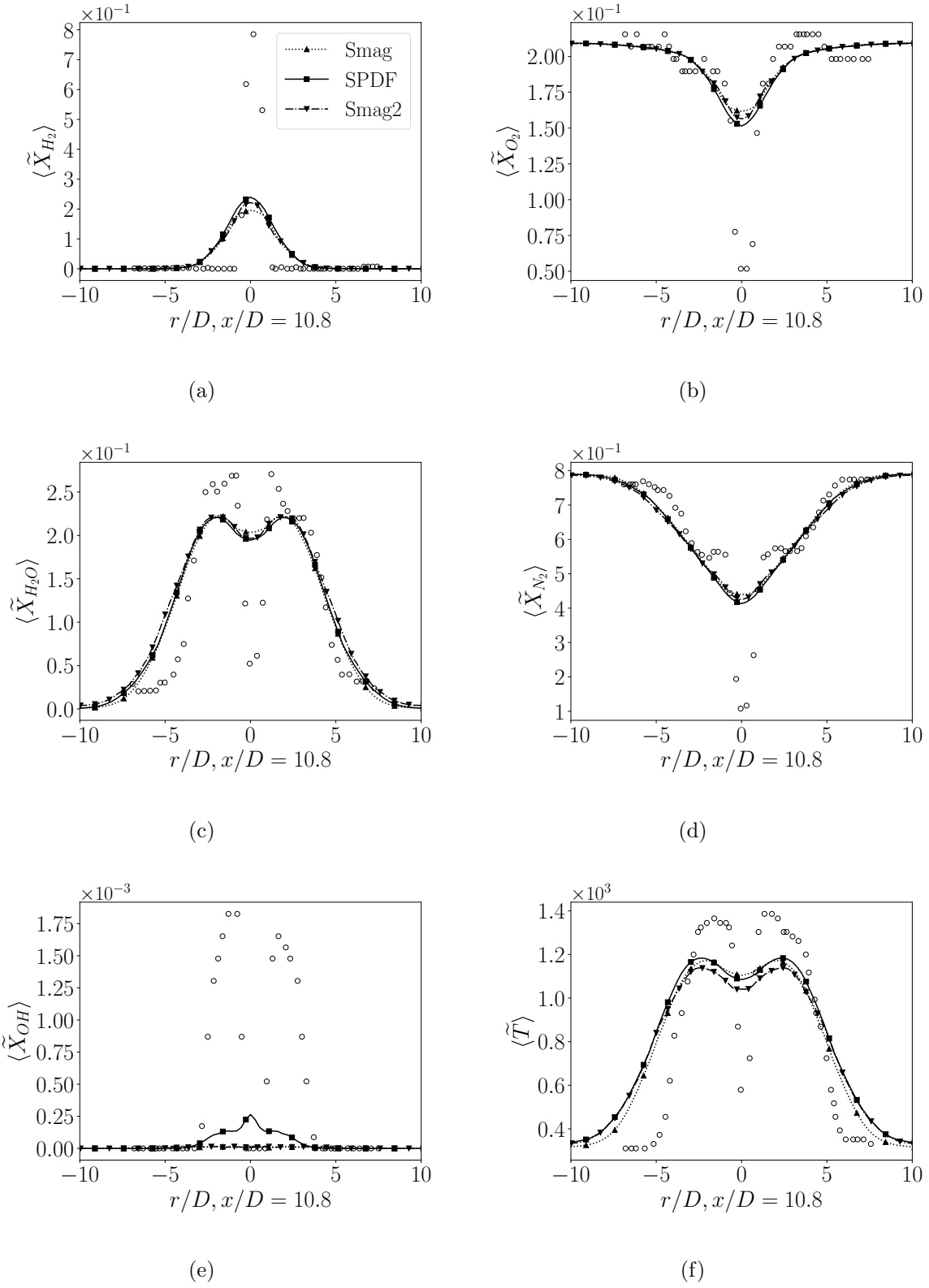

Figure 4.46: Averaged results for mole fractions and temperature. Experimental data of Cheng *et al.* [7] (∘).

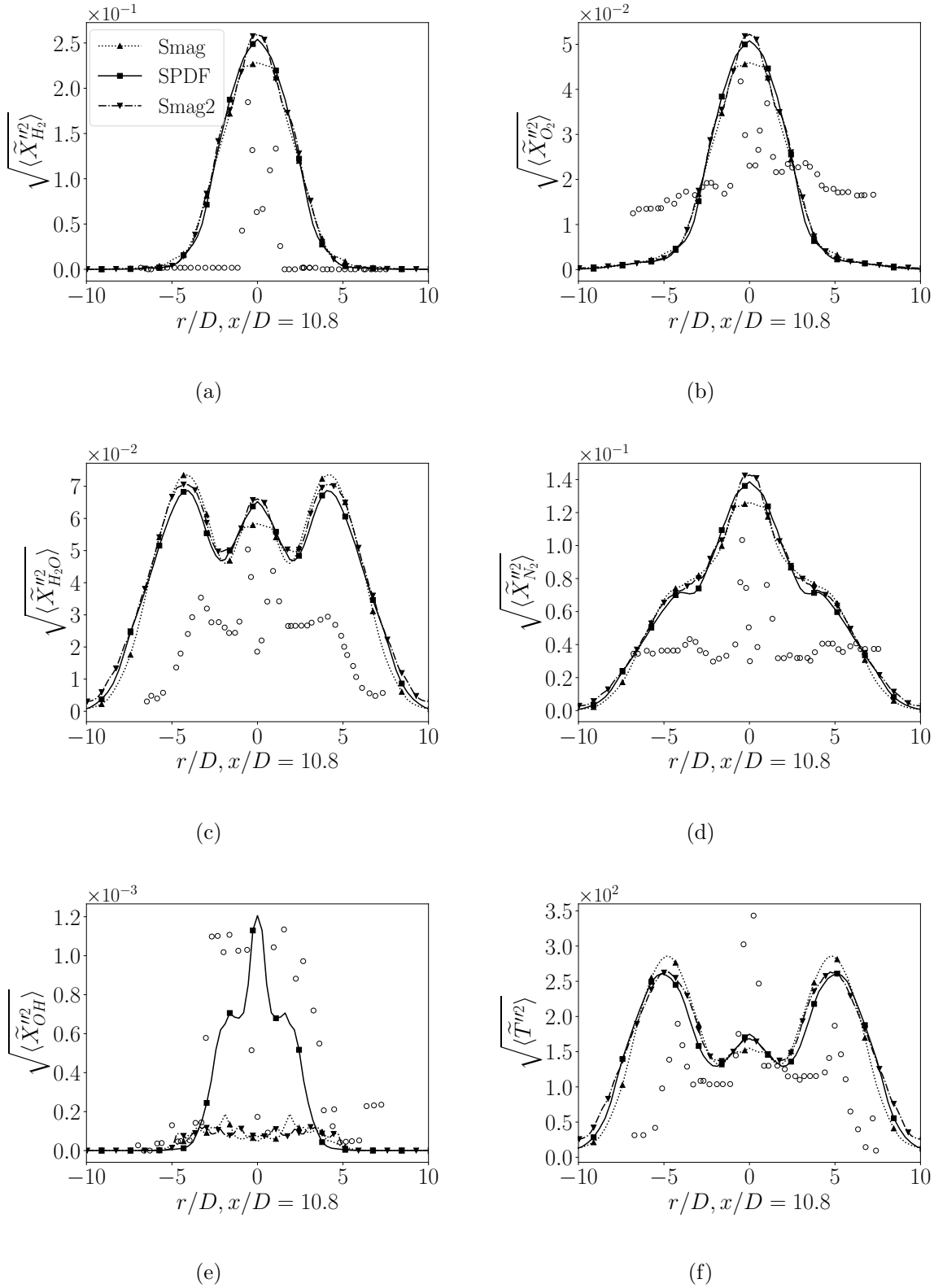

Figure 4.47: Averaged mole fractions and temperature rms results. Experimental data of Cheng *et al.* [7] (○).

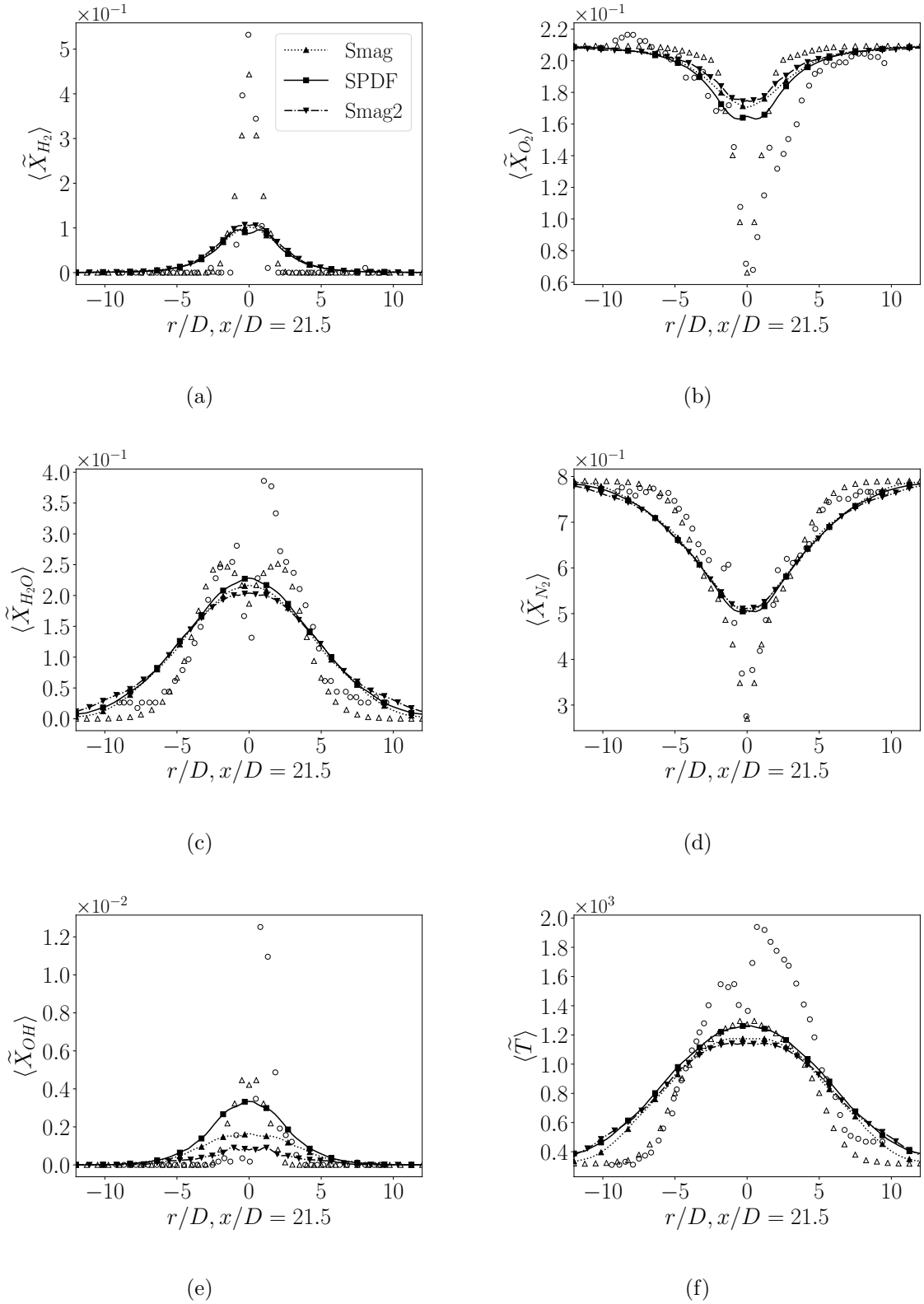

Figure 4.48: Averaged results for mole fractions and temperature. Experimental data of Cheng *et al.* [7] (○) and numerical SPDF data of Almeida and Navarro-Martinez [142] (△).

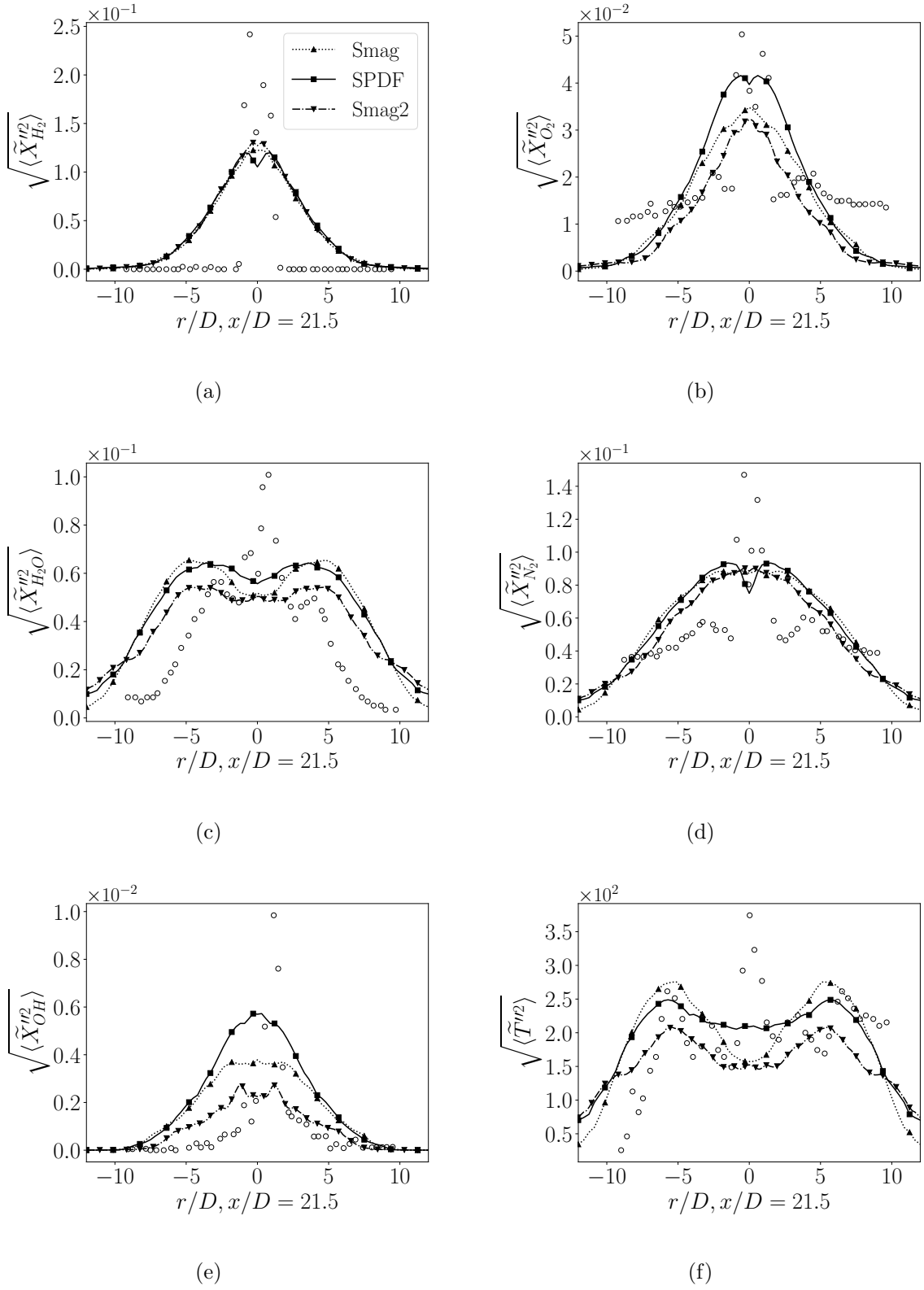

Figure 4.49: Averaged mole fractions and temperature rms results. Experimental data of Cheng *et al.* [7] (○).

Only for the hydrogen that the Smagorinsky with MESH2 presents a slightly better agreement. The temperature is around 10% higher in the SPDF case in comparison to both Smagorinsky simulations. The rms results for the SPDF, shown in Figure 4.51, possess in general higher values, again closer to the experiments. The rms profiles are also wider than the experiments, a consequence of the flame being larger in the numerical simulations.

The last radial comparison is shown in Figures 4.52 and 4.53. The results in Figure 4.52 are presented along with the radial profiles of Bouheraoua *et al.* [18], that used 268 millions points and the same levels of velocity rms at the inlet of the jets, and of Almeida and Navarro-Martinez [142]. At this position, the simulated results are fairly similar. Other numerical studies obtained similar quantitative results, although the results presented here demonstrate a wider flame. The rms results, exposed in Figure 4.53, also presents quantitative and qualitative similar profiles and overall reasonable to the experiments.

The averaged temperature and OH radical centreline profiles are evaluated and presented in Figure 4.54. The profiles presented similar qualitative behaviour. The flame base is well-defined through the OH concentration, although the experimental values are greater. The temperature profile is somewhat smaller than the experimental values. The work in [142] used a coarser mesh and obtained closer results. The coarse mesh yields greater values for the turbulent viscosity, which highly trigger the stochastic model.

The lift-off height for each model, obtained through the maximum spatial gradient of OH, is shown on Table 4.4. The results are again fairly similar and the SPDF is slightly better. The experimental lift-off height is approximately $x/D = 25$. The results are, overall, in accord with other values in the obtained through different numerical investigations.

Despite the wider flame generated in all cases, the flame base height is captured and the radial profiles present reasonable agreement with the experimental data. It is worth mentioning that this supersonic burner is highly unstable at the inlet, with large fluctuation values and transonic fuel injection. In general, the SPDF outperforms

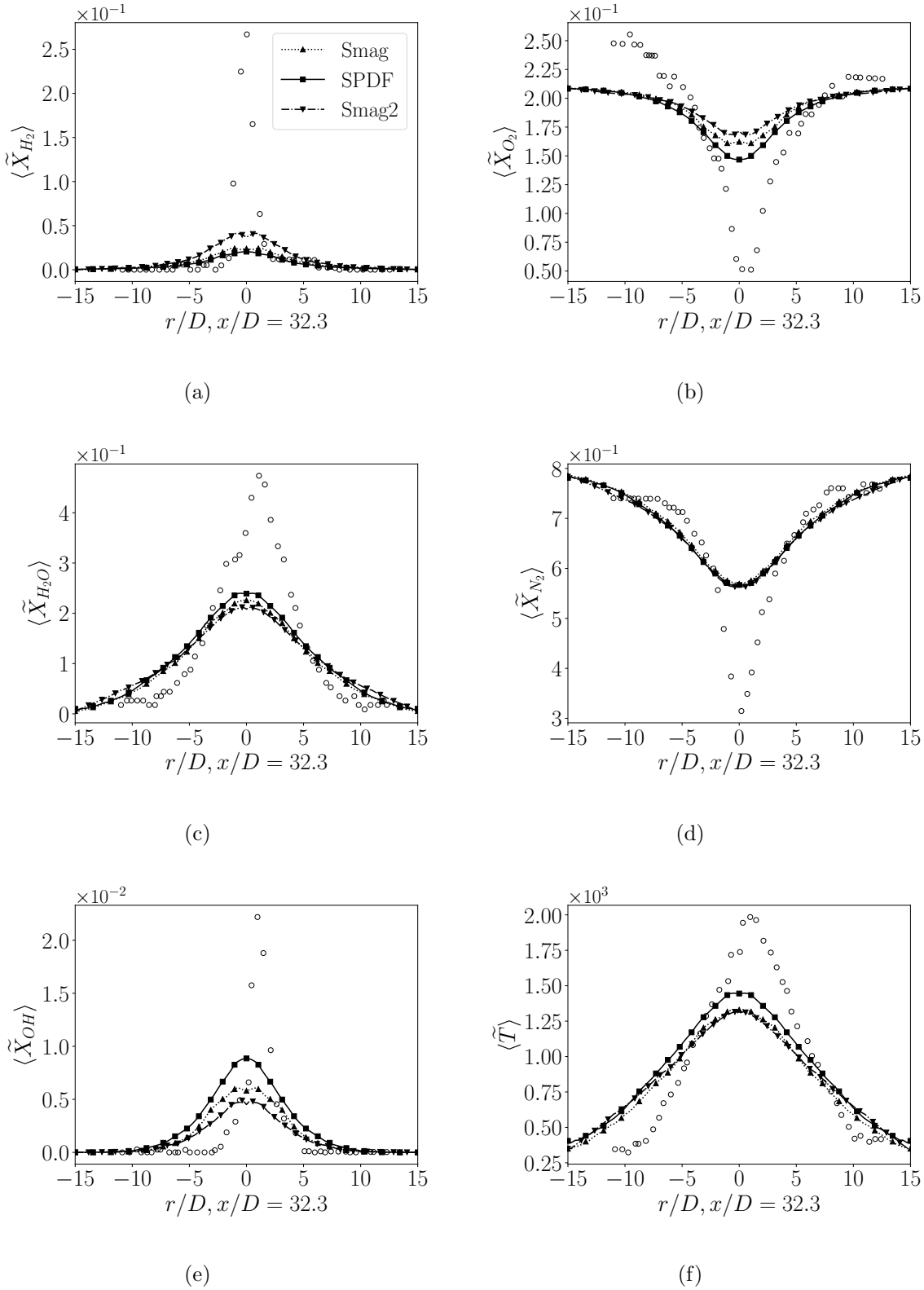

Figure 4.50: Averaged results for mole fractions and temperature. Experimental data of Cheng *et al.* [7] (∘).

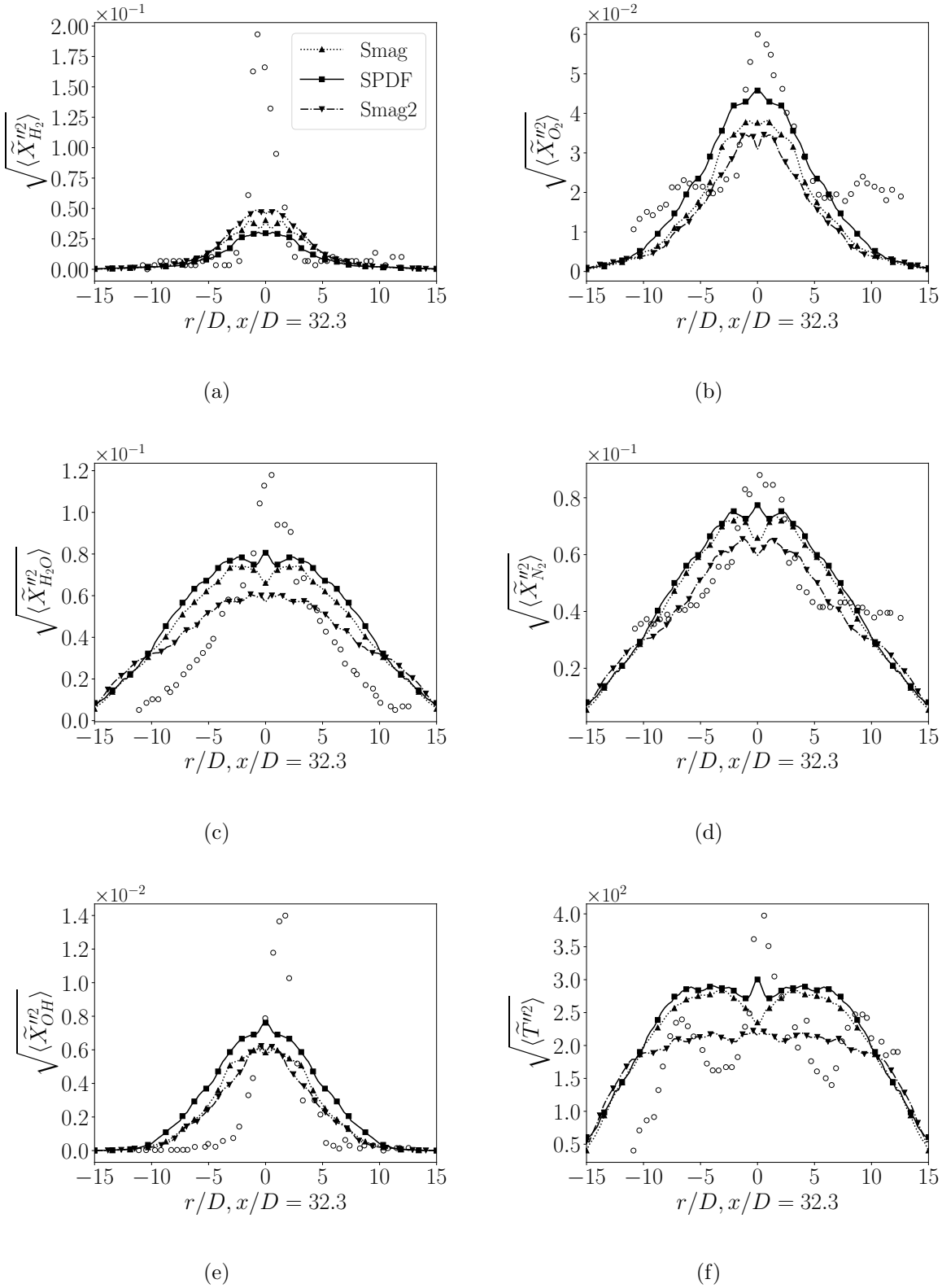

Figure 4.51: Averaged mole fractions and temperature rms results. Experimental data of Cheng *et al.* [7] (○).

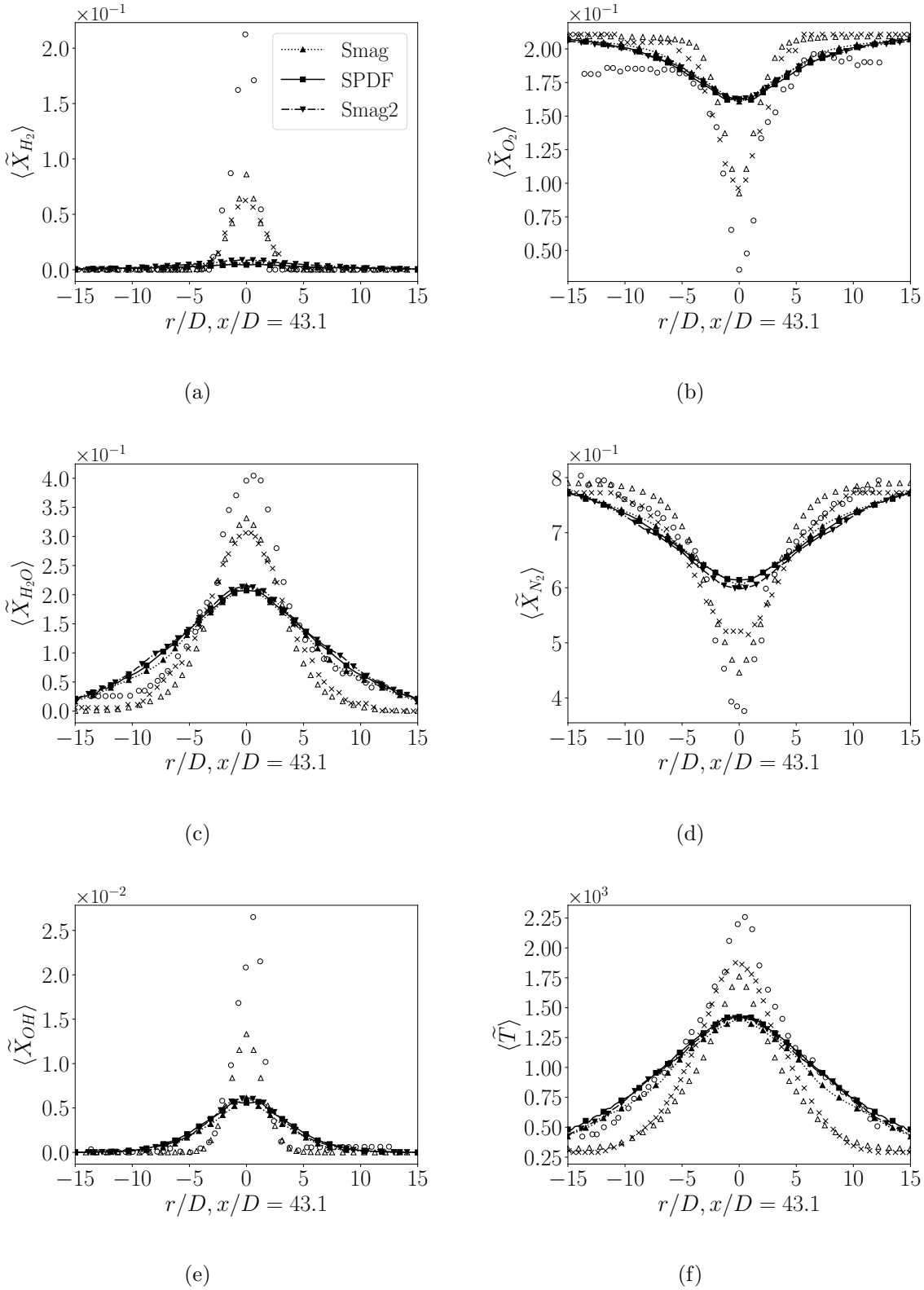

Figure 4.52: Averaged results for mole fractions and temperature. Experimental data of Cheng *et al.* [7] (○). Numerical SPDF data of Almeida and Navarro-Martinez [142] (△) and numerical Smagorinsky data of Bouheraoua *et al.* [18] (x).

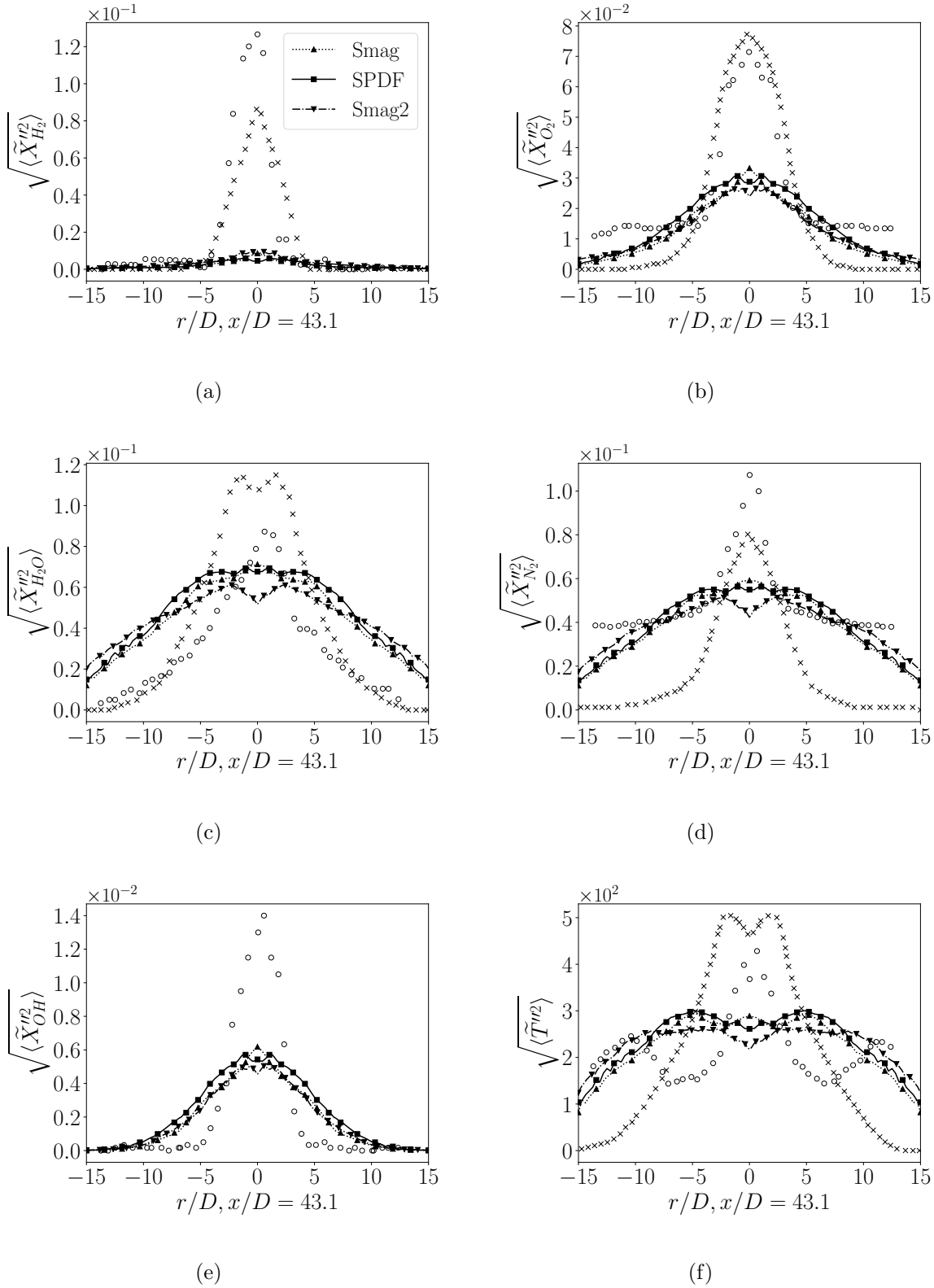

Figure 4.53: Averaged mole fractions and temperature rms results. Experimental data of Cheng *et al.* [7] (○) and numerical Smagorinsky data of Bouheraoua *et al.* [18] (x).

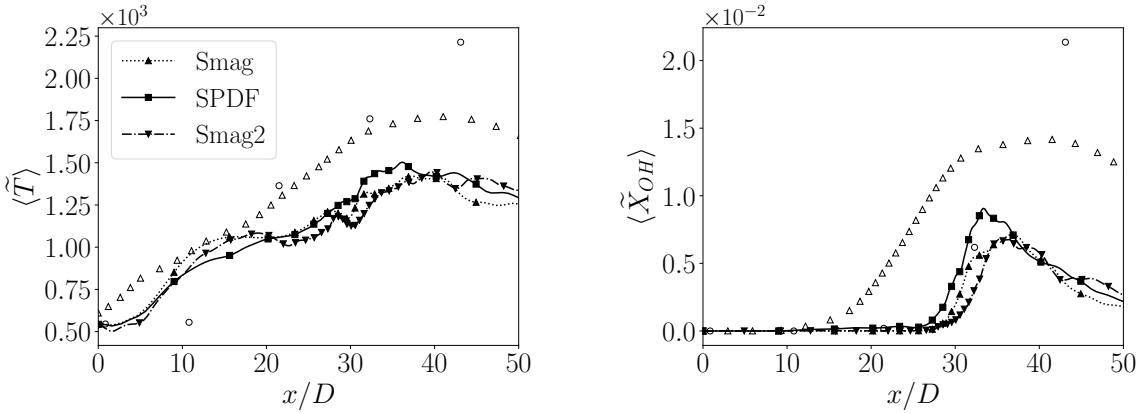

(a) (b)

Figure 4.54: Averaged results for OH mole fraction and temperature at the centreline. Experimental data of Cheng *et al.* [7] (○) and numerical SPDF data of Almeida and Navarro-Martinez [142] (△).

the simulations with Smagorinsky and quasi-laminar approximation for both meshes. Nevertheless, the model can be improved and by reducing the micromixing influence or increasing somehow the influence of the stochastic term. The SPDF model is also computationally cheaper in comparison to the fine mesh simulation.

4.5.2 Evans' burner

The Evans' burner setup is presented on Table 4.5. It is also a supersonic hydrogen flame with a co-flow of vitiated air. The injection of the fuel, however, occurs at Ma = 2.0, a purely supersonic inflow instead of the transonic regime of the Cheng's burner. The co-flow of air is also injected at supersonic speed Ma = 1.9 at hot temperatures. The

Case	x/D
Cheng *et al.* [7]	25
Boivin *et al.* [166]	26.12
Bouheraoua *et al.* [18]	30.00
Almeida and Navarro-Martinez [142]	26.25
Smagorinsky - MESH1	31.15
SPDF - MESH1	30.90
Smagorinsky - MESH2	33.13

Table 4.4: Flame base position for several cases. Numerical lift-off height here calculated based on the position of the maximum gradient of OH radical.

domain size used is of $35D \times 30D \times 30D$, where D is the fuel injector inner diameter equals to $9.525mm$.

In this test case two meshes are also employed, employing the same methodology as in the Cheng's burner. The first mesh has $168 \times 168 \times 168$ - 4.7 millions - points (MESH1) while the second mesh (MESH2) uses $252 \times 252 \times 252$ - 16.0 millions - points. The SPDF and the Smagorinsky with the quasi-laminar approach are evaluated in MESH1, while only the latter model is used in the finer mesh. The simulations with the MESH2 are also performed using ARCHER, under the UK Turbulent Reacting Flows Consortium (UKCTRF).

The discretisation schemes are exactly the same as in the Cheng's burner simulation, so as the LES parameters. A time-step of $4.0 \times 10^{-8}s$ for MESH1 and $2.5 \times 10^{-8}s$ for MESH2 is used to ensure a CFL number smaller than 0.4. The simulations are ran for 29 and 18 time steps, for the MESH1 and MESH2 cases, respectively, to ensure statistical convergence. The boundary conditions are zero-gradient except at the inlet of fuel, air and the surface of the surrounding air, where an inlet of $20m/s$ is imposed.

Table 4.5: Supersonic burner configuration of Evans *et al.* [152].

Dimensions	
Nozzle exit inner diameter	65.30 mm
Fuel injector inner diameter	9.525 mm
Fuel injector outer diameter	12.525 mm
Vitiated air exit conditions	
Pressure	100 kPa
Temperature	1495 K
Mach number	1.9
Velocity	1510 m/s
O_2 mass fraction	0.241
N_2 mass fraction	0.478
H_2O mass fraction	0.281
Reynolds number	5.72×10^5
Fuel exit conditions	
Pressure	100 kPa
Temperature	251 K
Mach number	2.0
Velocity	2432 m/s
H_2 mass fraction	1.0
Reynolds number	9.94×10^5

Velocity fluctuations are included through synthetic turbulence using a digital filter. The fluctuation values are set to 3% of the jets values, which seems appropriate to reproduce the non-reported experimental levels. The Yetter *et al.* [162] hydrogen mechanism is also employed in this test case.

Figure 4.55 shows the contour plots for instantaneous temperature for the MESH1 and MESH2. The flame is longer than the ones of the Cheng's burner. Both simulations also presents many small turbulent structures, indicating the highly convective behaviour of this case. The discretisation schemes also appear to generate less diffusion than in the previous case. Figure 4.56 presents contour plots for H_2O radical, where it is possible to see the formation of H_2O much closer to the burner than in the Cheng's burner case. In both cases, the flame height is reasonably the same, although the for the coarse mesh the mixing is much more diffusive than convective.

The instantaneous pressure contour plots are shown in Figure 4.57. It is possible to identify shock diamonds structures close to the injectors in both meshes. The pressure waves follow a similar and expected pattern for this burner. In general, both models and meshes are able to reproduce this test case at least qualitatively.

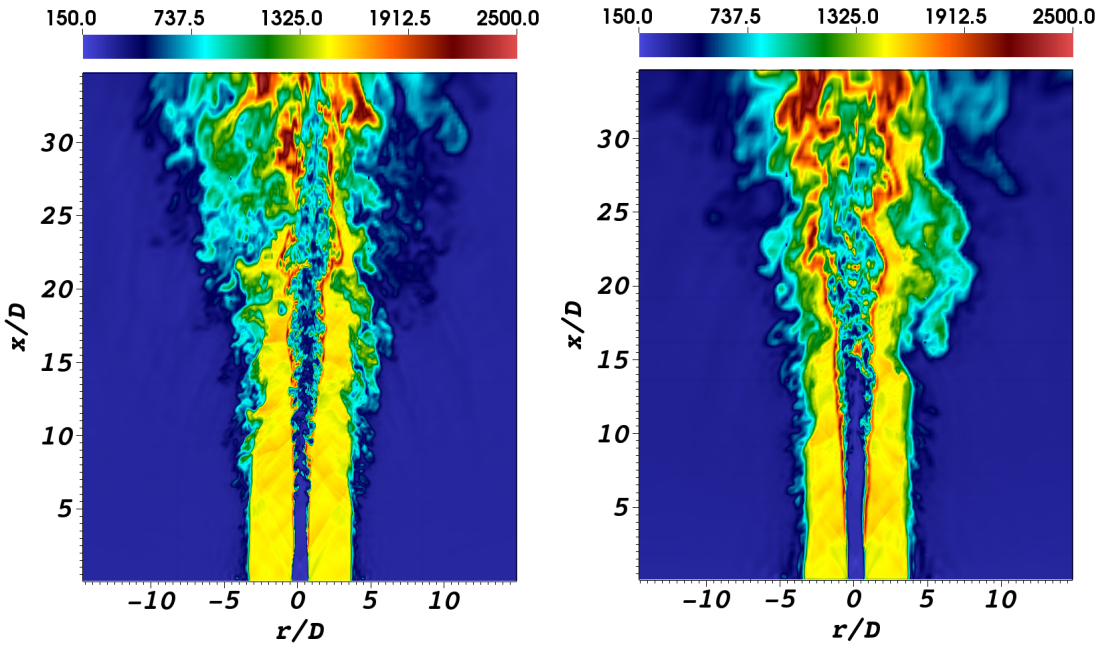

(a) Smagorinsky - MESH2.

(b) SPDF - MESH1.

Figure 4.55: Instantaneous $\widetilde{T}(K)$ contour plot.

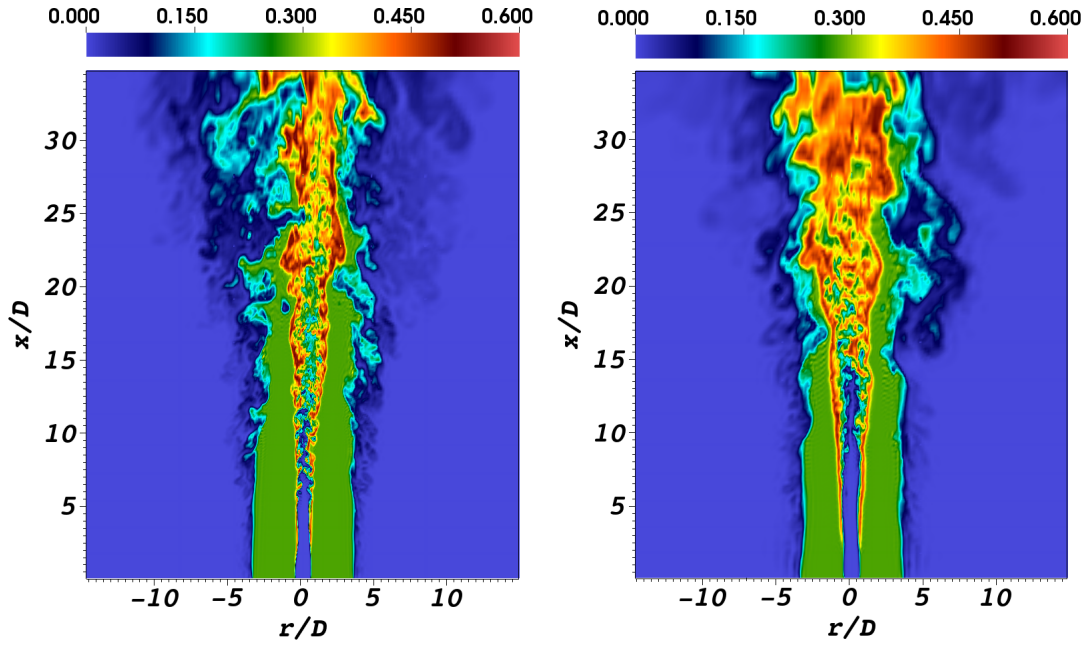

(a) Smagorinsky - MESH2. (b) SPDF - MESH1.

Figure 4.56: Instantaneous $\widetilde{Y}_{H_2O}$ contour plot.

The first quantitative results are shown in Figure 4.58, which presents the averaged Pitot pressure, or stagnation pressure. The stagnation pressure must be calculated bearing in mind that the flow is supersonic and the Pitot tube will generate a bow shock in

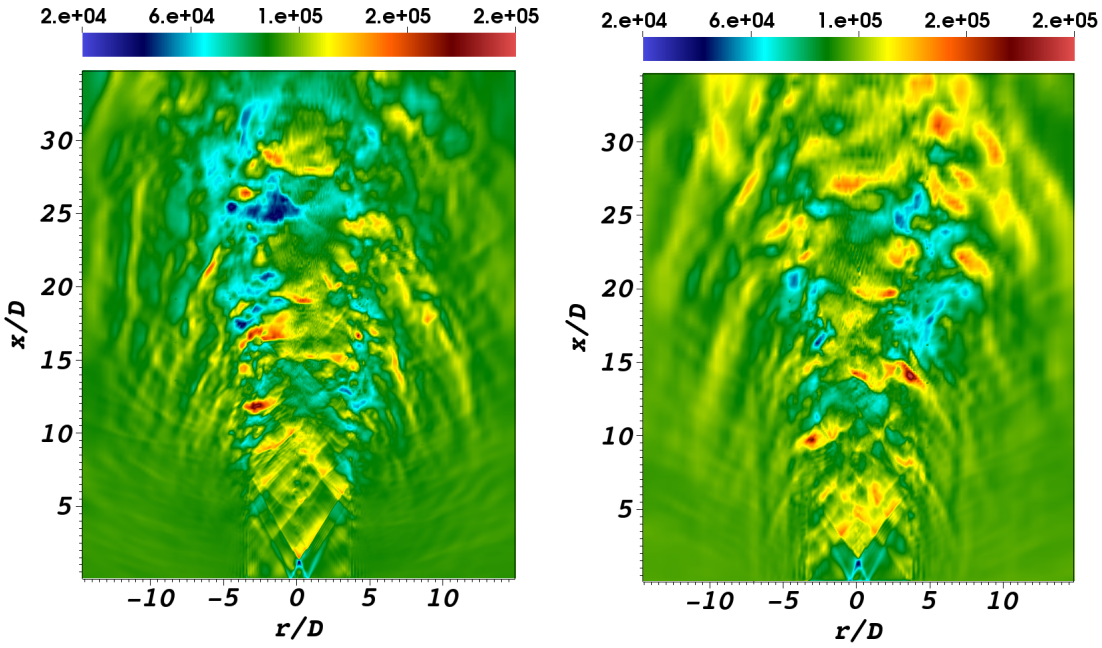

(a) Smagorinsky - MESH2. (b) SPDF - MESH1.

Figure 4.57: Instantaneous $\overline{p}(Pa)$ contour plot.

the flow. As a consequence, the pressure perceived by the Pitot tube is not the same as the pressure in the flow, and they are correlated by isentropic shock relations.

The Pitot pressure in supersonic regions therefore follows the Rayleigh Pitot tube formula [169] to relate the pressure on the Pitot tube, p_{pitot} with the thermodynamic pressure in flow, p:

$$\frac{p_{pitot}}{p} = \left(\frac{(\gamma+1)^2 \, \mathrm{Ma}^2}{4\gamma \mathrm{Ma}^2 - 2(\gamma-1)} \right)^{\gamma/(\gamma-1)} \frac{1-\gamma+2\gamma \mathrm{Ma}^2}{\gamma+1} \tag{4.23}$$

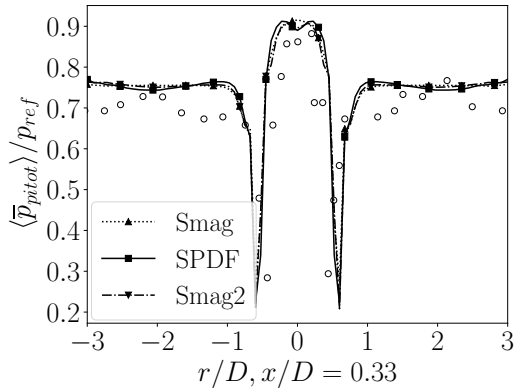

(a) p_{ref}=676 (kPa).

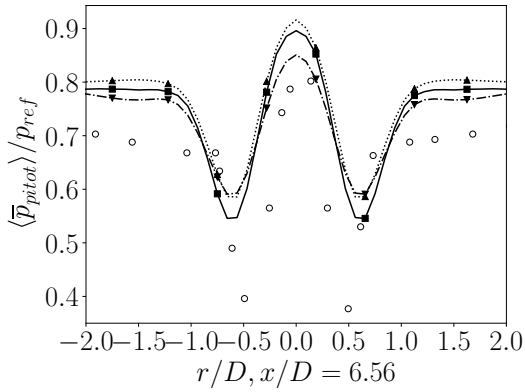

(b) p_{ref}=680 (kPa).

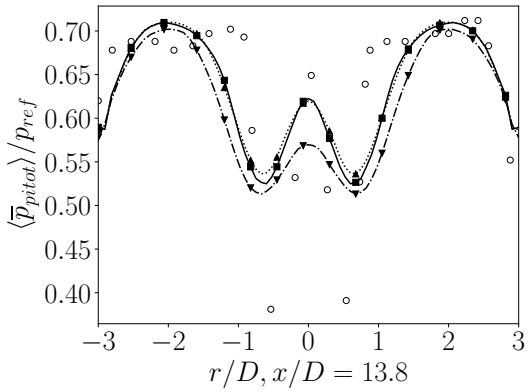

(c) p_{ref}=703 (kPa).

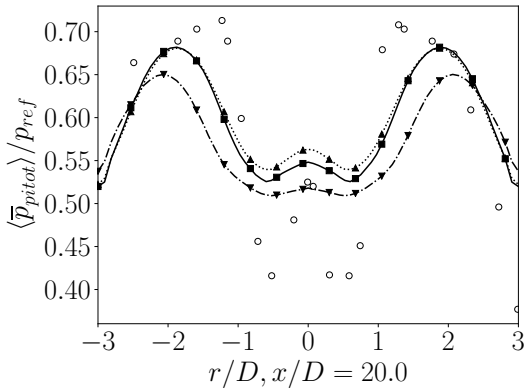

(d) p_{ref}=680 (kPa).

Figure 4.58: Time averaged normalised Pitot pressure results. Experimental data of Evans *et al.* [152] (○).

and for subsonic regions:

$$\frac{p_{pitot}}{p} = \left(1 + \frac{\gamma - 1}{2}\mathrm{Ma}^2\right)^{\gamma/(\gamma-1)} \tag{4.24}$$

After establishing the previous formulas, Figure 4.58 is generated. The Pitot pressure at $x/D = 0.33$, representing the boundary condition at the fuel and air injectors, is accurately captured. As expected, there is small to no difference between the models and mesh size used. At $x/D = 6.56$ and further downstream positions the models present different outcomes. The Smagorinsky model with MESH2 profiles are wider than the other simulations, with a more diffusive behaviour. The higher resolution allowed a higher mixing level. The SPDF also generates higher mixing, but the difference to the Smagorinsky model with MESH1 is small. Agreement with experimental data is sound for all the simulations.

Figure 4.59 presents the average mass fractions for H_2, O_2, H_2O and N_2 chemical species at $x/D = 8.26$. Overall experimental agreement is reasonable. The MESH1 simulations with Smagorinsky and SPDF models present similar behaviour with little distinction between the profiles. The heavy simulation with MESH2 shows flatter profiles for all species, in agreement with the Pitot pressure results.

The profiles at the position $x/D = 15.5$ are shown in Figure 4.60. On this position the differences between the coarse mesh and a finer mesh is more evident. The SPDF alone is not able to provide the combustion levels of MESH2. The fine mesh simulation presents higher production of H_2O and fewer O_2 mass fraction. Although the SPDF has higher concentration of H_2O in comparison to the Smagorinsky profile, the difference is marginal. It should be highlighted the N_2 profiles, as it is a non-reacting specie indicates the mixing level of the flame. Again, the MESH2 results are more diffusive but has a higher mixing level than the experimental data.

At last, the mass fraction results at $x/D = 21.7$ are shown in Figure 4.61. The flames of the Smagorinsky and SPDF simulations with the MESH1 are well defined now, as the H_2O levels are reasonably higher at the fuel jet region $r/D \leq 0.5$. The profiles for all models are close, without showing much quantitative and qualitative difference. Overall,

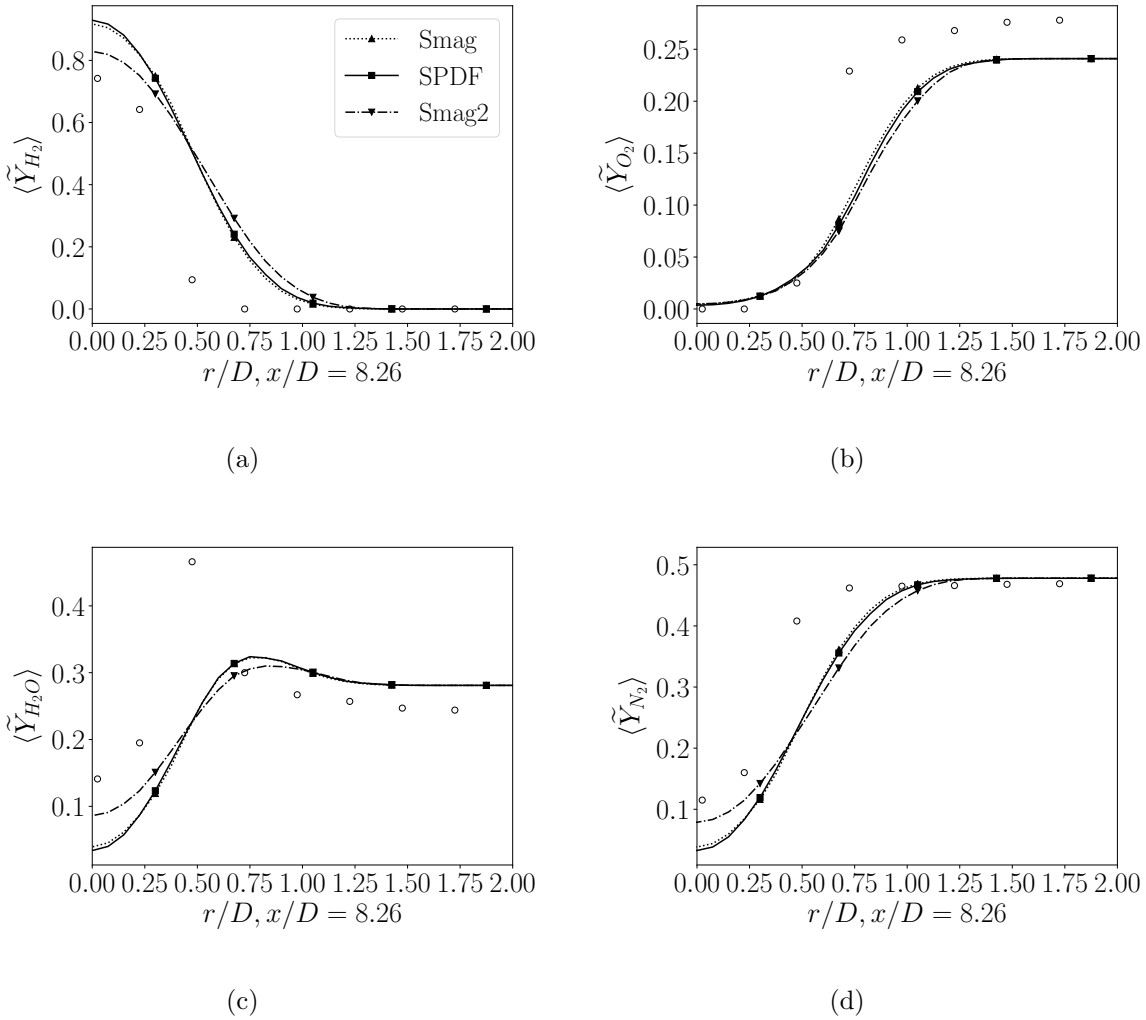

Figure 4.59: Averaged mass fraction results at $x/D = 8.26$. Experimental data of Evans *et al.* [152] (∘).

the flames are wider than the actual experimental data, a trend identified in all positions evaluated.

The Evans' burner has higher speed than the Cheng's case, and it is therefore more sensitive a priori to compressibility modelling. However, the approximation performed in the SPDF to not include an extra thermodynamic variable to close the source term may be insufficient in this test case. The more sparse profiles generated indicate a higher mixing level than the experimental data. A drawback of simulating the Evans' burner is the absence of rms data, in which a proper fluctuation level capturing at the inlet would improve the overall agreement.

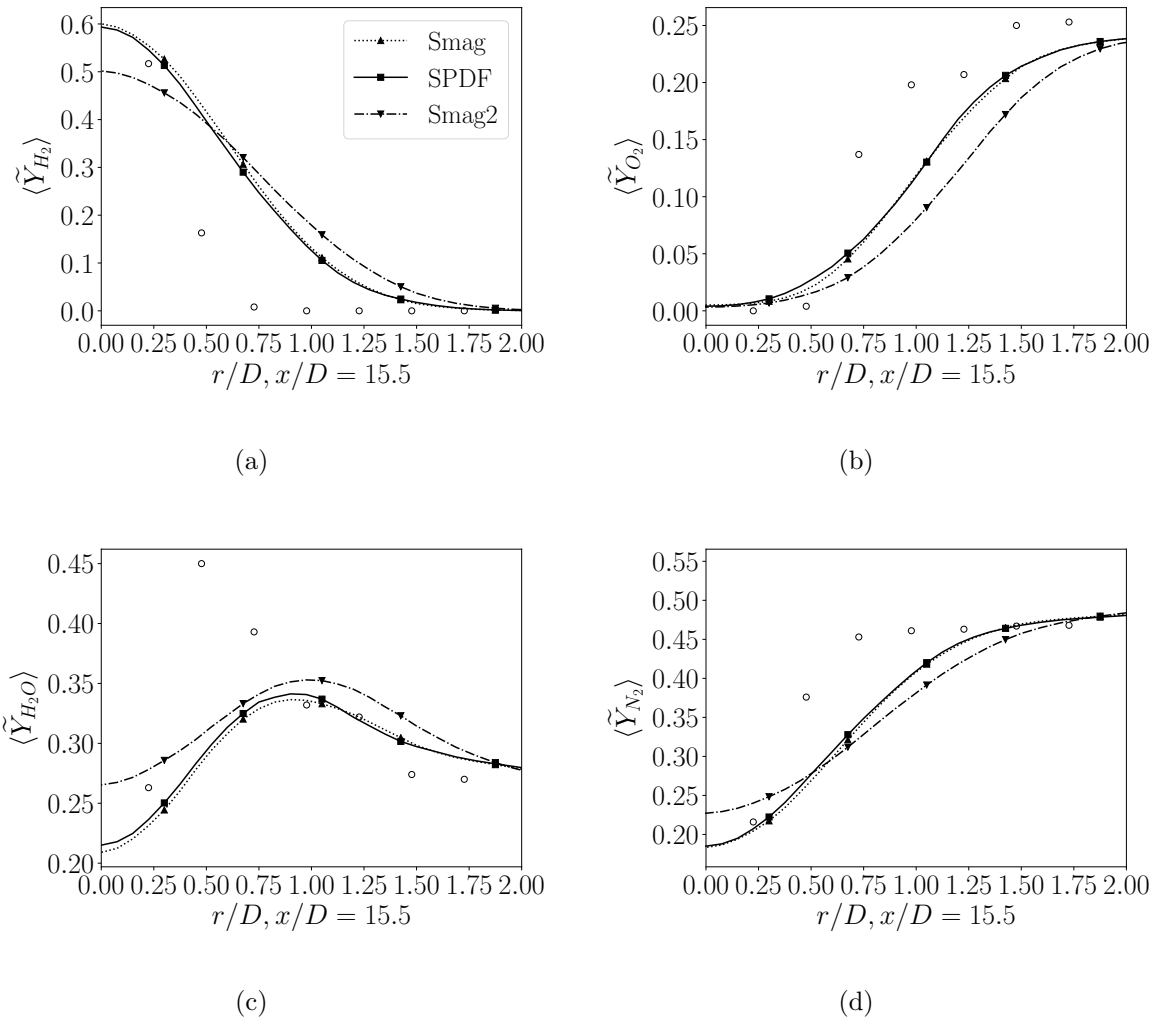

Figure 4.60: Averaged mass fraction results at $x/D = 15.5$. Experimental data of Evans *et al.* [152] (○).

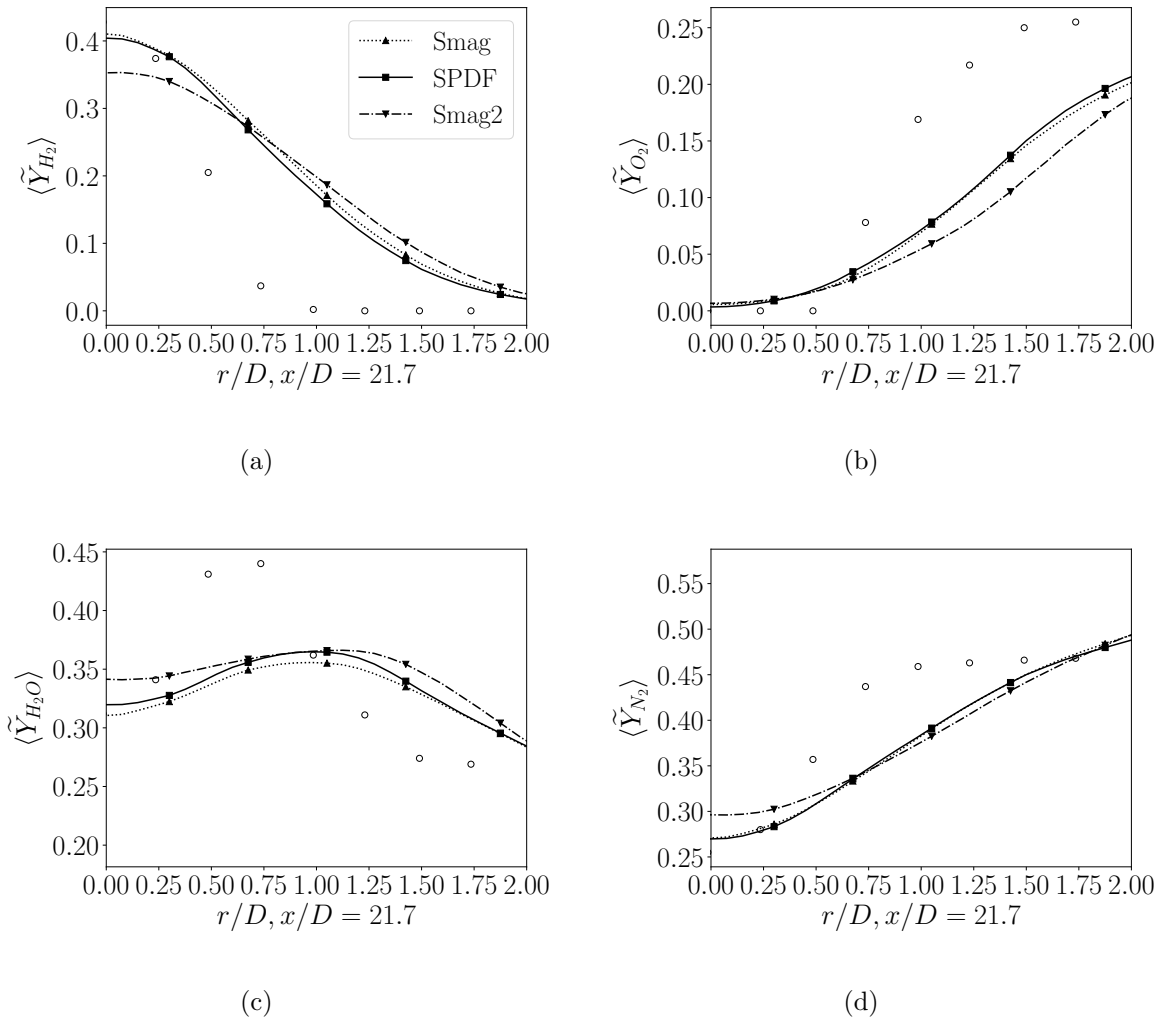

Figure 4.61: Averaged mass fraction results at $x/D = 21.7$. Experimental data of Evans *et al.* [152] (○).

4.6 Summary

This chapter presented the numerical assessment, verification and validation of the developed stochastic models into CompReal. The code evaluation has been performed through a series of canonical test cases, including a homogeneous isotropic turbulence configuration, an one-dimensional reactive shock tube, a two and three-dimensional mixing layers and two supersonic burners.

The homogeneous isotropic turbulence case is throughly evaluated in order to study the discretisation performance of the code. A series of kinetic energy spectra have been obtained to assess the discretisation schemes diffusion and accuracy levels. In compressible flows, the accuracy of the discretisation plays a major role into the proper reproduction of real configurations. The hybrid DRP/HLLC-TVD scheme has shown a good compromise to achieve accuracy with stability to solve the convective terms. The SPDF and VSPDF are also further investigated, demonstrating their ability to access larger composition spaces, which is very useful to describe combustion phenomena with higher accuracy. This case also sheds a light into the VSPDF requirement of a better closure or constant calibration.

The reactive shock tube case is used to demonstrate the ability of the SPDF and VSPDF model to represent DNS data in a simplified configuration. In this test case the importance of the micromixing IEM model becomes evident in premixed flames. The stochastic convergence is evaluated through local and integral moments convergence rates. The SPDF presents a rate of convergence slightly smaller than the theoretical value of $N_f^{-0.5}$. The VSPDF, however, presents high convergence rate of $N_f^{-1.0}$ for the first moment, but low and around $N_f^{-1/4}$ for the remaining moments. It is also established here, by simulating up to 8192 stochastic fields that 8 fields are sufficient to achieve reasonable statistical convergence for the first moment.

The reactive and compressible mixing layer simulations provided valuable data to evaluate the performance of the models in a more challenging environment. Although both SPDF and VSPDF models are able to reproduce DNS data with good accuracy for the two-dimensional simulation, the three-dimensional mixing layer indicates that the

VSPDF closures may need further investigation. The SPDF reproduces the vorticity thickness growth, a flow variable, through the pressure coupling of the flow solver with the stochastic fields represented in Eq. (3.17).

The VSPDF model, in contrast, has smaller level of dissipation and the instabilities generated by the stochastic term in the momentum equation overshoots the mixing layer growth. Although the VSPDF holds more potential, the model does not accuratelly reproduce the vorticity growth and therefore the SPDF is used from here onwards. The VSPDF may also require challenging velocity field initialisation with some level of subgrid fluctuation between the stochastic fields, which has not been tested here. In the test cases, all fields share the same initial condition, which creates low dissipation.

Two supersonic burners are also evaluated to validate the numerical model in a real configuration. The Cheng's burner and the Evans' burner present different numerical challenges suitable to fully assess the SPDF model and compare it with the Smagorinsky model coupled with the quasi-laminar approach. Both burners have been successfully reproduced, although with higher diffusion levels than the experimental data. Overall, the SPDF presents better agreement than the Smagorinsky model in the Cheng's burner simulation, however the Evans' burner results show very small differences between these two approaches.

The SPDF and the VSPDF have been therefore widely evaluated in several simulations, using a wide range of scales, complexity and different environments. The SPDF is a more consistent model regarding statistical convergence and accuracy in complex simulations. Although the VSPDF is a promising formulation, it has closure issues that needs to be addressed before its usage in highly computational demanding cases, such as supersonic burners and scramjets.

Chapter 5

Scramjet simulation

5.1 Introduction

This chapter summarises the challenges of the scramjet simulation to be carried out, as it includes all the numerical techniques presented so far. It is a wall-bounded supersonic flow including shock/turbulence, shock/boundary-layer and strong turbulence/chemistry interactions. There have been several experimental investigations of such engines in the literature. The flight experiments of the HIFiRE (Hypersonic International Flight Research Experimentation) programme [1] and the HyShot programme [2] are regarded as the most investigated scramjet flight experiments [22].

There have also been attempts to reproduce the in-flight conditions using ground-based facilities. In this way, the scramjet experimental investigation reduces in complexity and cost. It should be highlighted two projects: the German Aerospace Center (DLR) scramjet facility [170] and the University of Virginia (UVa) scramjet [8, 171, 12]. These experimental configurations have been used for code assessment, validation and supersonic combustion numerical investigation, including, but not limited to, the works of [27, 172, 29] for the DLR and [173, 8, 12, 33] for the UVa scramjet.

The objective of this chapter is to perform a scramjet simulation and present the feasibility of the new developed SPDF model and the implemented solver to reproduce a complex configuration. The Smagorinsky model along with the quasi-laminar approach

to close the reactive terms is also used for comparison purposes. Simulations of the UVa scramjet configuration A [33] are therefore performed to evaluate the models. In the next sections, the UVa scramjet is described, along with the numerical tools used to simulate it and the obtained results.

5.2 University of Virginia (UVa) Scramjet

The UVa scramjet has several geometrical configurations, from A to D [174]. On these configurations, hydrogen is injected through a wall-mounted compression-ramp injector. Rockwell *et al.* [175] investigated a Configuration E, where ethylene is used as fuel and a cavity is employed to establish the flame. The configuration A, nonetheless, offers a higher amount of experimental data and it is chosen to be simulated in this work. The Coherent Anti-Stokes Raman Spectroscopic (CARS) [171] and hydroxyl radical planar laser-induced fluorescence (OH-PLIF) [174] measurements have been performed on the UVa configuration A whereas Rockwell *et al.* [8] measured the top-wall pressure.

5.2.1 UVa design - Configuration A

The full description of the experimental supersonic combustion facility is available in the literature [12, 171, 174, 8]. The geometry employed to represent the configuration A is shown in Figure 5.1 and it is the same as in Chan and Ihme [33]. It consists of three parts, the isolator, the combustor and the extender. The hydrogen is provided through a injector with 2.54 mm diameter at the compression-ramp of the combustor, that has height $H = 0.25$ in (6.35 mm). The nozzle responsible for generating the air-intake conditions is not represented in this work, following other numerical studies [33]. The geometry has been drawn using the open-source computer-aided design FreeCAD and it can also be visualised in Figure 5.1.

The fuel is injected at 1804.25 m/s (Ma = 1.7) normal to the injector surface and it consists of pure hydrogen. The temperature and pressure are 94 kPa and 190 K, respectively. The air-intake has the same configuration as in [33] to reproduce the nozzle output conditions. The inflow of air has velocity of 1025.44 m/s, Ma = 2.0, and ambient air composition, while the temperature is set to 667 K and the pressure is 38 kPa.

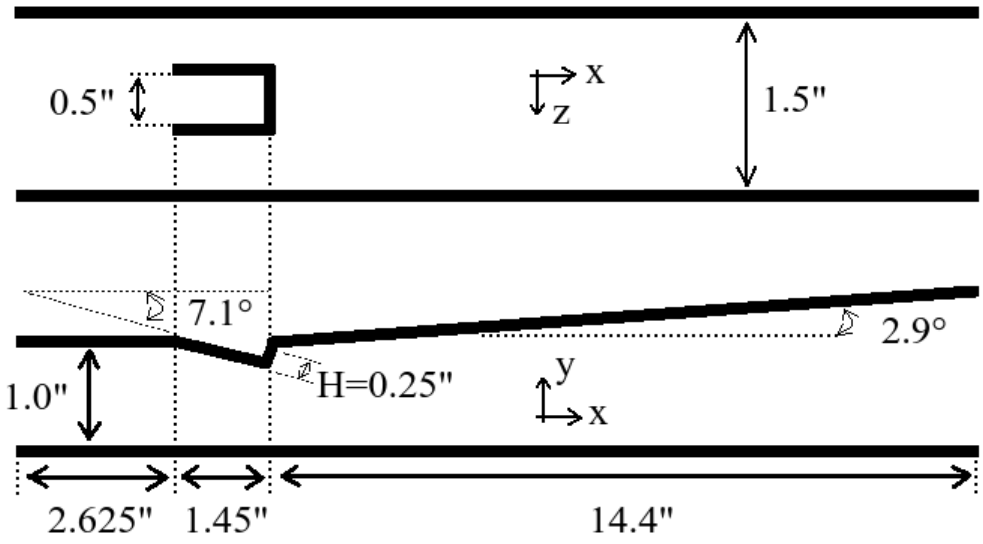

(a) Geometrical parameters (not in scale).

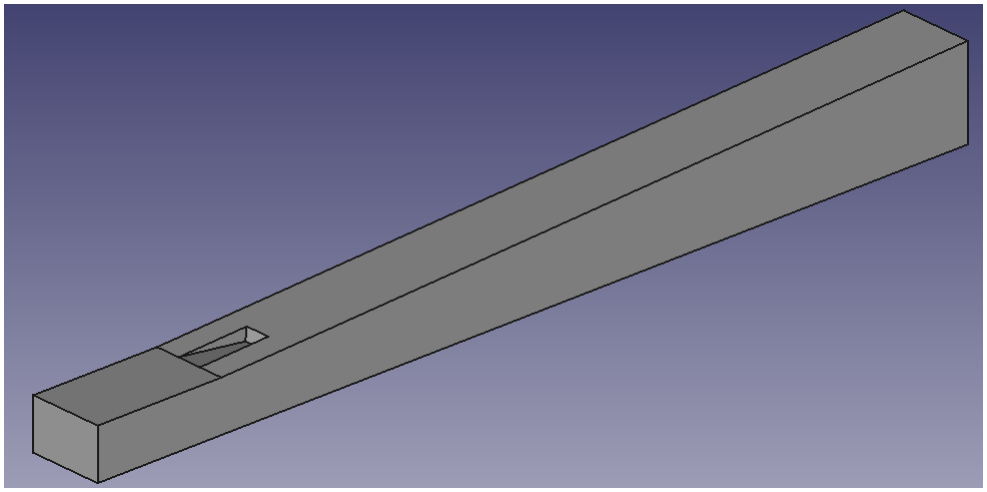

(b) CAD design.

Figure 5.1: UVa geometry - Configuration A.

5.2.2 Numerical modelling

The CAD geometry, presented in Figure 5.1, is converted into a GNU Triangulated Surface (GTS) file that can be read by CompReal, as described in Section 3.4. The GTS geometry determines the surfaces to be read within the IBC method, as shown in Figure 3.4.

A uniform mesh has been employed in this case, since the resolution close to the wall is also important. However, wall functions are not yet available in CompReal, which can a source of inaccuracy if the mesh is not fine enough close the walls. The mesh has

$336 \times 108 \times 108$ - 3.9 millions - points and it is used for the simulation of both Smagorinsky and SPDF models. The y^+ values range from 70 to 85. The SPDF simulations have also been performed using eight stochastic fields. The mesh is relatively coarse than other numerical studies that used on average 40 millions points [12, 33]. It is therefore a good test to verify if the SPDF is able to reproduce highly resolved simulations using less points.

The temporal and spatial discretisation schemes employed here are the same as in the Cheng's and Evans' burners and it is mentioned here for completeness. The convective terms are discretised using the hybrid scheme between the DRP, 13-point stencil and fourth order accurate, and HLLC-TVD scheme, second order accurate and applied to strong gradient regions. Remaining spatial derivatives are also discretised with fourth order central difference scheme. The third order Runge-Kutta is used as temporal integrator, being weak first order accurate for the stochastic equations. The time step of 5×10^{-8} s is used and the CFL number is kept below the threshold value of 0.2. The simulations are ran for 16 residence times in order to obtain temporal averaged data.

The LES parameters are also similar to the ones used for the supersonic burners cases. The boundary conditions for the air and fuel inlets are as described previously. Synthetic turbulence with fluctuation level of 5% is inserted at the air intake through a digital filter. A fluctuation of 5% is also included into the fuel inlet ($\widetilde{u}_{rms}$), however, using a random sine perturbation with 8 modes (N_{mod}):

$$\widetilde{u}'_j(y,z) = \sum_{n=1}^{N_{mod}} \widetilde{u}_{rms}\sqrt{2/n}\sin\left[f_n t + n\left(\gamma(y,z) + r(y,z)/l_{ref}\right) + 2\pi\varepsilon_1\right] \tag{5.1}$$

where $\varepsilon_1 \in [0,1]$ is a random number, l_{ref} is the injector radius, and $f_n = 2\pi/t_n$ is the frequency of the fluctuation, where t_n is characteristic time of the n^{th}-mode $t_n = l_{ref}/(n\widetilde{u}_{rms})$. The variable t represents the time, $\gamma(y,z)$ is the angle at the position (y,z) and $r(y,z)$ is the radius at the position $\gamma(y,z)$.

Zero-gradient and wall boundary conditions are set for remaining boundaries. In the z-direction a slip wall condition for the axial velocity is used to prevent early shocks in

the flow cross-direction.

The hydrogen combustion mechanism used here is the Yetter *et al.* [162], which includes 9 species and 19 reactions. This model has not yet been assessed for the UVa scramjet. Chan and Ihme [33] employed the Burke *et al.* [176] mechanism whereas Fulton *et al.* [12] evaluated the performance of both Jachimowski [177] and Burke *et al.* [176] hydrogen combustion mechanisms. Edwards *et al.* [173] investigated the mechanism of Jachimowski [177] and O'Conaire *et al.* [164]. The usage of a different model can provide new insights into the scramjet behaviour, such as adequate flame position and radicals positions.

5.2.3 Results

Several contour plots describing the flow behaviour are shown in Figure 5.2. The instantaneous temperature for the SPDF model can be seen in Figure 5.2(a). The positions of $x/H = 6$, $x/H = 12$ and $x/H = 18$ in the combustor are highlighted as they are the locations of the CARS measurements. It can be seem in the temperature profile that the flame quickly attaches to the top-wall in both models.

The fuel jet in both models appears too laminar, although a turbulent boundary condition has been used. Nevertheless, the SPDF flame is longer and the closer to the fuel injector.

The topwall averaged pressure on its centreline has been calculated and shown in Figure 5.3. The topwall pressure is an interesting variable as it can be related to the thrust of the scramjet engine [33]. The results are also exposed along with the experimental measurements of Cutler *et al.* [171] and numerical results from Chan and Ihme [33] and Fulton *et al.* [12]. The pressure at the end of the extender is recovered in both simulations and the agreement with experimental data is good in this region.

However, the expected increase of pressure occurs at further downstream positions on the combustor region. On the simulations performed, the pressure on the topwall increases in two stages, the first between $x/H = 0$ and $x/H = 5$ and the second from $x/H = 12$ until $x/H = 20$. The first pressure rise is a consequence of the combustion

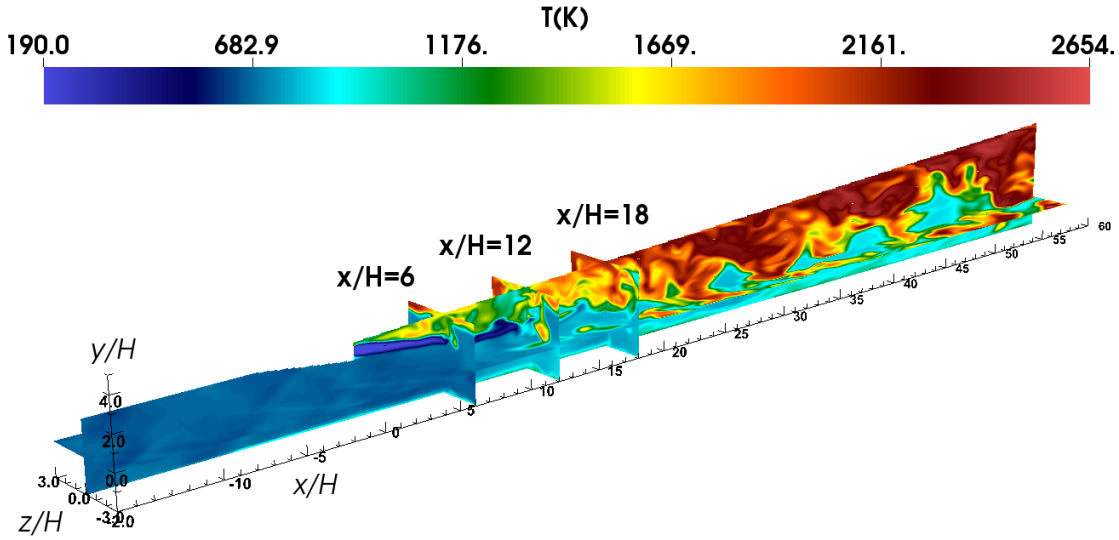

(a) Instantaneous $\widetilde{T}$(K) contour plots for the SPDF model.

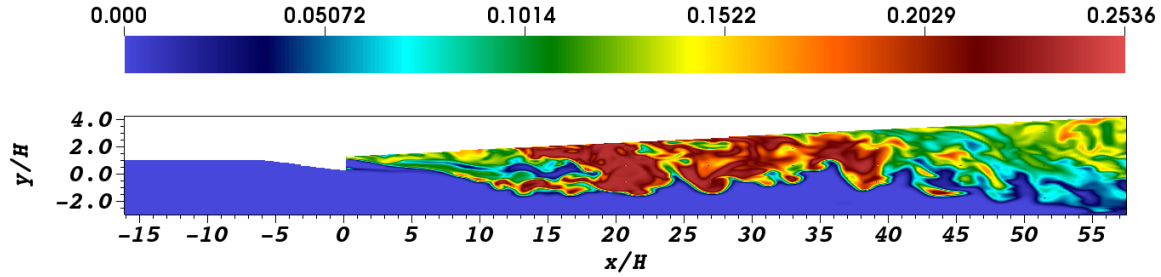

(b) Instantaneous $\widetilde{Y}_{H_2O}$ contour plot for the Smagorinsky model at $z/H = 0$.

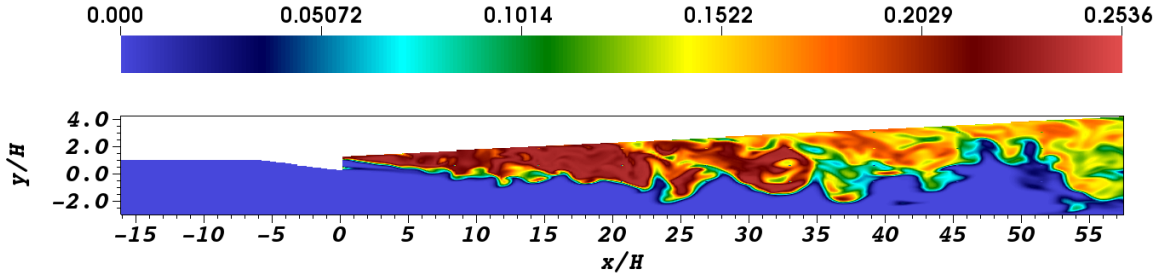

(c) Instantaneous $\widetilde{Y}_{H_2O}$ contour plot for the SPDF model at $z/H = 0$.

Figure 5.2: Contour plots for the UVa scramjet - Configuration A simulation.

process. It should be noticed that the on the experiments, the pressure firstly increases because of the compression ramp located between $x/H = -6$ and $x/D = 0$, which generates a shock wave. On both simulations, this effect presents minor influence as the pressure remains barely the same, increasing to $p/p_{ref} = 1.2$ and returning to $p/p_{ref} = 1.0$ shortly afterwards. This indicates the lack of mesh resolution in the non-reactive region. The experimental data also shows a rapid increase of pressure immediately downstream the injector position until $x/H = 8$, where it rises with constant rate until the end of the

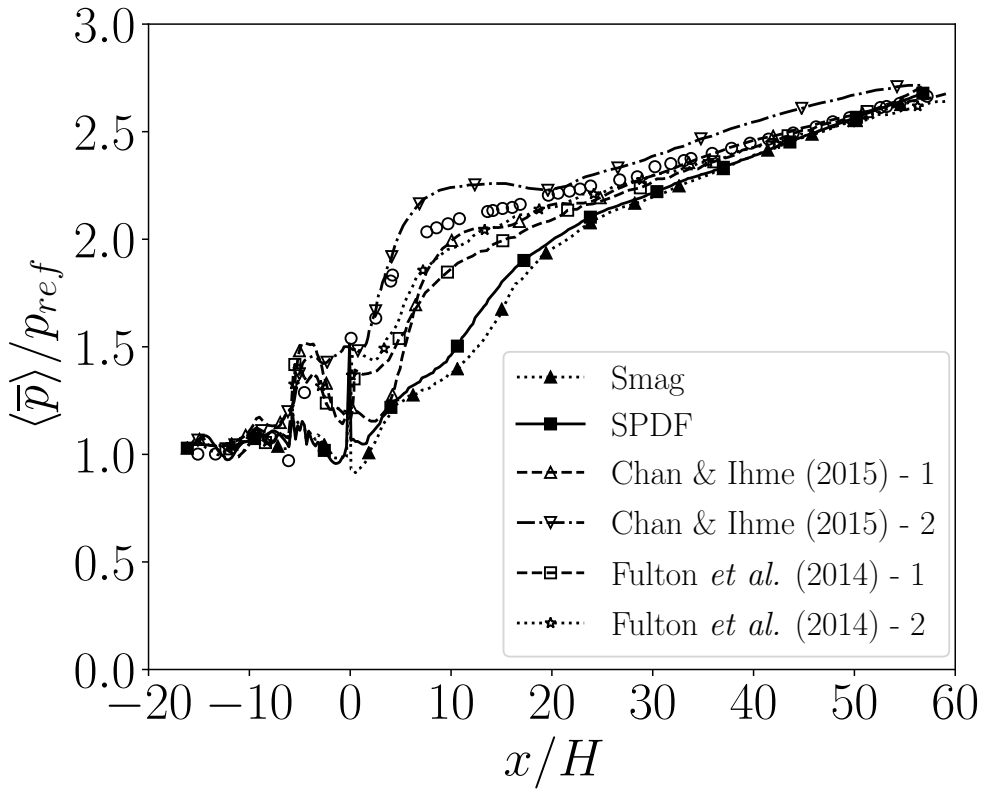

Figure 5.3: Topwall pressure at the centreline, where $p_{ref} = 37$(kPA). Experimental data from Cutler *et al.* [171] (○). Simulations from Chan and Ihme [33] using the FPV (1) and the quasi-laminar model (2), employing the Burke *et al.* [176] mechanism. Simulations from Fulton *et al.* [12] using the quasi-laminar approach employing the Jachimowski [177] (1) and the Burke *et al.* [176] (2) chemical mechanism.

extender.

The numerical studies of Chan and Ihme [33] investigated the quasi-laminar and the flamelet/progress variable (FPV) approaches, employing the Burke *et al.* [176] combustion mechanism and approximately 40 millions cells. The FPV model underpredicts the pressure output, while the quasi-laminar shows opposite behaviour. Their agreement in the injector region is better, which could be related to the higher mixing achieved through the better mesh resolution. The investigation of Fulton *et al.* [12] also employed an approximately 40 millions cells mesh and used the quasi-laminar approach to deal with the reactive term. Both simulations show a faster pressure rise without any source term modelling. The higher mixing level have been achieved through a better resolution close to the burner.

Although the SPDF model improves the topwall pressure experimental agreement, the limitations of the Smagorinsky model to close the convective terms when applied to a coarse mesh possibly drove the reaction further downstream. The mixing level is increased through the usage of the new SPDF formulation, which relates the pressure with the stochastic variables. The Smagorinsky model coupled with the quasi-laminar model is able to provide reasonable results, but a finer mesh is very important in the quasi-linear approach.

The top-wall pressure indicates that the mixing level is fundamental to simulate this scramjet configuration. The mesh resolution and proper mixing close to the injector region seems to be the key factor to trigger combustion at the correct position and reproduce the top-wall pressure. The mesh resolution close to the wall is not fine in the simulations, however, the pressure at the beginning and a the end of the domain are correctly captured, which suggests that the resolution close to the injector is more relevant in this case.

Figure 5.4 presents the averaged temperature contour plots at the positions $x/H = 6$, $x/H = 12$ and $x/H = 18$. These positions are also highlighted at Figure 5.2(a). The plots presents overall good agreement to the CARS measurements. The topwall temperature distribution in regions from $z/H = [-3, -2]$ and $z/H = [2, 3]$, close to the corners, presents greater values than the experiments.

The temperature profiles seems also more sparse close to the top wall, which is a consequence of the poor near-wall mesh resolution. Fulton *et al.* [12] used a $y^+ \approx 1$, employing a mesh spacing of 0.005 mm to the wall. The mesh spacing employed here results in distances up to $y^+ \approx 85$. A wall-function approach is therefore required to improve the accuracy of the simulations.

The SPDF model, nonetheless, predicts results with temperature profiles closer to the CARS measurement, achieving higher values than the Smagorinsky model at $x/H = 18$. The higher values are derived from the faster combustion rate, a consequence from the better mixing and turbulence-chemistry modelling.

The averaged hydrogen mole fraction results are shown in Figure 5.5. The experimental agreement is good for both models. At the position of $x/H = 6$, the hydrogen profile

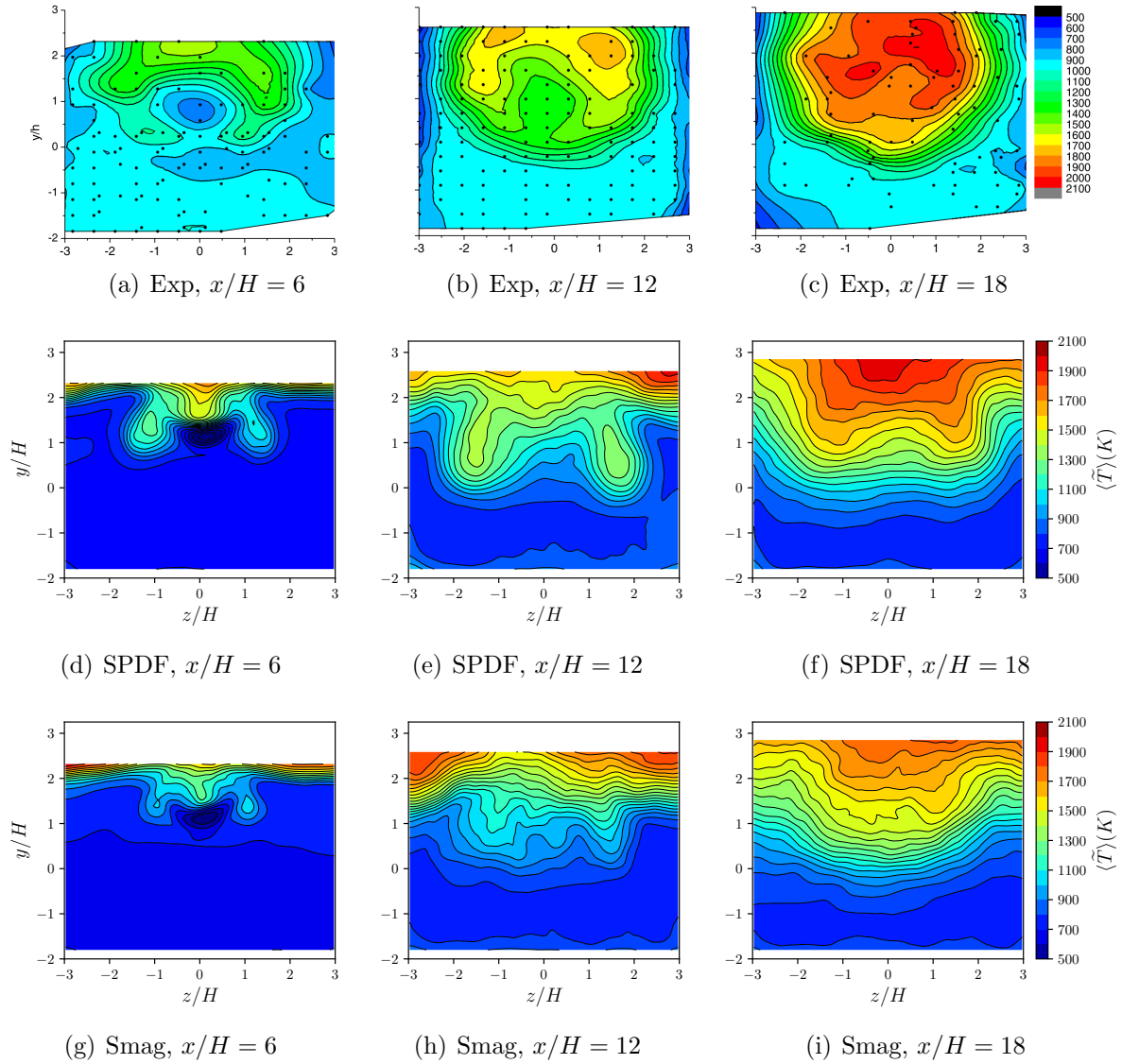

(a) Exp, $x/H = 6$ (b) Exp, $x/H = 12$ (c) Exp, $x/H = 18$

(d) SPDF, $x/H = 6$ (e) SPDF, $x/H = 12$ (f) SPDF, $x/H = 18$

(g) Smag, $x/H = 6$ (h) Smag, $x/H = 12$ (i) Smag, $x/H = 18$

Figure 5.4: Averaged temperature contour plots. CARS measurements performed by Cutler *et al.* [171] and reproduced here with permission from the copyright owner, Prof. Andrew D. Cutler.

is less round than the CARS measurement and more concentrated. At the downstream positions $x/H = 12$ and $x/H = 18$, the results are closer qualitatively and quantitatively to the experimental data.

Figure 5.6 shows the mole fraction of N_2. The simulations with both models present reasonable agreement with the experimental data from Cutler *et al.* [171]. At the position closer to the injector, $x/H = 6$, the profiles are again less sparse at the center. At downstream positions, the mixing level increases and at $x/H = 18$ the experimental agreement is good.

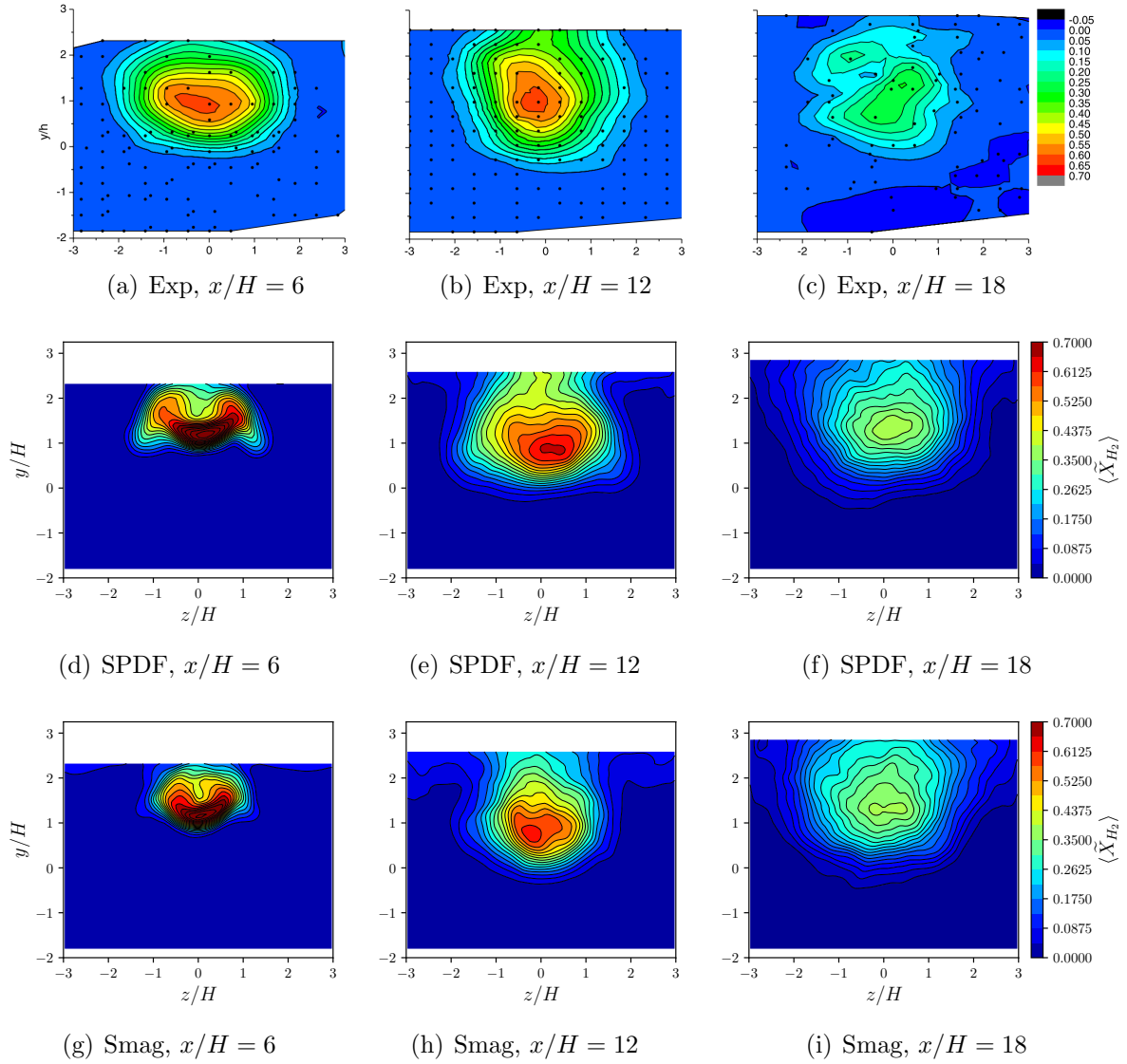

(a) Exp, $x/H = 6$ (b) Exp, $x/H = 12$ (c) Exp, $x/H = 18$

(d) SPDF, $x/H = 6$ (e) SPDF, $x/H = 12$ (f) SPDF, $x/H = 18$

(g) Smag, $x/H = 6$ (h) Smag, $x/H = 12$ (i) Smag, $x/H = 18$

Figure 5.5: Averaged mole fraction of H_2 contour plots. CARS measurements performed by Cutler *et al.* [171] and reproduced here with permission from the copyright owner, Prof. Andrew D. Cutler.

The top wall region presents different behaviour for both models than the experimental data. This unexpected behaviour is slightly more intense for the quasi-laminar approach. At the walls the diffusion effects are bigger than expected, which is a consequence of a coarse resolution in this region. The turbulence/combustion interactions are better solved in the SPDF model, which contributes to a better overall solution.

At last, the results for the averaged mole fraction of O_2 are presented in Figure 5.7. Overall the contour plots present reasonable agreement with the CARS measurements. The shape of the contour plots for the O_2 are not too different than the N_2 profiles, shown

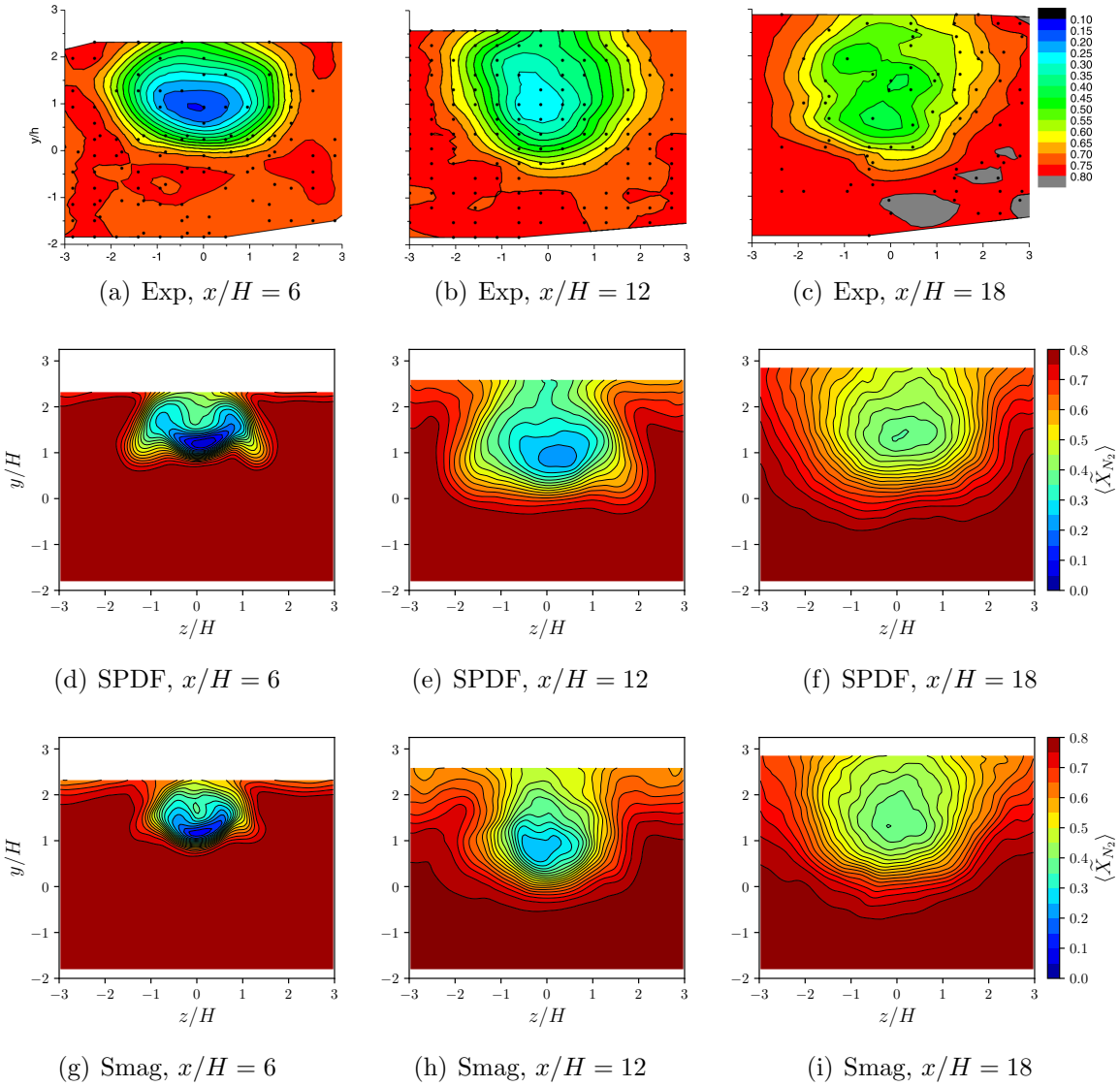

(a) Exp, $x/H = 6$ (b) Exp, $x/H = 12$ (c) Exp, $x/H = 18$

(d) SPDF, $x/H = 6$ (e) SPDF, $x/H = 12$ (f) SPDF, $x/H = 18$

(g) Smag, $x/H = 6$ (h) Smag, $x/H = 12$ (i) Smag, $x/H = 18$

Figure 5.6: Averaged mole fraction of N_2 contour plots. CARS measurements performed by Cutler *et al.* [171] and reproduced here with permission from the copyright owner, Prof. Andrew D. Cutler.

in Figure 5.6. However, the O_2 mole fraction of the SPDF model at the positions $x/H = 6$ and $x/H = 12$ are in better agreement with the experimental data. The concentration of O_2 is smaller in the regions of the fuel jet, indicating its higher reaction rate than in comparison to the Smagorinsky/quasi-laminar approach.

The topwall O_2 concentration profiles present the same issue as the other chemical species. It is overly diffused in the boundary layer, where the turbulent subgrid viscosity is too high because of lack of resolution. On the SPDF model, nonetheless, this behaviour is diminished.

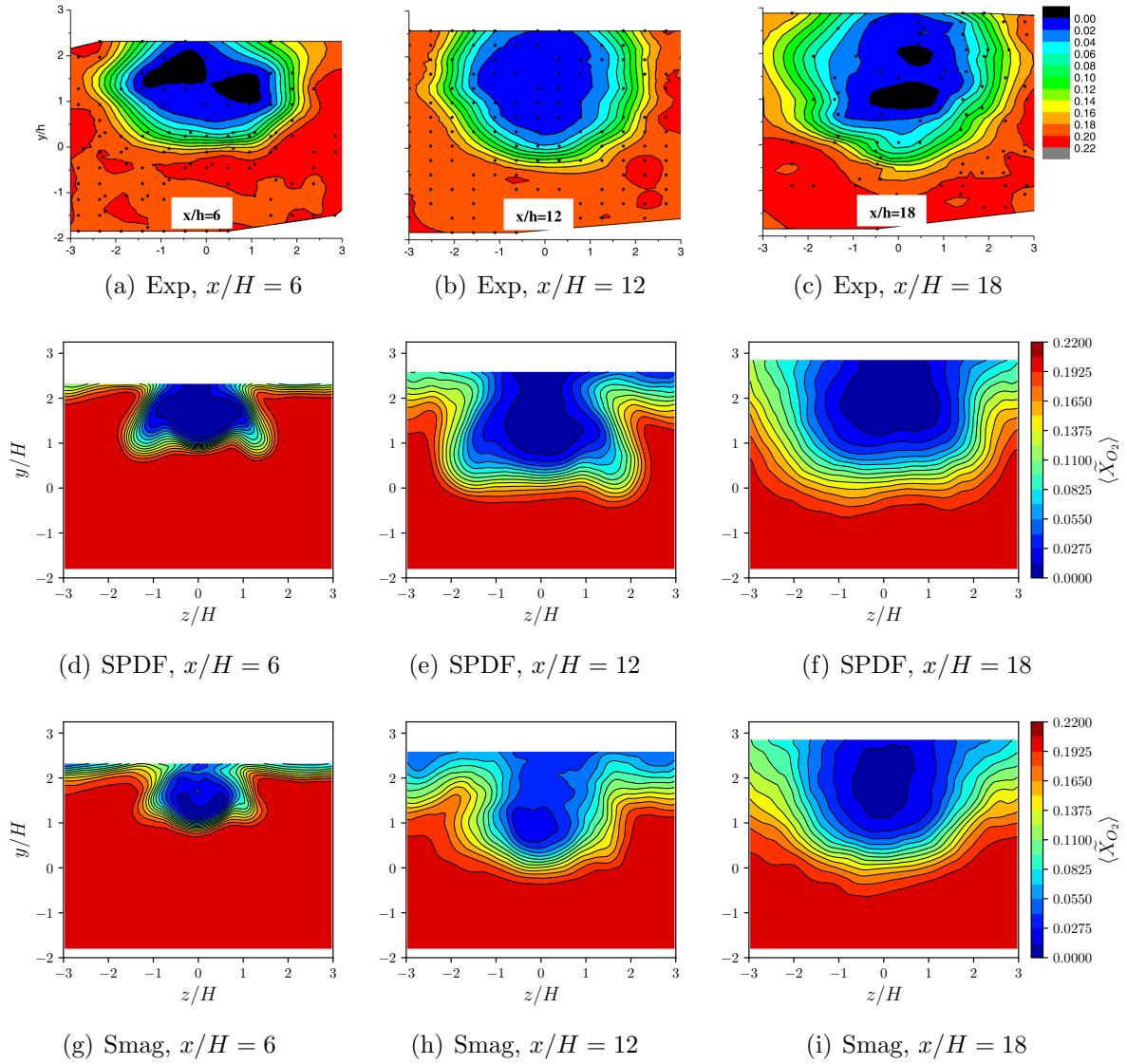

(a) Exp, $x/H = 6$ (b) Exp, $x/H = 12$ (c) Exp, $x/H = 18$

(d) SPDF, $x/H = 6$ (e) SPDF, $x/H = 12$ (f) SPDF, $x/H = 18$

(g) Smag, $x/H = 6$ (h) Smag, $x/H = 12$ (i) Smag, $x/H = 18$

Figure 5.7: Averaged mole fraction of O_2 contour plots. CARS measurements performed by Cutler *et al.* [171] and reproduced here with permission from the copyright owner, Prof. Andrew D. Cutler.

In general, reasonable experimental agreement has been achieved for the mole fractions and temperature, despite the limitations presented in both simulations. The SPDF shows an expected superior performance than the quasi-linear approach, improving the topwall pressure results and generating a flame plume with better qualitatively agreement to the CARS measurements of Cutler *et al.* [171].

5.3 Summary

This chapter presented the ability of the SPDF model to simulate a scramjet. The supersonic combustion ground-based facility of the University of Virginia presents a fairly simple geometry in comparison to other combustion engines, however, its numerical simulation is still a daunting task. The simulation presents a wall-bounded flow with supersonic inlets and hydrogen combustion, and several other complex physical features.

In this chapter all the numerical tools presented so far have been used. The geometry has been designed with an open-source CAD tool and converted to a GTS file, which could be read into the IBC method to simulate a non regular geometry within a uniform mesh.

The simulations have been performed using these techniques along with the Eulerian stochastic equations to solve the SPDF model. The SPDF model employs the Smagorinsky model to close the convective terms too, which makes it still dependent on high mesh resolution on complex simulations. The quasi-laminar approach has also been evaluated and it seems too sensitive to the mesh resolution on this test case. This approach shows limitations to generate good quality data, unless it is used in conjunction with a fine mesh [12, 33].

The topwall pressure has been evaluated and both models are able to generate reasonable experimental agreement. The pressure at the extender region is recovered. The shock wave at the compression-ramp leading edge, however, is weak in comparison to other results in the literature. The pressure rise at the combustor region takes more time to occur, although the SPDF is able to reduce this delay. The lack of enough mesh resolution seems to be the main reason for this issue.

The average temperature and mole fractions have also been assessed for both models and compared to the CARS measurements of [171]. The results are overall reasonable, with the SPDF generating a flame plume closer to the experimental data. In both simulations there are deficiencies with the accuracy close to the corners of the scramjet, which is due to the absence of a wall function and higher mesh resolution.

The Yetter *et al.* [162] mechanism has been employed for the first time to simulate this

scramjet configuration. A possible future investigation must evaluate other combustion mechanisms with the current numerical model. The models of Jachimowski [177] and Burke *et al.* [176] are specially designed to operate at high speed, which could provide new insights when used with the SPDF model.

Overall, the developed SPDF model has been proven to offer a reliable option to simulate supersonic combustion, capable of increasing mixing levels and simulating turbulence/chemistry interactions with better accuracy than the quasi-linear approach.

Chapter 6

Conclusion

6.1 Summary of Thesis Achievements

This work has developed and investigated two models to be used in supersonic combustion context and Large Eddy Simulation (LES) environment. The Probability Density Function (PDF) method has the ability to exactly close one-point statistics if the necessary information required is contained within the PDF sample space. Two PDFs have been investigated, a conservative formulation including enthalpy and mass fractions into the PDF sample space (SPDF); and a more complete model, including density, mass fractions, velocity and total energy in the PDF sample space (VSPDF). These formulations considerably reduce the unknowns in classical LES equations of compressible flows, however, they require sophisticated solution method to be computationally feasible.

The SPDF formulation has a more well-established research ground, with several applications to low Mach number combustion. Its application in high-speed combustion can be performed by implementing the Eulerian stochastic equations into a compressible code and account for compressible effects. However, the source term is not exactly closed, as it is necessary one extra thermodynamic variable, such as pressure or density, to solve it. The SPDF model also require the convective subgrid terms to be closed, which is performed here with the Smagorinsky model. The new formulation employs the information from the Eulerian stochastic fields to exactly solve the pressure field, an approach only

used in Lagrangian formulation before. In this way, the SPDF model also improves the flow field.

The VSPDF formulation is a more complete approach and exactly closes the convective and reactive terms within the LES framework. The Eulerian stochastic field method is used to solve the VSPDF transport equation. The stochastic equations require mild assumptions in order to preserve mass and prevent numerical shocks. This new formulation greatly reduces the number of unknowns, mainly those derived from the convective terms. The model requires the use of the micromixing and the Langevin models for closure. Because of its new formulation and assumptions, these closures may require new calibration or additional closures.

The new developed stochastic equations have been implemented into the in-house fortran-based compressible multicomponent code CompReal. High order spatial and temporal discretisation, which is important in compressible fluid dynamics, are available. The discretisation performance has been evaluated through the homogeneous isotropic turbulence test case, where variables such as enstrophy and energy spectra have been investigated. *The hybrid discretisation method is regarded as the best compromise between accuracy and numerical stability within the present context.*

The PDF models have also been evaluated through a series of numerical tests to assess their performance and accuracy. The one-dimensional reactive shock tube has been investigated and the scatter plots show that the SPDF presents higher mixing level than the VSPDF for the chemical species. This may occur because of the Wiener term in the mass fraction equations in the SPDF model, which increases the dispersion. The VSPDF, although theoretically more complete, presents scatter plots more condensed in some regions, which limits the advantage of the PDF model in accessing several composition spaces. This suggests that *the VSPDF model requires further closures in the stochastic equations.*

The reactive shock tube has also been used to verify the Monte Carlo convergence rate, simulating between 2 and 8192 fields. It is shown that the number of *eight stochastic fields* is enough for the SPDF model to achieve, on average, less than 1% error for the first

moment. For the VSPDF, the number of eight stochastic fields has also demonstrated sufficient to achieve first moment convergence with 1% error for chemical species and at most 5% error for the velocity.

Two and three-dimensional reactive and high-speed mixing layers have been investigated, using the configuration of Ferrer [26]. These test cases reveals the ability of both SPDF and VSPDF models to capture flow variables and reproduce DNS data with good agreement. The VSPDF, though, seems to overestimate the turbulence levels. The rate of growth of the vorticity thickness in the SPDF simulations is in better agreement with DNS data. The velocity fluctuations of the VSPDF are closer to the DNS data, however, still larger in general. *The present VSPDF formulation seems to consistently provide higher turbulence levels and overestimates growth of shear layers. This suggests that additional modelling is required for the Langevin model in high-speed LES or additional effort have to be put to initialise the sub-grid velocity field. The SPDF provide closer agreement and has shown higher numerical consistency and convergence rate.*

Two supersonic burners have been investigated in order to ensure the numerical validation of the SPDF model. The SPDF and the Smagorinsky model employing the quasi-laminar approach have been used to simulate the supersonic burners of Cheng *et al.* [7] and Evans *et al.* [152]. These simulations are complex and include a wide range of physical features. The SPDF model shows good agreement and improvement compared to the quasi-laminar approach. The SPDF results for a a coarse mesh are closer to the experimental data than the results of a fine mesh simulation for the Cheng *et al.* [7] burner with the quasi-laminar approach. For the Evans *et al.* [152], however, the experimental agreement is not as good as the fine mesh. Both models with coarse mesh seem to overpredict turbulence/diffusion levels.

Finally, the scramjet UVa configuration A [171] has been simulated. The results show the ability of the SPDF model to reproduce at a certain extent the topwall averaged pressure, an important property for the scramjet thrust measurement. The SPDF model presents better experimental agreement than the Smagorinsky model coupled with the quasi-laminar approach. The mole fractions and temperature results also show that the

SPDF reproduces better the experimental flame plume. The present simulations are limited, however, and require the implementation of wall-functions to better agree with data value.

Overall, the SPDF model along with the Eulerian stochastic field method presents good results. Improvements can be made in the micromixing model to allow better mixing in high-speed cases such as in the supersonic burners. The VSPDF is a more complete approach, however, the current formulation requires further examination. The Langevin model constant may be need to be calibrated to also capture higher moments and deal with pressure fluctuations that were not included in this formulation.

The SPDF and VSPDF formulations developed in this work shed light into PDF methods applied to LES and supersonic combustion. Their limitations and advantages have been concisely exposed through simulating different test cases and experimental configurations. This work shows that both models are promising formulations, as they present many desirable features to simulate supersonic combustion with high accuracy and feasible computational power.

6.2 Future Work

There are several topics presented here that can be further investigated. The following suggestions can be implemented to improve the models robustness, accuracy and generality:

- The SPDF may benefit from a better or more specific micromixing model. The correction included to deal with low Reynolds number improved the results for the reactive shock tube. However, the IEM micromixing constants C_{Y_α} and C_H have values extracted from the low Mach number combustion literature. The values could be calibrated for supersonic combustion in order to allow a reasonable level of stochastic fluctuations. The use of a more complex micromixing model can also be evaluated, although it may require a larger number of stochastic fields to achieve statistical convergence.

- The VSPDF may benefit from improved closures instead of the ones used in this work. The Langevin model of Delarue and Pope [20] should also be evaluated, as it includes correction to include compressible effects. The inclusion of a stochastic pressure to prevent the numerical shocks may have imposed a strong assumption and requires additional examination. The IEM micromixing part can also be improved through a better constant choice, as pointed out in the previous item.

- Most part of this work has been conducted using the Yetter *et al.* [162] mechanism. One major advantage of the PDF models is their ability to capture detailed chemistry, since the reaction term does not need closure within the large eddy simulation environment. The hydrogen combustion mechanisms of Jachimowski [177] and Burke *et al.* [176] can be used in the test cases presented, as they are optimised to work in high speed/high pressure flames. A different chemical mechanism could offer better understanding on the limitations presented in the supersonic burners and in the scramjet cases.

- The Navier-Stokes Characteristics Boundary Conditions [147] can be used in all test cases presented here. They are potentially more accurate than the first order boundary conditions used in this work, since they are specially designed to operate with compressible solver and help with pressure reflections from the boundaries. As the focus of this work has not been on the acoustics of the flames, these boundary conditions have not been further explored. However, the characteristics may be complex to implement into the VSPDF method, since each field can possess a different boundary condition for velocity.

- The use of wall functions are of paramount importance when the flow is not well resolved in near-wall regions. The absence of enough mesh resolution to capture the viscous sublayer have interfered in the quality of the results close to corners on the scramjet. In such cases, the use of a wall function is vital. The simulation of near-wall regions in a large eddy simulation framework is an extensive topic and must be explored in scramjet simulations.

- Adaptive mesh refinement has been implemented into the in-house code CompReal to deal with sharp gradients. This capability could be extended to the PDF models in order to refine the mesh in critical regions of the flow like shocks or flame front. The adaptive refinement can be applied only to the mean flow and not necessarily to each individual stochastic field. The AMR can be used in the experimental supersonic burners to solve the mixing layer between fuel jet/air co-flow and air-flow/surrounding air. On the scramjet simulations, it can be applied not only to the sharp gradients regions but close to walls on the very first time step, obtaining a highly resolved mesh in all important regions of the flow.

Bibliography

[1] K. Bowcutt, A. Paull, D. Dolvin, and M. Smart. Hifire: An international collaboration to advance the science and technology of hypersonic flight. In *28th International Congress of the Aeronautical Sciences*, Brisbane, 2012, 2012.

[2] N. E. Hass, M. K. Smart, and A. Paull. Flight data analysis of HyShot 2. *13th AIAA/CIRA International Space Planes and Hypersonic Systems and Technologies Conference*, 2005.

[3] C. Fureby, M. Chapuis, E. Fedina, and J. Tegnér. A computational study of scramjet combustion. *27th International Congress of the Aeronautical Sciences*, 2010.

[4] H. Koo, V. Raman, and P. L. Varghese. Direct numerical simulation of supersonic combustion with thermal nonequilibrium. *pci*, 35:2145–2153, 2015.

[5] A. D. Cutler, P. M. Danehi, R. R. Springer, S. O'Byrne, D. P. Capriotti, and R. DeLoach. Coherent Anti-Stokes Raman Spectroscopic Thermometry in a Supersonic Combustor. *AIAA Journal*, 41(12), 2003.

[6] A. D. Gardner, K. Hannemann, J. Steelant, and A. Paull. Ground testing of the hyshot supersonic combustion flight experiment in heg and comparison with flight data. In *40th AIAA Joint Propulsion Conference*, Fort Lauderdale, Florida, 2004.

[7] T. S. Cheng, J. A. Wehrmeyer, R. W. Pitz, O. Jarrett Jr, and G. B. Northam. Raman measurement of mixing and finite-rate chemistry in a supersonic hydrogen-air diffusion flame. *Combust. Flame*, 99:157–173, 1994.

[8] R. D. Rockwell, C. P. Goyne, B. E. Rice, and J. R. Edwards. Collaborative Experimental and Computational Study of a Dual-Mode Scramjet Combustor. *Journal of Propulsion and Power*, 30(3):530–538, 2014.

[9] H. Koo. *Large-Eddy Simulations of Scramjet Engines*. PhD thesis, University of Texas, Austin, 2011.

[10] P. Cocks. *Large Eddy Simulation of Supersonic Combustion with Application to Scramjet Engines*. PhD thesis, University of Cambridge, Cambridge, 2011.

[11] R. Pecnik, V. E. Terrapon, F. Ham, and G. Iaccarino. Full system scramjet simulation. *Center for Turbulence Research Annual Research Briefs*, pages 33–45, 2009.

[12] J. A. Fulton, J. R. Edwards, H. A. Hassan, J. C. McDaniel, C. P. Goyne, R. D. Rockwell, A. D. Cutler, C. T. Johansen, and P. M. Danehy. Large-Eddy/Reynolds-Averaged Navier-Stokes Simulations of Reactive Flow in Dual-Mode Scramjet Combustor. *Journal of Propulsion and Power*, 30(3):558–575, 2014.

[13] P. J. Colucci, F. A. Jaberi, P Givi, and S. B. Pope. Filtered density function for large eddy simulation of turbulent reacting flows. *Physics of Fluids*, 10(2):499–515, 1998.

[14] H. Möbus, P. Gerlinger, and D. Brüggemann. Scalar and joint scalar-velocity-frequency Monte Carlo PDF simulation of supersonic combustion. *Combustion and Flame*, 132:3–24, 2003.

[15] A. Banaeizadeh, Z. Li, and F. A. Jaberi. Compressible Scalar Filtered Mass Density Function Model for High-Speed Turbulent Flows. *AIAA Journal*, 49(10):2130–2143, 2011.

[16] M. B. Nik. *VS-FMDF and EPSV-FMDF for large eddy simulation of turbulent flows*. PhD thesis, University of Pittsburgh, Pittsburgh, 2012.

[17] F. Gao and E. E. O'Brien. A large-eddy simulation scheme for turbulent reacting flows. *Physics of Fluids*, 5:1282–1284, 1993.

[18] L. Bouheraoua, P. Domingo, and G. Ribert. Large-eddy simulation of a supersonic lifted jet flame: Analysis of the turbulent flame base. *Combust. Flame*, 179:199–218, 2017. ISSN 00102180.

[19] L. Valiño. A Field Monte Carlo Formulation for Calculating the Probability Density Function of a Single Scalar in a Turbulent Flow. *Flow, Turbulence and Combustion*, 60:157–172, 1998.

[20] B. J. Delarue and S. B. Pope. Application of PDF methods to compressible turbulent flows. *Physics of Fluids*, 9(9):2704–2715, 1997.

[21] M. B. Nik, P. Givi, C. K. Madnia, and S. B. Pope. EPVS-FMDF for LES of high-speed turbulent flows. In *50th AIAA Aerospace Sciences Meeting including the New Horizons Forum and Aerospace Exposition*, Tennessee, 2012, January 2012.

[22] J. Urzay. Supersonic Combustion in Air-Breathing Propulsion Systems for Hypersonic Flight. *Annual Review of Fluid Mechanics*, 50(1):593–627, 2018.

[23] L. Vervisch and T. Poinsot. Direct numerical simulation of non-premixed turbulent flames. *Annual Review of Fluid Mechanics*, 30:655–691, 1998.

[24] T. Jin, K. Luo, S. Lu, and J. Fan. DNS investigation on flame structure and scalar dissipation of a supersonic lifted hydrogen jet flame in heated coflow. *International Journal of Hydrogen Energy*, 38(23):9886–9896, 2013.

[25] T. Jin, K. Luo, S. Lu, and J. Fan. Direct numerical simulation of a supersonic lifted hydrogen jet flame: A priori study on combustion models. *Acta Astronautica*, 109: 52–64, 2015.

[26] P. J. M. Ferrer. *Simulation numérique directe dans la combustion turbulente sur une couche de cisaillement*. PhD thesis, Ecole Nationale Supérieure de Mécanique et d'Aérotechique, Poitiers, 2013.

[27] M. Berglund and C Fureby. LES of supersonic combustion in a scramjet engine model. *Proc. Combust. Inst.*, 31(2):2497–2504, 2007.

[28] J. Smagorinsky. General circulation experiments with the primitive equations. *Monthly Weather Review*, 91(3):99–164, 1963.

[29] C. Gong, M. Jandi, X. Bai, J. Liang, and M. Sun. Large eddy simulation of hydrogen combustion in supersonic flows using an eulerian stochastic fields method. *International Journal of Hydrogen Energy*, 42:1264–1275, 2017.

[30] F. Genin and S. Menon. Simulation of Turbulent Mixing Behind a Strut Injector in Supersonic Flow. *AIAA Journal*, 48(3):526–539, 2010.

[31] R. E. Bensow and C. Fureby. On the justification and extension of mixed models in LES. *Journal of Turbulence*, 8:N54, 2007.

[32] Y. Moule, V. Sabelnikov, and A. Mura. Highly resolved numerical simulation of combustion in supersonic hydrogen–air coflowing jets. *Combust. Flame*, 161(10): 2647–2668, 2014.

[33] W. L. Chan and M. Ihme. Large-eddy simulations and turbulent combustion model analysis of a dual-mode scramjet combustor. *Center for Turbulence Research Annual Research Briefs*, pages 115–124, 2015.

[34] A. W. Vreman. An eddy-viscosity subgrid-scale model for turbulent shear flow: Algebraic theory and applications. *Physics of Fluids*, 16(10):3670–3681, 2004.

[35] R. Pecnik, V. E. Terrapon, F. Ham, G. Iaccarino, and H. Pitsch. Reynolds-Averaged Navier-Stokes Simulations of the HyShot II Scramjet. *AIAA Journal*, 50(8):1717–1732, 2012.

[36] H. Koo, P. Donde, and V. Raman. A quadrature-based LES/transported probability density function approach for modeling supersonic combustion. *Proc. Combust. Inst.*, 33:2203–2210, sep 2011. ISSN 15407489.

[37] P. Donde, H. Koo, and V. Raman. A multivariate quadrature based moment method for LES based modeling of supersonic combustion. *J. Comput. Phys.*, 231(17):5805–5821, 2012. ISSN 00219991.

[38] K. K. Kuo and R. Acharya. *Fundamentals of Turbulent and Multiphase Combustion*. John Wiley and Sons, Inc., 1st edition, 2012.

[39] T. Poinsot and D. Veynante. *Theoretical and Numerical Combustion*. R.T. Edwards, Philadelphia, 1st edition, 2001.

[40] G. G. Stokes. On the theories of the internal friction of fluids in motion, and of the equilibrium and motion of elastic solids. *Transactions of the Cambridge Philosophical Society*, 8(287-319), 1845.

[41] S. B. Pope. *Turbulent Flows*. Cambridge University Press, Cambridge, 1st edition, 2000.

[42] E. Garnier, N. Adams, and P. Sagaut. *Large Eddy Simulation for Compressible Flows*. Springer, Berlin, 1st edition, 2009.

[43] M. Germano, U. Piomelli, P. Moin, and W. Cabot. A dynamic subgrid-scale eddy viscosity model. *Physics of Fluids*, 3(7):1760–1765, 1991.

[44] D. K. Lilly. A proposed modification of the germano subgrid-scale closure model. *Physics of Fluids*, 4:633–635, 1992.

[45] A. Yoshizawa and K Horiunti. A statiscally-derived subgrid-scale kinetic energy model for the large-eddy-simulation of turbulent flows. *Journal of Physical Society of Japan*, 54:2834–2839, 1985.

[46] E. D. Gonzalez-Juez, A. R. Kerstein, R. Ranjan, and S. Menon. Advances and challenges in modeling high-speed turbulent combustion in propulsion systems. *Progress in Energy and Combustion Science*, 60:26–67, 2017.

[47] B. F. Magnussen. On the structure of turbulence and a generalized eddy dissipation concept for chemical reaction in turbulent flow. *19th American Institute of Aeronautics and Astronautics Aerospace Science Meeting*, 1981.

[48] H. G. Weller, G. Tabor, A. D. Gosman, and C. Fureby. Application of a flame-wrinkling LES combustion model to a turbulent mixing layer. *Twenty-Seventh*

Symposium (International) on Combustion/The Combustion Institute, pages 899–907, 1998.

[49] A. Y. Klimenko. Multicomponent diffusion of various admixtures in turbulent flow. *Fluid Dynamics*, 25(3):327–334, 1990.

[50] C. G. Speziale, G. Erlebacher, T. A. Zang, and M. Y. Hussaini. A thickened flame model for large eddy simulations of turbulent premixed combustion. *Physics of Fluids*, 12(7):1843–1863, 2000.

[51] H. Pitsch. Large-Eddy Simulation of Turbulent Combustion. *Annu. Rev. Fluid Mech.*, 38(1):453–482, 2006. ISSN 0066-4189.

[52] C. Fureby. Large eddy simulation modelling of combustion for propulsion applications. *Phil. Trans. A*, 367(1899):2957–69, jul 2009.

[53] L. Vervisch. Turbulent Combustion Modeling. Technical report, Imperial College London, 2018.

[54] J. D. Van der Waals. *Over de Continuiteit van den Gas - en Vloeistoftoestand*. PhD thesis, University of Leiden, Leiden, 1873.

[55] O. Redlich and J. N. S. Kwong. On the Thermodynamics of Solutions. V. An Equation of State. Fugacities of Gaseous Solutions. *Chemical Reviews*, 44(1):233–244, 1949.

[56] D. Peng and D. Robinson. A new two-constant equation of state. *Industrial and Engineering Chemistry Fundamentals*, 15:59–64, 1976.

[57] G. Ribert, X. Petit, and P. Domingo. High-pressure methane-oxygen flames. Analysis of sub-grid scale contributions in filtered equations of state. *Journal of Supercritical Fluids*, 121:78–88, 2017.

[58] J. O. Hirschfelder, C. F. Curtiss, and R. B. Bird. *Molecular Theory of Gases and liquids*. John Wiley and Sons, New York, 1 edition, 1954.

[59] C. R. Wilke. A viscosity equation for gas mixtures. *The Journal of Chemical Physics*, 18(4):517–519, 1950.

[60] A. Liñán, M. Vera, and A. L. Sánchez. Ignition, Liftoff, and Extinction of Gaseous Diffusion Flames. *Annual Review of Fluid Mechanics*, 47(1):293–314, 2015.

[61] A. Almagro, O. Flores, M. Vera, A. Liñán, A.L. Sánchez, and F.A. Williams. Effects of differential diffusion on nonpremixed-flame temperature. *Proceedings of the Combustion Institute*, 2018.

[62] W. P. Jones, S. Lyra, and S. Navarro-Martinez. Large eddy simulation of a swirl stabilized spray flame. *Proc. Combust. Inst.*, 33:2153–2160, 2011.

[63] R. P. Linsdtedt and S. A. Louloudi. Joint-scalar transported PDF modeling of soot formation and oxidation. *Proceedings of the Combustion Institute*, 30:775–783, 2005.

[64] D. C. Haworth. Progress in probability density function methods for turbulent reacting flows. *Progress in Energy and Combustion Science*, 36:168–259, 2010.

[65] T. S. Lundgren. Distribution functions in the statistical theory of turbulence. *The Physics of Fluids*, 10(5):969–975, 1967.

[66] T. S. Lundgren. Model equation for nonhomogeneous turbulence. *Physics of Fluids*, 12(2):485–497, 1969.

[67] C. Dopazo. Probability density function approach for a turbulent axisymmetric heated jet. Centerline Evolution. *Physics of Fluids*, 18:397–404, 1975.

[68] S. B. Pope. PDF methods for turbulent reactive flows. *Progress in Energy and Combustion Science*, 11:119–192, 1985.

[69] C. Dopazo and E. E. O'Brien. An approach to the autoignition of a turbulent mixture. *Acta Astronautica*, 1:1239–1266, 1974.

[70] C. Dopazo and E. E. O'Brien. Statistical Treatment of Non-Isothermal Chemical Reactions in Turbulence. *Combustion Science and Technology*, 13(1-6):99–122, 1976.

[71] J. Villermaux and J. C. Devillon. Représentation de la coalescence et de la redispersion des domaines de ségrégations dans un fluide par un modèle d'interáction phénoménologique. In *2nd International Symposium on Chemical Reaction Engineering*, Netherlands, 1972, 1972.

[72] S. B. Pope. The probability approach to the modelling of turbulent reacting flows. *Combustion and Flame*, 27:299–312, 1976.

[73] S. B. Pope. The implications of the probability equations for turbulent combustion models. *Combustion and Flame*, 29:235–246, 1977.

[74] S. B. Pope. The statistical theory of turbulent flames. *Philosophical Transactions of the Royal Society of London. Serier A, Mathematical and Physical Sciences*, 291: 529–568, 1979.

[75] S. B. Pope. The probability approach to the modelling of turbulent reacting flows. *Journal of Non-Equilibrium Thermodynamics*, 24:309–320, 1979.

[76] R. O. Fox. *Computational Models for Turbulent Reacting Flows*. Cambridge, 1st edition, 2003.

[77] S. B. Pope. The relationship between the probability approach and particle models for reaction in homogeneous turbulence. *Combustion and Flame*, 35:41–45, 1979.

[78] C. W. Gardiner. *Handbook of Stochastic Methods*. Springer, Berlin, 3rd edition, 2003.

[79] S. B. Pope. A Monte Carlo Method for the PDF Equations of Turbulent Reactive Flow. *Combustion Science and Technology*, 25:159–174, 1981.

[80] J. Janicka, W. Kolbe, and W. Kollmann. The solution of a PDF-transport equation for turbulent diffusion flames. *Proceedings of the 1978 Heat Transfer and Fluid Mechanics Institute*, 1978.

[81] P. Langevin. Sur la theorie du mouvement brownien. *C. R. Acad. Sci. (Paris)*, 146: 530–533, 1908.

[82] D. C. Haworth and S. B. Pope. A generalized Langevin model for turbulent flows. *Physics of Fluids*, 29:387–405, 1986.

[83] W. P. Jones and B. E. Launder. The prediction of laminarization with a two-equation model of turbulence. *Int. J. Heat Mass Transfer*, 15:301–314, 1972.

[84] B. E. Launder and D. B. Spalding. The numerical computation of turbulent flows. *Computer Methods in Applied Mechanics and Engineering*, 3(2):269–289, 1974.

[85] J. Xu and S. B. Pope. PDF calculations of turbulent nonpremixed flames with local extinction. *Combustion and Flame*, 123(3):281 – 307, 2000.

[86] R. R. Cao and S. B. Pope. The influence of chemical mechanisms on PDF calculations of nonpremixed piloted jet flames. *Combustion and Flame*, 143(4):450 – 470, 2005. Special Issue to Honor Professor Robert W. Bilger on the Occasion of His Seventieth Birthday.

[87] R.P. Lindstedt, S.A. Louloudi, and E.M. Váos. Joint scalar probability density function modeling of pollutant formation in piloted turbulent jet diffusion flames with comprehensive chemistry. *Proceedings of the Combustion Institute*, 28(1):149 – 156, 2000.

[88] W. Kollmann. A PDF closure for compressible turbulent chemically reacting flows. Technical Report NAG 3-836, National Aeronautics and Space Administration - NASA, 1992.

[89] P. Eifler and W. Kollmann. AIAA 93-0448. PDF prediction of supersonic hydrogen flames. In *31st Aerospace Sciences Meeting & Exhibit*, Reno, 1993, January 1993.

[90] J. Bakosi and J. R. Ristorcelli. Exploring the beta distribution in variable-density turbulent mixing. *Journal of Turbulence*, 11(37), 2010.

[91] J. Bakosi and J. R. Ristorcelli. Extending the Langevin model to variable-density pressure-gradient-driven turbulence. *Journal of Turbulence*, 12(19), 2011.

[92] J. Bakosi and J. R. Ristorcelli. Probability density function method for variable-density pressure-gradient-driven turbulence and mixing. *AIAA Paper*, 2011.

[93] W. C. Welton and S. B. Pope. A PDF-based particle method for compressible turbulent flows. *AIAA 33rd Aerospace Sciences Meeting and Exhibit*, pages 1–14, 1995.

[94] W. C. Welton and S. B. Pope. PDF Model Calculations of Compressible Turbulent Flows Using Smoothed Particle Hydrodynamics . *Journal of computational physics*, 134:150–168, 1997.

[95] T. Dreeben and S. B. Pope. Probability density function and Reynolds-stress modelling of near-wall turbulent flows. *Physical Review Letters*, 9:154–163, 1997.

[96] B. J. Delarue and S. B. Pope. Calcularions of subsonic and supersonic turbulent reacting mixing layers using probability density function methods. *Physics of Fluids*, 10(2):487–498, 1998.

[97] O. Zeman. On the decay of compressible isotropic turbulence. *Physics of Fluids A: Fluid Dynamics*, 3(5):951–955, 1991.

[98] Jayesh and S. B. Pope. Stochastic model for turbulent frequency. *Technical report, FDS 95-05, Cornell University*, 1995.

[99] G. Hauke and L. Valiño. Computing reactive flows with a field monte carlo formulation and multi-scale methods. *Computational Methods in Applied Mechanics and Engineering*, 193:1455–1470, 2004.

[100] R. Mustata, L. Valiño, C. Jiménez, W. P. Jones, and S. Bondi. A probability density function eulerian monte carlo field method for large eddy simulations: Application

to a turbulent piloted methane/air diffusion flame (sandia d). *Combustion and Flame*, 145:88–104, 2006.

[101] V. Sabel'nikov and O. Soulard. Rapidly decorrelating velocity-field model as a tool for solving one-point Fokker-Planck equations for probability density functions of turbulent reactive scalars. *Physical Review E*, 72:1282–1284, 2005.

[102] L. Valiño, R. Mustata, and K. B. Letaief. Consistent Behavior of Eulerian Monte carlo fields at Low Reynolds Numbers. *Flow, Turbulence and Combustion*, 96: 503–512, 2016.

[103] O. Soulard and V. A. Sabel'nikov. Eulerian Monte Carlo Method for the Joint Velocity and Mass-Fraction Probability Density Function in Turbulent Reactive Gas Flows. *Combustion, Explosion and Shock Waves*, 42:753–762, 2006.

[104] O. Soulard and V. Sabel'nikov. Eulerian Monte Carlo Method for solving joint velocity-scalar PDF : numerical aspects and validation x Introduction. Technical report, The French Aerospace Lab ONERA, 2008.

[105] N. Petrova. *Turbulence-chemistry interaction models for numerical simulation of aeronautical propulsion systems*. PhD thesis, Ecole Polytechnique, Paris, 2015.

[106] F. Guillois, N. Petrova, O. Soulard, R. Duclous, and V. Sabelnikov. Stochastic partial differential equations as a tool for solving the joint velocity-scalar probability density function transport equation. In *Stochastic Processes: Fundamentals, Concepts and Applications*, pages 1–43. 2017.

[107] D. Azarnykh, S. Litvinov, and N. A. Adams. Numerical methods for the weakly compressible Generalized Langevin Model in Eulerian reference frame. *Journal of Computational Physics*, 314:93–106, 2016.

[108] P. Givi. Model-Free simulations of turbulent reactive flows. *Prog. Energy Combust. Sci.*, 15:1–107, 1989.

[109] S. B. Pope. Computations of turbulent combustion: progress and challenges. *Twenty-Third Symposium (International) on Combustion/The Combustion Institute*, pages 591–612, 1990.

[110] L. Wang. On discrete representation of filtered density functions for turbulent combustion. *Center for Turbulence Research Annual Research Briefs*, pages 219–229, 2007.

[111] F. A. Jaberi, P. J. Colucci, S. James, P. Givi, and S. B. Pope. Filtered mass density function for large-eddy simulation of turbulent reacting flows. *Journal of Fluid Mechanics*, 401:85–121, 1999.

[112] P. Givi. Filtered density function for subgrid scale modeling of turbulent combustion. *AIAA Journal*, 44(1):16–23, 2006.

[113] V. Raman, H. Pitsch, and R. O. Fox. Hybrid large-eddy simulation/Lagrangian filtered-density-function approach for simulating turbulent combustion. *Combustion and Flame*, 143(1):56 – 78, 2005.

[114] H. Wang, P. P. Popov, and S. B. Pope. Weak second-order splitting schemes for Lagrangian Monte Carlo particle methods for the composition pdf/fdf transport equations. *Journal of Computational Physics*, 229:1852–1878, 2010.

[115] H. Wang and S. B. Pope. Large eddy simulation/probability density function modeling of a turbulent CH4/H2/N2 jet flame. *Proceedings of the Combustion Institute*, 33:1319–1330, 2011.

[116] M. Yaldizli, K. Mehravaran, and F.A. Jaberi. Large-eddy simulations of turbulent methane jet flames with filtered mass density function. *International Journal of Heat and Mass Transfer*, 53(11):2551 – 2562, 2010.

[117] N. Ansari, G. M. Goldin, M. R. H. Sheikhi, and P. Givi. Filtered density function simulator on unstructured meshes. *Journal of Computational Physics*, 230:7132–7150, 2011.

[118] N. Ansari, G. M. Goldin, M. R. H. Sheikhi, and P. Givi. Scalar-Filtered Mass-Density-Function Simulation of Swirling Reacting Flows on Unstructured Grids. *AIAA Journal*, 50(11):2476–2482, 2012.

[119] P. P. Popov, H. Wang, and S. B. Pope. Specific volume coupling and convergence properties in hybrid particle/finite volume algorithms for turbulent reactive flows. *Journal of Computational Physics*, 294:110–126, 2015.

[120] R. R. Tirunagari and S. B. Pope. LES/PDF for premixed combustion in the DNS limit. *Combustion Theory and Modelling*, 20(5):834–865, 2016.

[121] L. Han, S. Gong, Y. Li, Q. Ai, H. Luo, Z. Liu, and Y. Liu. A novel theoretical model of breakage rate and daughter size distribution for droplet in turbulent flows. *Chemical Engineering Science*, 102:186–199, 2013.

[122] L. Y. M. Gicquel, P Givi, F. A. Jaberi, and S. B. Pope. Velocity filtered density function for large eddy simulation of turbulent flows. *Physics of Fluids*, 14(3): 1196–1213, 2002.

[123] M. R. H. Sheikhi, T. G. Drozda, P. Givi, and S. B. Pope. Velocity-scalar filtered density function for large eddy simulation of turbulent flows. *Physics of Fluids*, 15 (8):2321–2337, 2003.

[124] M. R. H. Sheikhi, P. Givi, and S. B. Pope. Velocity-scalar filtered mass density function for large eddy simulation of turbulent reacting flows. *Physics of Fluids*, 19 (9):095106, 2007.

[125] M. B. Nik, S. L. Yilmaz, P. Givi, M. R. H. Sheikhi, and S. B. Pope. Simulation of Sandia Flame D Using Velocity-Scalar Filtered Density Function. *AIAA Journal*, 48(7):1513–1522, 2010.

[126] W. P. Jones and S. Navarro-Martinez. Large eddy simulation of autoignition with a subgrid probability density function method. *Combust. Flame*, 150:170–187, 2007.

[127] W. P. Jones and A. Tyliszczak. Large Eddy Simulation of Spark Ignition in a Gas Turbine Combustor. *Flow, Turbulence and Combustion*, 85:711–734, 2010.

[128] W. P. Jones, A. J. Marquis, and V. N. Prasad. LES of a turbulent premixed swirl burner using eulerian field method. *Combustion and Flame*, 159(10):3079–3095, 2012.

[129] M. Jangi, M. Altarawneh, and B. Z. Dlugogorski. Large-eddy simulation of methanol pool fires using an accelerated stochastic fields method. *Combustion and Flame*, 173:89 – 98, 2016.

[130] S. Gallot-Lavallée, W.P. Jones, and A.J. Marquis. Large Eddy Simulation of an ethanol spray flame under MILD combustion with the stochastic fields method. *Proceedings of the Combustion Institute*, 36(2):2577 – 2584, 2017.

[131] F. Sewerin and S. Rigopoulos. An LES-PBE-PDF approach for modeling particle formation in turbulent reacting flows. *Physics of Fluids*, 29(10):105105, 2017.

[132] F. Sewerin and S. Rigopoulos. An LES-PBE-PDF approach for predicting the soot particle size distribution in turbulent flames. *Combustion and Flame*, 189:62 – 76, 2018.

[133] A. Avdić, G. Kuenne, F. Di Mare, and J. Janicka. LES combustion modeling using the eulerian stochastic field method coupled with tabulated chemistry. *Combustion and Flame*, 175:201 – 219, 2017.

[134] L. L. C. Franke, A. K. Chatzopoulos, and S. Rigopoulos. Tabulation of combustion chemistry via Artificial Neural Networks (ANNs): Methodology and application to LES-PDF simulation of Sydney flame L. *Combustion and Flame*, 185:245 – 260, 2017.

[135] M. A. Picciani, E. S. Richardson, and S. Navarro-Martinez. A Thickened Stochastic Fields Approach for Turbulent Combustion Simulation. *Flow, Turbulence and Combustion*, 2018.

[136] B. Chen and M. Oevermann. An Eulerian stochastic field cavitation model coupled to a pressure based solver. *Computers & Fluids*, 162:1 – 10, 2018.

[137] P. Gerlinger. Lagrangian transported MDF methods for compressible high speed flows. *Journal of Computational Physics*, 339:68–95, 2017.

[138] A. G. Nouri, M. B. Nik, P. Givi, D. Livescu, and S. B. Pope. Self-contained filtered density function. *Phys. Rev. Fluids*, 2:094603, 2017.

[139] A. Banaeizadeh, A. Afshari, H. Schock, and F. Jaberi. Large-eddy simulations of turbulent flows in internal combustion engines. *International Journal of Heat and Mass Transfer*, 60:781 – 796, 2013.

[140] A. Irannejad, A. Banaeizadeh, and F. Jaberi. Large eddy simulation of turbulent spray combustion. *Combustion and Flame*, 162(2):431 – 450, 2015.

[141] L. Zhang, J. Liang, M. Sun, H. Wang, and Y. Yang. An energy-consistency-preserving large eddy simulation-scalar filtered mass density function (LES-SFMDF) method for high-speed flows. *Combustion Theory and Modelling*, 22(1): 1–37, 2018.

[142] Y. P. Almeida and S. Navarro-Martinez. Large Eddy Simulation of a supersonic lifted flame using the Eulerian stochastic fields method. *Proceedings of the Combustion Institute*, 37(3):3693 – 3701, 2019. ISSN 1540-7489. doi: https://doi.org/10.1016/j.proci.2018.08.040.

[143] C. K. W. Tam and J. C. Webb. Dispersion-Relation-Preserving Finite Difference Schemes for Computational Acoustics. *J. Comput. Phys.*, 107:262–281, 1993.

[144] J. Berland, O. Bogey, C.and Marsden, and C. Bailly. High-order, low dispersive and low dissipative explicit schemes for multiple-scale and boundary problems. *Journal of Computational Physics*, 224:637–662, 2007.

[145] E. F. Toro, M. Spruce, and W. Speares. Restoration of the contact surface in the HLL-Riemann solver. *Shock Waves*, 4:25–34, 1994.

[146] X. Jiang and C.H. Lai. *Numerical Techniques for Direct and Large-Eddy Simulations*. CRC Press, Boca Raton, 1 edition, 2009.

[147] T.J. Poinsot and S.K. Lele. Boundary conditions for direct simulations of compressible viscous flows. *Journal of Computational Physics*, 101(1):104 – 129, 1992.

[148] C. S. Peskin. Numerical analysis of blood flow in the heart. *Journal of Computational Physics*, 25(3):220 – 252, 1977.

[149] N. Alferez, S. Navarro-Martinez, T. Szemberg O'Connor, E. Touber, and Y. P. Almeida. CompReal User & Developer Manual. Technical report, Imperial College London, 2018.

[150] E. Garnier, M. Mossi, P. Sagaut, P. Comte, and M. Deville. On the Use of Shock-Capturing Schemes for Large-Eddy Simulation. *Journal of Computational Physics*, 153:273–311, 1999.

[151] R. P. Fedkiw, B. Merriman, and S. Osher. Numerical methods for thermally perfect gas flows with chemistry. *Journal of Computational Physics*, 132:175–190, 1997.

[152] J. S. Evans, C. J. Schexnayder Jr, and H. L. Beach Jr. Application of a Two-Dimensional Parabolic Computer Program to Prediction of Turbulent Reacting Flows. Technical report, NASA, 1978.

[153] C. Fureby, G. Tabor, H. G. Weller, and A. D. Gosman. A comparative study of subgrid scale models in homogeneous isotropic turbulence. *Physics of Fluids*, 9(5): 1416–1429, 1997.

[154] S. Hickel, C. P. Egerer, and J. Larsson. Subgrid-scale modeling for implicit large eddy simulation of compressible flows and shock-turbulence interaction. *Physics of Fluids*, 26(10):106101, 2014.

[155] A. N. Kolmogorov. The local structure of turbulence in incompressible viscous fluid for very large reynolds numbers. *Dokl. Akad. Nauk SSSR*, 30 (4), 1941.

[156] A. Y. Klimenko and R. W. Bilger. Conditional moment closure for turbulent combustion. *Progress in Energy and Combustion Science*, 25:595–687, 1999.

[157] S. Navarro-Martinez, A. Kronenburg, and F. Di Mare. Conditional Moment Closure for Large Eddy Simulations. *Flow, Turbulence and Combustion*, 75:245–274, 2005.

[158] R. J. Kee, J. F. Grcar, M. D. Smooke, J. A. Miller, and E. Meeks. A Fortran Program for Modeling Steady Laminar One-Dimensional Premixed Flames. Technical report, Sandia National Laboratories, 1985.

[159] P. J. M. Ferrer, G. Lehnasch, and A. Mura. Compressibility and heat release effects in high-speed reactive mixing layers I.: Growth rates and turbulence characteristics. *Combustion and Flame*, 180:284–303, 2017.

[160] P. J. M. Ferrer, G. Lehnasch, and A. Mura. Compressibility and heat release effects in high-speed reactive mixing layers II. Structure of the stabilization zone and modeling issues relevant to turbulent combustion in supersonic flows. *Combustion and Flame*, 180:304–320, 2017.

[161] D. Papamoschou and A. Roshko. The compressible turbulent shear layer: an experimental study. *Journal of Fluid Mechanics*, 197:453–477, 1988.

[162] R. A. Yetter, F. L. Dryer, and H. Rabitz. A Comprehensive Reaction Mechanism For Carbon Monoxide/Hydrogen/Oxygen Kinetics. *Combustion Science and Technology*, 79:97–128, 1991.

[163] J. H. Bell and R. D. Mehta. Development of a two-stream mixing layer from tripped and untripped boundary layers. *AIAA Journal*, 28(12):2034–2042, 1990.

[164] M. O'Conaire, H. J. Curran, J. M. Simmie, W. J. Pitz, and C. K. Westbrook. A Comprehensive Modeling Study of Hydrogen Oxidation. *International Journal of Chemical Kinetics*, 36(11):603–622, 2004.

[165] B. W. Spencer and B. G. Jones. Statistical investigation of pressure and velocity in the turbulent two-stream mixing layer. *AIAA Journal*, 71:613–628, 1971.

[166] P. Boivin, A. Dauptain, C. Jiménez, and B. Cuenot. Simulation of a supersonic hydrogen–air autoignition-stabilized flame using reduced chemistry. *Combust. Flame*, 159(4):1779–1790, apr 2012.

[167] A. T. Hsu, Y. L. P. Tsai, and M. S. Raju. Probability density function approach for compressible turbulent reacting flows. *AIAA Journal*, 32(7):1407–1415, 1994.

[168] M. Klein, A. Sadiki, and J. Janicka. A digital filter based generation of inflow data for spatially developing direct numerical or large eddy simulations. *Journal of Computational Physics*, 186(2):652 – 665, 2003. ISSN 0021-9991.

[169] J. D. Anderson. *Fundamentals of Aerodynamics*. McGraw-Hill, 2nd edition, 1991.

[170] W. Waidman, F. Alff, U. Brummund, M. B ohm, W. Clauss, and M. Oschwald. Experimental investigation of the combustion process in a supersonic combustion ramjet (SCRAMJET). Technical Report 1-10, German Aerospace Lab - DLR, 1994.

[171] A. D. Cutler, G. Magnotti, L. Cantu, E. Gallo, R. Rockwell, and C. Goyne. Dual-Pump Coherent Anti-Stokes Raman Spectroscopy Measurements in a Dual-Mode Scramjet. *Journal of Propulsion and Power*, 30(3):539–549, 2014.

[172] Z. Huang, G. He, F. Qin, and X. Wei. Large eddy simulation of hydrogen combustion in supersonic flows using an eulerian stochastic fields method. *International Journal of Hydrogen Energy*, 40:9815–9824, 2015.

[173] J. Edwards, A. Potturi, and J. Fulton. Large Eddy/Reynolds-Averaged Navier-Stokes Simulations of Scramjet Combustor Flow Fields. In *48th AIAA/ASME/SAE/ASEE Joint Propulsion conference & Exhibit*, Atlanta, Georgia, July 2012.

[174] C. T. Johansen, C. D. McRae, P. M. Danehy, E. Gallo, L. Cantu, G. Magnotti, A. Cutler, R. D. Rockwell, C. P. Goyne, and J. C. McDaniel. OH PLIF visualization of the UVa supersonic combustion experiment: Configuration a. Technical Report 20120011956, National Aeronautics and Space Administration - NASA, 2012.

[175] R. D. Rockwell, C. P. Goyne, B. E. Rice, H. Chelliah, J. C. McDaniel, J. R. Edwards, L. M. L. Cantu, E. C. A. Gallo, A. D. Cutler, and P. M. Danehy. Development of a Premixed Combustion Capability for Dual-Mode Scramjet Experiments. In *53rd AIAA Aerospace Sciences Meeting*, Kissimmee, Florida, 2015, January 2015.

[176] M. P. Burke, M. Chaos, Y. Ju, F. L. Dryer, and S. J. Klippenstein. Comprehensive H2/O2 kinetic model for high-pressure combustion. *International Journal of Chemical Kinetics*, 44(7):444–474, 2012.

[177] C. J. Jachimowski. An analysis of combustion studies in shock expansion tunnels and reflected shock tunnels. Technical Report 3224, National Aeronautics and Space Administration - NASA, 1992.

Appendix A

Copyright permission

The following is the copyright permission provided by Prof. Andrew Cutler on 11/12/2018 to reproduce the CARS measurements from Cutler *et al.* [171] for comparison purposes.

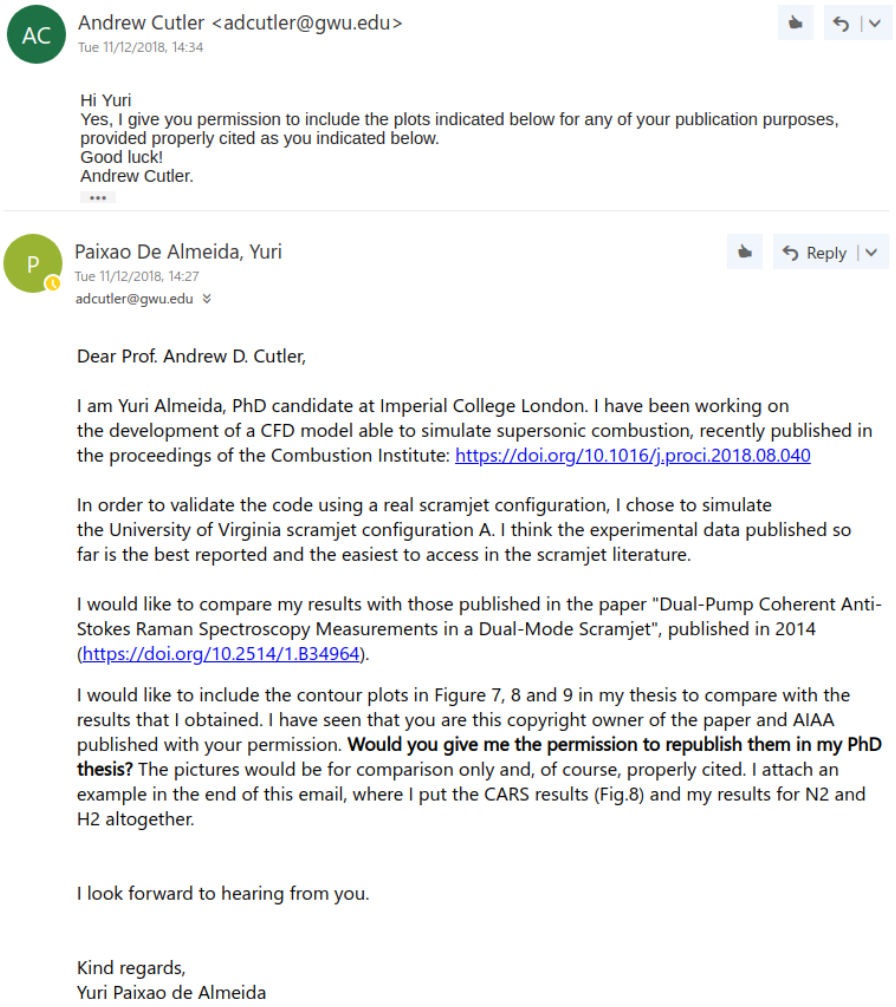

AC

Andrew Cutler <adcutler@gwu.edu>

Tue 11/12/2018, 14:34

Hi Yuri
Yes, I give you permission to include the plots indicated below for any of your publication purposes, provided properly cited as you indicated below.
Good luck!
Andrew Cutler.

P

Paixao De Almeida, Yuri

Tue 11/12/2018, 14:27

adcutler@gwu.edu

Reply

Dear Prof. Andrew D. Cutler,

I am Yuri Almeida, PhD candidate at Imperial College London. I have been working on the development of a CFD model able to simulate supersonic combustion, recently published in the proceedings of the Combustion Institute: https://doi.org/10.1016/j.proci.2018.08.040

In order to validate the code using a real scramjet configuration, I chose to simulate the University of Virginia scramjet configuration A. I think the experimental data published so far is the best reported and the easiest to access in the scramjet literature.

I would like to compare my results with those published in the paper "Dual-Pump Coherent Anti-Stokes Raman Spectroscopy Measurements in a Dual-Mode Scramjet", published in 2014 (https://doi.org/10.2514/1.B34964).

I would like to include the contour plots in Figure 7, 8 and 9 in my thesis to compare with the results that I obtained. I have seen that you are this copyright owner of the paper and AIAA published with your permission. **Would you give me the permission to republish them in my PhD thesis?** The pictures would be for comparison only and, of course, properly cited. I attach an example in the end of this email, where I put the CARS results (Fig.8) and my results for N2 and H2 altogether.

I look forward to hearing from you.

Kind regards,
Yuri Paixao de Almeida

Figure A.1: Copyright permission by Prof. Andrew Cutler from [171] to reproduce figures.